Ph.D. Thesis

Université de Limoges

University of Limoges
ED 653 - Sciences et Ingénierie (SI)
XLIM CNRS UMR-7252 Axe Photonique/Fibre

ALPhANOV
Centre Technologique Optique et Lasers

A thesis submitted to University of Limoges
in partial fulfillment of the requirements of the degree of

Doctor of Philosophy

High Frequency Electronics, Photonics and Systems

Presented and defended by

Joelle YOUSSEF

On July 23, 2026

Improvement of advanced surface plasmonic resonance biosensing platform toward a prototype unit for cancer diagnosis

Thesis supervisors: Georges Humbert, Shuwen Zeng, Sébastien Vergnole

JURY:
Jury President
M. Fabrice Lalloué, Professor, University of Limoges, France
Reporters
Mme. Isabel D. Alves, DR CNRS UMR5248, CBMN Bordeaux
M. Aaron Ho Pui Ho, Professor, Chinese Univ. Hong Kong
Examiners
Mme. Céline Elie-Caille, MCF-HDR, Institut FEMTO-ST
M. Georges Humbert, DR, CNRS – XLIM, Université de Limoges
Mme. Shuwen Zeng, Chargée de recherche CNRS – LN2, Université de technologie de Troyes
M. Sébastien Vergnole, ALPhANOV, Limoges

Licence CC BY-NC-ND 4.0

To everyone who supported me throughout this journey.

Licence CC BY-NC-ND 4.0

Education sows seeds not in you but make your seeds grow

Gibran Khalil Gibran

Licence CC BY-NC-ND 4.0

Acknowledgements

It is with a heart full of emotions that I write these final lines of my thesis. After three and a half years of work, dedication, doubts, challenges, and perseverance, this journey is finally coming to an end. During this period, this thesis occupied a very large place in my life, often requiring long days, continuous effort, and a commitment sometimes leading to 7/7 working days. Many things happened throughout these years, on many levels, and each step contributed in its own way to shaping this experience. Although the path was not always easy, I am grateful for what it taught me, for the people I met, and for the memories I will carry with me. Today, I close this chapter with relief, gratitude, and the joy of having reached the end.

I would like to thank each of my supervisors individually, as each of them has left a unique mark on this thesis. Sébastien, thank you for your valuable remarks, your guidance, and the perspective you brought to this work. Working with you taught me a great deal, especially about how to approach research in an industrially oriented environment, with rigor and efficiency. Shuwen, thank you for your constant scientific and technical support throughout this thesis. Your expertise was extremely valuable in overcoming many experimental and scientific challenges. Georges, thank you for your continuous encouragement, your trust, and your constant presence throughout these years. I am deeply grateful for all the fruitful discussions we had, for the time you dedicated to following the progress of this work, and for the frequent meetings that helped me clarify my ideas, improve the direction of the thesis, and push the work toward better scientific potential.

One of my deepest thanks goes to my friends, whose continuous support helped me reach the end of this thesis. I truly believe that I would not have been able to finish this journey without the people who stood by me, encouraged me, listened to me, and made difficult moments lighter. During these years, some friends became like family to me, and I was lucky to build friendships that I hope will last a lifetime. I would like to warmly thank my closest friends at XLIM, listed alphabetically: Thamila (you're always first), Bruno, Heinich, Kostia, Lucas and Rosu. I am also very grateful to my good friends I met in the way in XLIM and Limoges: Céline, Dina, Emma, Georgia, Giovanni, Hafsa, Igor, Lynn, Malek, Manal, Rehab, Sahar, Yago, and Yassin, for their presence, kindness, and support in different moments of this journey. A special thank you also goes to my office mates and friends, Baptiste and Flavien, for sharing the everyday life of the lab with me, with its discussions, laughs, and challenges. I would also like to thank my favorite and closest Lebanese friends: Fatima, Helena, Isabella, Nicole, Ola, Pascale, and Rand. Your friendship, whether near or far, has always brought me comfort and a sense of home. I am also thankful to all my colleagues at XLIM and ALPhANOV who, in one way or another, contributed to the progress of this thesis and made this experience richer. Finally, I would like to thank my childhood friends, Carole and Noura. Even though life has taken us on different paths and we may have lost touch over time, you still hold a very special place in my heart.

My final and deepest thanks go to my close family and extended family, including my uncles and aunts, for their genuine support from the very first day I arrived in Limoges. Even from a distance, your encouragement, care, and presence accompanied me throughout this journey and gave me strength during difficult moments.

Licence CC BY-NC-ND 4.0

Rights

This creation is available under a Creative Commons contract:
« Attribution-Non Commercial-No Derivatives 4.0 International »
online at https://creativecommons.org/licenses/by-nc-nd/4.0/



Licence CC BY-NC-ND 4.0

Table of Contents

Acknowledgements 5
Rights 6
Table of Contents 7
List of Figures 11
List of Tables 21
Introduction 22
Chapter I. Introduction 24
I.1. Introduction 24
I.2. Surface plasmon resonance biosensors 24
I.2.1. Brief history 24
I.2.2. Fundamentals of SPR 25
I.3. Coupling strategies 28
I.3.1. Coupling incident light to SPWs using prism: Kretschmann and Otto configurations 28
I.3.1.1. Coupling incident light to SPWs using the Kretschmann configuration 28
I.3.1.2. Coupling incident light to SPWs using in Otto configuration 30
I.3.2. Coupling incident light to SPWs using diffraction gratings 30
I.3.3. Coupling incident light to SPWs using guided modes 31
I.3.4. Conclusion 32
I.4. Overview of sensitivity interrogation methods in SPR 33
I.4.1. SPR sensitivity assessment based on intensity, angle and wavelength interrogation methods 33
I.4.2. SPR sensitivity assessment using the phase interrogation method 36
I.4.2.1. Phase interrogation using ellipsometry 37
I.4.2.2. Phase detection using optical heterodyne 38
I.4.2.3. Phase detection using interferometry 38
I.4.3. Conclusion 39
I.4.4. SPR sensitivity assessment based on the GH shift 39
I.5. Overview of commercial SPR platforms and instruments 41
I.6. Presentation of the thesis project 49
I.6.1. Context 49
I.6.2. Presentation of the thesis project 49

Licence CC BY-NC-ND 4.0

Chapter II. Development of a SPR GH prototype 51
II.1. Overview of the original SPR platform 51
II.2. Excitation source 54
II.3. Optimization of the Polarization Control Module 55
II.3.1. Procedure for determining the TM polarization 56
II.3.2. Prevention of PSD saturation with a controlled attenuator 58
II.3.3. Influence of the piezoelectric motor positioning on the GH shift 62
II.3.4. Comparison of the GH measurements with and without a polarization filter after the laser 63
II.4. Optimization of the SPR module 64
II.4.1. Optimization of the prism holder 64
II.4.2. Procedure for determining the resonance angle 67
II.5. Optimization of the detection system 69
II.5.1. Comparison of the diode laser and HeNe laser beam profiles 69
II.5.2. Laser beam displacement without the SPR chip: PSD vs Camera 72
II.5.3. Measurement of the GH shift with a camera and PSD using air as the surrounding environment 73
II.5.4. Measurement of the GH shift with a camera and PSD in a liquid environment 75
II.6. Stability studies 78
II.6.1. Analysis of mechano-optical drifts 78
II.6.1.1. Analysis of the stability of the prototype's optical components 78
II.6.1.2. Analysis of the effect of the environment on the GH measurements 81
II.6.2. Analysis of SPR-related-drift 82
II.6.2.1. Analysis of oil stability 83
II.6.2.2. Analysis of the effect of the holder design 85
II.6.2.3. Analysis of the effect of polarization on the measured drift 87
II.7. Conclusion 88
Chapter III. Development and optimization of SPR chips 89
III.1. Introduction 89
III.1.1. Theoretical background 89
III.1.2. Presentation of the TMM theoretical model 95
III.2. Presentation of SPR chips based on Vandium dioxide and gold 98
III.2.1. Simulation results of SPR chips based on VO_2 using the TMM 100
III.2.2. Experimental testing of the VO_2 based SPR chip 102

Licence CC BY-NC-ND 4.0

III.3. Presentation of SPR chips based on embedded silver NPs in alumina with a gold thin layer above 108
III.3.1. Presentation of the analytical model to simulate SPR chips with embedded NPs in a matrix 110
III.3.2. Experimental evaluation of the SPR chips with embedded NPs 114
III.3.3. Finite-Difference Time-Domain simulations of the N24 SPR chip 118
III.3.3.1. Presentation of the FDTD model 119
III.3.3.2. Validation of the FDTD simulation model with a commercial SPR chip 122
III.3.3.3. FDTD simulation of the N24 SPR chip 123
III.4. Conclusion and perspectives 129
Chapter IV. Analysis of the GH Shift in SPR under rotating incident polarization 131
IV.1. Introduction and context 131
IV.2. Fundamentals of ellipsometry 132
IV.3. Theoretical modelling of the prototype using Jones formalism 136
IV.4. Experimental tests to measure the GH shift under rotating incident polarization 142
IV.5. GH measurements with fast and continuous rotation of the incident polarization 147
IV.6. Comparison of the GH sensitivity obtained at TM polarization and that at an optimized polarization under continuous rotation 150
IV.7. Measurement of the GH sensitivity of the N24 chip with a rotating incident polarization 151
IV.8. Conclusion 152
Chapter V. Application of the SPR sensing platform for the detection of EVs 153
V.1. Introduction and Context 153
V.2. First bio-detection test with the commercial chip 158
V.3. Analysis of the protocol of gold surface functionalization 164
V.3.1. Functionalization protocol based on the modification of the antibody's structure 164
V.3.2. Functionalization of the gold's surface through intermediate linkers 167
V.4. Biodetection tests using APTES-functionalized gold surfaces 172
V.4.1. Detection of CD81 with U87-MG EVs 174
V.4.2. Control experiment: binding of EGFRvIII EVs to c-MET antibodies 179
V.5. Optimization of experimental parameters 182
V.6. Conclusion 184
Conclusion 185
Bibliography 188

Licence CC BY-NC-ND 4.0

Appendices 201
Appendix 1.....202
Appendix 1.1. HeNe laser specifications 202
Appendix 1.2. PSD specifications.....202
Appendix 1.3. Ondax diode laser specifications 203
Appendix 1.4. Piezoelectric motor specifications 203
Appendix 1.5. Updated holder design.....204
Appendix 1.6. Motorized rotational stage selection guide 205
Appendix 1.7. Specifications of the Brushed DC Servo Motor 206

Licence CC BY-NC-ND 4.0

List of Figures

Figure 1 Schematic illustration of the oscillation of SPWs, a) Electric field and charge distribution at the surface of metallic nanoparticles (NPs) and b) Excitation of SPWs at the metal-surrounding interface. 25

Figure 2 Illustration of the wavevector components at the metal-surrounding interface of a multilayer structure consisting of air, metal and surrounding medium. 26

Figure 3 Schematic showing the coupling of the incident light to SPWs with a TM polarized light. 27

Figure 4 Illustration of the dispersion relation of light, where the red lines represent the dispersion relation of light in free space and the blue curve represents the dispersion relation of SPWs. 28

Figure 5 Schematic of the Kretschmann configuration showing the coupling of incident light to SPWs via a prism. 29

Figure 6 Dispersion relations of SPWs (blue curve), light in vacuum (red curve, $\omega = c.k$) and light inside a prism (red dashed curve, $\omega = cn_{prism}\sin\theta$. k). 29

Figure 7 Schematic of the Otto configuration showing the coupling of incident light to SPWs via a prism and gap. 30

Figure 8 Schematic showing the coupling of incident light to SPWs via diffraction gratings. .31

Figure 9 Schematic showing the coupling light of incident light to SPWs with guided modes. 32

Figure 10 Principle of SPR sensing showing the coupling of light to SPWs. The coupling results in a reflectivity dip at the resonance angle θ. Variations in the refractive index of the surrounding induce a shift of the resonance angle Δθ. R and R' represent the incident and reflected intensity, λ and λ' the wavelengths, Δ and Δ' the phases and D the detector. 33

Figure 11 Illustrations showing two different configurations for measuring the resonance angle, a) Schematic of the SPR instrument involving mechanical scanning of the resonance angle, (A) laser, (B) mirror, (C) piezomotor, (D) semi-cylindrical prism, (E) translation stage, (F) quadrant photodiode (QPD), (G) data acquisition (DAQ) card, (H) computer [45] and b) Schematic representing the procedure of finding the resonance angle via a wide-angle incident beam and a CCD camera [47]. 34

Figure 12 Influence of the FWHM on the reflectivity variations at fixed angle. Both curves are simulated using the transfer matrix model (explained in Chapter 3) with air as the surrounding medium. (a) represents a bare Au SPR chip and b) a bare Ag SPR chip.....35

Figure 13 Principle of spectral interrogation in SPR showing the shift of the resonance wavelength (Δλ) with respect to the change in the refractive index of the surrounding medium. The curves are simulated using the transfer matrix model for a bare Au chip with air as the surrounding medium (explained in Chapter 3). 35

Figure 14 Reflectivity and phase vs incident angle in the Kretschmann configuration. The curves are simulated using the transfer matrix model (explained in Chapter 3) for a SPR structure consisting of Ag NPs embedded in alumina with a thin Au layer above with water as the surrounding medium. 36

Licence CC BY-NC-ND 4.0

Figure 15 Principle of phase interrogation in SPR showing the phase variation with respect to the change in the refractive index of the surrounding medium. The curves are simulated using the transfer matrix model for a bare Au chip with water as the surrounding medium (explained in Chapter 3). 37

Figure 16 Schematic representation of an optical heterodyne setup for the extraction of phase. PBS: polarizing beam splitter; M: mirror; BS: beam splitter; AOM: acousto-opto-modulator; Pol: polarization filter; PhD: photo-detector [59]. 38

Figure 17 Schematic of the Mach-Zehnder interferometer for extracting phase in SPR [62]. 39

Figure 18 Schematic showing a SPR chip configuration based on the GH shift. 41

Figure 19 Bionavis MP-SPR system. a) Schematic of the experimental setup consisting of a rotating excitation source (laser), SPR module consisting of SPR chip and a rotating photodetector to measure the SPR reflectivity curves. b) SPR reflectivity curves obtained at 4 excitation wavelengths (670, 785, 850 and 980 nm) with Bionavis MP-SPR system [72].....42

Figure 20 Schematics of Bruker SPR systems, a) Illustration of the experimental setup showing a high-power laser, Acousto-Optic Deflector (AOD) ensuring fast scanning of the incident angle to find the resonance angle, SPR module and high-speed camera as a detector. b) Illustration of the muli-channel architecture and HI technology [74]. 43

Figure 21 Schematic of Nicoya's LSPR detection principle [75]. 44

Figure 22 Illustration of Nicoya's DMF module [77]. 44

Figure 23 Illustration of Biosensing instruments SPR system based on the angular interrogation method. The angular shift of the resonance angle is detected by measuring the spatial displacement of the reflectivity dip [78]. 45

Figure 24 Illustration of Biosensing instruments SPRM setup. It consists of a light source, microfluidic module, SPR module and SPRM detector [79]. 46

Figure 25 Illustration of Reichert technologies SPR system based on the angular interrogation method. a) A divergent beam is incident on a fixed SPR module, and the angular change of the resonance angle is detected by a photodiode array. b) Typical SPR reflectivity curves obtained by Reichert SPR systems [81].....46

Figure 26 Schematic illustration of the original SPR platform [67]. 49

Figure 27 Reference platform showing a neutral density filter (ND), mirrors (M), polarized beam splitters 1 and 2 (PBS1 and PBS 2), chopper (C), rotational stage (RS), prism holder (PH) and position sensitive detector (PSD). 51

Figure 28 Photograph of the SPR module. It consists of a prism, a SPR chip, a fluidic channel, an injection tube, a mechanical joint, manual rotation and translation stages. The holder along with a screw pressing mechanism and a 3d printed v-groove are used to fix the assembly altogether. 53

Figure 29 Schematic of the prototype showing a motorized mulitposition slider with neutral density filters (MND), mirrors (M1 and M2), polarization filter (P), half waveplate (λ/2), rotational stage (RS), prism holder (PH) and position sensitive detector (PSD). 56

Figure 30 Schematic of the commercial SPR chip coupled with a SF11 prism. 57

Licence CC BY-NC-ND 4.0

Figure 31 Measurement of the reflected intensity vs the polarization angle of the waveplate. The TM and TE polarizations respectively correspond to the polarization angles producing the minimum and maximum reflected intensity. 57

Figure 32 Illustration of the SPR prototype composed of mirrors (M1 and M2), two polarization filters (P1 and P2), a half waveplate (λ/2), a rotational stage (RH), a prism holder (PH) and position sensitive detector (PSD). 59

Figure 33 Measurement of the position x of the reflected beam. The red curves represent the attenuation with P2 and the black curves represent the attenuation using neutral density filters placed on the motorized slider. 60

Figure 34 Measurement of the GH shift between water and 1% glycerin, a) Without P2 and b) With P2.....61

Figure 35 Illustration of the holder used for air measurements. 62

Figure 36 Measurement of the position x of the reflected beam for 10 cycles of TM and TE.63

Figure 37 Measurement of the GH shift between water and PBS, a) With P1 and b) without P1.....64

Figure 38 Illustration of the newly developed holder. The commercial chip coupled with SF11 prism was installed on the holder.....65

Figure 39 Illustration of the commercial SPR chip fixed on a prism via an oil drop. 65

Figure 40 Illustration of the prism-chip assembly placed on the v-groove of the holder.....66

Figure 41 Illustration of the final assembly. 66

Figure 42 Schematic of the commercial SPR chip coupled with SF11 prism. It shows the two reflection spots known as R and SPR. 67

Figure 43 Geometrical layout of the optical components in the prototype. The dashed line and dotted lines represent two laser beams reflecting from Mirror 2, with an angular span of 0.4°. 68

Figure 44 Measurement of the GH shift versus the incident angle inside the prism. 69

Figure 45 Visualization of the laser beams, a) HeNe laser beam profile and b) Ondax Diode laser beam profile. 70

Figure 46 Measurement of the GH shift between water and PBS with the commercial chip. a) The GH shit was measured with the reference platform and b) with the prototype. 70

Figure 47 Schematic of the N1 chip. The diameter of the Ag NPs is 4.4 ± 1.4 nm. Alumina and Au thickness are 12 and 50 ± 1 nm respectively. 71

Figure 48 Measurement of the GH shift between water and PBS with the N1 chip. a) The GH shit was measured with the reference platform and b) with the prototype. 71

Figure 49 Visualization of the diode laser beam spot directly after PBS2. 72

Figure 50 Schematic of a SPR chip consisting of 47 nm Au deposited on sapphire with 3 nm titanium.....74

Figure 51 Visualization of the laser beam spot in air using the commercial SPR chip at, a) TM polarization and b) TE polarization. 74

Licence CC BY-NC-ND 4.0

Figure 52 Visualization of the laser beam spot in air using the sapphire chip at, a) TM polarization and b) TE polarization. 74

Figure 53 Visualization of the R and the SPR spots while measuring the GH shift in water, a) TM polarization and b) TE polarization. R represents the beam reflected at the SF11-BK7 interface and SPR represents the beam that refracts at the SF11-BK7 interface and couples with SPWs. 76

Figure 54 Fresnel reflection coefficient at the interface between SF11 prism and BK7 for TM and TE polarizations. 77

Figure 55 Measurement of the position x of the excitation source directly after turning on the laser. 79

Figure 56 Position x measured when the PSD is placed, a) after mirror 1, b) after mirror 2 and c) after the polarization switching module. 80

Figure 57 Influence of the ambient temperature on, a) Position x, b) Power of the reflected beam under TM polarization. 81

Figure 58 Effect of stray light on, a) Position x and b) Power of the reflected beam under TM polarization. 82

Figure 59 Measurement of the, a) Position x and b) Power using oil Bottle 1. 83

Figure 60 Measurement of the, a) Position x and b) Power using oil Bottle 2. 84

Figure 61 Measurement of, a) Position x and b) Power under TM polarization for 5 minutes and using the old holder. 85

Figure 62 Measurement of, a) Position x and b) Power under TE polarization for 5 minutes and using the old holder. 85

Figure 63 Measurement of, a) Position x and b) Power under TM polarization for 5 minutes and using the newly developed holder. 86

Figure 64 Measurement of, a) Position x and b) Power under TE polarization for 5 minutes and using the newly developed holder 86

Figure 65 Measurement of the position x under alternating TM and TE polarizations. 87

Figure 66 Schematic of the coupling of incident light to SPWs in the Kretschmann configuration. 90

Figure 67 Schematic of the experimental procedure to measure the reflectivity curve illustrating the angular scanning of the incident light. 91

Figure 68 Reflectivity (R) versus the angle if incidence inside the prism for various Au thicknesses 15-110 nm. The SPR chips consist of a BK7 prism, Titanium adhesion layer of 2 nm, Au and air as the surrounding medium. 92

Figure 69 Reflectivity and phase vs incident angle inside the prism (simulated using the TMM explained in Section III.1.3). 93

Figure 70 Schematic of a multilayer system showing an incident TM polarized light on a multilayer SPR chip. $\mathrm{E}+$ and $\mathrm{E}-$ are defined as the forward and backward transmitted fields along the normal of the interfaces. $\mathrm{En}+$ and $\mathrm{En}-$ represent the electric fields at the interface of layer n-n+1 and $\mathrm{En}'+$ and $\mathrm{En}'-$ at the interface of layer (n-1)-n (in this case n=2). 96

Licence CC BY-NC-ND 4.0

Figure 71 Experimental and theoretical reflectivity curves for a structure consisting of 48 nm Au, 2 nm Ti and BK7 prism tested in air as the surrounding medium. 98

Figure 72 Schematic of the proposed SPR chip composed of VO_2 layer deposited on sapphire substrate with an Au layer above. 99

Figure 73 TM reflection coefficient calculated at the interface between sapphire-VO_2 and between SF11-BK7. 99

Figure 74 Schematics comparing the reflection between SF11-BK7 and sapphire-VO_2. 100

Figure 75 Complex refractive index of VO_2 vs wavelength at 20°C. 100

Figure 76 Reflectivity vs incident angle at the base of SF11 prism for a) Au: 45-50 nm, Ti: 2 nm and VO_2: 7 nm, b) Au: 47 nm, Ti: 1-4 nm and VO_2 7 nm and c) Au: 47 nm, Ti: 2 nm and VO_2 0-9 nm.....101

Figure 77 SPR curves comparing two chips with and without VO_2. a) Reflectivity vs incident angle and b) GH shift vs incident angle. 102

Figure 78 Illustration of the Magnetron sputtering process [110].....103

Figure 79 Measurements of the experimental reflectivity curve. The blue curve represents the SPR chip without VO_2 and the red with VO_2. 103

Figure 80, a) Measured differential GH shift for different glycerin concentrations for the SPR chip (a) without a VO_2 layer (b) with a VO_2 layer, c) Linear fit of the experimental data. 105

Figure 81 Variation of resonance ($\Delta\theta$) angle calculated with respect to the refractive index of the surrounding medium. 105

Figure 82 Calculated GH shift for three different solutions, Water, PBS and $n_{PBS}+10^{-4}$ RIU. 106

Figure 83 Measurement of the GH shift with diluted BSA solutions and the VO_2-based chip, a) Evolution of the GH shift during successive injections of BSA, b) logarithmic fit of the experimental data. 107

Figure 84 Schematic of the SPR structure consisting of embedded Ag NPs in alumina with a thin layer of Au above. 108

Figure 85 Schematic representation of the PLD chamber and Pulsed Laser NP generator chamber. The entire nanostructure is produced inside the reactor within a singular deposition process. Thin films are generated using PLD, while the Ag NPs are synthesized with the NP generator. The alumina oxide matrix and the Ag NPs are deposited by a combination of PLD and the NP generator, either sequentially or simultaneously. Finally, a Au top layer is deposited by PLD [117]. 109

Figure 86 Schematic of the FCG. 109

Figure 87 Illustration representing, a) Maxwell-Garnett and b) Bruggeman structures [126]. 110

Figure 88 Schematic of the multilayer model used to represent the embedded Ag NPs in alumina in the TMM. 111

Figure 89 Calculated reflectivity curves for different NPs concentrations for a structure consisting of Ag NPs with a radius of 1 nm, embedded in an alumina matrix of 12 nm, with Au

Licence CC BY-NC-ND 4.0

layer (t = 49 nm) on the top, a) Reflectivity vs incident angle and b) Minimum reflectivity vs concentration of NPs. 112

Figure 90 Reflectivity curves showing the effects of a) Au thickness with 12 nm alumina, r =1 nm and f=16%, b) radius of the NPs with alumina 12 nm, Au 49 nm and f=16%, c) effect of alumina thickness with r =1 nm, f=16% and Au 49 nm. 113

Figure 91 Measurement of the commercial, N1, VAl8, N4 and N5 chips with diluted glycerin. Au and alumina thicknesses are 48 and 12 nm respectively for all samples except the commercial. VAl8 is composed of a layer of alumina with NPs and N1, N4, N5 have Ag NPs embedded with concentrations ranging from the lowest (N1) to the highest (N5). Figures (a), (b), (c), (d),(e) show the differential GH shift for different glycerin concentrations, a) N1 chip, b) N4 chip, c) N5 chip, d) VAl8 chip, e) Commercial chip, and f) Linear fit of the experimental data. 114

Figure 92 Measurement of the reflected intensity versus the incident angle for N5 and commercial chips tested in water. 115

Figure 93 Measurement of the GH shift with diluted BSA solutions and the N5 chip, a) Evolution of the GH shift during successive BSA injections and b) Logarithmic fit of the experimental data. 116

Figure 94 Measurement of, a) N5, b) N24 chips with diluted glycerin solutions and c) Linear fit of the experimental data. 117

Figure 95 Cross-sectional images of N24 chip taken using HRTEM. a) HR-TEM image of Ag NPs deposited on a TEM grid, 200000× magnification. b) The corresponding statistical analysis over the diameter of the particles. The center of the distribution and mean diameter is μ = 2.3 nm, the standard deviation is σ = 0.8 and the FWHM is ξ = 1.7 nm. c) HR-TEM cross section image presents the architecture of the nanocomposite, 100000× magnification. Images from [117]. 118

Figure 96 Illustration of the FDTD model for coupling the incident light to SPWs excited between Ag and air. 119

Figure 97 SPR reflection curve obtained by varying the position of the source with respect to the glass-metal boundary. Position 1 at 200 nm, Position 2 at 400 nm and Position 3 at 600 nm from the interface.....120

Figure 98 Reflectivity curve of a glass-Ag-air SPR chip computed with FDTD. In this case, the source is positioned at the glass-Ag boundary.....120

Figure 99 Electric field map, normalized amplitude Re (Ex) and phase Imaginary (Ex), a-b) for normal incidence, c-d) at 20^{o} incidence and e-f) at the SPR resonance angle (46.8^{o}). 121

Figure 100 Schematic of the FDTD model used to simulate the commercial chip in water. The green rectangle represents a mesh point that can be used to extract phase data. 122

Figure 101 SPR curves for a commercial chip computed by the TMM and by FDTD, a) Reflectivity vs incident angle inside the prism and b) Phase vs incident angle inside the prism. 123

Figure 102 Schematic of the FDTD model used for simulating the N24 sample. 123

Licence CC BY-NC-ND 4.0

Figure 103 Normalized power map for a chip with NPs, a) at resonance θ=54.09°, b) outside resonance θ=52.93°, c) Without NPs at resonance θ=54.12° and d) represents the 2D distribution of the NPs inside alumina. 124

Figure 104 Optical absorption spectrum of N24 (without an Au layer). 125

Figure 105 2D phase map of, a) Chip without NPs at resonance, b) Chip with NPs outside of resonance, c) Chip with NPs at resonance, d) phase shift with respect to incident angle at the base of the prism for both chips with and without NPs. The curves were extracted from a mesh point in the reflection region. 126

Figure 106 Phase maps of SPR chips with two types of NPs: Ag NPs and Au NPs, both of which are embedded in alumina. (a) Phase vs incident angle incident prism obtained with FDTD for Ag NPs (red) and Ag NPs (black) embedded in Al_2O_3. (b) Phase map at the resonance angle with Ag NPs embedded in a 12 nm alumina. (c) Phase map at the resonance angle with Au NPs embedded in 12 nm alumina. 127

Figure 107 Comparison of the effects of different dielectric matrixes with Ag NPs, a) Phase vs incident angle incident prism obtained with FDTD for Alumina matrix (red), silica matrix (black) and Air matrix (blue). b) Phase map at the resonance angle with Ag NPs embedded in a 12 nm alumina. (c) Phase map at the resonance angle with Ag NPs embedded in 12 nm Silica matrix. (d) Phase map at the resonance angle with Ag NPs embedded in 12 nm Air matrix. 128

Figure 108 Identification of TM polarization using a waveplate. a) Illustration of the setup consisting of a diode laser at 633 nm, mirrors (M1 and M2), polarization filters 1 and 2 (P1 and P2), half-waveplate (λ/2) on a rotational mount, rotational stage (RS), prism holder (PH) and PSD. b) Reflected intensity vs polarization angle of the waveplate. TM is identified as the polarization angle with the minimal reflected power at resonance. 131

Figure 109 Schematic illustration of the principles of ellipsometry measurements showing (a) a laser (L), polarization filter (P), sample (S), analyzer (or A, rotating polarization filter) and detector (D). β is the rotation angle of the analyzer and β_m is the azimuth of the polarization ellipse of the reflected beam. r_{TM} and r_{TE} are the Fresnel reflection coefficients for TM and TE polarization. b) Schematic illustration of a sample three-layers structure tested in ellipsometry where I and R respectively represent the incident and reflected lights, θ the angle of incidence and d the thickness of layer 1. 132

Figure 110: Typical intensity vs polarization angle obtained in ellipsometry. r_{TM} and r_{TE} respectively represent the amplitudes of measured at TM (0°) and TE (90°) polarizations and β_m represents the azimuth of the polarization ellipse defined as the analyzer angle at which the detected intensity is maximal. 134

Figure 111 a) Representation of the prototype with a rotating waveplate showing a laser (L), polarization filters 1 and 2 (P1 and P2), rotating waveplate (W), sample (S), and PSD. (b) Representation of the prototype with Jones matrices. In this configuration, the z axis represents the TM polarization and y the TE polarization. 137

Figure 112 Simulated SPR reflectivity curves versus the angle (β) of the waveplate, for water, 1% glycerin and 5% glycerin. 139

Figure 113 Simulated SPR reflectivity curves versus the angle of the waveplate for water, 1% glycerin and 5%. a) γ=90° (P2 oriented parallel to TE polarization, meaning it transmits all TE

Licence CC BY-NC-ND 4.0

polarized light), and b) γ=0° (P2 oriented parallel to the TM polarization, meaning it transmits all TM polarized light). The intersection of the three curves is marked by a circle. 140

Figure 114 Simulated SPR reflectivity curves versus the waveplate polarization angle for water, 1% glycerin and 5% glycerin. a) γ=20°, b) γ=10°, c) γ=1° and d) γ=0.1°. In all four cases γ<45° meaning P2 transmits more TM polarized light and attenuates TE. The dashed lines in black, red and blue respectively represent the angular position of the first maximum. The circle represents the intersection points of the three curves. 141

Figure 115 Simulated SPR reflectivity curves versus the angle of the waveplate for water, 1% glycerin and 5% glycerin. The polarization angle of P2 is 10°. TE polarization is located at 135° and TM at 180°. 142

Figure 116 Stability measured over 10 minutes using the commercial chip at the TM polarization and with water as the surrounding environment. (a) Power and (b) x Position on the PSD. 143

Figure 117 Measurement of (a) x Position and (b) Power with respect to the angle of the waveplate for 3 solutions: water, 1% and 5% glycerin. 144

Figure 118 Differential GH shift between glycerin solutions and water as a function of the polarization angle. 145

Figure 119 Measurement of the position x of the reflected beam versus the angle of the waveplate. The curves were obtained at the resonance angle of the commercial SPR chip with water as the surrounding environment. The curves were acquired at r =0.5,1 and 2.5. Δθ represents the difference between the angles of the first maximum and the first minimum. 146

Figure 120 Measurement of the velocity profile of the brushed DC servo motor. The blue curve represents the actual velocity profile obtained and the red dashed line represents the expected velocity profile.....147

Figure 121 Measurement of the position x of the reflected beam for 10 cycles (10x360°) of the waveplate rotation. Evolution of a) the position x, b) zoom in section of (a), c) the position of the minima, d) the time difference bewteen 2 consecutives mimuma and maxima, e) the exctracted position at a fixed polarization angle of 100°.....148

Figure 122 Illustration showing the angular position shift and the minimum position shift between water and 5% glycerin. 149

Figure 123 Measurement of the GH shift between water and 1% glycerin measured at, a) the TM polarization subtracted from TE and b) at the optimized polarization angle subtracted from TE. 150

Figure 124 Evaluation of the N24 chip under rotating incident polarization, a) Position x of the reflected beam measured by the PSD vs waveplate rotation, b) zoom in section of a), c) Linear fit of the GH shift extracted for 3 different configurations: Displacement of the minimum, GH shift at TM polarization (extracted from Chapter 3, Section III.3.2) and GH shift at the optimized polarization angle 70°, d) shift of the polarization angle, experimental and linear fit. 151

Figure 125 Illustration showing the glioblastoma detection procedure. 153

Figure 126 Illustration of surgical and liquid biopsies. 154

Figure 127 Illustration showing the composition of EVs [163]. 154

Licence CC BY-NC-ND 4.0

Figure 128: Position x measured for 10 minutes at the resonance angle under TM polarization and with water as the surrounding environment. 158

Figure 129 Calibration of the commercial chip before biodetection, a) GH shift for Water, PBS and different glycerin concentrations, b) Linear fit. 159

Figure 130 Illustration showing the effect of the choice of the measurement angle (measurement angle is the resonance angle found experimentally) on the measured GH shift, a) The measurement angle found is exactly at the resonance angle of the PBS GH curve and b) The measurement angle is far from the resonance angle of the PBS GH curve. 160

Figure 131 Illustration of the functionalization procedure of the gold's surface based on Au-SH semi-covalent bonds 161

Figure 132 Measurement of the GH shift as a function of time for successive injections of PBS, CD81 AB and PBS to rinse antibodies. 161

Figure 133 Measurement of the GH shift as a function of time for successive injections of PBS, EGFRvIII EVs diluted at 10^6 EVs/ml and PBS. 162

Figure 134 Functionalization of gold with CD81 antibodies. a) Position x with respect to the waveplate rotation, b) zoom in of (a) and c) GH shift of the minima subtracted from TE. 163

Figure 135 Attachment of EGFRvIII EVs at 10^6 EVs/ml to CD81 ABs. a) Position x with respect to the waveplate rotation, b) zoom in of (a) and c) GH shift of the minima subtracted from TE. 164

Figure 136 Schematic of the antibody's structure. 165

Figure 137 Illustrations showing the modification of the antibody structure by (a) partial reduction of AB using TCEP. The disulfide bridges (marked in red) are broken and free -SH groups are liberated. (b) The creation of free thiol groups. First, the structure of the antibody is broken using Pepsin. Then, the disulfide bonds are broken through TCEP reduction agent. (c) The thiolation of the AB using Traut's agent. Free amine molecules on lysine groups (represented by green lines) are replaced by thiol groups (represented by black lines). 166

Figure 138 Illustration showing the functionalization of gold with MUA (11-Mercaptoundecanoic acid). 167

Figure 139 Illustration showing the binding of antibodies to gold through their COO- groups, and with an intermediate layer of APTES. 168

Figure 140 Illustration showing the attachment of antibodies with an intermediate layer of APTES and an oxidized gold surface. 168

Figure 141 Illustration of the binding of AB on gold with intermediate layers of MPTMS and APTES. 169

Figure 142 Illustration of the binding of AB on gold with intermediate layers of MUA and protein A (oriented immobilization of AB) 170

Figure 143 Visualization of the commercial chips treated with secondary fluorescent CD81 antibodies, I) No treatment+ fluorescent antibody, II) No treatment + CD81 antibody +fluorescent antibody, III) KOH+ water + CD81 antibody + fluorescent antibody, IV) KOH + water + APTES+ CD81 antibody+ fluorescent antibody, and V) APTES+ CD81 antibody+ fluorescent antibody. 171

Licence CC BY-NC-ND 4.0

Figure 144 Position x measured for 5 minutes at the resonance angle of water under TM polarization. 172

Figure 145 Calibration curves of the N24 chip with the rotation waveplate interrogation method, a) Position x of the reflected beam vs waveplate rotation, b) zoom in section of (a), c) Differential GH shift extracted for 2 different configurations: GH shift at the optimized polarization angle 100° and average displacement of the minima and, d) shift of the polarization angle (experimental and linear fit). 173

Figure 146 Functionalization of gold with APTES, a) Position x with respect to the waveplate rotation, b) zoom in of (a) and c) GH shift of the minima subtracted from TE. 174

Figure 147 Attachment of CD81 AB to APTES, a) Position x with respect to the waveplate rotation, b) Zoom-in of a) and c) Evolution of the position of the minima (each point represents the average of 4 minima) within 1 hour incubation of the AB. 176

Figure 148 Attachment of U87 MG EVs diluted at 10^2 EVs/ml to CD81, Position x measured with respect to the waveplate rotation, b) Zoom-in of a) and c) Evolution of the position of the minima (each point represents the average of 4 minima) within 1 hour incubation of the EVs. 177

Figure 149 Attachment of U87 MG EVs diluted at 10^4 EVs/ml to CD81, Position x with respect to the waveplate rotation, b) Zoom-in of a) and c) Evolution of the position of the minima (each point represents the average of 4 minima) within 1 hour incubation of the EVs. 178

Figure 150 Functionalization of gold with APTES, a) Position x with respect to the waveplate rotation, b) zoom in of (a) and c) GH shift of the minima subtracted from TE. 180

Figure 151 Attachment of c-MET ABs to APTES, a) Position x measured with respect to the waveplate rotation, b) zoom in of (a) and c) GH shift of the minima subtracted from TE. 181

Figure 152 Attachment of EGFRvIII EVs to c-MET ABs, a) Position x of the reflected beam measured with respect to the waveplate rotation, b) zoom in of (a) and c) GH shift of the minima subtracted from TE. 182

Figure 153 Binding curve of CD81 to APTES adsorbed on a commercial gold chip, a) PBS rinse with a 500 µl/min flow rate and b) PBS rinse with a 1000 µl/min flow rate. 183

Figure 154 Binding of APTES to gold after using the N24 chip 7 times. 184

Licence CC BY-NC-ND 4.0

List of Tables

Table 1 Overview of commercial SPR systems where RU refers to response unit (1 RU=10^{-6} RIU=1 pg/mm^2), pg/mm^2 refers to the mass absorbed per unit area. 48

Table 2 Laser selection guide. 55

Table 3 Standard deviation in x and y positions measured using two different attenuation methods: neutral density filters on a motorized slider and P2. There are a total of 360 measurement points for each test. 60

Table 4 GH shift measured with and without P2. 61

Table 5 Comparison between the PSD and the camera by measuring the diode laser position shift after the rotating mirror M2. 73

Table 6 GH shift measured by the PSD and Camera with commercial and sapphire chips in air. 75

Table 7 GH shift between water and 1% glycerin measured by the PSD and camera. 78

Table 8 Standard deviation of the position x measured when the PSD is placed, after mirror 1, after mirror 2 and after the polarization switching module. 80

Table 9 Stability comparison of oil bottles 1 and 2 for a total of 120 data points per test. 84

Table 10 Stability of the position x of the reflected beam under TM and TE polarizations and over 20 minutes continuous measurements. 88

Table 11 Summary of SPR structures and their experimental sensitivities. (GST = $Ge_2Sb_2Te_5$, TNFα = Tumor Necrosis Factor alpha). 94

Table 12 Refractive index of diluted glycerin solutions. 104

Table 13 Angular distance between first maximum and first minimum for 3 different r values. 146

Table 14 Comparison of commonly used techniques for the detection of EVs. 156

Table 15 PBS baseline-APTES GH shift after PBS rinse measured with C1, C2 and C3. 175

Table 16 PBS baseline-AB GH shift after PBS rinse measured with C1,C2 and C3. 176

Table 17 PBS baseline-U87 MG EVs (at 10^2 EV/ml) GH shift after PBS rinse measured with C1, C2 and C3. 178

Licence CC BY-NC-ND 4.0

Introduction

Recent studies have shown increasing tendency for younger generations (born between 1981 and 1996) to develop various types of cancer partly due to the recent changes in environmental and lifestyle conditions [1]. In particular, the International Agency for Research on Cancer predicts that the number of new cancer cases will reach around 35 million by 2050, representing a 77% increase compared with 2022. Furthermore, they anticipate a doubling of cancer mortality by 2050 [2]. This fact highlights the urgent need for new prevention and treatment techniques, as well as the development of early diagnostic tools to improve treatment efficiency and expand survival rate.

Biosensors have emerged as tools for early cancer diagnostics owing to their interesting characteristics allowing specific, non-invasive and fast detection along with their compatibility with complex biological media. In simple terms, a biosensor is a device that measures the concentration of a biological molecule and identifies its type. This can be achieved by tracking the binding of the molecule (analyte) to a target recognition probe (such as an antibody AB, aptamer, DNA or enzyme). A readable signal proportional to the concentration of the target analyte bound to the surface is then generated and analyzed [3].

The earliest use of biosensors dates to the 1950s when Leland C. Clark, Jr, developed the first oxygen detector enabling the future measurement of glucose levels, later known as the 'Clark electrode' [3]. This was then followed by decades of scientific progress towards the development of biosensors for various applications: drug discovery, disease detection, environmental monitoring and food quality monitoring [3]. In 1975, Yellow Springs Instrument Co. (YSI) developed the first commercial biosensor intended to detect glucose based on Clark's early findings representing the first time a biosensor was sold for clinical usage [3,4].

Biosensors can be classified into various types depending on the transduction mechanism (detection method). The interaction between a target probe and analyte can be detected by [5]:

- **Optical biosensors:** They detect changes in the properties of light such as intensity, phase, wavelength, polarization. These include but are not limited to interferometric, ellipsometry, resonators, refractometers, Raman and plasmonic biosensors.
- **Electrochemical biosensors:** They measure changes in the electrical signal such as current, potential and conductance [6]. These include amperometric, potentiometric, impedimetric and voltammetric biosensors [7].
- **Piezoelectric biosensors:** They detect changes in mass at a sensor surface, typically a quartz crystal microbalance (QCM) [8].
- **Thermal biosensors:** They detect changes in heat or temperature absorbed during biological interactions. These include calorimetric, thermometric and thermistor-based biosensors [9].

Optical biosensors, in particular, have attracted attention due to their high sensitivity and capacity to monitor biomolecular interactions in a non-invasive manner. In particular, plasmonic biosensors, notably surface plasmon resonance (SPR) detectors, have emerged as powerful tools due to their ability to perform fast, real-time detection with high sensitivity and without additional labelling steps, making them particularly suited to biomedical applications [10]. Due to its many advantages, SPR has been widely used in literature for a variety of

Licence CC BY-NC-ND 4.0

applications. Moreover, commercial SPR platforms have been developed and sold by several companies, most notably Biacore and Bruker.

An existing SPR platform was originally introduced at XLIM by Shuwen Zeng. It is based on a novel detection method that uses the Goos–Hänchen (GH) shift to improve the sensitivity of SPR. This thesis focuses on developing a miniaturized, stable and easy-to-use version of the SPR platform for primarily detecting glioblastoma biomarkers, an aggressive form of brain cancer. To better explain the development of the prototype, this thesis is divided into five chapters.

The first chapter offers a detailed introduction to SPR, providing an overview of its operating principles and theory. It presents the various coupling and interrogation methods used in SPR, highlighting the GH effect. It also reviews the various commercial SPR platforms available in the market.

The second chapter outlines the primary limitations of the reference platform and describes the process of designing the new prototype. We also validate the performance and stability of the prototype to ensure the reliability of future measurements.

Chapter 3 covers the two types of SPR chips that were designed in collaboration with our partners to improve GH sensitivity. It introduces the simulations and experiments conducted as part of these developments.

After presenting the SPR chips with improved sensitivity, we describe a modification made to the prototype to facilitate the experimental procedure in chapter 4. Furthermore, we present the related theoretical framework and experimental tests.

Finally, Chapter 5 introduces the biodetection experiments that were performed to demonstrate the reliability of the prototype for future cancer detection.

Licence CC BY-NC-ND 4.0

Chapter I. Introduction

I.1. Introduction

The first chapter of this thesis aims to present the scientific and technological context of SPR. It starts with an overview of the history of SPR biosensors. It then presents the fundamental principles of SPR, the different configurations and interrogation methods. Special attention is given to explaining the concept of the GH shift, which represents the detection method employed in this thesis. In short term, the GH shift represents the later displacement of the reflected beam observed at total internal reflection. We then present an overview of commercial SPR sensors available in the market. The final part of the chapter outlines the thesis project, which focuses on developing an easy-to-use SPR prototype for the detection of extracellular vesicles (EVs).

I.2. Surface plasmon resonance biosensors

I.2.1. Brief history

In 1902 Wood noticed an interesting phenomenon consisting of dark and light bands upon illumination of a metallic grating with polarized light. This observation was not understood at the time and was labelled back then as “Wood anomaly” [11]. The first theoretical interpretation of these anomalies was conducted by Rayleigh in 1907 by shining a white light source on a metallic diffraction grating [12]. He observed that the intensity of reflected light varies abruptly at certain wavelengths. These wavelengths, now known as Rayleigh wavelengths, correspond to the case where one of the diffraction orders can no longer propagate in air, but instead travels in a direction parallel to that of the diffraction grating [13]. Palmer experimentally confirmed this information by demonstrating that the existence of anomalies is rather polarization dependent, particularly with deeper diffraction gratings [14,15].

In 1939, Fano presented his interpretation of Wood anomalies, suggesting that they might be associated with the excitation of electromagnetic surface waves at the interface between the metal and air. These waves propagate along the interface, with their electromagnetic field decaying exponentially in the perpendicular direction. Fano demonstrated that light in air cannot excite these waves since it lacks the necessary momentum. However, the diffraction grating structure provided the additional momentum required to satisfy the coupling conditions, enabling the incident light to couple with these surface waves [16]. In the early fifties, further experimentation was performed on metallic thin films with Pines and Bohm suggesting that energy loss (attenuation of light) is due to the excitation of the metal’s conduction electrons leading to the formation of plasma waves [17–19].

It was not until 1957 that Ritchie theoretically demonstrated the existence of surface plasmon waves (SPWs) at the surface of metal [20]. Later on in 1958, Stern and Ferrell calculated for the first time the dispersion relation of the SPWs at the surface of the metal [21]. Subsequently in 1960, Powell and Swan experimentally demonstrated the existence of SPWs by observing the excitation of collective electronic modes at the interface of a metal through electron energy-loss spectroscopy [22].

Shortly after, in 1968, Otto proposed an experimental configuration to couple incident light to SPWs via a high refractive index prism [23] which was modified by Kretschmann in the same year [24]. The first documented usage of SPR was conducted by Nylander and Liedberg for the detection of gas in 1982 using Kretschmann configuration [25].

Licence CC BY-NC-ND 4.0

I.2.2. Fundamentals of SPR

Plasmonic metals such as gold (Au), silver (Ag), copper (Cu) or aluminum (Al) typically possess a high density of free electrons in their conduction band (~10^{22} particles/cm^3 [26]). These electrons are delocalized and can move freely within the metal. They can be induced into resonance when excited by incident light that satisfies certain conditions. This produces a highly localized electromagnetic field near the metal's surface, which decays exponentially in both media (Figure 1). The collective oscillation of free electrons is known as SPWs. This results in a high sensitivity of the metal with respect to its surrounding environment due to the strong electromagnetic field created at the vicinity of the metal [27].

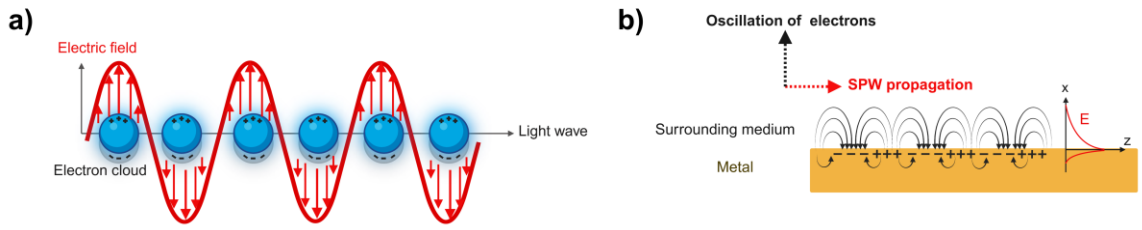


Figure 1 Schematic illustration of the oscillation of SPWs, a) Electric field and charge distribution at the surface of metallic nanoparticles (NPs) and b) Excitation of SPWs at the metal-surrounding interface.

The existence of surface plasmons can be described by Drude's model where the permittivity of the metal $\varepsilon_m(\omega)$ is expressed as [27]:

$$\varepsilon_m(\omega) = 1 - \frac{\omega_p^2}{\omega^2 + i\gamma\omega} \quad (1)$$

Where :

- ω_p: plasma frequency, $\omega_p = \sqrt{\frac{ne^2}{\varepsilon_0 m}}$, where n is the free electron density, e: the electron charge, ε_0 the permittivity of vacuum and m: the effective electron mass. The plasma frequency corresponds to the natural frequency of collective oscillations of the free electron gas inside the metal. For frequencies lower than ω_p, the real part of the permittivity of the metal becomes negative representing a highly reflective metallic behavior of the material, otherwise, for frequencies higher that ε_p the material behaves as a dielectric.
- γ: corresponds to the damping coefficient associated with ohmic losses inside metals.

SPWs are propagating waves (Figure 1) traveling along the metal-surrounding interface and exponentially decaying along the normal of the interface. Their dispersion relation is obtained by solving Maxwell's equations at the interface between a metal and its surroundings. The wavevector of SPWs, k_{SPR},(Figure 2), is defined by:

Licence CC BY-NC-ND 4.0

$$k_{SPR} = k_{light}\sqrt{\frac{\varepsilon_m \varepsilon_s}{\varepsilon_m + \varepsilon_s}} \quad (2)$$

Where: k_{light} is the wavevector of light ($k_{light} = \frac{2\pi}{\lambda}$), ε_m and ε_s are the permittivity of respectively the metal and surrounding.

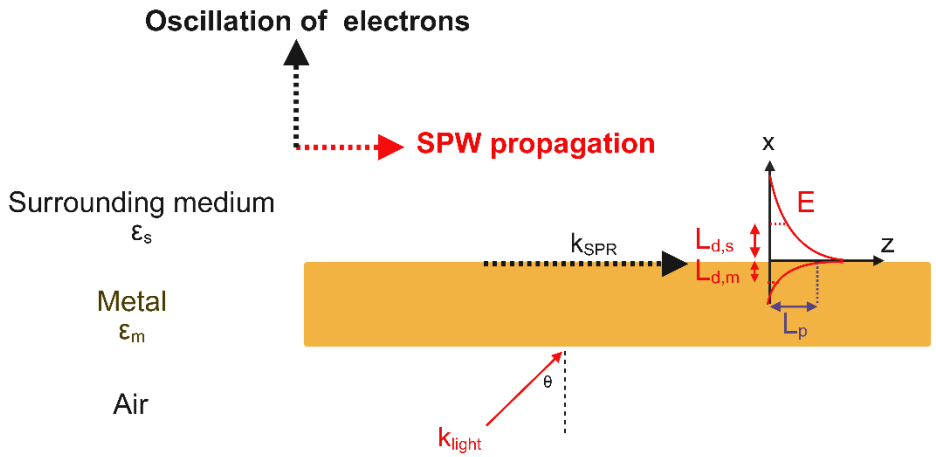


Figure 2 Illustration of the wavevector components at the metal-surrounding interface of a multilayer structure consisting of air, metal and surrounding medium.

SPWs oscillations are characterized by 2 parameters [28]:

- A penetration length (L_d) which defines the depth at which the evanescent field perpendicular to the interface falls to 1/e of its original value:

$$L_{d,s} = \frac{\lambda}{2\pi}\sqrt{\left(\frac{\varepsilon'_m + \varepsilon_s}{\varepsilon_s^2}\right)} \quad (3)$$

$$L_{d,m} = \frac{\lambda}{2\pi}\sqrt{\left(\frac{\varepsilon'_m + \varepsilon_s}{\varepsilon_m^2}\right)} \quad (4)$$

  Where $L_{d,s}$ and $L_{d,m}$ represent the penetration depths in the surrounding environment and metal respectively, λ the excitation wavelength, ε'_m the real part of permittivity of the metal and ε_s the permittivity of the surrounding. $L_{d,s}$ is generally approximated by λ/2. For λ=600 nm, $L_{d,s}$= 280 nm and $L_{d,m}$= 31 nm at the Au-air interface.

- A propagation length (L_p) which represents the distance at which SPWs can still propagate along the interface before decaying. Thus, it corresponds to the length at which the intensity of SPWs propagation decreases to 1/e of its original value.

$$L_p = \frac{1}{2k''_z} \quad (5)$$

  Where k''_z is the imaginary part of the wavevector k_z parallel to the interface. L_p is estimated at 8 µm for SPWs propagating between the Au-air interface at 600 nm [29].

To couple incident light with SPWs, certain conditions must be satisfied. First, only a transverse magnetic (TM) polarized light can be coupled with SPWs since the electric field lies in the plane

Licence CC BY-NC-ND 4.0

of incidence. The plane of incidence contains the coupling wavevector k_{light} and the vector normal to the metal-surrounding interface (x direction, Figure 3). Since free electrons oscillate along the x direction, the coupling electric field must have a component along this direction.

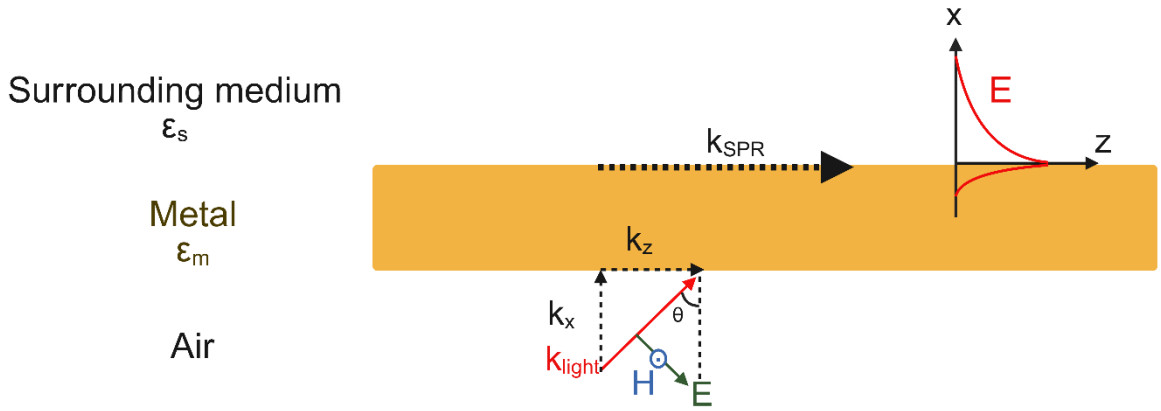


Figure 3 Schematic showing the coupling of the incident light to SPWs with a TM polarized light.

Additionally, light propagating in free space (with wavevector k_{light}) does not possess the necessary wavevector to couple with surface plasmons at the metal–surrounding interface. SPWs propagate along the metal-surrounding interface (z direction; Figures 1-2). To induce them into resonance the wavevector component of the light parallel to the interface (Equation 6) must match that of SPWs (Equation 2):

$$k_z = k_{light}\sqrt{\varepsilon_0}\,\sin\theta \tag{6}$$

Where ε_0 is the permittivity of vacuum and θ the angle of incidence.

For all values of ω and θ, $k_{SPR} > k_z$. This means that light in free space (defined by $\omega = \frac{c}{\sin\theta}k$ and $\omega = c.k$ for θ=90°) can never couple with SPWs (Figure 4). To overcome wavevector mismatch, different coupling strategies have been developed to provide the additional momentum required for coupling with SPWs.

Licence CC BY-NC-ND 4.0

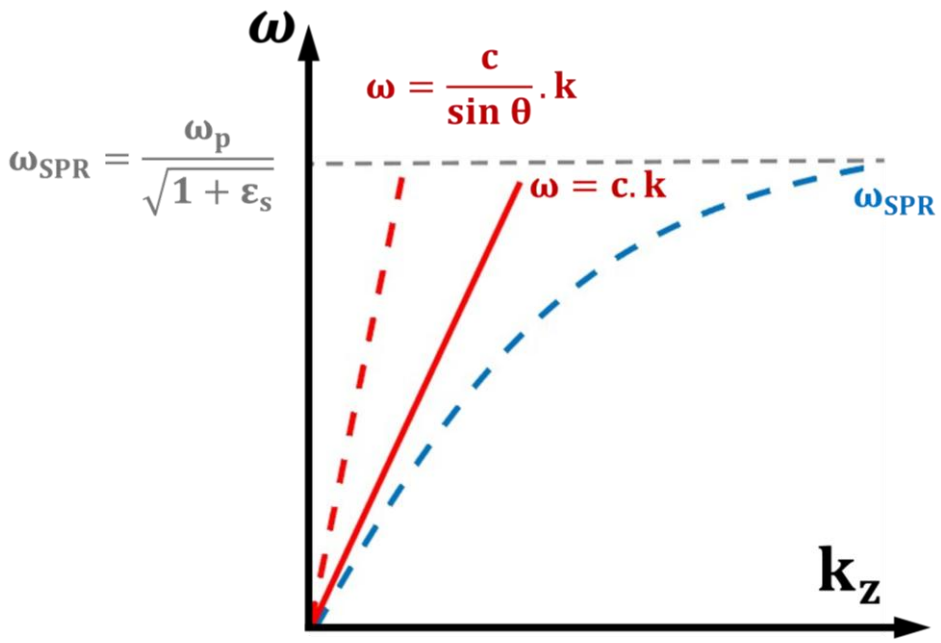


Figure 4 Illustration of the dispersion relation of light, where the red lines represent the dispersion relation of light in free space and the blue curve represents the dispersion relation of SPWs.

I.3. Coupling strategies

To compensate for the mismatch between the wavevector of light in free space and that required for surface plasmon excitation, a coupling medium is needed. Wavevector matching can be provided through several methods:

- Prism coupling**:** Kretschmann and Otto configurations,
- Grating coupling,
- Guided modes coupling: fibers and waveguides,

Each of these methods relies on a different physical principle and offers various advantages and limitations with regard to stability, fabrication, and integration. The following subsections will present each technique, provide a summary of the theoretical framework, and describe its functions and limitations.

I.3.1. Coupling incident light to SPWs using prism: Kretschmann and Otto configurations

Prism configurations suggested by Kretschmann, Rether, and Otto, are currently among the most widely used coupling techniques in SPR. In the Kretschmann configuration, the total internal reflection between a prism with a high refractive index and a metal increases the wavevector of the incident light to match that of SPWs. In the Otto configuration, this occurs between the prism and a gap (n_{prism}>n_{gap}). While the Kretschmann and Otto configurations are based on the same physical principle, their respective architectures result in variations in sensitivity, flexibility, stability and ease of operation.

I.3.1.1. Coupling incident light to SPWs using the Kretschmann configuration

In the Kretschmann configuration, a dielectric substrate with a high refractive index, such as a glass prism, is placed in direct contact with a thin metal film to couple light with SPWs. The

Licence CC BY-NC-ND 4.0

Kretschmann configuration was introduced in 1968 by Erich Kretschmann and Heinz Ruder [30] (Figure 5).

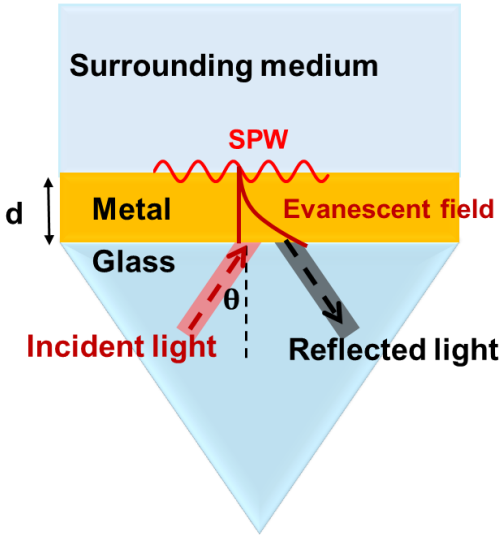


Figure 5 Schematic of the Kretschmann configuration showing the coupling of incident light to SPWs via a prism.

The total internal reflection between a glass prism and a metal surface creates an exponentially decaying evanescent field (Figure 5). This field with higher wavevector penetrates inside the metal and interacts with the free electrons travelling near the metal–surrounding interface. Resonance occurs when the wavevector of incident light matches that of SPR (Figure 6) [31]:

$$k_{prism} = k_0\sqrt{\varepsilon_{prism}}\,\sin\theta = K_{SPR} \tag{7}$$

Where: k_{prism} is the wavevector of the incident light inside the prism, ε_{prism} the permittivity of the prism, θ the incident angle and K_{SPR} the wavevector of the surface plasmons defined by Equation 2.

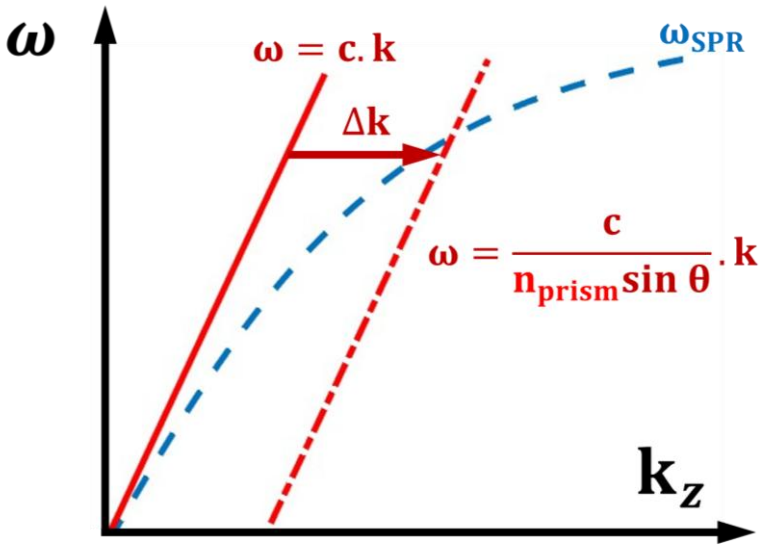


Figure 6 Dispersion relations of SPWs (blue curve), light in vacuum (red curve, $\omega = c.k$) and light inside a prism (red dashed curve, $\omega = \frac{c}{n_{prism}\sin\theta}.k$).

Licence CC BY-NC-ND 4.0

Kretschmann prism configurations offer many advantages, including precise control over the incidence angle (which facilitates alignment of the SPR resonance angle and enhances sensitivity), the ability to excite SPWs without direct contact between the incident beam and the biological environment, and ease of operation. However, the main obstacle remains the difficulty of miniaturizing prism-based SPR setups due to the prisms' larger size [32]. This configuration is the most widely used in commercial SPR systems (Biacore, Horiba, Nicoya and Reichert) and in experimental laboratory setups.

I.3.1.2. Coupling incident light to SPWs using in Otto configuration

The Otto configuration was developed by A. Otto in 1968, prior to the introduction of the Kretschmann configuration [23]. In this case, the total internal reflection between a prism with a high refractive index and a gap ($n_{prism}>n_{gap}$) creates an evanescent field with a large in-plane wavevector (Figure 7). The evanescent field penetrates the gap and couples with SPWs at the metal-air interface. It is important to adjust the thickness of this gap. This allows the evanescent wave created between the prism and the gap to penetrate the gap and reach the metal-gap interface.

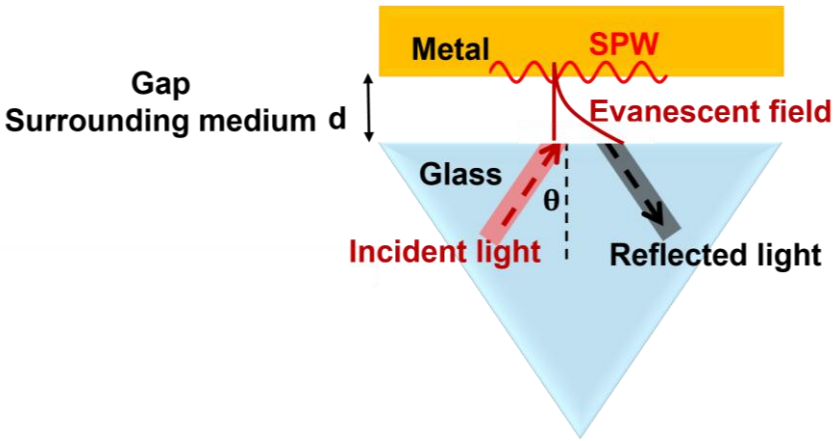


Figure 7 Schematic of the Otto configuration showing the coupling of incident light to SPWs via a prism and gap.

After the development of SPR sensors based on Kretschmann, Otto based structures were disregarded due to the difficulty of carefully adjusting the gap which has shown to be a critical parameter to optimize the sensitivity. On the other hand, the Otto-based structure offers several advantages, including the possibility of tuning the resonance conditions by varying the gap-metal distance. Furthermore, coupling through a gap eliminates the need for an additional adhesion layer to secure the metal to the prism [33,34].

I.3.2. Coupling incident light to SPWs using diffraction gratings

The use of diffraction gratings for SPR sensing was advocated by Cullen et al. as an alternative to Kretschmann bulky prism's coupling [35]. Unlike Kretschmann and Otto, in the case of diffraction grating, the supplementary wavevector is provided by a periodic diffraction grating [28]. When light hits a grating, it is usually diffracted in many directions following the grating equation (Figure 8) [36]:

Licence CC BY-NC-ND 4.0

$$m\lambda=\Lambda(\sin\theta+\sin\theta_m) \quad (8)$$

Where m is an integer value that represents the diffraction order ($m=\pm1,2,\dots$) , Λ represents the spacing between the grating's grooves, θ represents the angle of the incident light and θ_m is the angle of the diffracted light (Figure 8).

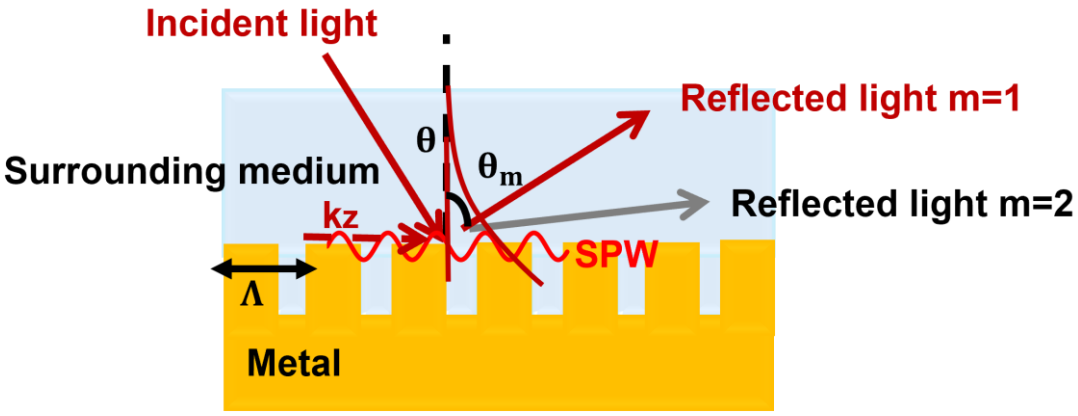


Figure 8 Schematic showing the coupling of incident light to SPWs via diffraction gratings.

To couple light to SPWs, one diffraction order should satisfy the following condition:

$$k_z + G = k_{SPR} \quad (9)$$

Where k_z is the wavevector of the incident light parallel to the Au-surrounding interface (Figure 8) and G is the grating vector ($G=\frac{2\pi}{\Lambda}$). G represents the additional wavevector provided by the gratings. As such Equation 9 becomes:

$$k_z + m\frac{2\pi}{\Lambda} = k_{SPR} \quad (10)$$

Coupling with diffraction gratings offers many advantages over prism-based systems, including a more compact design with greater miniaturization potential, tunable resonance by adjusting the grating geometry, and multiple diffraction orders available for coupling. However, grating-based systems have not yet achieved the sensitivity of prism-based configurations, and their performance is extremely dependent on grating geometry [37]. Additionally, in this configuration, light is incident on the surrounding medium. This means that any change to the properties of the medium (e.g. refractive index, noise or temperature) affects the propagation of light within the medium and modifies the coupling conditions, which limits the stability of the system [38].

I.3.3. Coupling incident light to SPWs using guided modes

Coupling light to SPWs can also be achieved through guided structures, notably waveguides and optical fibers. The propagation of optical modes within a waveguide produces an evanescent field that extends outside the core of the guide to the adjacent region where a thin metallic layer can be deposited (Figure 9). When the wavevector of the guided modes equals that of SPWs at the metal-surrounding interface, SPWs are excited, leading to a drop in light intensity at a particular wavelength [37,39].

Licence CC BY-NC-ND 4.0

$$k_{gm} = K_{SPR} \quad (11)$$

Where k_{gm} is the wavevector of the guided mode.

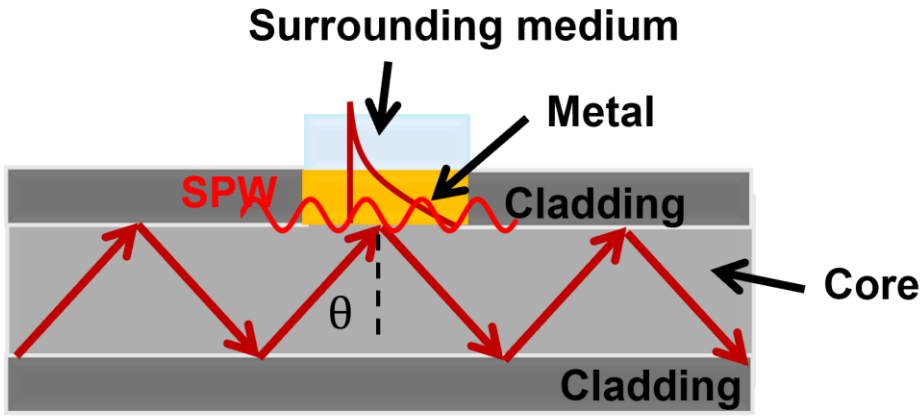


Figure 9 Schematic showing the coupling light of incident light to SPWs with guided modes.

The first reported coupling of incident light to SPWs with optical fibers was introduced by Jorgenson et Yee in 1990s, where the cladding was removed and a metallic thin layer was deposited on the silica core. This allowed the fabrication of the first miniaturized SPR fiber sensor [40]. The sensitivity of early SPR fiber sensors is influenced by the presence of multiple modes, which allow SPWs to be excited at different resonant conditions, broadening the SPR dip and thereby reducing the sensitivity [41].

The cladding is usually removed in classical SPR fiber sensors to allow the guided light in the core to interact with the metal. This means that careful polishing of the cladding is required. To address this, structures such as long-period fiber gratings (LPFGs) [42] and tilted fiber Bragg gratings (TFBGs) [43] have been developed. These configurations enable light to be coupled from the core to specific cladding modes (i.e modes that propagate in the cladding) without removing part of the cladding. The controlled coupling provided by these structures limits the broadening effects observed in multimode fibers, resulting in a narrower resonance dip and, consequently, improved sensitivity [44].

I.3.4. Conclusion

Various coupling strategies have been developed to address the wavevector mismatch between the incident light and SPWs, primarily by using prisms, gratings, and optical guiding structures. The prism-based approach, particularly the Kretschmann configuration, remains the most widely used method, primarily due to its higher sensitivity [41]. Although the other configurations provide higher integration possibility, they present additional limitations relating to fabrication and lower sensitivities [32].

Once SPWs have been coupled, the detection of biological interactions can be achieved by analyzing variations in the resonance condition. To this end, many interrogation methods have been developed to measure these variations and maximize SPR sensitivity.

Licence CC BY-NC-ND 4.0

I.4. Overview of sensitivity interrogation methods in SPR

Once the coupling conditions between the incident light and SPWs has been satisfied, some of the energy is transmitted to the SPWs. This happens at the resonance angle where the wavevector of light matches that of SPWs. The coupling of light to SPWs is represented by the SPR reflectivity curve (Figure 10). At the resonance angle, the intensity of the reflected light drops, leading to the appearance of a reflectivity dip at the resonance angle. The angular position of this minimum depends on the refractive index of the surrounding medium. Therefore, any variation in the refractive index due to adsorption of biomolecules on the metal's surface modifies the resonance conditions alongside the modification of the properties of the reflected light (intensity, wavelength and phase).

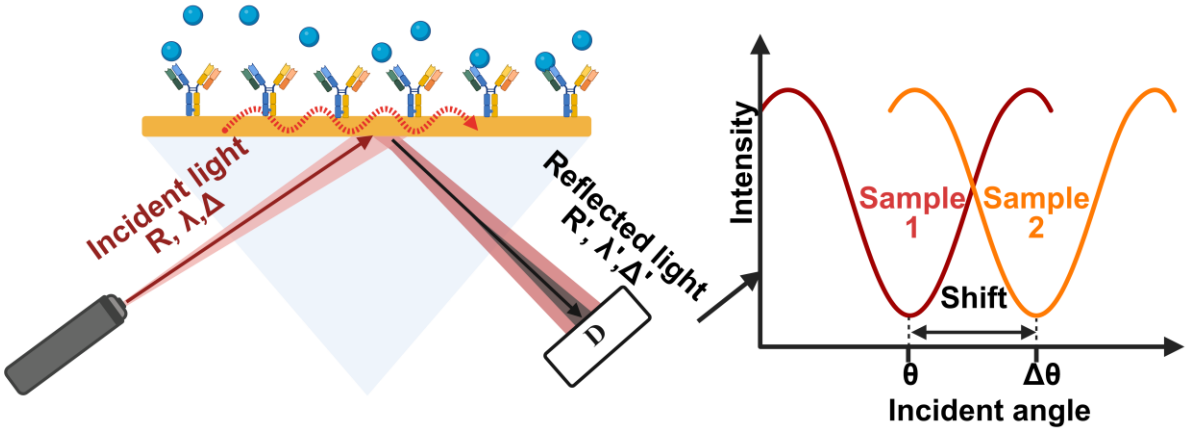


Figure 10 Principle of SPR sensing showing the coupling of light to SPWs. The coupling results in a reflectivity dip at the resonance angle θ. Variations in the refractive index of the surrounding induce a shift of the resonance angle Δθ. R and R' represent the incident and reflected intensity, λ and λ' the wavelengths, Δ and Δ' the phases and D the detector.

I.4.1. SPR sensitivity assessment based on intensity, angle and wavelength interrogation methods

The angular interrogation method is one of the most widely used techniques in SPR for evaluating sensitivity. The resonance angle is particularly sensitive to variations in the refractive index of the surrounding environment due to changes in the wavevector of the surface plasmon propagating at the metal–surrounding interface. Therefore, any modification to the surrounding environment (e.g. adsorption of biomolecules onto the metal surface) leads to a change in the resonance conditions and the position of the reflectivity minimum (Figure 10).

The variation of the resonance angle can be determined via many experimental approaches. In the first configuration the incident angle can be scanned mechanically via a scanning mirror [45]. In this case, the intensity of light is measured for each angular step and the resonance angle is identified as the angle corresponding to the minimum reflected intensity (Figure 11-a).

In the second configuration, a light beam passes through a lens system that generates a wide range of incident angles (Figure 11-b). In this case the SPR sensor is fixed, and the angular spectrum is analyzed with a single acquisition using a CCD camera. The resonance angle is similarly identified as the angle corresponding to the minimum reflected intensity [46].

Licence CC BY-NC-ND 4.0

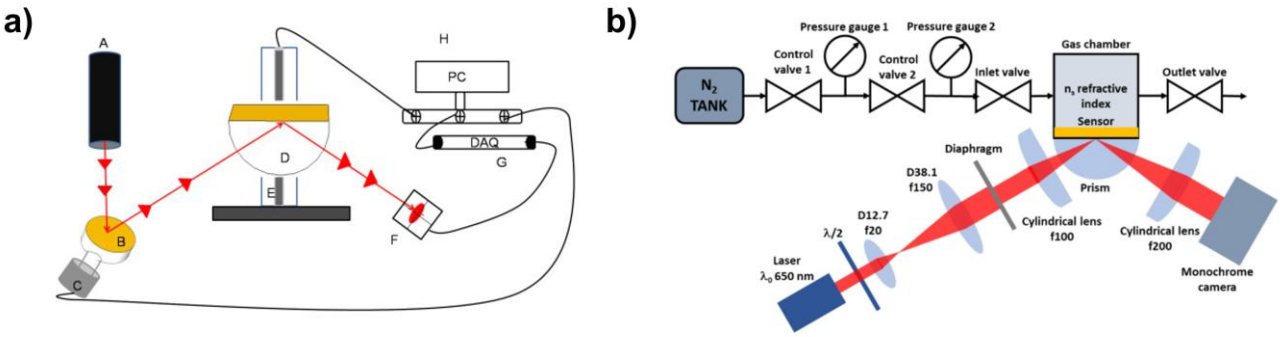


Figure 11 Illustrations showing two different configurations for measuring the resonance angle, a) Schematic of the SPR instrument involving mechanical scanning of the resonance angle, (A) laser, (B) mirror, (C) piezomotor, (D) semi-cylindrical prism, (E) translation stage, (F) quadrant photodiode (QPD), (G) data acquisition (DAQ) card, (H) computer [45] and b) Schematic representing the procedure of finding the resonance angle via a wide-angle incident beam and a CCD camera [47].

Angular sensitivity can be optimized by maximizing the change in resonance angle with respect to variations in the surrounding medium. This not only depends on the SPR structure employed, but also on the experimental setup. These elements determine the angular resolution and the system's susceptibility to external noise, such as vibrations and fluctuations in laser intensity. Consequently, multiple approaches have been proposed in the literature to enhance the sensitivity, precision and reliability of angular measurements.

The sensitivity of the SPR chip (which consists of dielectric substrate, multilayer system and metal designed for the excitation of SPWs) can be also measured by tracking the change of reflectivity at fixed incident angle. This occurs at the maximum slope (inflection point) of the reflectivity curve [31].

The sensitivity of the SPR chip to detect variations in the refractive index (n) of the surrounding medium via intensity interrogation schemes is theoretically defined as [48]:

$$\frac{dR}{dn} = \frac{d\theta}{dn} \cdot \frac{dR}{d\theta} \tag{12}$$

Where:

- $\frac{d\theta}{dn}$: represents the change in resonance angle with respect to the surrounding's refractive index. For small variations in n, the variation of resonance angle with respect to n is considered linear (Explained in Chapter 3).
- $\frac{dR}{d\theta}$: is the derivative of reflectivity with respect to the incident angle. It represents the change of reflectivity at fixed angle. Close to the inflection point (steepest slope), the variation of reflectivity with respect to θ is considered linear.

Equation 12 shows that, to achieve maximum sensitivity through intensity interrogation, it is essential to optimize the change in resonance angle $\frac{d\theta}{dn}$, the change in reflectivity at a fixed

Licence CC BY-NC-ND 4.0

angle, and to reduce the full width at half maximum (FWHM) of the reflectivity curve to enhance $\frac{dR}{d\theta}$ (Figure 12).

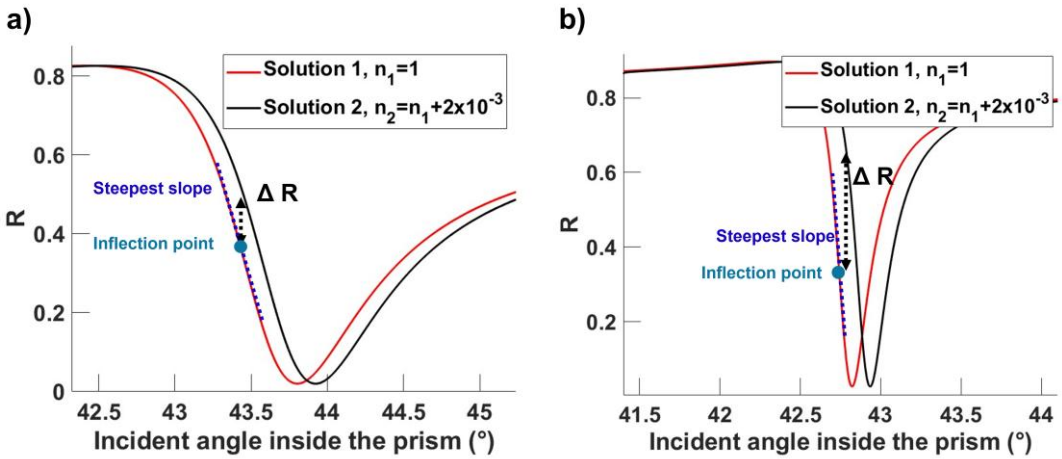


Figure 12 Influence of the FWHM on the reflectivity variations at fixed angle. Both curves are simulated using the transfer matrix model (explained in Chapter 3) with air as the surrounding medium. (a) represents a bare Au SPR chip and b) a bare Ag SPR chip.

One additional technique for evaluating the sensitivity of SPR relies on the spectral interrogation approach. This involves monitoring changes in the resonant wavelength by measuring the reflectivity using a broadband spectral source. In this approach, the incidence angle is fixed, and reflectivity is measured with respect to wavelength via a spectrometer. SPR resonance is identified as the wavelength at which the minimum of reflectivity is measured. The wavelength of the reflectivity dip is sensitive to changes in the surrounding medium (Figure 13) [49,50].

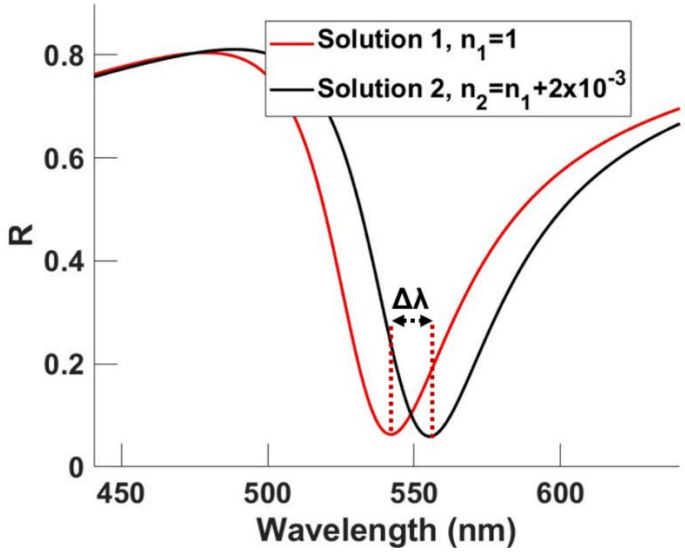


Figure 13 Principle of spectral interrogation in SPR showing the shift of the resonance wavelength (Δλ) with respect to the change in the refractive index of the surrounding medium. The curves are simulated using the transfer matrix model for a bare Au chip with air as the surrounding medium (explained in Chapter 3).

Licence CC BY-NC-ND 4.0

I.4.2. SPR sensitivity assessment using the phase interrogation method

The theoretical sensitivity obtained using traditional intensity, angular and spectral methods are reported to be 10^{-5} , 5.10^{-7} and 10^{-6} RIU (refractive index unit) respectively [41,51,52]. These performances have shown to be sufficient for monitoring many biomolecular interactions (antigen-antibody, DNA-DNA,….). Practically, these approaches may face some challenges when detecting analytes with low molecular weights (<500 Da) or biomarkers present in low concentrations (< pM) [53]. However, it has been demonstrated that the theoretical sensitivity of SPR sensors is not linked to the plasmonic effect itself but rather the choice of the interrogation method and experimental setup [53,54].

During SPR, the incident light couples with the SPWs, resulting in a reduction in intensity on the reflection side. It is well known that, when light intensity is very low, the phase becomes undefined [55]. This results in a phase jump at resonance, where the phase value is undetermined (Figure 14).

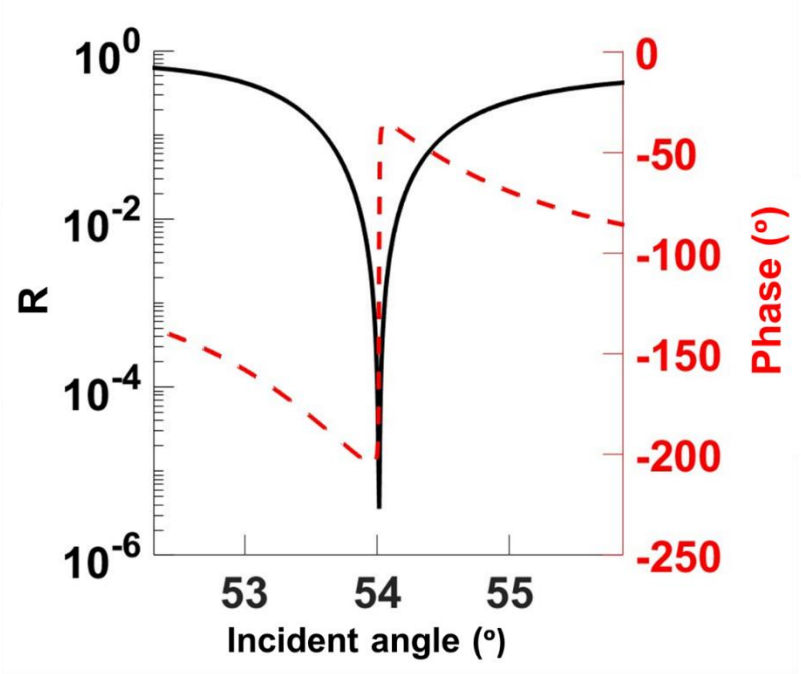


Figure 14 Reflectivity and phase vs incident angle in the Kretschmann configuration. The curves are simulated using the transfer matrix model (explained in Chapter 3) for a SPR structure consisting of Ag NPs embedded in alumina with a thin Au layer above with water as the surrounding medium.

Under SPR, the reflectivity at resonance is characterized by a low reflection dip known as the topological darkness point and a sudden phase jump. In this regime, even a small variation of refractive index can lead to a large phase shift (Figure 15) [53]. However, the intrinsically higher sensitivity is often counterbalanced by a narrower RIU measurement range [52].

Licence CC BY-NC-ND 4.0

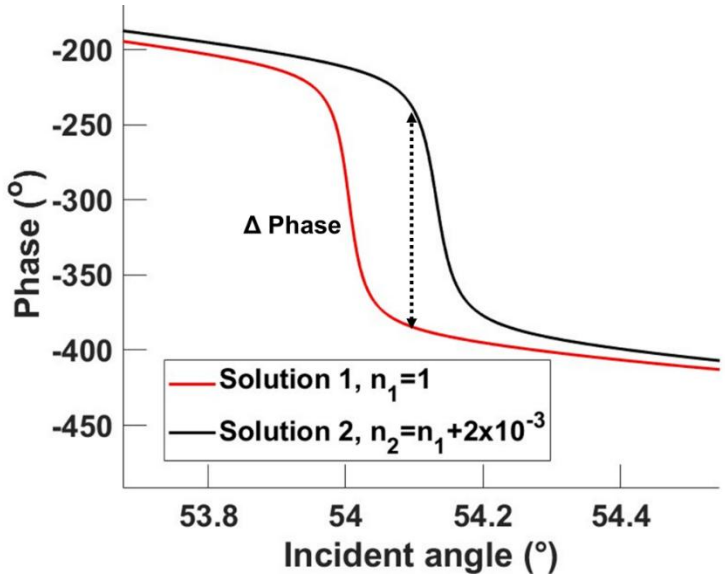


Figure 15 Principle of phase interrogation in SPR showing the phase variation with respect to the change in the refractive index of the surrounding medium. The curves are simulated using the transfer matrix model for a bare Au chip with water as the surrounding medium (explained in Chapter 3).

The existence of phase jump under SPR and a stronger sensitivity to refractive index variations has been first reported by Abeles in 1976 through ellipsometry measurements. Later on, by adjusting the Au layer thickness, Kabashin and Nikitin theoretically reported for the first time a large phase sensitivity of 10^5 °/RIU and estimated a limit of detection (LOD) of 10^{-8} RIU [53].

More recently, Kabashin, Kravets and Grigorenko conducted a review of optical biosensors. They demonstrated that detectors using phase measurements combined with SPR structures producing near-zero reflectivity can achieve sensitivities in the order of fg/mm² (where fg/mm² represents the mass of molecules attached to the surface per unit area, 1 fg/mm²=10^{-9} RIU). This is many orders of magnitude lower than the sensitivities achieved with conventional SPR platforms. Complete darkness can be achieved in SPR by reengineering the sensor's multilayer system to create multiple interferences and reach a zero reflection coefficient [56].

Due to the high frequency of light in the visible spectrum (~10^{14} Hz), direct extraction of phase can be challenging. Therefore, phase information must be converted into a readable signal. This can be achieved using various experimental setups based on polarimetry, optical heterodyne and interferometry [51,52,54,56,57].

I.4.2.1. Phase interrogation using ellipsometry

Ellipsometry refers to the method of extracting phase information of light, based on analyzing the polarization state of light after reflection from a multilayer structure. A linearly polarized incident light (with an intermediate polarization between TM and TE) becomes elliptically polarized after reflection due to the difference of phase and amplitude acquired by the two polarizations states. The analyses of the polarization of light after reflection allows the extraction of phase and amplitude variables [57,58].

The phase-polarization properties of light in SPR were widely used long before the implementation of modern SPR biosensors. In 1976, Abeles proposed a theoretical description of phase variation as a function of the parallel wavevector in a Kretschmann configuration. He suggested that ellipsometry is an efficient tool to study interactions occurring at the Au-

Licence CC BY-NC-ND 4.0

surrounding interface [51,57,58]. Since then, SPR ellipsometry sensors have undergone many improvements due to their high sensitivity. A more detailed description of the experimental configuration and theory will be presented in Chapter 4.

I.4.2.2. Phase detection using optical heterodyne

Optical heterodyne is a frequency-mixing technique in which the interference between two coherent waves with slightly different frequencies generates a signal whose frequency is typically in the KHz-GHz range. This conversion allows the measurement of a phase difference with standard electronics (phase meter or lock-in).

A heterodyne-based SPR sensor is based on the comparison of two electric signals from the same source, which are divided into two branches: the reference and measurement arms. In both branches, the TM and TE (transverse electric) frequencies are slightly shifted via AOM (acousto-opto-modulator) and then combined to generate a low-frequency signal that can be detected by a photodiode. In the measurement branch, after SPR, the reflection induces a phase shift only of the TM component. The electronic comparison of these signals allows the extraction of the phase shift induced by the plasmonic resonance (Figure 16) [59].

Typical optical heterodyne approaches reported detection resolutions in the order of 3.10^{-9} RIU and a LOD of 10 $fg.ml^{-1}$ for the detection of mouse IgG-anti mouse IgG [60].

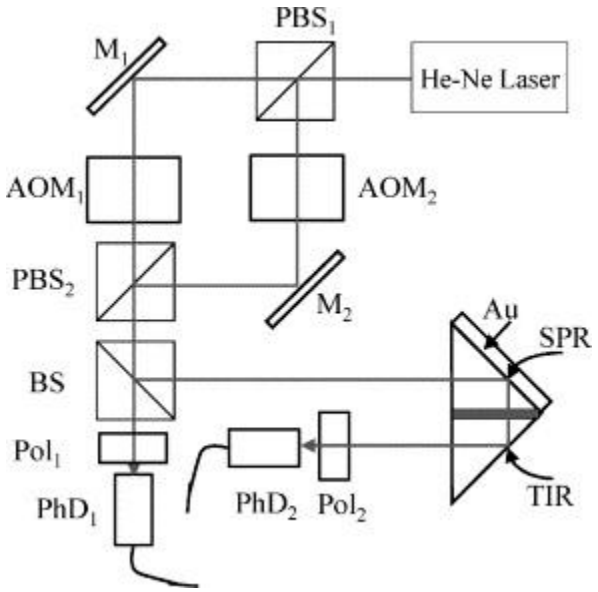


Figure 16 Schematic representation of an optical heterodyne setup for the extraction of phase. PBS: polarizing beam splitter; M: mirror; BS: beam splitter; AOM: acousto-opto-modulator; Pol: polarization filter; PhD: photo-detector [59].

I.4.2.3. Phase detection using interferometry

Interferometry relies on the direct interference between a signal undergoing plasmonic resonance (TM polarized) and a reference beam (TE polarized). This configuration is based on the spatial superposition of two beams, generating interference fringes whose position and shape depends on their relative phase shift (Figure 17). Every phase variation occurring in

Licence CC BY-NC-ND 4.0

SPR, mainly by the TM polarized light, translates into a measurable displacement or deformation of the interference fringes [51,53,54,57,61].

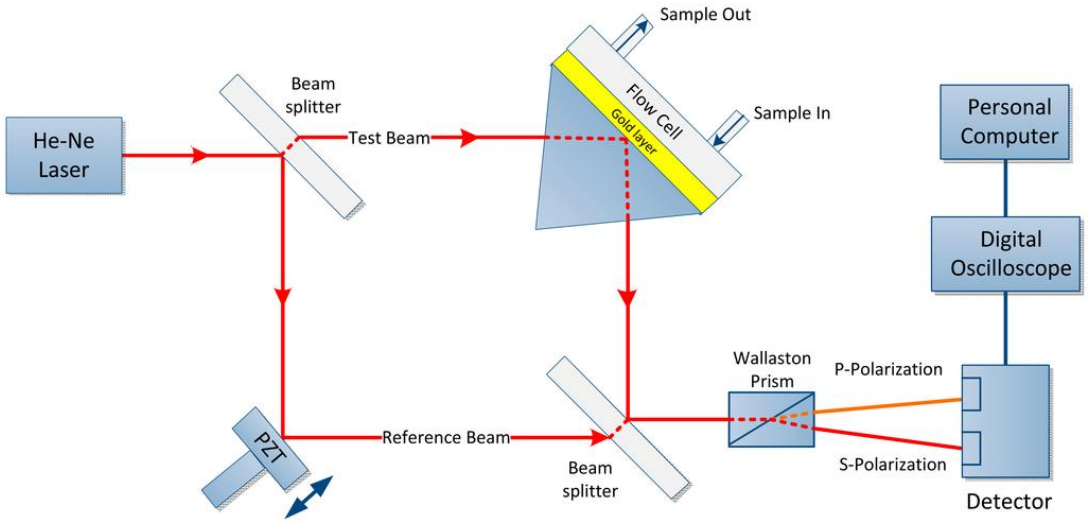


Figure 17 Schematic of the Mach-Zehnder interferometer for extracting phase in SPR [62].

Interferometric experimental setups in SPR were first proposed by Kabashin and Niktin in the late 1990s, who obtained a phase cartography via Mach-Zehnder interferometers. They estimated a sensitivity of 4.10^{-8} RIU for the detection of of Ar/N_2 gas mixture [63]. Later on, the experimental setup underwent serval variations by introducing differential interferometry, multi-pass (Michelson, Fabry-Perot) interferometers and 2D imaging experimental benches [51,54,57,64].

I.4.3. Conclusion

Phase interrogation in SPR constitutes one of the most sensitive detection schemes for enhancing the sensitivity of conventional SPR sensors. Phase undergoes a sudden jump near resonance where the incident light is mostly attenuated by the structure. This property provides higher intrinsic sensitivity for phase measurements, irrespective of the plasmonic effect itself.

The literature reviewed in this chapter demonstrates the ability of the phase interrogation to achieve LOD in the order of 10^{-8} RIU, representing a two-fold sensitivity enhancement in comparison with the intensity, angular and spectral methods.

Phase information can experimentally be recovered via many techniques. Polarimetry and ellipsometry rely on the polarization mixing of TE and TM via a polarizer, providing a compact and highly sensitive experimental setup. Optical heterodyne introduces a controlled frequency shift between two perpendicular polarizations, yielding low LOD at the expense of more complicated and less compact experimental benches. Finally, SPR interferometry represents the most general approach for phase detection, as it enables the phase to be extracted directly and visually but also at the expense of bulky experimental bench.

I.4.4. SPR sensitivity assessment based on the GH shift

Maintaining a high phase sensitivity usually requires complex experimental setups to limit the effect of surrounding and instrumental noise. With ellipsometry, the phase is not measured

Licence CC BY-NC-ND 4.0

directly but rather deduced from the analysis of the intensity of the polarization ellipse after reflection making it more sensitive to fluctuations of laser intensity and limiting the sensitivity. As such, SPR sensors incorporating ellipsometry included additional modulators to improve resolution, thereby making the experimental setup more complicated. On the other hand, heterodyne and interferometry allow the direct access to phase information, and offer very low LODs but at the price of complicated and bulky instruments. Therefore, despite phase measurements surpassing that of intensity, angular and spectral methods, the experimental implementation remains challenging and incompatible with compact, transportable systems. These considerations open the way towards the implementation of different interrogation schemes to preserve the high sensitivity of the SPR sensor with a simpler experimental setup.

In this context, Goos and Hänchen conducted an experiment in 1943 to analyze the behavior of a light beam during total internal reflection, where light penetrates the medium with low refractive index and re-emerges to the medium with high refractive index. They expected total reflection to behave as a special case of partial reflection. However, subsequent experiments revealed the existence of an electromagnetic field inside the medium of lower refractive index, where its intensity decays exponentially away from the surface in the normal direction and becomes practically undetectable within several wavelengths. Subsequently, researchers observed and measured a relative lateral displacement of the reflected beam relative to the point of incidence. This shift, known as the GH shift (Figure 18) was not predicted by geometrical ray optics [65]. While the GH shift is present in all total internal reflection scenarios, its magnitude is typically limited to a few nanometers.

Shortly after this discovery, K. Artmann formulated the first theory for computing the GH shift in 1948, based on the equations of Fresnel and Maxwell. He demonstrated that the shift observed could be explained by the difference in phase between the incident and reflected wave and obtained GH expressions for two perpendicular polarizations. These results were later experimentally validated by Goos and Hänchen. Artman's approach is known as the stationary phase method, and the GH shift is expressed as the first order derivative of the phase:

$$\mathrm{GH} = -\frac{\lambda}{2\pi}\frac{\mathrm{d}\Delta}{\mathrm{d}\theta} \tag{13}$$

Where λ is the wavelength of the incident light, Δ the phase difference and θ the incident angle [65,66].

Fragstein developed another theory based on the subsequent work of Picht, Schäfer and Pich [65]. He eventually found the same analytical expressions derived by Artmann, which validated the phenomenon observed by Goos and Hänchen. Additionally, both Fragstein and Artmann acknowledged the difficulty of precisely measuring this shift experimentally, given its very low amplitude [65].

Later on, Renard clarified that, when a plane wave with a finite width undergoes total internal reflection, a portion of its energy penetrates the medium with the lower refractive index as an evanescent wave before re-emerging inside the medium with the higher refractive index [65]. This surface wave is not stationary but transports an energy flux parallel to the interface (Figure 18). The amplitude of the GH shift can be determined analytically by applying the principle of conservation of energy and balancing the energy flux transported parallel to the interface with the energy flux of the spatially shifted reflected wave [65]. The expressions obtained with this method slightly differ from the ones obtained by Artmann and Fragstein but are found to

Licence CC BY-NC-ND 4.0

produce same results when the angle of incidence is close to the critical angle of total internal reflection [65].

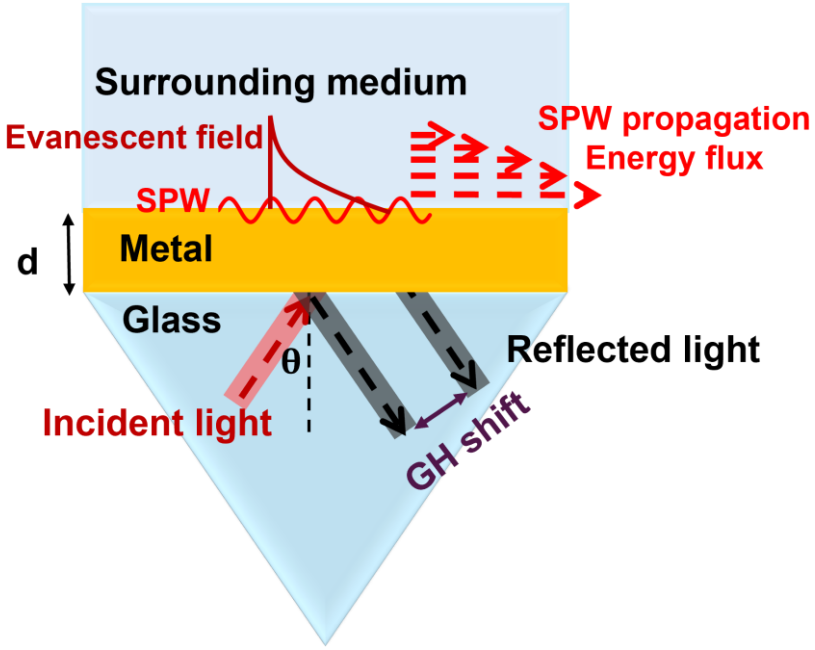


Figure 18 Schematic showing a SPR chip configuration based on the GH shift.

In 1982, Wild and Giles conducted further analysis of Artmann's theory applied to absorbing media such as metals. In this case, total internal reflection experiences some loss, and the material absorbs light [66]. They demonstrated that the GH shift is dominated by the angular derivative of the phase and can be expressed in a manner similar to that described by Artmann. When the reflection medium is characterized by a non-zero extinction coefficient, the phase can exhibit rapid variations, resulting in enhanced GH shifts [66].

In the case of SPR, the GH shift is significantly enhanced due to the stronger electromagnetic field penetrating the metal–surrounding interface and the steeper phase change occurring at resonance. As the first order derivative of the phase, GH shift measurements possibly offer higher sensitivity (steeper GH changes near resonance in comparison with phase) with simpler detection benches (in comparison with interferometry and optical heterodyne configurations [67]). A GH experimental setup will be presented in detail in Chapter 2.

I.5. Overview of commercial SPR platforms and instruments

Over the past decade, numerous commercial instruments have been developed and employed in biomedical, pharmaceutical, and environmental research. SPR has become one of the most effective biosensing techniques owing to its unique capabilities. SPR sensors provide a quantitative sensogram , enabling direct monitoring of the displacement of the SPR variable (angle, intensity, wavelength, phase or GH shift) with respect to time [68].

The industrialization of SPR began in the early 1990s, when Pharmacia Biosensor launched the first commercial SPR sensor, Biacore. This platform set the standard for sensitivity, reproducibility and ease of use, establishing SPR as the gold standard for biodetection and securing Biacore's dominant position in the SPR market, accounting for over 80% of sales. Over the years, many industries have emerged as suppliers of SPR: in 1995 IBIS technologies launched a cuvette based SPR system compatible with Bioacore Au-chips, employing the

Licence CC BY-NC-ND 4.0

angular interrogation technique, and, in 1997 introduced a newer system with 2 channels and an autosampler [68]. Since then, commercial SPR instruments has significantly increased and diversified, with performance depending on the optics used, degree of automatization, microfluidics, ease of usage, flexibility, cost as well as technical parameters as noise, drift, sensitivity and measurement range [69–71].

A commercial SPR system integrates three main elements: optics (laser, polarizers, detection), SPR chips and the liquid handling system [68]. The three main interrogation methods used in SPR systems are angular, intensity, and spectral. The vast majority of commercial SPR commercial systems employ a basic Au chip on glass with pre-functionalized surfaces. The microfluidic part is the most changing part in SPR systems whose architecture depends on the type of pumps, number of detection and reference channels, injection volume and delivery system [68].

To illustrate the industrial development of this technique, we will now present several examples of commercial SPR systems.

Bionavis

Bionavis developed multiparametric approach systems (MP-SPR) which differ from the conventional commercial SPR systems by the complete acquisition of SPR reflectivity curves with a large angular scan (40-78°) [68,72]. A MP-SPR approach uses a rotating SPR configuration where the excitation source and detector are rotated to scan the full reflectivity curve (Figure 19) [73]. Additionally, they use multiple lasers with different wavelengths to obtain additional information as the effective refractive index, and thickness of the adsorbed molecules via a theoretical model based on Fresnel equations (explained in Chapter 3) [72]. A higher excitation wavelength is typically associated with deeper penetration into the surrounding environment (Equation 3), meaning the system is more sensitive to thick layers and large molecules. However, in this case, thinner and smaller layers are affected by noise, since the evanescent field extends far beyond the metal's surface. Using multiple lasers offers the possibility of detecting molecules of different sizes with greater precision.

This approach improves the application of the SPR sensor towards the study of polymers, thick films (~ µm), NPs and living cells, as well as air and liquid environments with a dynamic range of 1-1.45 RIU.

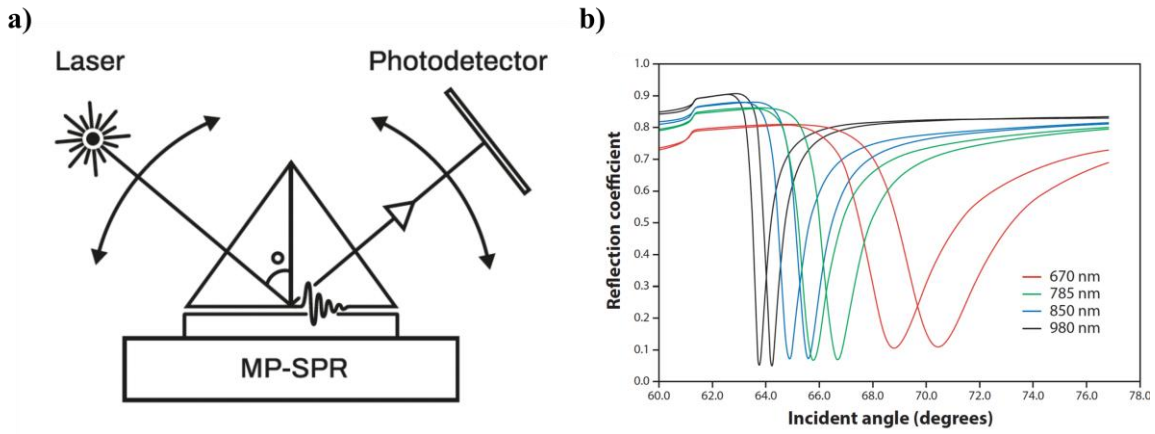


Figure 19 Bionavis MP-SPR system. a) Schematic of the experimental setup consisting of a rotating excitation source (laser), SPR module consisting of SPR chip and a rotating photodetector to measure the SPR reflectivity curves. b) SPR reflectivity curves obtained at 4 excitation wavelengths (670, 785, 850 and 980 nm) with Bionavis MP-SPR system [72].

Licence CC BY-NC-ND 4.0

Unlike classical SPR system in a Kretschmann configuration, Bionavis uses a polymer to fix the Au chip onto the prism, rather than refractive index-matching oil which enhances the mechanical stability of the system [68,72].

Bruker

Bruker developed high-throughput SPR systems for screening applications dedicated to drug discovery. Their system relies on the measurement of intensity at a fixed angle and the usage of a laser with high intensity and a high-speed camera as the detector (known as SPR+). These features reduce noise and enhance the system's signal to noise ratio [44].

These platforms also allow simultaneous analysis of numerous biomolecular interactions using a CCD camera. Light is incident on a large area consisting of numerous detection spots (SPR gold chips placed in a 2D configuration) and multiple microfluidic channels (Figure 20) [72] . In order to deliver the analyte to the chips, the system is equipped with a Hydrodynamic Isolation (HI) patented technology (Figure 20-b). HI technology enables several fluids to circulate simultaneously and independently at multiple detection spots. Figure 20-b shows a system consisting of eight microfluidic channels arranged parallel to each other, each containing four prefunctionalised detection spots. HI technology enables the independent circulation of eight different fluids, allowing multiple biological interactions to be analyzed. Bruker SPR systems are generally designed for high throughput tests for analytes with refractive indices between 1.33 and 1.4 RIU and the reported sensitivity of their system is in the order of 10 pM [44,74].

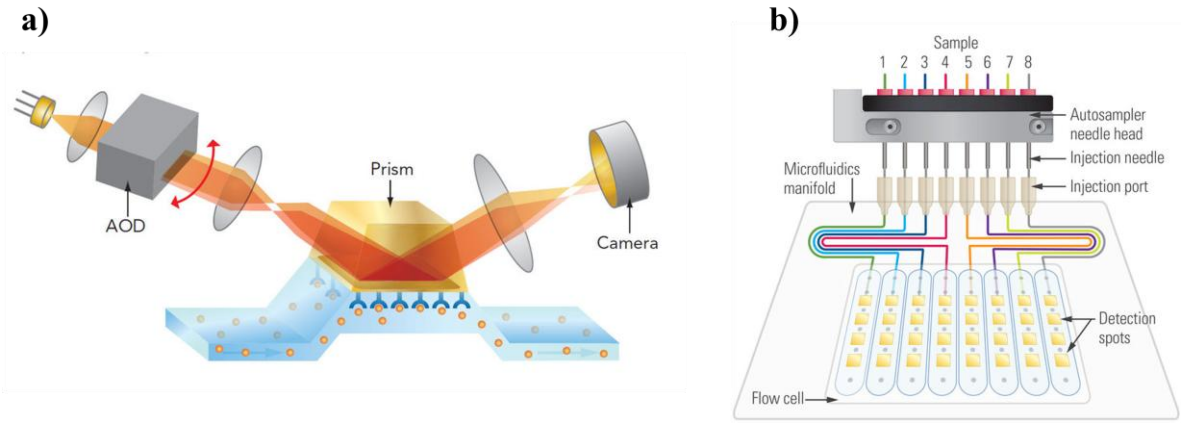


Figure 20 Schematics of Bruker SPR systems, a) Illustration of the experimental setup showing a high-power laser, Acousto-Optic Deflector (AOD) ensuring fast scanning of the incident angle to find the resonance angle, SPR module and high-speed camera as a detector. b) Illustration of the muli-channel architecture and HI technology [74].

Nicoya

Nicoya developed instruments based on localized surface plasmon resonance (LSPR) with Au NPs immobilized on the sensor surface. Their system relies on monitoring the spectral shift using a spectrophotometer (Figure 21). The lower penetration depth of the evanescent field and the larger spectral width of the LSPR resonance limit the sensitivity of these systems in comparison with prism-based SPR [44].

Licence CC BY-NC-ND 4.0

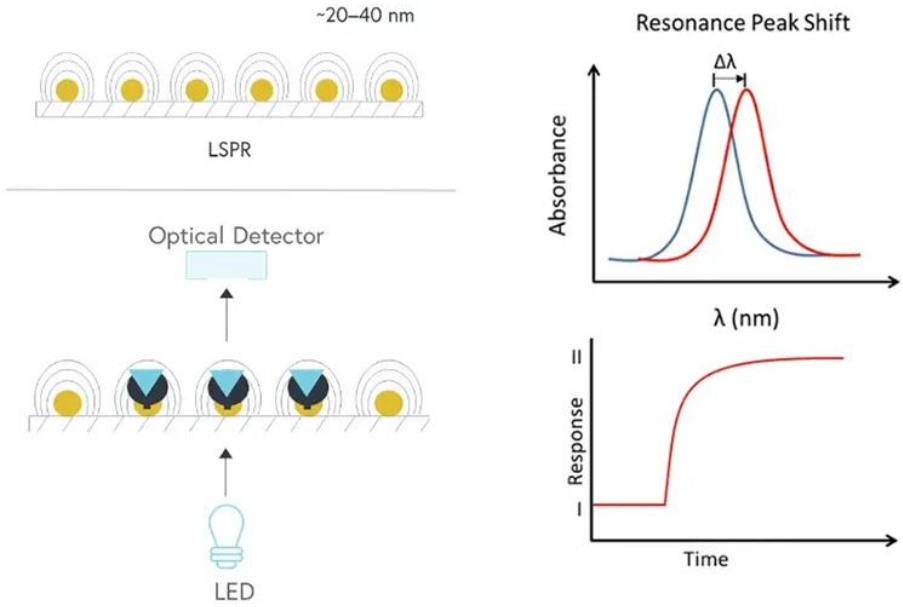


Figure 21 Schematic of Nicoya's LSPR detection principle [75].

Nicoya's systems integrates an autosampler module which allows the automatic injection of different liquid samples on several detection spots (Figure 22) [75]. In addition, their system integrates a Digital microfluidic (DMF) module that can automatically manipulate liquids at very low volumes (several nanoliters) reducing the volume required to 2 µL per channel. The LOD of Nicoya's systems is reported to be around 10^{-6}-10^{-5} RIU [76].

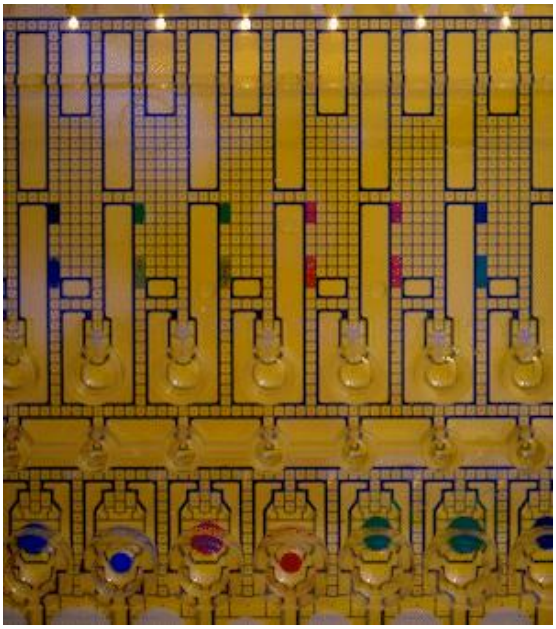


Figure 22 Illustration of Nicoya's DMF module [77].

Biosensing instruments

Biosensing Instruments has developed a series of SPR systems based on the angular interrogation method. In this approach, a divergent beam is incident on the SPR chip, and the

Licence CC BY-NC-ND 4.0

angular displacement of the resonance angle is detected by measuring its spatial displacement on the detector (Figure 23) [78].

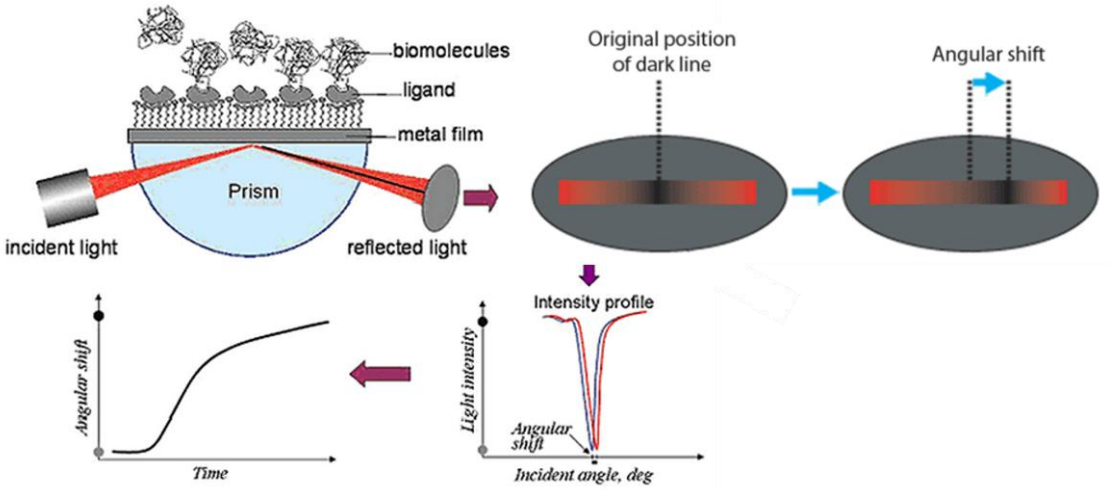


Figure 23 Illustration of Biosensing instruments SPR system based on the angular interrogation method. The angular shift of the resonance angle is detected by measuring the spatial displacement of the reflectivity dip [78].

Biosensing instruments typically incorporate multiple microfluidic channels for measuring various biological interactions. The advantage of multichannel systems lies in their ability to use one microfluidic channel as a reference. In this case, a buffer solution flows through the reference channel to compensate for drifts originating from the system. The reference signal is then subtracted from the detection signal (measured in the other microfluidic channel), enhancing the reliability of the measurements. Additionally, these systems are equipped with an autosampler module that enables the automatic injection of different liquid samples into several detection spots. Their platform is adapted for measuring protein-protein interactions, ligand-receptor recognition, DNA hybridization or for the development of drugs [44,79].

The second range of biosensing instruments involves SPR microscopy (SPRM, Figure 24). In this configuration, the surface of the sensor is illuminated at fixed angle and the change in reflectivity is measured pixel by pixel via a camera [80]. Each pixel consists of a measurement zone for visualizing biological interactions and obtaining individual SPR sensograms. Due to its high spatial resolution (in the order of micrometers), SPRM enables the detection of small molecules, such as viruses and bacteria, which are difficult to access in traditional SPR systems [79].

Licence CC BY-NC-ND 4.0

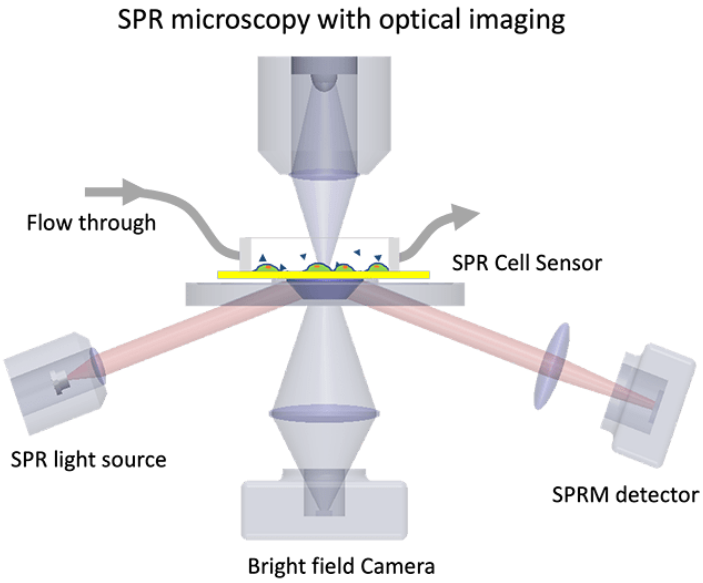


Figure 24 Illustration of Biosensing instruments SPRM setup. It consists of a light source, microfluidic module, SPR module and SPRM detector [79].

Reichert technologies

Reichert technologies developed SPR systems based on the angular interrogation method. In their configuration, a divergent beam is incident on the SPR chip, and the angular displacement of the resonance angle is detected by a photodiode array (Figure 25).

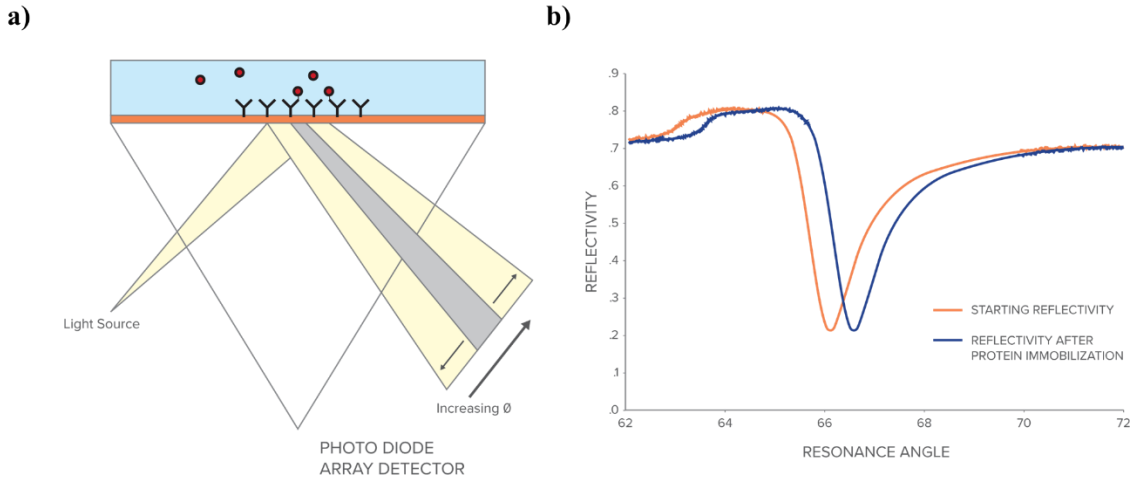


Figure 25 Illustration of Reichert technologies SPR system based on the angular interrogation method. a) A divergent beam is incident on a fixed SPR module, and the angular change of the resonance angle is detected by a photodiode array. b) Typical SPR reflectivity curves obtained by Reichert SPR systems [81].

Reichert Technologies typically incorporates multiple microfluidic channels to measure various biological interactions and subtract baseline drifts (i.e. drifts originating from the system), thereby enhancing the reliability of its systems.

Reichert instruments propose configurations allowing the usage of SPR with complementary techniques such as electrochemistry, fluorescence and mass spectrometry. These approaches

Licence CC BY-NC-ND 4.0

enable the analysis of different physical signals, providing additional information regarding the type of interaction (e.g. protein-protein, ligand-receptor or antibody-antigen) and the nature of the molecules involved (e.g. proteins, DNA, lipids, cells, viruses or bacteria), which are not accessible by SPR alone [44].

Conclusion

The analysis of the main commercial SPR platforms revealed a wide variety of architectures, demonstrating SPR's ability to adapt to different experimental conditions. Commercial SPR systems rely on the angular, spectral or intensity interrogation and are predominantly based on the Kretschmann configuration. On the other hand, SPR imaging techniques monitor changes in intensity at fixed points, providing visualization of the specific interaction zone on the sensor's surface. The following table presents a summary of the performance of commercial SPR systems.

Licence CC BY-NC-ND 4.0

Table 1 Overview of commercial SPR systems where RU refers to response unit (1 RU=10^{-6} RIU=1 pg/mm^2), pg/mm^2 refers to the mass absorbed per unit area.

Manufacturer	Interrogation method	LOD	Baseline drift
Biacore	Angular with a fan-shaped beam	- 0.1 nM for > 10 KDa -1 nM for < 10 KDa	< 0.3 RU/min
Horiba	SPR imaging Change of reflectivity at fixed angle	- A minimal detectable concentration of 300 ng/mL for molecules weighing 100-1000 kDa - A minimal detectable concentration of 10 µg/mL for molecules weighing 4-20 kDa - Minimal detectable molecular weight: > 240 Da -LOD: 5 pg/mm^2	-
BioNavis	Multiparametric SPR	-	-
Biosensing instruments	Angular with a fan-shaped beam	-	3 RU/hr (0.5 mDeg/hr)
Bruker	SPR imaging Change of reflectivity at fixed angle	> 10 pM	< 0.15 RU/min
Nicoya	LSPR, spectral	≈ 10^{-6}–10^{-5} RIU	-
Reichert	Angular with a fan-shaped beam	-	< 0.1 RU/min
Plexera	SPR imaging Change of reflectivity at fixed angle	Nanogram quantities for arrayed sample	-

Although SPR commercial platforms (Table 1) offer high performance and robustness, further developments are still required to improve sensitivity while reduce the complexity of the experimental setup.

Licence CC BY-NC-ND 4.0

I.6. Presentation of the thesis project

I.6.1. Context

A SPR platform based on the GH interrogation method was developed by Shuwen Zeng at XLIM (Figure 26). An innovative SPR chip consisting of a thin layer of Au with germanium-antimony-tellurium (GST) deposited on top was also developed. The setup and the SPR chip were used for the detection of small molecules, such as biotin (244.31 Da) with a LOD of 10 fM. Additionally, this performance was exploited for the detection of cancer biomarkers, such as tumor necrosis factor alpha (TNFα), with a LOD of 1 fM, which highlights furthermore the high sensitivity of the experimental bench [67].

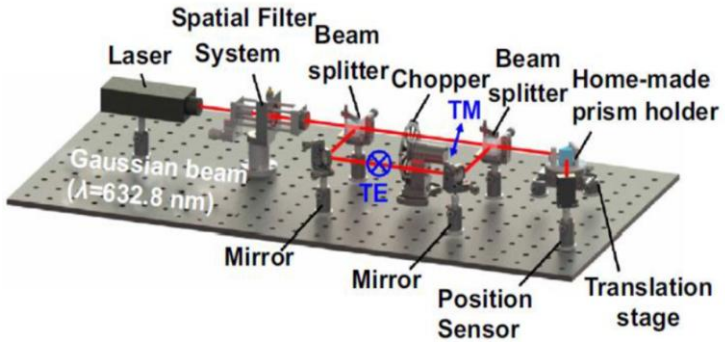


Figure 26 Schematic illustration of the original SPR platform [67].

The GST SPR chip and platform were used to detect EVs in collaboration with colleagues from CAPTuR. CAPTuR is a biology-oncology laboratory (INSERM, CHU de Limoges, University of Limoges) specialized in studying cancer-related biomarkers present in EVs. The collaboration between XLIM and CAPTuR focuses on the use of the SPR for the detection of specific biomarkers on EVs. The platform, along with the GST-based SPR chip, was able to detect EVs at concentrations as low as 10^4 EVs/mL. Furthermore, EVs were detected directly in the cell culture supernatant, which eliminates the need for further purification steps in future biosensing experiments and reduces overall experiment time [82].

I.6.2. Presentation of the thesis project

This platform was developed in an optical bench, as illustrated in Figure 26. The biosensing experiments were realized in XLIM after meticulous alignments, which limit it use by biologists under real-time conditions. For this reason, a CIFRE thesis project was initiated to transform this SPR platform into a more compact, stable and easy-to-use system that could be moved to CAPTuR. The project was developed as part of a collaboration between XLIM, ALPhANOV (Centre technologique Optique & Lasers) and L2n (CNRS, University of technology of Troyes). ALPhANOV's main role is to provide expertise in designing photonic systems, mechanical integration and automation. The main role of L2n (including Shuwen Zeng) involves providing expertise on SPR. In this frame, the main objectives of my thesis project are the following:

- The main one consists of developing a miniaturized, robust, easy-to-use SPR-prototype based on the GH method, compatible with biosensing experiments in CAPTuR.

Licence CC BY-NC-ND 4.0

- The development of sensitive SPR-chip. This includes chips associating an Au layer (on the top) with a vanadium dioxide (VO_2) layer (deposited at XLIM). This also include participating to the collaborative project between XLIM, L2N and IRCER (the Institute of Research in Ceramics, CNRS – Limoges University). This project aims to develop novel SPR chips by associating the plasmonic properties of Ag NPs and of thin Au film.
- The demonstration of bio-detection applications in collaboration with colleagues from CAPTuR. The main objective is to detect specific biomarkers on the surface of EVs that are linked to glioblastoma (brain cancer).

Licence CC BY-NC-ND 4.0

Chapter II. Development of a SPR GH prototype

The main objective of Chapter 2 is to introduce a simpler, more stable and easier-to-use version of the reference platform [67]. First, an overview of the reference platform will be provided, highlighting its limitations in terms of size and operation. Based on these constraints, the second part of this chapter describes the developments we made to obtain the prototype. The final section analyzes the causes of instabilities obtained in the measurements which were classified as optical and SPR drifts.

II.1. Overview of the original SPR platform

The reference platform previously developed at XLIM by Shuwen Zeng is shown in Figure 27 [67].

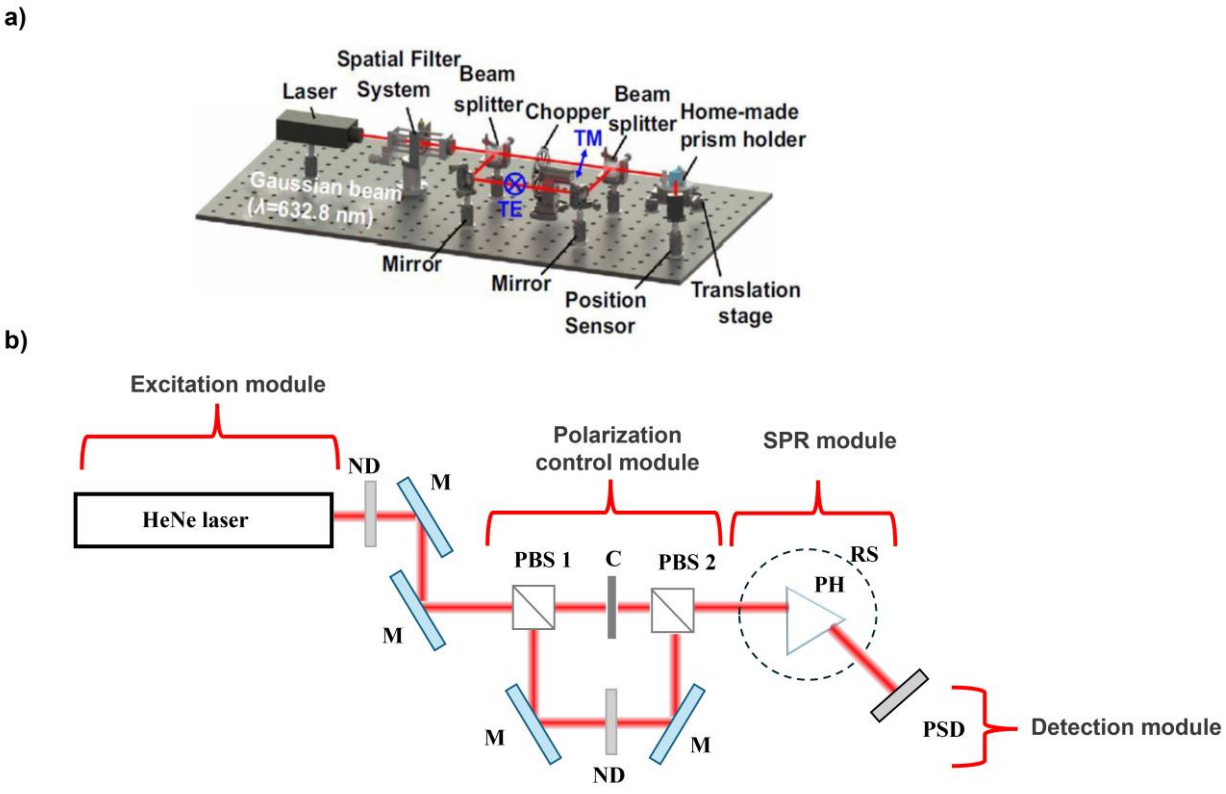


Figure 27 Reference platform showing a neutral density filter (ND), mirrors (M), polarized beam splitters 1 and 2 (PBS1 and PBS 2), chopper (C), rotational stage (RS), prism holder (PH) and position sensitive detector (PSD).

Licence CC BY-NC-ND 4.0

The reference platform includes:

- **An excitation source:** It consists of a coherent, monochromatic and linearly polarized HeNe light source. Coupling SPWs in metals such as Au or Ag requires a single-mode, near-infrared laser with a narrow linewidth. Due to its interesting properties and long-term stability, the HeNe laser can be used for SPR experiments. The main drawback of the HeNe laser is its size: a 10-mW laser is around 50 cm in length.
- **A polarization control module:** SPWs can only be coupled by a TM polarized light. The TE polarization serves as a reference to account for variations unrelated to SPR. Therefore, the polarization control module contains:
    - *Polarized Beam Splitter 1:* It separates the incident linearly polarized laser beam (initially at a polarization angle between TM and TE) into two perpendicular polarizations. The selected PBS has a high extinction ratio (Extinction ratio= $\frac{\text{Transmitted power of TM polarization}}{\text{Transmitted power of TE polarization}}$) of 1000:1, ensuring efficient polarizations splitting.
    - *Chopper:* The chopper alternately blocks the optical path of one polarization while allowing the other to pass. It allows us to measure the position of one polarization at a time.
    - *Polarized Beam Splitter 2:* PBS2 aligns the TM and TE beams in the same direction. This reduces the deviation in position between the two beams prior to their interaction with the SPR chip.
- **A SPR module:** A manual rotational stage (RS) and translational stage are used to position the prism holder (PH) at the resonance angle (Figure 28). The PH serves as the mechanical support that aligns the assembly, which consists of:
    - *A prism,*
    - *A SPR chip,*
    - *A refractive index-matching oil:* to establish the optical contact between the prism and the substrate,
    - *A fluidic channel:* it is made of polydimethylsiloxane PDMS. It contains one injection tube (inner diameter 0.7 mm, length 30 cm),
    - *A mechanical joint:* it is placed between the fluidic channel and the chip. It holds the elements of the holder in place and prevents liquid leakage outside the fluidic channel,
    - *A Screw pressing mechanism:* it applies pressure on the elements of the holder. This ensures stable mechanical contact and proper alignment of the holder.
    - *A 3d printed v-groove:* it protects the prism from cracking under high pressure.
- **Detection module:** A position sensitive detector (PSD) is used to measure the lateral displacement and power of the reflected wave. A PSD from Thorlabs was chosen due to its high resolution in the visible light (resolution of 0.75 µm at 635 nm). Additionally, it has a sensor area of 9x9 mm^2 which is suitable for detecting GH shifts less than 1 mm. The operating power range is between 25 and 100 µW at 633 nm. Therefore, an attenuator is required to enable the detector to operate under optimal conditions.

The intensity arriving at the PSD depends on the amount of light attenuated by SPR in TM polarization. On the other hand, the TE beam is not affected by plasmonic resonance. In this configuration, since the TM and TE beams follow different optical paths, the intensity of the TE beam can be attenuated by placing an additional attenuator. This ensures that the intensity of the TM and TE beams remain within the working range of the PSD.

Licence CC BY-NC-ND 4.0

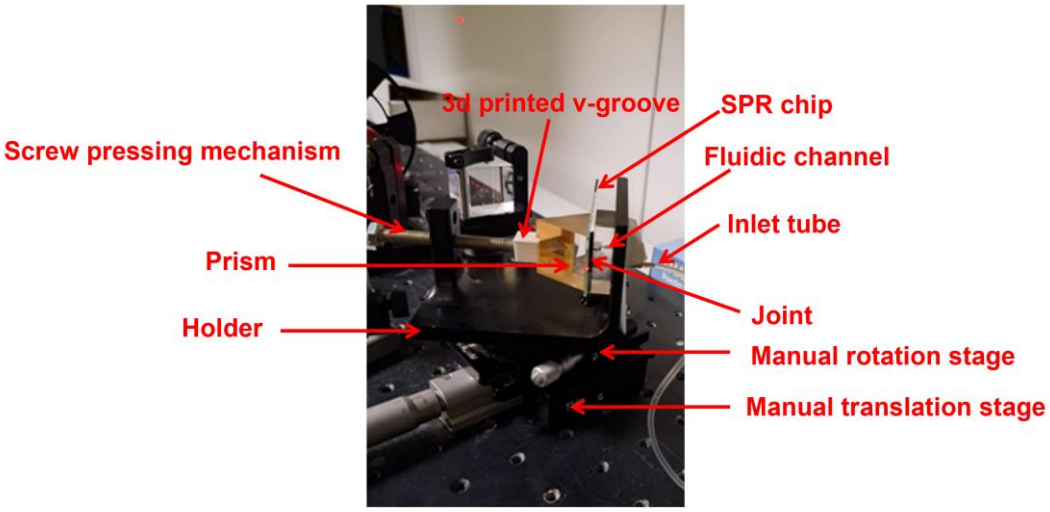


Figure 28 Photograph of the SPR module. It consists of a prism, a SPR chip, a fluidic channel, an injection tube, a mechanical joint, manual rotation and translation stages. The holder along with a screw pressing mechanism and a 3d printed v-groove are used to fix the assembly altogether.

The original holder (Figure 28) design was difficult to install and presented several practical limitations that compromised the overall stability of the reference platform:

- **Complicated installation of the holder:** The installation of the assembly on the holder presented many difficulties:
    1. The fluidic channel was placed on the holder without mechanical fixation,
    2. The joint was placed on the fluidic channel also without mechanical fixation,
    3. The SPR chip (attached to the prism through refractive index oil) was placed on the fluidic channel without fixation.
    4. As the screw was pressed, the assembly will often slip.

- **Unstable mechanical pressing:** The assembly was pressed together by a screw mechanism with a 3D-printed V-shaped groove. However, the mismatch between the prism and V-groove geometry led to misalignments, tilting of the prism and mechanical drifts.
- **Lack of fixed mounting:** As the holder was not fixed to the rotational stage, it was subject to unwanted displacements during operation. This affected the position measurements and the accuracy of the results.
- **Unsecured tubing:** The injection tubes were loosely fixed using a scotch tape, causing liquid leakage, formation of air bubbles and mechanical instabilities after each injection.
- **No output tube:** When the liquid inside the fluidic channel overflows, it can re-enter the prism-SPR chip interface and mix with the refractive index-matching oil. This alters the coupling conditions, reduces the oil's viscosity, and causes additional drifts.

In addition, the SPR the resonance angle was identified manually by measuring the intensity of the reflected beam as function of the incident angle. First, large rotation steps are applied (1°), followed by small increments of 0.04° to identify the resonance angle.

Licence CC BY-NC-ND 4.0

In conclusion, this section presented the reference platform used for the excitation of SPWs in the Kretschmann configuration. Even though this platform was used for several years to perform measurements, it was difficult to use and required precise alignment. As such the experiments could be only performed with trained experts in the field. The various modifications that have been made to the platform will be presented in the following sections.

II.2. Excitation source

The HeNe laser was chosen for coupling SPWs. However, its main disadvantage includes its large size, which is 50 cm in length. The replacement of the laser must be less voluminous while conserving the same characteristics:

- Wavelength: in the red spectrum (600-800 nm),
- Linewidth: in the order of pm,
- Linearly polarized,
- Single mode.

Au or Ag are typical metals chosen to couple incident light to SPWs. Au exhibits strong plasmonic resonance in the visible to near-infrared spectrum. Its permittivity allows for the efficient excitation of SPWs at these wavelengths. In this spectrum, the penetration depth of the evanescent wave in the surrounding environment is about hundreds of nanometers (~ $\lambda/2$). Increasing the excitation wavelength decreases gold's absorption coefficient, leading to sharper plasmonic resonance and higher sensitivity to the surrounding medium. However, this effect is counterbalanced by the relatively high penetration depth, which makes SPWs less confined to the surface. Consequently, SPWs are more sensitive to noise outside the detection region. In our case, we use the prototype to detect the binding of EVs to antibodies. Since the size of EVs typically range from 50 to 150 nm [82], the evanescent field's penetration (~300 nm) is suitable for measuring their binding. For this reason, we chose to use an excitation source at 633 nm [83].

Using an excitation source with a large spectral linewidth in SPR presents many disadvantages. In fact, the resonance angle and the reflectivity depth vary with respect to the wavelength. This is mainly because the permittivity of the metal is strongly influenced by the wavelength (see Chapter 1). When the excitation source has a large linewidth, many wavelengths are present and can be coupled to SPWs at different resonance angles. Consequently, the SPR resonance dip is broader and shallower. In conclusion, the use of a narrow linewidth is essential for high-precision SPR measurements, particularly those based on the GH [83].

The current objective is to identify a more compact laser source that retains the characteristics of the HeNe laser. Several candidates have been evaluated for this purpose. A summary of preselected lasers to replace the HeNe laser is provided in Table 1.

Licence CC BY-NC-ND 4.0

Table 2 Laser selection guide.

Supplier	Name	Wavelength (nm)	Extinction ratio	Size (mm)	Linewidth	Price (k€)
Opton	iBeam smart Wavelength-Stabilized Diode Laser	633	> 50 : 1, linearly polarized	40x40x100	~25MHz << pm	8
Optorim	Cobolt 08-NLD	633	> 100 : 1, linearly polarized	100x40x40	< 1 pm	7.3
Coherent	Ondax RO-USB Series	633	> 100 : 1, linearly polarized	25.4x76.2	150 MHz	3

The lasers shown in Table 2 conserve the characteristics of the HeNe laser: wavelength at 633 nm, linear polarization and thin linewidth. The laser module “Ondax’s RO USB series” has been chosen as a potential alternative due to its small size (< 8 cm length) and relatively lower price. Additional information is provided in Table S3 of the Annex.

II.3. Optimization of the Polarization Control Module

This section introduces the modifications made to the polarization control module. In the reference platform, PBS cubes were used to separate the laser beam into TM and TE components, which made the experimental bench bulky. To reduce the size of the polarization control module, we placed a half-wave plate on a motorized piezoelectric mount (see section S4 of the annex for additional information). In this configuration, the TM and TE beams originate from the same source and travel in the same direction.

After placing the waveplate, the intensities of the TM and TE beams arriving at the SPR module are equal. After the SPR module, however, the TM beam is highly attenuated while the TE beam remains unaffected. The power difference between the two beams is too high to be accommodated by the PSD. Therefore, a selective attenuation solution is needed—one that only attenuates the TE beam. Thus, we attempted to place attenuation filters on a motorized multiposition slider (Figure 29).

Although the excitation source is initially linearly polarized with an extinction ratio of 100:1, residual TE could potentially affect GH measurements. Therefore, we chose a nanoparticle linear film polarizing filter due to its high extinction ratio of 100 000:1. This ensures that the beam reaching the SPR module is purely TM.

Licence CC BY-NC-ND 4.0

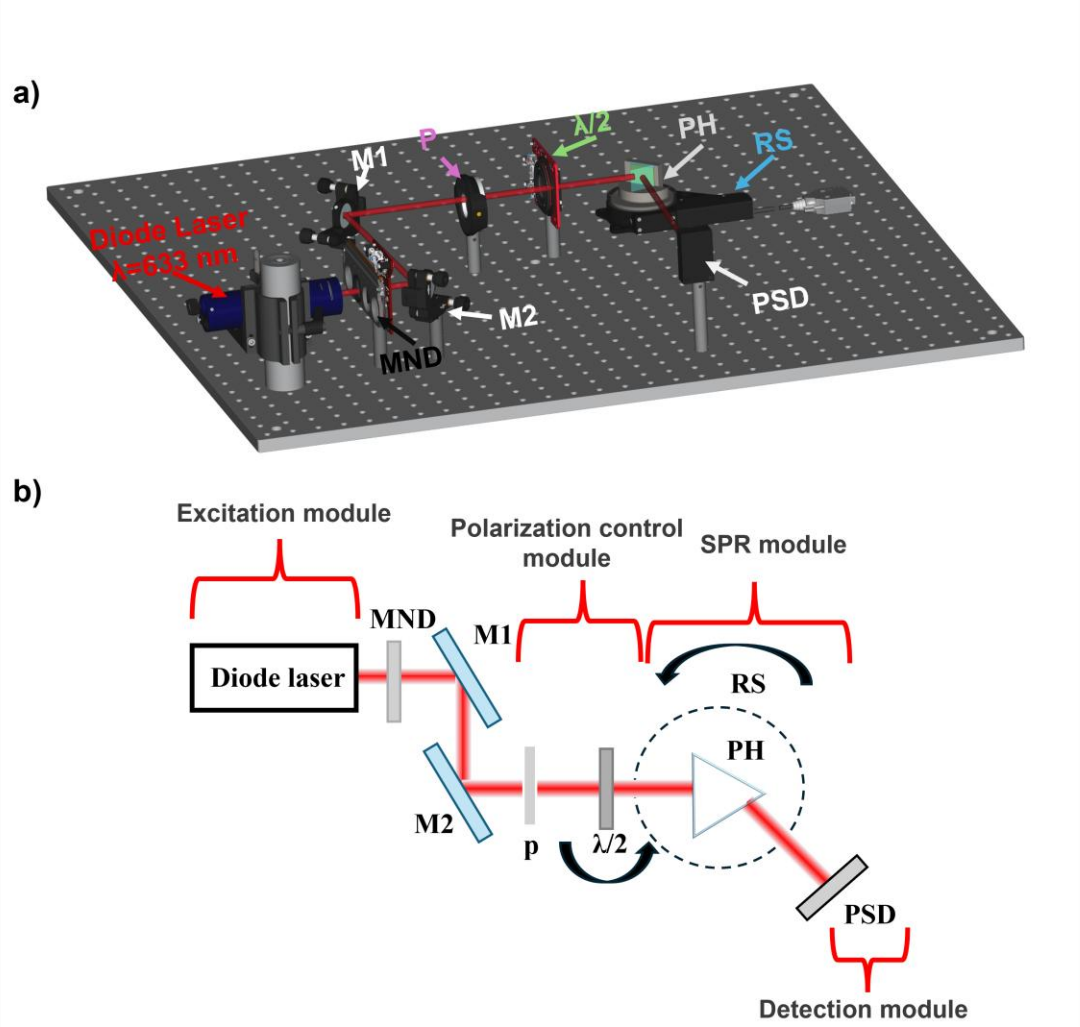


Figure 29 Schematic of the prototype showing a motorized mulitposition slider with neutral density filters (MND), mirrors (M1 and M2), polarization filter (P), half waveplate (λ/2), rotational stage (RS), prism holder (PH) and position sensitive detector (PSD).

II.3.1. Procedure for determining the TM polarization

This section aims to introduce the experimental procedure we follow to determine the TM polarization. The prototype (Figure 29) was used without the motorized slider and with a power meter instead of the PSD. The commercial chip coupled with SF11 prism (Figure 30) was first installed on the newly developed holder (presented in Section II.4.1).

Licence CC BY-NC-ND 4.0



Figure 30 Schematic of the commercial SPR chip coupled with a SF11 prism.

Water was then injected into the fluidic channel. First, the waveplate was placed at a polarization angle between TM and TE. The resonance angle was found by identifying the angle with the minimum reflected intensity. Then, the waveplate was rotated by 2° increments and the intensity recorded for each polarization angle. TM polarization is determined by identifying the polarization angle that results in the lowest reflected intensity (Figure 31). Consequently, the TE polarization angle is identified as follows:

$$\mathrm{Angle}_{\mathrm{TE}} = \mathrm{Angle}_{\mathrm{TM}} + 45^{\mathrm{o}} \tag{14}$$

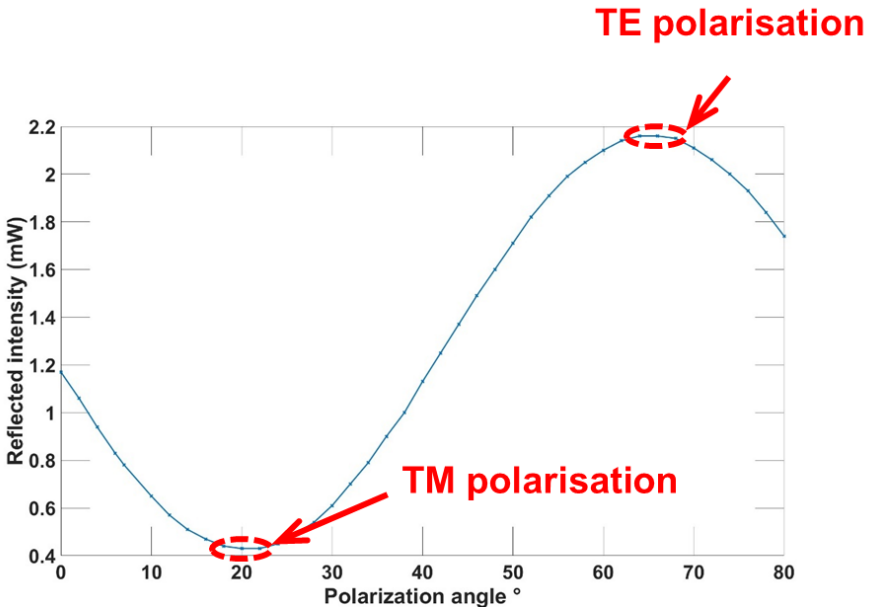


Figure 31 Measurement of the reflected intensity vs the polarization angle of the waveplate. The TM and TE polarizations respectively correspond to the polarization angles producing the minimum and maximum reflected intensity.

Licence CC BY-NC-ND 4.0

The curve (Figure 31) presents a sinusoidal shape where the maximum power corresponds to TE polarization and the minimum to TM polarization. The waveplate rotation gradually changes the polarization state of the beam where, at a certain polarization angle, the incident electric field lies in the plane of incidence. This results in optimum coupling of the SPWs and therefore maximum attenuation of the incident light. When the polarization angle is rotated further, the electric field vector has a component outside the plane of incidence, which leads to less pronounced coupling with the SPWs.

II.3.2. Prevention of PSD saturation with a controlled attenuator

This section aims to introduce two methods we investigated to attenuate TM and TE polarizations separately:

1) Neutral density filters were placed on a motorized, multiposition slider (Figure 29). To attenuate TM, we placed the slider in position one (corresponding to attenuator one) via Python code. Conversely, we placed the slider in position two to attenuate TE (corresponding to attenuator two).

2) A fixed polarization filter was placed before PSD (P2, Figure 32). The power ratio between TE and TM beams can be adjusted by rotating the polarization angle of P2. This reduces the number of motorized components in the system but could affect the GH measured by the PSD.

Licence CC BY-NC-ND 4.0

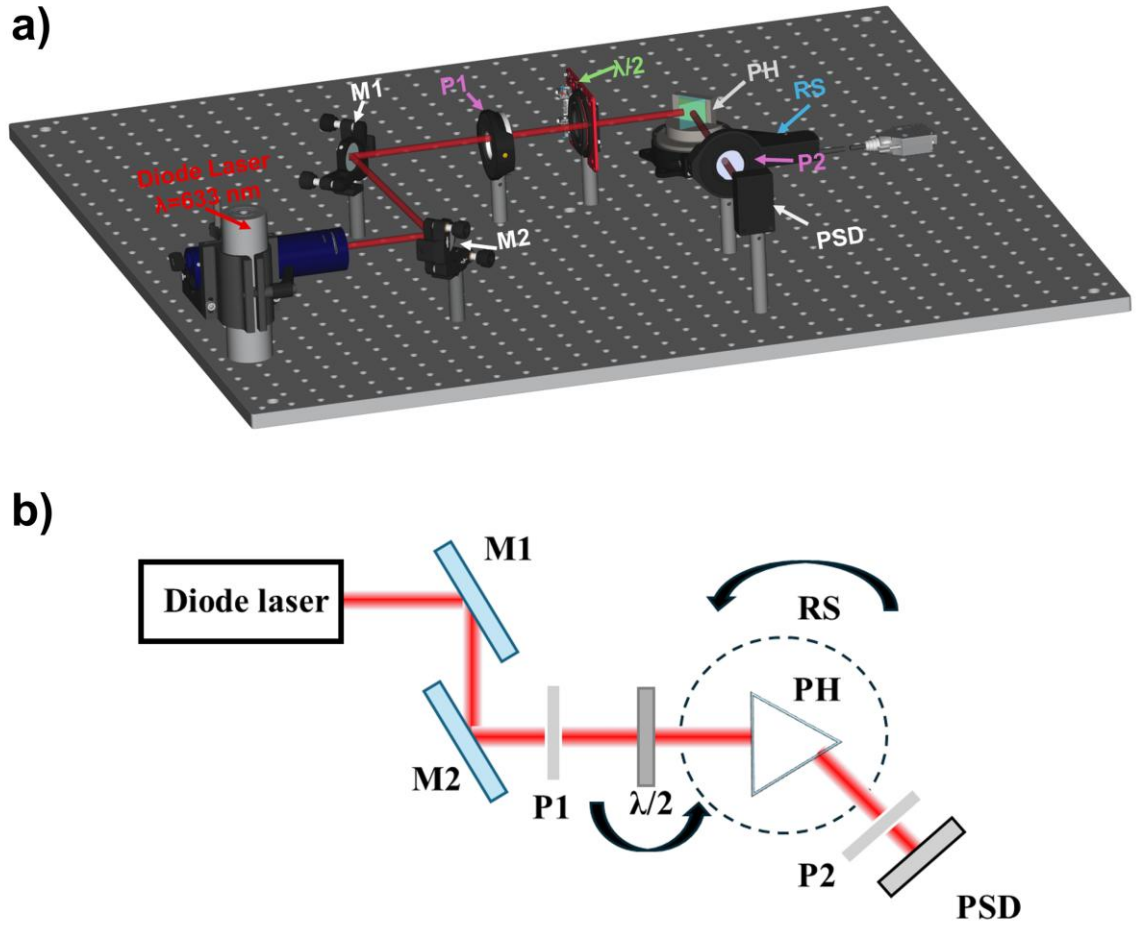


Figure 32 Illustration of the SPR prototype composed of mirrors (M1 and M2), two polarization filters (P1 and P2), a half waveplate (λ/2), a rotational stage (RH), a prism holder (PH) and position sensitive detector (PSD).

To compare the stability of the motorized slider to that of P2, the experiment was conducted as following. The slider was placed in front of the laser (Figure 29), and then P2 was placed in front of the PSD (Figure 32). For both cases, a commercial chip coupled with SF11 prism (Figure 30) was installed on the newly developed holder (Presented in Section II.4.1). Water was then injected into the fluidic channel. The position x of the reflected beam was measured in TM polarization for 50 seconds and in TE for 30 seconds. The average of the TE measurements is computed and then subtracted from TM.

The results are presented in Figure 33 and Table 3.

Licence CC BY-NC-ND 4.0

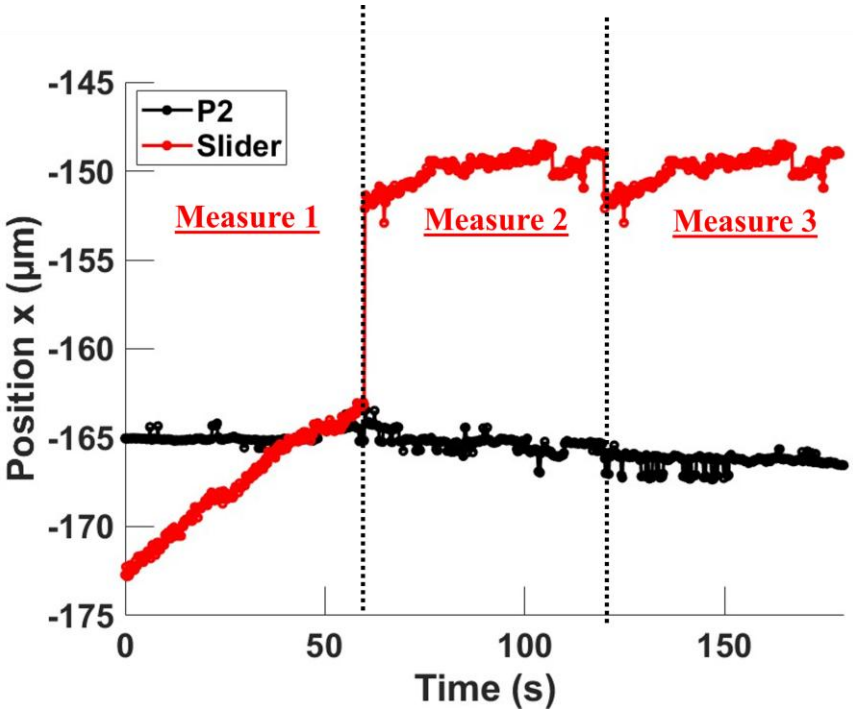


Figure 33 Measurement of the position x of the reflected beam. The red curves represent the attenuation with P2 and the black curves represent the attenuation using neutral density filters placed on the motorized slider.

Table 3 Standard deviation in x and y positions measured using two different attenuation methods: neutral density filters on a motorized slider and P2. There are a total of 360 measurement points for each test.

Attenuation method	Polarization	Position x Average standard deviation (µm)	Position y Average standard deviation (µm)
Motorized slider	TM	8.5	2.7
	TE	5.7	0.7
Polarization filter	TM	0.7	0.9
	TE	1.4	1.1

We found a 24 µm change in the position x between the first and final measurements when the neutral density filters were placed on the slider (Figure 33, Table 3). The errors in the position and the standard deviation are too high and could not be reliable for measuring the GH shift. On the other hand, there was no change in the position x when measuring with P2. As a result, the motorized slider was replaced with the P2 in the prototype.

Licence CC BY-NC-ND 4.0

Comparison of the GH sensitivity with and without a polarization filter in front of the PSD

The objective of this section is to evaluate the effect of adding P2 after the SPR module. Even though P2 was used as an attenuator, it could modify the GH shift. We conducted a comparison test in two configurations: one with P2 and one without.

The commercial chip coupled with SF11 prism (Figure 30) was placed on the newly developed holder (presented in Section II.4.1). Water was then injected into the fluidic channel. In the first case without P2, the laser beams (representing TM and TE) were attenuated manually via a filter density wheel (placed in front of the PSD). The resonance angle was found, and then the TM polarization was determined as described Section II.3.1. The position x of the reflected beam was measured in TM polarization for 50 seconds and in TE for 30 seconds. The average of the TE measurements is computed then subtracted from TM. Water was removed from the fluidic channel, and 1% glycerin (diluted in water) was injected. The position x was measured similarly. The GH shift between water and 1% glycerin was then computed.

The chip was then rinsed with water, and P2 was placed in front of the PSD. We repeated the same experimental procedure. In principle, P2 is oriented close to the TM direction to preserve the TM component and attenuate the TE component.

The results are presented in Figure 34 and Table 4.

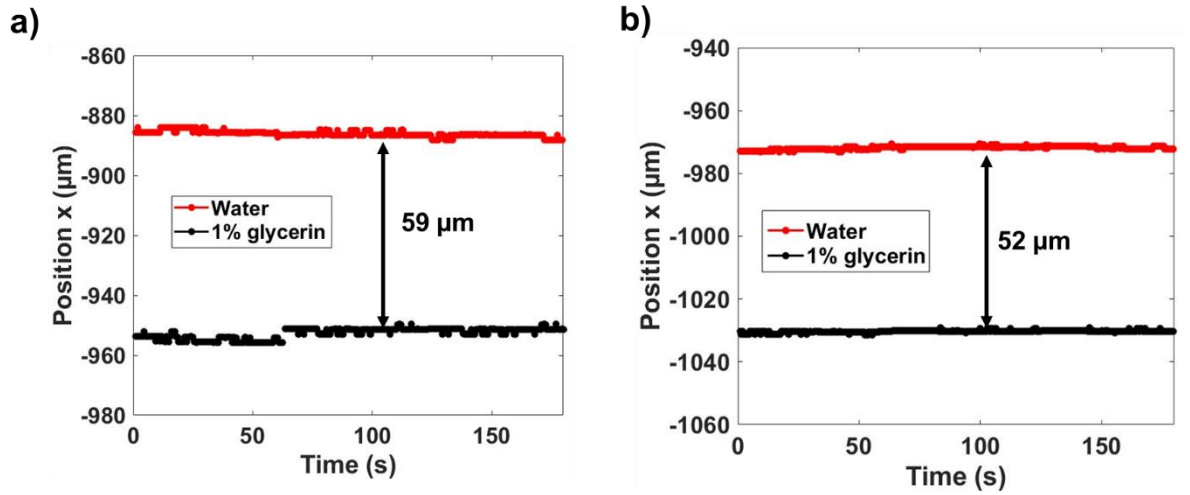


Figure 34 Measurement of the GH shift between water and 1% glycerin, a) Without P2 and b) With P2.

Table 4 GH shift measured with and without P2.

Case	x Position shift (µm)	y Position shift (µm)
Without P2	59	4
With P2	52	3

Licence CC BY-NC-ND 4.0

It is important to emphasize that the GH shift is linked to the position x shift of the reflected beam. For this reason, stability parameters such as rinse recovery and standard deviations are quantified using the x-component. Taking into consideration the contribution of the y component (Table 4), the modulus $M = \sqrt{GH_x^2 + GH_y^2}$ can be derived. For the case with P2, the modulus of the GH shift between water and PBS was M=52 µm, while for the case without P2, M=59 µm. The GH shift, calculated using the modulus, is shown to be equal to that measured by the displacement of the x-position, indicating the negligible effect of the y component on overall GH sensitivity. Consequently, the GH shift will from now on be computed in terms of position x displacement.

In conclusion, the difference of 7 µm between the two cases was small enough. Therefore, P2 was selected as the attenuation source in the prototype.

II.3.3. Influence of the piezoelectric motor positioning on the GH shift

This section evaluates whether the position of the piezoelectric motor remains consistent during repeated TM and TE cycles. This step is important because any error or backlash from the motor will result in a change in the polarization angle. This will cause an incorrect GH measurement on the PSD. The experiment was conducted as described below.

The commercial chip (Figure 30) coupled with BK7 prism was installed on the holder of Figure 35. In this case, the surrounding medium is air.



Figure 35 Illustration of the holder used for air measurements.

The position x of the reflected beam was measured for 10 cycles of TM and TE. Each polarization state was recorded for 100 seconds using the PSD. The results are presented in Figure 36.

Licence CC BY-NC-ND 4.0

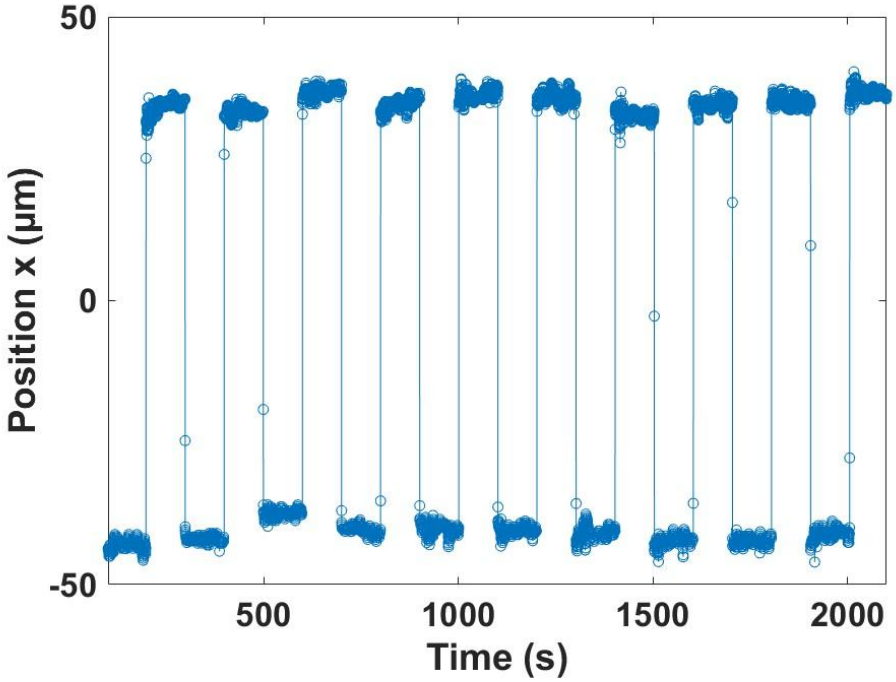


Figure 36 Measurement of the position x of the reflected beam for 10 cycles of TM and TE.

We observed an overall jump (Figure 36) in position x (~ 90 µm). This corresponds to the GH shift between TM and TE. The difference in position x of the TM beam between its maximum and minimum values was found to be 4 µm. Meanwhile, the variation between the first and last measurements was approximately 2 µm. Similarly, the position x of the TE beam changed by 4 µm over the 10 cycles. Consequently, the difference in position x between TM and TE remains constant. This validates the stability of the prototype under repeated polarization switching. This is achieved by subtracting the TM position from the TE position. For this reason, the waveplate on the piezoelectric motor was adopted as the polarization switching mechanism in the prototype.

II.3.4. Comparison of the GH measurements with and without a polarization filter after the laser

The objective of this section is to determine whether a polarization filter is required after the laser. As the laser diode is initially linearly polarized with a high extinction ratio (100:1), the need for an extra polarization filter (P1) in the prototype was thoroughly studied.

The commercial chip coupled with SF11 prism (Figure 30) was placed on the holder of Figure 28 (without 3d printed v-groove). The experimental procedure is the same as that described in Section II.3.2, except that PBS is used instead of 1% glycerin. First, the GH shift was measured with P1, and then it was measured without P1. For both cases, the TM polarization was found as described in Section II.3.1. The results are presented in Figure 37.

Licence CC BY-NC-ND 4.0

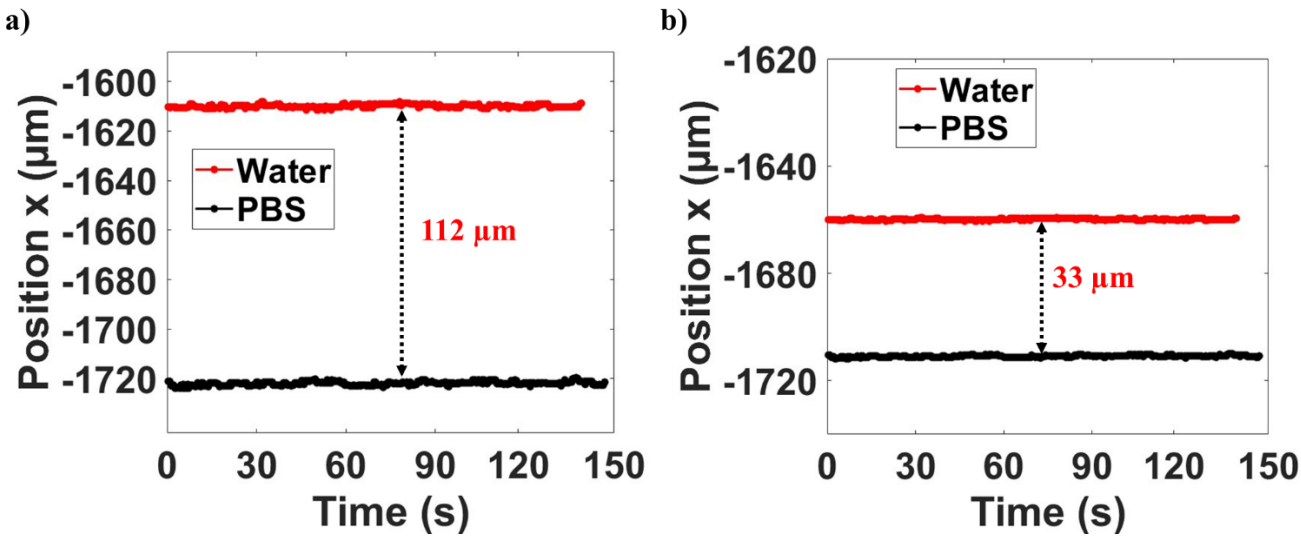


Figure 37 Measurement of the GH shift between water and PBS, a) With P1 and b) without P1.

To evaluate the stability of the tests, the standard deviation of all the measurements of water and PBS were extracted. The standard deviation was approximately 1 µm for water and 2 µm for PBS for both cases (Figure 37, with 600 measurement points for each test). The sensitivity improved by a factor of four when a polarization filter was added. This result highlights the need to add P1 in the prototype as the presence of residual TE in the beam was found to have a big influence on the PSD's GH reading. Therefore, P1 will be left in place in the prototype.

II.4. Optimization of the SPR module

II.4.1. Optimization of the prism holder

In this section, we present the holder that was designed to facilitate the installation of the SPR chip. The holder of Figure 38, was used for most of the experiments owing to its ease of installation and secure fixation. Compared to the old holder (Figure 28), the prism is placed in a v-groove in this configuration, which prevents it from moving during installation. Additionally, the joint is fitted into a circular groove cut into the fluidic channel. Likewise, the fluidic channel is secured in a rectangular groove. Then, two tubes (one for injection and the other for output) were tightly connected to the fluidic channel using connectors. Finally, the holder is screwed onto a rotational stage, ensuring it remains in place during experiments.

Licence CC BY-NC-ND 4.0

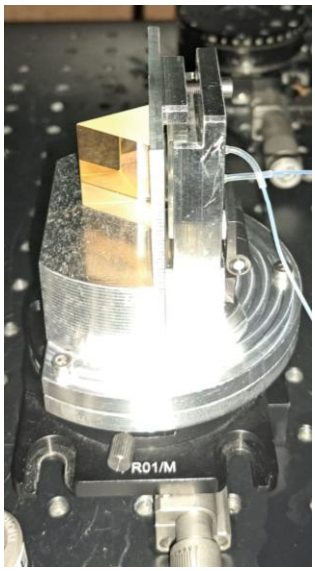


Figure 38 Illustration of the newly developed holder. The commercial chip coupled with SF11 prism was installed on the holder.

The installation of the assembly on the newly developed holder involves many steps:

1. Place a drop of oil on the substrate and fix it to the prism. Note that the substrate must always be smaller than the prism's area (<2 x 2 cm^2). Otherwise, the oil drop will escape from the sides when the assembly is pressed together. Additionally, the quantity of oil must be adjusted (~ 1 µl) so that the SPR chip is firmly attached to the prism and does not slip when held vertically.

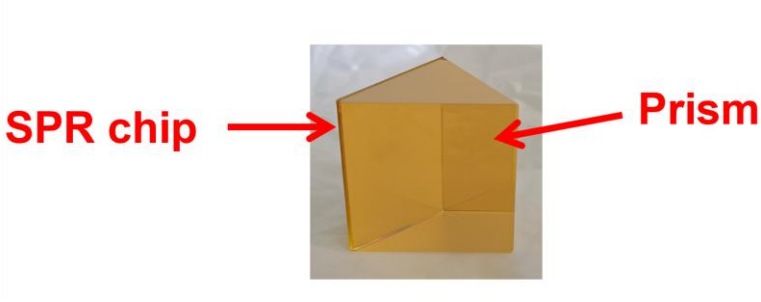


Figure 39 Illustration of the commercial SPR chip fixed on a prism via an oil drop.

Licence CC BY-NC-ND 4.0

2. Place the chip-prism on the corresponding v-groove (Figure 40).

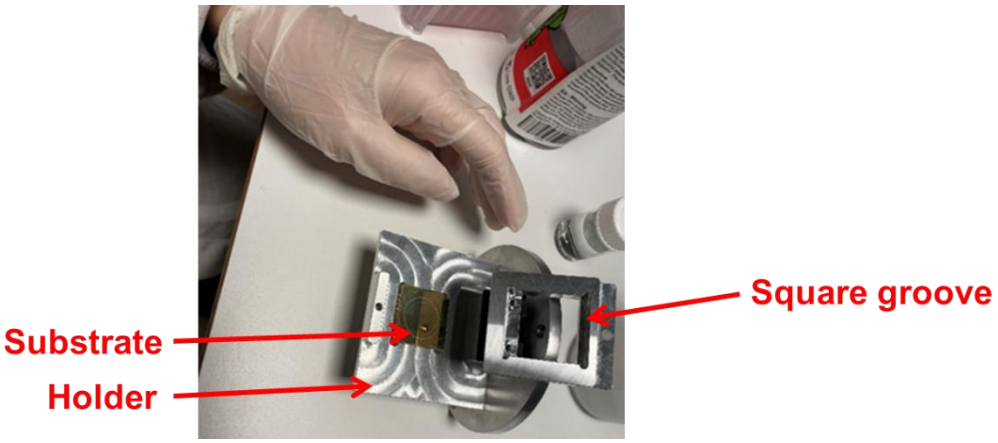


Figure 40 Illustration of the prism-chip assembly placed on the v-groove of the holder.

3. Place the fluidic channel in the corresponding square groove and press the entire system together. Finally, place the connectors and tube on the fluidic channel (Figure 41). The tubes are 20 cm in length and have an inner diameter of 0.5 mm.

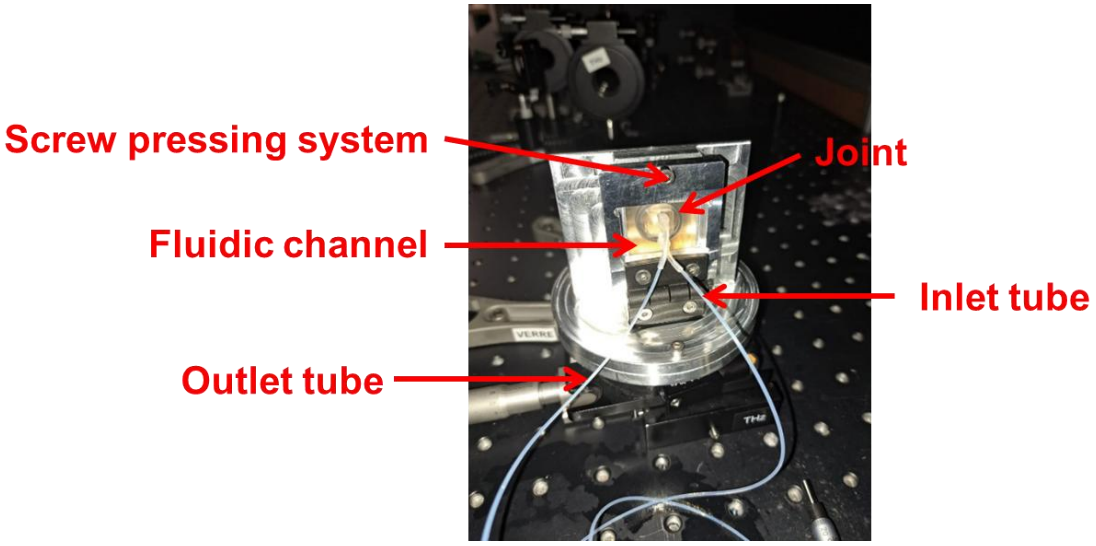


Figure 41 Illustration of the final assembly.

The newly developed holder design could be improved by adjusting several parameters:

- If a high pressure is applied, the prism may crack slightly along the edges. To prevent this, we can use a torque driver to adjust the pressure and ensure that it is applied equally during each installation.
- Due to design and manufacturing inaccuracies, the slightly inclined door applied uneven pressure to the assembly when the screw was pressed. This resulted in uneven oil distribution, causing oil to leak from the edges of the prism and leaving air gaps. To prevent this issue, the oil volume was controlled at approximately 1 µl for a 2 x 2 cm^2 SPR chip. This ensures that the SPR chip is tightly fixed to the prism with no excess oil that could escape.

Licence CC BY-NC-ND 4.0

To further improve the holder, a newer design was proposed (Annex-S5) but was not implemented due to the lack of time. As such the holder presented in Figure 38 was later used for most of the experiments.

II.4.2. Procedure for determining the resonance angle

After fabricating the new holder (Figure 38), we investigated whether a motorized rotating mirror or rotational stage should be used to determine the resonance angle. The advantage of using a motorized mirror is its low cost, as Thorlabs has a motorized piezoelectric stage compatible with the rotational mount of the waveplate. However, this stage has a maximum load capacity of 200 g, so it is only suitable for mounting the mirror. Simultaneously, we considered whether it was necessary to position the PSD on a moving stage. For this reason, we used FreeCAD to determine the maximum allowable rotation range of the mirror. This was achieved by considering the dimensions of the PSD and fluidic channel, ensuring that the reflected beam spot remained within their boundaries.

We considered a commercial chip (Figure 42) coupled with an SF11 prism and water as the surrounding medium to draw the sketches. Commercial Au chips are deposited on BK7 substrates with a thickness of 0.7 mm and an index of refraction of 1.52. We use an SF11 prism (n = 1.78) to couple SPWs for GH tests in liquids. In this configuration, resonance occurs at an angle that can easily be found experimentally (~54° with an SF11 prism and ~72° with a BK7 prism). The difference in refractive index between SF11 and BK7 causes light to be partially reflected when it reaches the SF11-BK7 interface. This creates an additional reflected beam, R. The transmitted beam (T) enters the structure and couples with SPWs. That beam then remerges in the prism and is known as the SPR beam. As such, we consider the distance between the two reflection spots to be 4.3 mm.

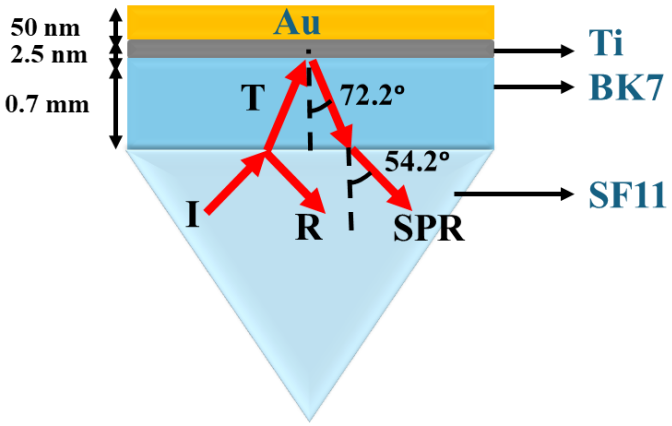


Figure 42 Schematic of the commercial SPR chip coupled with SF11 prism. It shows the two reflection spots known as R and SPR.

Additionally, we set the distance between mirror M2 and the center of the fluidic channel to 27 cm. Then, we fixed the distance between the PSD and the center of the fluidic channel at 19 cm (Figure 43). The diameter of the laser beam was set to 1 mm.

Licence CC BY-NC-ND 4.0

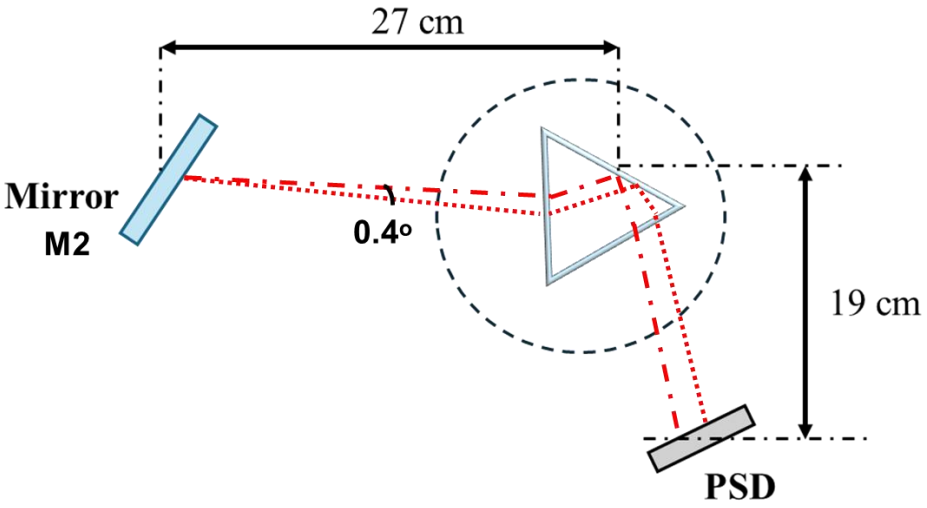


Figure 43 Geometrical layout of the optical components in the prototype. The dashed line and dotted lines represent two laser beams reflecting from Mirror 2, with an angular span of 0.4°.

The maximum allowable angular range of M2 was found to be ±0.4° (Figure 43). This corresponds to an angular variation of ±0.22° within the prism. Using a motorized rotating stage would enable a maximum rotation of ±0.6° within the prism without surpassing the PSD boundaries. Therefore, the decision was made to use a motorized stage to rotate the holder. The rotation axis of the holder was aligned with the incident light (in other terms, the rotation axis of the rotational stage passes through the point where the beam hits the prism). This minimizes displacement of the beam spot inside the prism during rotation, contrary to configuration shown in Figure 43. The selection of the motorized rotational stage was based on three main criteria: minimal incremental angle, compact size, sufficient load capacity to support the holder and price (Annex section S6).

To identify the resonance angle, we first perform a pre-rotation step to position the holder close to its theoretical resonance angle (approximately 54° for commercial Au chips). Then, we perform a fine rotation step (approximately ±0.3° motor rotation) to adjust the resonance angle based on the maximum TM-TE shift measured. To illustrate this procedure, we experimentally measured the GH curve versus the incident angle inside the prism. The commercial chip was coupled with a SF11 prism (Figure 30) and placed on the newly developed holder (Figure 38). Water was then injected into the fluidic channel. The angle of the rotational stage was varied in 0.1° increments via a Python code. The position x of the TE beam was measured for 30 seconds at each step. The average was computed and subtracted from the TM measurement, which was taken for 50 seconds. The results are shown in Figure 44.

Licence CC BY-NC-ND 4.0

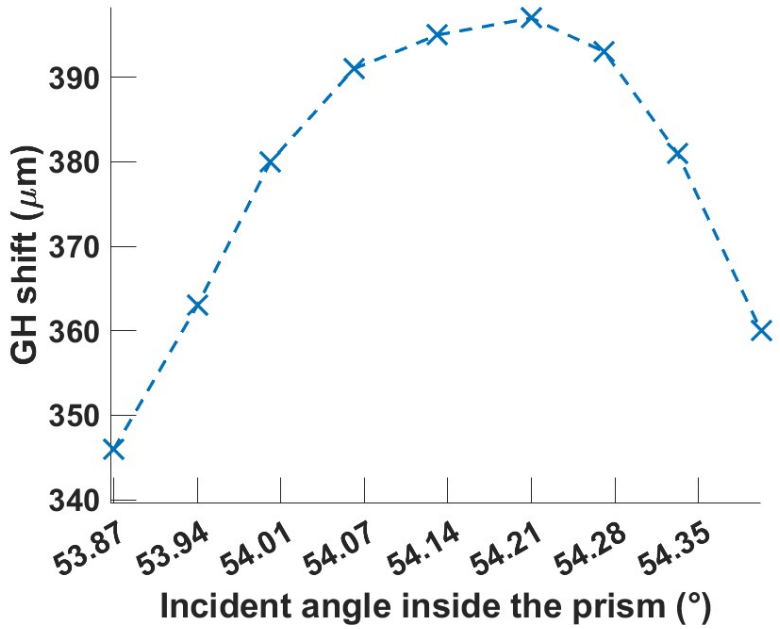


Figure 44 Measurement of the GH shift versus the incident angle inside the prism.

We observe that the GH shift increases progressively as the incident angle becomes larger until reaching a maximum (Figure 44). This maximum corresponds to the SPR resonance angle. Away from that, the GH decreases, indicating a weaker coupling of the incident light to SPWs.

II.5. Optimization of the detection system

A PSD was originally employed in the reference platform (Figure 27) to measure the GH shift. In this section, we investigated the possibility of replacing the PSD with a CCD camera, which has a larger sensor area and a lower price. Experiments were carried out following these three steps :

1. Measurements of the displacement of the laser beam without a chip,
2. Measurement and comparison of the GH shift for a SPR chip in air,
3. Measurement and comparison of the relative GH shift for a SPR chip in liquids.

This work was carried out in part-in collaboration with a M2 student during her internship.

II.5.1. Comparison of the diode laser and HeNe laser beam profiles

Before comparing the camera to the PSD, the beam profile of the diode and HeNe lasers were visualized using a beam profiler Spiricon BGS-USB-SP620U (Figure 45). Neutral density filters were placed in front of the lasers, with the beam profiler positioned approximately 20 cm from them.

Licence CC BY-NC-ND 4.0

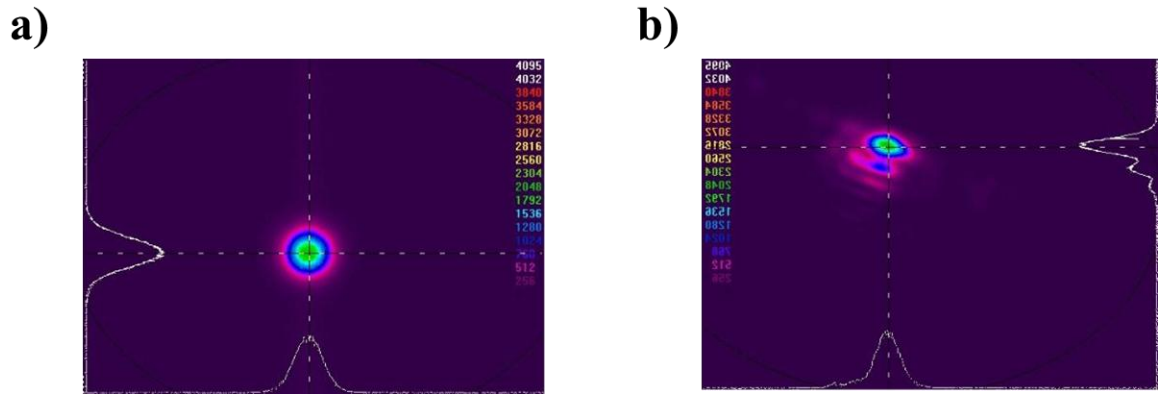


Figure 45 Visualization of the laser beams, a) HeNe laser beam profile and b) Ondax Diode laser beam profile.

The HeNe laser beam is circular in shape with a Gaussian intensity profile (Figure 45-a). In contrast, the diode laser beam has an elliptical profile and displays interference fringes (Figure 45-b). A comparison between the two detection benches was made to verify that the sensitivity of the prototype is not affected by the presence of these fringes.

Analysis of the effect of the laser beam shape on the GH sensitivity:

The experiments were conducted using the commercial chip coupled with a SF11 prism (Figure 30) and placed on the newly developed holder (Figure 38). The procedure was conducted as explained in Section II.3.2. The assembly was first installed on the reference platform (Figure 27) than on the prototype (Figure 32). In this part, the attenuation was manually adjusted using a neutral density filter wheel. We found the same resonance angle for both cases. This was determined by measuring the intensity of the reflected beam with and without water in air. We then defined the intensity ratio between air and water as $R = \frac{Iair}{Iwater}$. The same R was found for both cases. The results are shown in Figure 46.

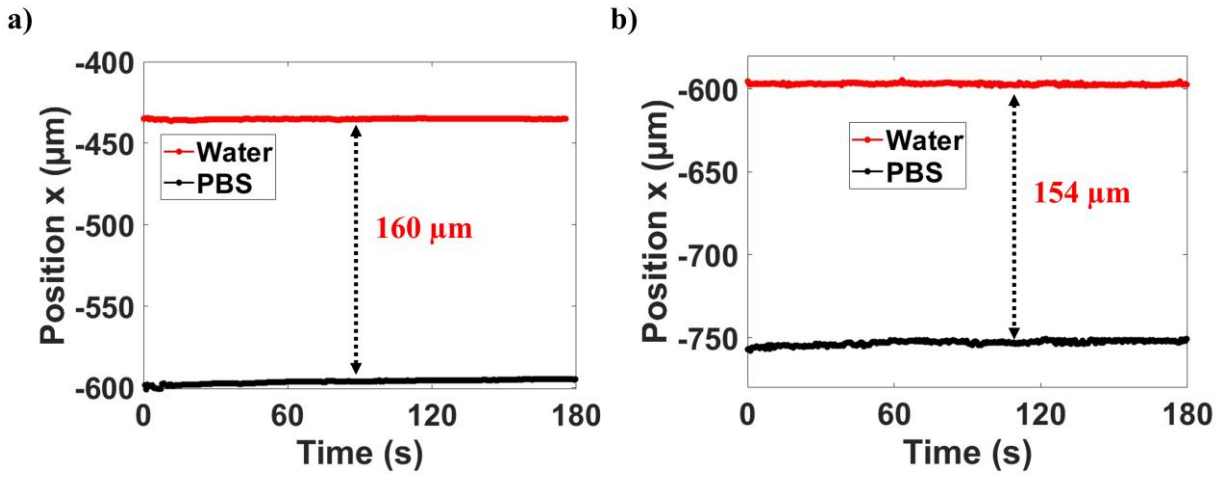


Figure 46 Measurement of the GH shift between water and PBS with the commercial chip. a) The GH shit was measured with the reference platform and b) with the prototype.

Licence CC BY-NC-ND 4.0

The standard deviations were found to be 0.3 µm for water and 0.2 µm for PBS on the reference platform. On the prototype, the standard deviations were 0.2 µm for both water and PBS (for 360 data points per measurement). These results indicate a comparable level of stability for both cases.

In the reference platform, the differential GH shift (GH shift of water subtracted from that of PBS) was at 160 µm. After rinsing the channel with water, the GH signal returned to its original value within 4 µm, corresponding to an error of 0.9%. Meanwhile, the GH shift with the prototype was found to be 157 µm, indicating a comparable level of sensitivity. In conclusion, these results prove that the prototype maintains the reference platform's sensitivity despite the presence of fringes in the beam's profile.

To validate these results, the experiment was repeated using another SPR chip N1 (Figure 47).

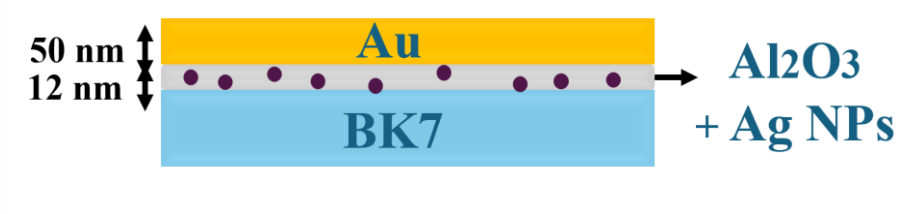


Figure 47 Schematic of the N1 chip. The diameter of the Ag NPs is 4.4 ± 1.4 nm. Alumina and Au thickness are 12 and 50 ± 1 nm respectively.

We followed the same experimental procedure as previously described to ensure that the comparison remained consistent across both detection benches. The results are presented in Figure 48.

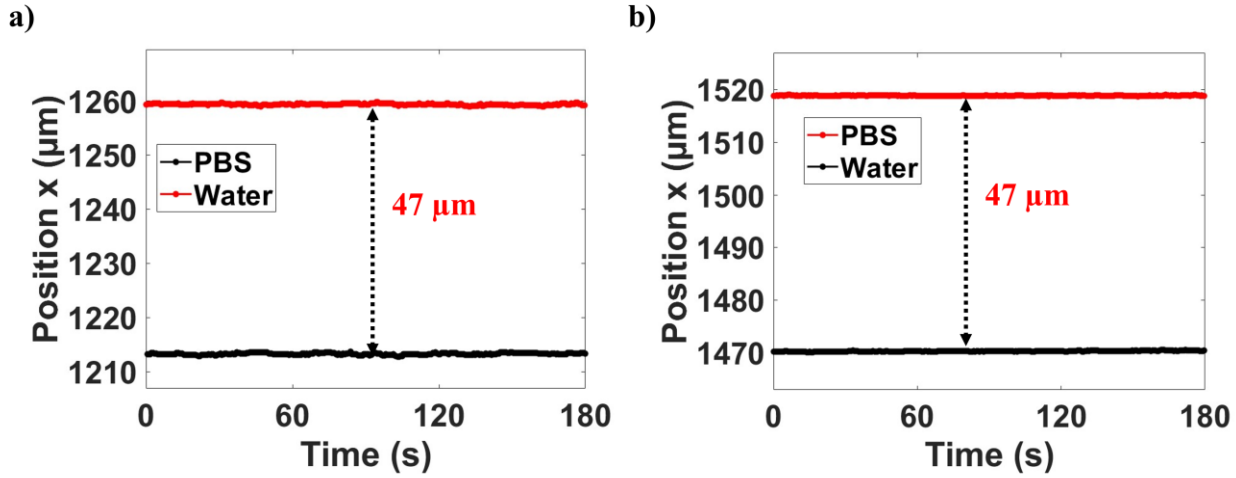


Figure 48 Measurement of the GH shift between water and PBS with the N1 chip. a) The GH shit was measured with the reference platform and b) with the prototype.

The measurements were relatively stable in the reference platform, with standard deviations of 0.6 µm for water and 0.4 µm for PBS (for a total number of 360 data points per measurement). Standard deviations of 0.9 µm were observed for both solutions in the prototype, demonstrating a comparable stability.

Licence CC BY-NC-ND 4.0

In the reference platform, the GH shift was 47 µm. After rinsing with water, the signal returned to its initial value within 2 µm, which corresponds to an error of 0.2%. In the prototype, the GH shift was 48 µm.

Overall, these two results demonstrate that the beam profile of the diode laser did not affect the sensitivity of the prototype. Hence, the diode laser was kept as the excitation source for the prototype.

II.5.2. Laser beam displacement without the SPR chip: PSD vs Camera

First, the camera and PSD were compared by measuring the displacement of the laser beam alone. For that, A DMK 27BUP031 USB 3.0 monochrome industrial CMOS camera from Imaging Source was used:

- **Sensor Size:** H: 36 mm, W: 36 mm, L: 25 mm,
- **Pixel Size:** H: 2.2 µm, V: 2.2 µm.

The following parameters were used for the camera measurements:

1. The attenuation and exposure time of the camera were regulated accordingly so as not to saturate the camera,
2. The acquisition time was set to 5 frames per second and 1 minute measurement for each variable,
3. The images were processed using imagej software to reduce noise,
4. The images were then converted to matrices,
5. The centroid of the laser beam was determined using imagej software find maxima tool.

The diode laser was placed instead of the HeNe laser on the reference platform (Figure 27). Before measuring the position difference with the camera, the diode laser spot was visualized after PBS2 to ensure that there is no additional interferences coming from the optics (Figure 49).

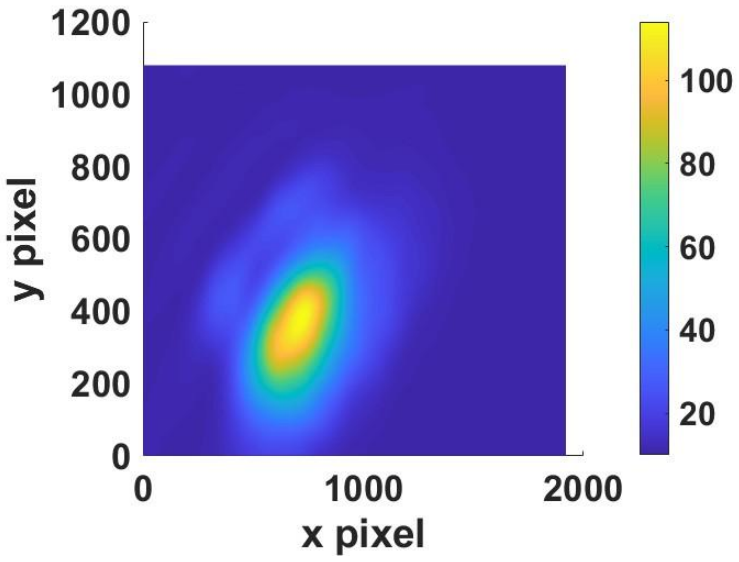


Figure 49 Visualization of the diode laser beam spot directly after PBS2.

Licence CC BY-NC-ND 4.0

A misalignment was purposely induced between the TM and TE optical paths by slightly rotating mirror M2. First, the position difference was measured by the PSD, and then by the camera. Since the PSD and camera have different operating power ranges, a polarization filter was placed in front of the detector (camera or PSD). An additional neutral density filter was used when measuring with the camera. The detectors were placed in the same location and oriented perpendicular to the TM beam. To account for misalignment errors related to repeatedly installing and reinstalling the sensors, the position difference was re-measured two more times using the PSD. The maximum and minimum positions were then derived. This process was repeated three times. The results are shown in Table 5.

Table 5 Comparison between the PSD and the camera by measuring the diode laser position shift after the rotating mirror M2.

Measurement	**Measured by PSD (µm)**	**Measured by camera using imagej (µm)**
1	Average: 81 Max value: 87 Min value: 74	117
2	Average: 97 Max value: 121 Min value: 72	96
3	Average: 179 Max value: 184 Min value: 175	171

The position difference measured by the camera (Table 5) was close to the average value obtained by the PSD. Despite variations in the absolute values of the PSD, this preliminary result allows us to proceed to the detection of the GH shift between TM and TE in air.

II.5.3. Measurement of the GH shift with a camera and PSD using air as the surrounding environment

The following experiment was conducted to compare the GH shift measured with the PSD and the camera in the prototype (Figure 32). The GH shift was measured using the PSD and then using the camera. Two SPR chips were tested: the commercial chip (Figure 30) and sapphire chip (Figure 50), both coupled with a BK7 prism.

Licence CC BY-NC-ND 4.0



Figure 50 Schematic of a SPR chip consisting of 47 nm Au deposited on sapphire with 3 nm titanium.

The two chips were installed on the air holder (Figure 35), and the position x of the reflected beam was measured at TM and TE polarizations for one minute for each. The average of each measurement was computed, and the GH shift was set as the difference between the two averages. The results are shown in Figures 51-52 and Table 6.

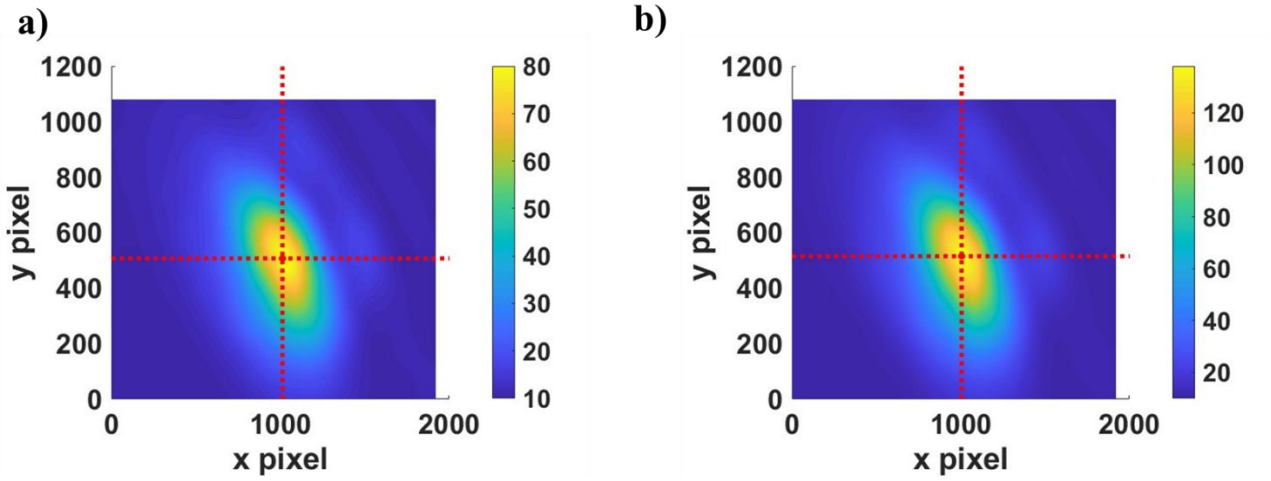


Figure 51 Visualization of the laser beam spot in air using the commercial SPR chip at, a) TM polarization and b) TE polarization.

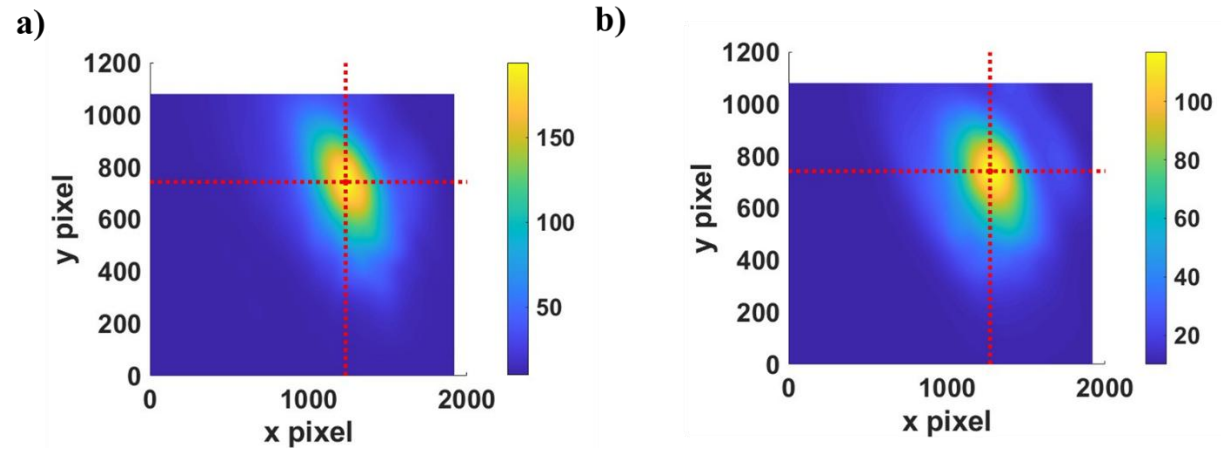


Figure 52 Visualization of the laser beam spot in air using the sapphire chip at, a) TM polarization and b) TE polarization.

Licence CC BY-NC-ND 4.0

Table 6 GH shift measured by the PSD and Camera with commercial and sapphire chips in air.

SPR chip	Measured by PSD (µm)	Measured by camera using imagej (µm)
Commercial chip	37	44
Sapphire chip	97	120

The GH shift detected by the camera was slightly larger than that measured by the PSD. An increase of 7 µm was observed with the commercial chip versus an improvement of 23 µm with the sapphire chip.

Overall, these results highlight the ability of CCD cameras to measure the GH shift. The actual SPR measurements are conducted in liquid environments, therefore additional tests were required to validate the performance of the camera in comparison to the PSD.

II.5.4. Measurement of the GH shift with a camera and PSD in a liquid environment

To validate the previous results, the commercial SPR chip was tested in a liquid environment. It was coupled with a SF11 prism (Figure 30) and installed on the newly developed holder (Figure 38). First, the GH shift in water was measured with both detectors, followed by the GH shift in 1% glycerin. Measurements using the PSD and camera (Figure 53) were performed as described in Section II.5.3.

Licence CC BY-NC-ND 4.0

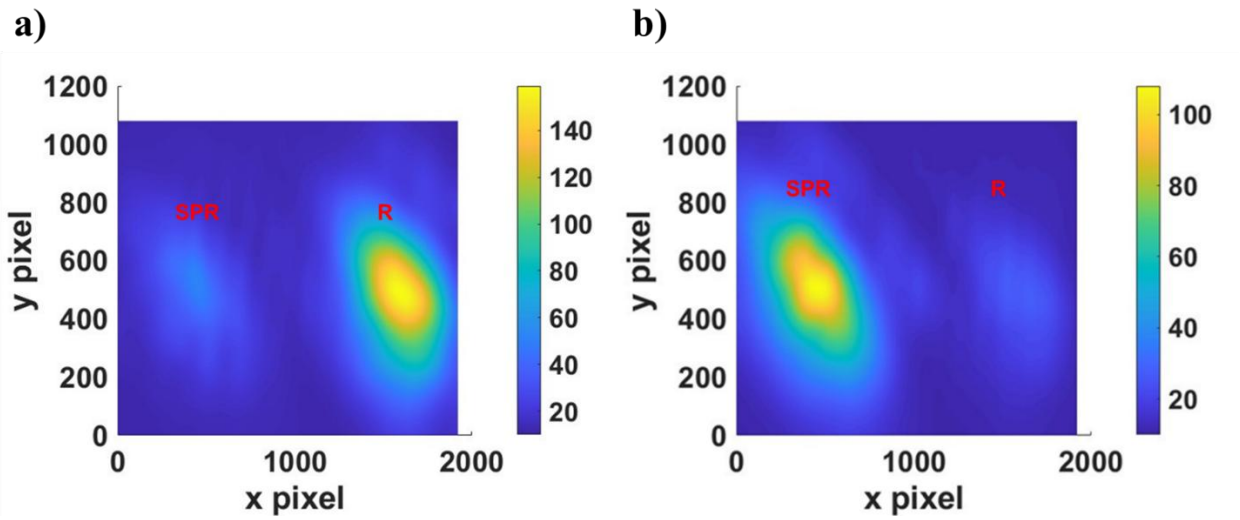


Figure 53 Visualization of the R and the SPR spots while measuring the GH shift in water, a) TM polarization and b) TE polarization. R represents the beam reflected at the SF11-BK7 interface and SPR represents the beam that refracts at the SF11-BK7 interface and couples with SPWs.

Two reflected spots can be identified from Figure 53: the first one denoted as SPR and the second R (explained in Figure 42). We noticed that, for TM polarization (Figure 53-a), the R spot is brighter than the SPR spot, whereas for TE polarization (Figure 53-b), it is the opposite. To better understand this observation, we calculated the reflection coefficients using the Fresnel equations (Equations 15-16and Figure 54). For this, we first determined the resonance angle of the commercial chip in water via transfer matrix simulations (presented in Chapter 3). Then, we extracted the reflection coefficients at the SF11-BK7 interface at the same resonance angle.

$$r_{TM} = \frac{n_{BK7}\cos\theta_{in} - n_{SF11}\cos\theta_t}{n_{BK7}\cos\theta_{in} + n_{SF11}\cos\theta_t} \quad (15)$$

$$r_{TE} = \frac{n_{SF11}\cos\theta_{in} - n_{BK7}\cos\theta_t}{n_{SF11}\cos\theta_{in} + n_{BK7}\cos\theta_t} \quad (16)$$

Where:

- r_{TM} and r_{TE} are Fresnel reflection coefficients in TM and TE polarizations.
- n_{BK7} and n_{SF11} are the refractive indices for BK7 substrate and SF11 prism.
- θ_{in} is the incident angle at the prism and BK7 interface.
- θ_t is the refracted angle at the prism and BK7 interface.

Licence CC BY-NC-ND 4.0

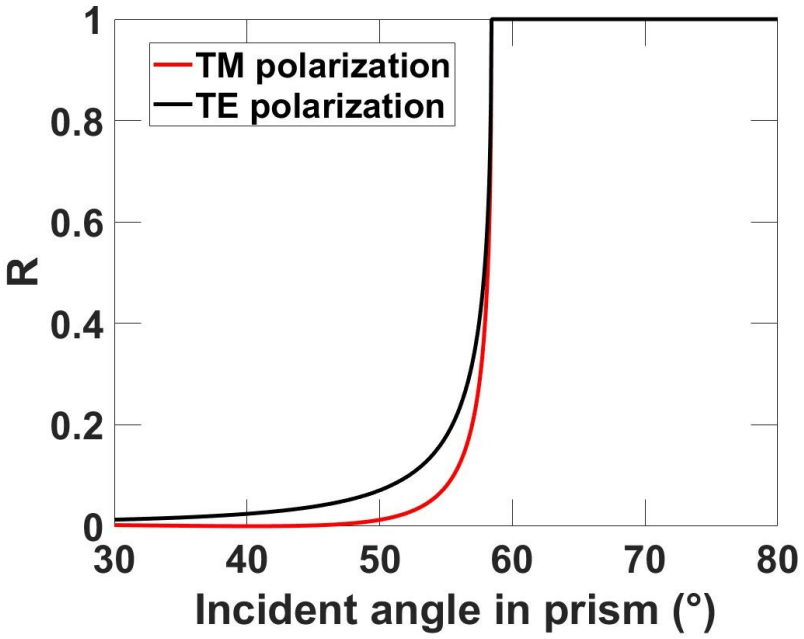


Figure 54 Fresnel reflection coefficient at the interface between SF11 prism and BK7 for TM and TE polarizations.

In the case of TM polarization (Figure 53-a), 5% of the incident beam is reflected at the SF11-BK7 interface (R spot, Equation 15 and Figure 54). The rest is transmitted inside BK7 where it reaches the metal-environment interface. It then couples with SPWs leading to a significant attenuation of light by plasmonic resonance. The emitted field at this interface penetrates again inside BK7 and reaches the SF11 prism. As a result, the intensity of the SPR spot is smaller than that of the R spot.

In the case of TE polarization (Figure 53-b), 14% of the incident light is reflected at the SF11-BK7 interface (Equation 16 and Figure 54). The remaining portion of light reaches Au-environment interface but cannot be coupled with SPWs. Consequently, the majority of light is reflected at the Au-environment interface and re-penetrates inside the prism. As a result, the intensity of the SPR spot is higher than that of the R spot.

On the other hand, the R spot appears to be more intense in the TM case in comparison with the TE case. In theory, the reflection coefficient is higher for TE polarization: r_{TM} =0.05 < r_{TE} =0.14. This apparent contradiction could be explained by the presence of P2 in front of the PSD. P2 is oriented to transmit TM component and attenuate TE. As a result, the intensity of the R spot seems brighter in TM polarization.

The GH shifts between water and glycerin measured by the camera and PSD are represented in Table 7.

Licence CC BY-NC-ND 4.0

Table 7 GH shift between water and 1% glycerin measured by the PSD and camera.

SPR chip	Measured by PSD (µm)	Measured by camera using imagej (µm)
Commercial SPR chip	31	53

The SPR spot was initially identified as the spot that produced the greatest GH shift between water and 1% glycerin. Table 7 demonstrates the camera's ability to detect a GH shift of the same order of magnitude (and even higher) as the PSD. The camera identifies the two beams and can therefore determine the displacement of each center individually. Conversely, the PSD averages the effect of the two spots based on their respective intensities, which reduces the GH shift measured.

In conclusion, the camera's ability to detect the GH shift was proven by all the measurements presented. Since only one test was performed in liquid environments, further investigation is needed to validate the results obtained. Additionally, the camera's resolution as a detector must be studied with small GH shifts (< 10 µm). Finally, the response of the camera with respect to deformation of the reflected beam spot must be thoroughly analyzed since it can be affected by imperfections in the chips. Meanwhile, the PSD remains the detector used in our prototype.

II.6. Stability studies

Throughout this thesis, we encountered drifts in the measurements that affected their reliability. Since the GH shift requires stability in the order of micrometers, even minor instabilities can result in significant errors. To better understand the origin of these drifts, we classified them into two main categories:

- **Mechano-Optical drifts:** originate from the instability of the optical components involved. It typically covers thermal expansion of mounts, mirrors, prisms, or rotational stages over time.
- **SPR-related drifts:** arise from the area of interaction between prism and metal. This encompasses refractive index matching oil stability, unequal dispersion or oil leakage. It also includes mechanical constraints of the holder that may cause tilting or uneven pressure inside the assembly.

II.6.1. Analysis of mechano-optical drifts

II.6.1.1. Analysis of the stability of the prototype's optical components

The primary step involves testing the stability of the prototype's optical components without the SPR module. It is important to first check the stability of the excitation source alone. To this end, the PSD was positioned directly in front of the laser, and the beam position was recorded

Licence CC BY-NC-ND 4.0

continuously for ten hours. To prevent damaging the PSD, a neutral density filter was placed in front of the laser. The result is represented in Figure 55.

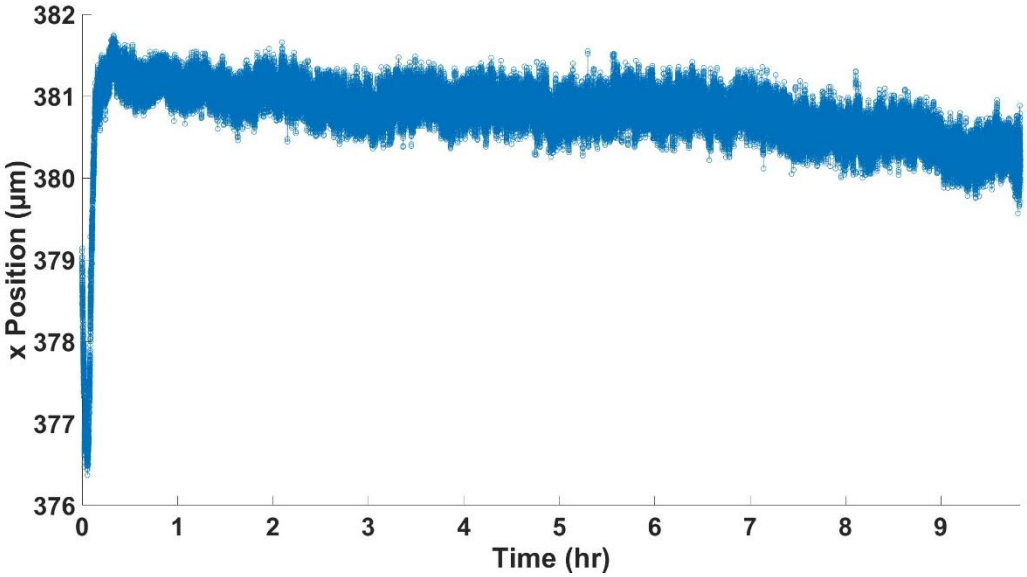


Figure 55 Measurement of the position x of the excitation source directly after turning on the laser.

The diode laser requires approximately 30 minutes of warm-up time to achieve operational stability (Figure 55). Considering a typical biodetection experiment that lasts approximately four hours, the measured drift after warm-up period is limited to 2 µm. This value indicates high stability of the laser over extended experimental durations.

To study the stability of the various optical components, the diode laser was switched on one hour before the beginning of the following measurements. The position x was measured by placing the PSD successively between the optical components (Figure 56 and Table 8). The total measurement time is about 1h30 minutes (30 minutes for each measurement/ component). The total number of data points per test is 3600.

Licence CC BY-NC-ND 4.0

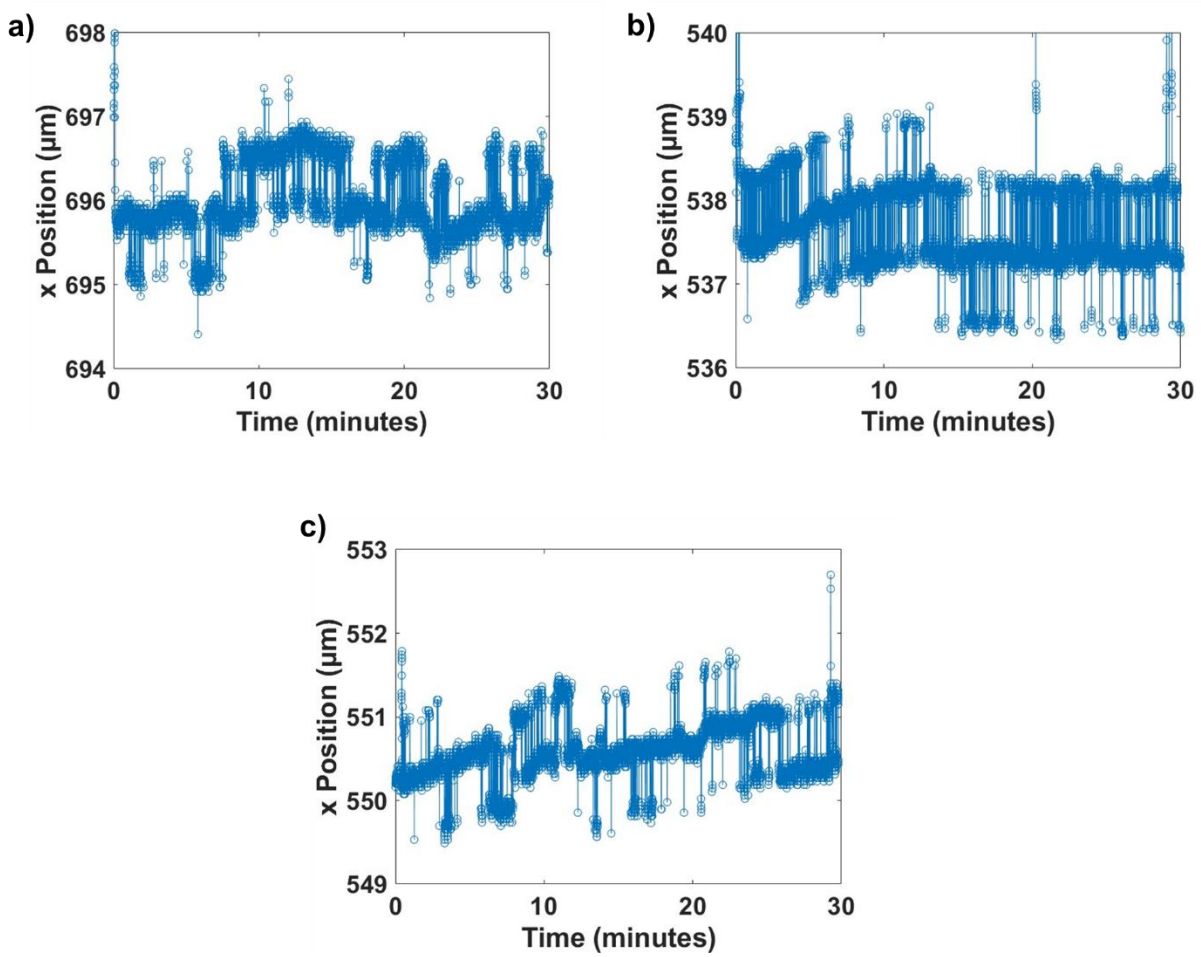


Figure 56 Position x measured when the PSD is placed, a) after mirror 1, b) after mirror 2 and c) after the polarization switching module.

Table 8 Standard deviation of the position x measured when the PSD is placed, after mirror 1, after mirror 2 and after the polarization switching module.

Element	Distance laser-PSD (cm)	Standard deviation (µm)
Mirror 1	22	0.4
Mirror 2	42	0.2
Polarization switching module	68	0.3

The beam's position remained highly stable across the setup. For mirror 1, placed at a distance of 22 cm from the laser, the standard deviation was about 0.4 µm. For mirror 2, situated at 42 cm, the same stability was observed, with a standard deviation of about 0.2 µm. After the polarization switching module, the standard deviation was 0.3 µm.

The stability level of the prototype's optical components guarantees that there are no optical drifts that could interfere with GH measurements, thus validating the prototype's reliability for SPR measurements.

Licence CC BY-NC-ND 4.0

II.6.1.2. Analysis of the effect of the environment on the GH measurements

The influence of environmental conditions on the stability of the SPR module was studied in two stages. First, we checked whether fluctuations in the ambient temperature were significant enough to affect the measurements. Due to thermal fluctuations, the optical mounts can undergo mechanical expansion. This can lead to position drifts in the measured beam position over time. The second phase focused on determining the impact of ambient lighting conditions. Stray light entering the optical path can interfere with the PSD's reading.

By evaluating these two parameters, it was possible to assess the degree of influence of the environment on the SPR measurement and take preventive measures to control these fluctuations.

<u>Effect of ambient temperature on the GH measurements:</u>

To assess the effect of the ambient temperature, an EL-USB-2 Temperature, Humidity and Dew Point Data Logger was placed near the SPR module. The temperature and SPR measurements were performed at the same time. The commercial chip coupled with a SF11 prism was installed on the old holder (Figure 28 with 3d printed v-groove). Water was then injected into the fluidic channel. The position x and power of the reflected beam were measured continuously for 30 minutes at the resonance angle and under TM polarization (Figure 57).

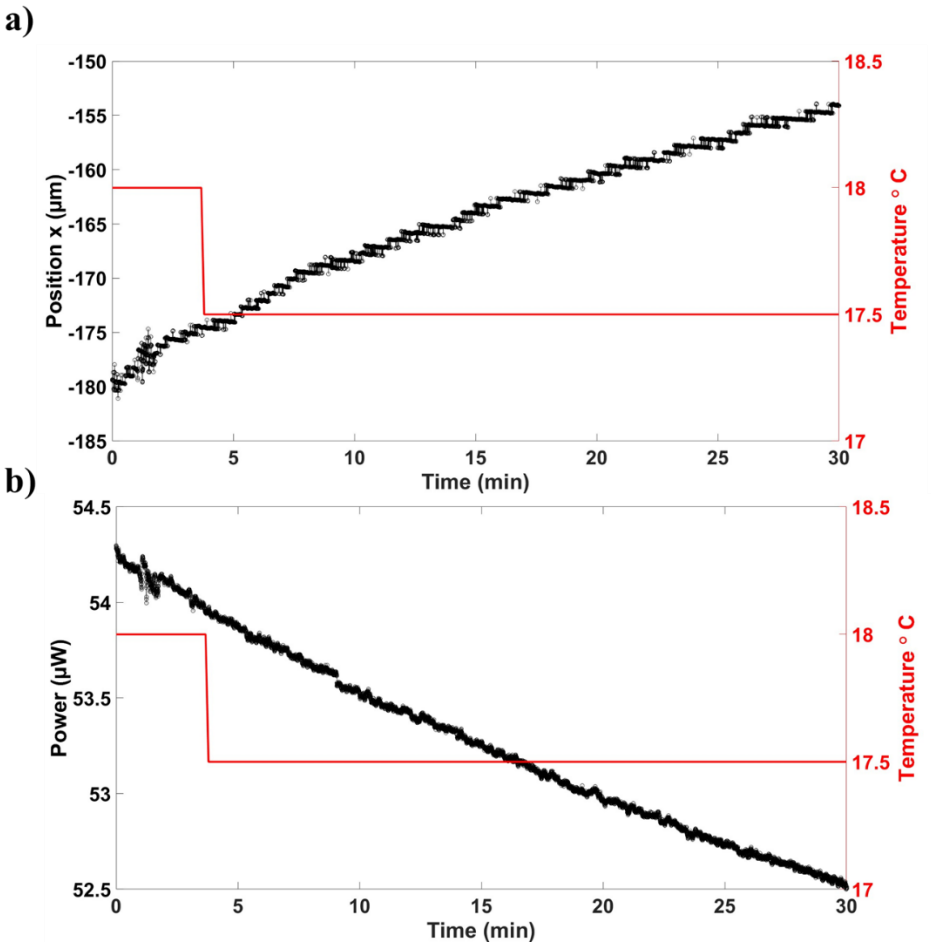


Figure 57 Influence of the ambient temperature on, a) Position x, b) Power of the reflected beam under TM polarization.

Licence CC BY-NC-ND 4.0

A position drift is visible with a large standard deviation of 8.3 µm (Figure 57-a). The detected power (Figure 57-b) decreased by 2.0 µW, with a standard deviation of 0.6 µW. On the other side, the temperature varied by only 0.5 °C. This value is too small to cause mechanical expansion or contraction of the optical mounts. This result confirms that the environmental conditions do not significantly impact the stability of the SPR module.

Effect of stray light on the GH measurements:

The following step was to study the influence of stray light on the SPR measurements. Since the detection is based on small lateral displacements of the reflected beam, any uncontrolled external light source entering the optical path could introduce additional noise on the PSD. The PSD is a lateral position photodetector that calculates the beam's position based on the intensity of the laser beam. Therefore, any fluctuations in light intensity can have a direct influence on the GH measurements. To evaluate this aspect, stability tests were conducted by leaving the SPR module unattended for 75 minutes (Figure 58).

The commercial chip coupled with a SF11 (Figure 30) was first installed on the newly developed holder (Figure 38). Water was then injected into the fluidic channel. The position x and power of the reflected beam were measured continuously at the resonance angle and under TM polarization (Figure 58).

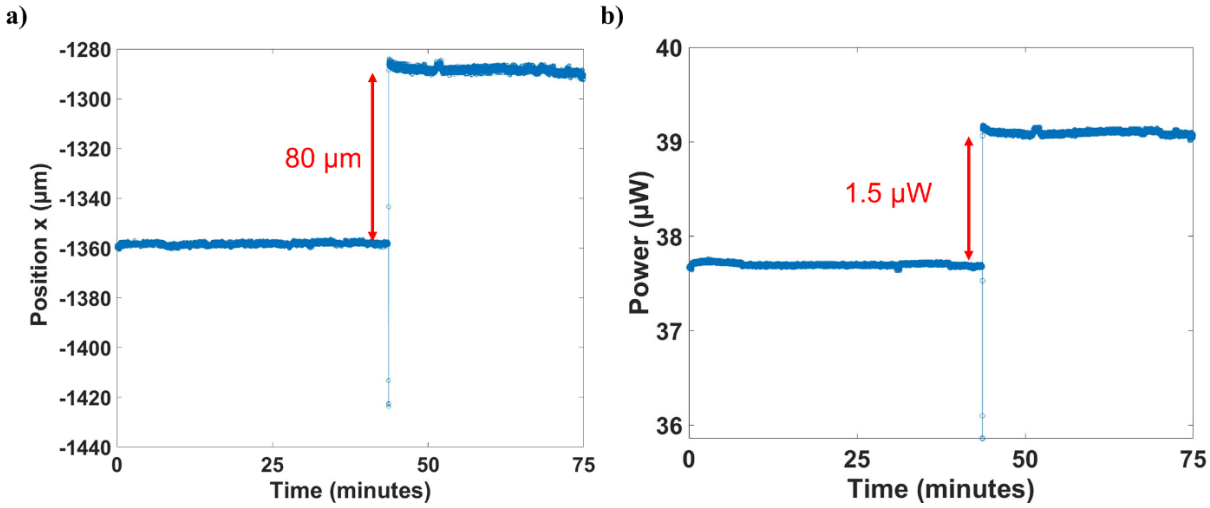


Figure 58 Effect of stray light on, a) Position x and b) Power of the reflected beam under TM polarization.

A sudden jump of 80 µm occurred after 45 minutes measurements (Figure 58). In parallel, the detected power increased by only about 2 µW. These jumps were caused by stray light entering the optical path during the experiment. Although the power variation was relatively negligible compared to the total laser power measured on the detector (37.5 µW), its impact on the beam's position measurements was considerable. This result demonstrates that stray light is a crucial source of error in GH shift experiments and that the prototype must be carefully shielded from external light sources.

II.6.2. Analysis of SPR-related-drift

After eliminating the possibility of drifts related to optics, other sources of drift related to SPR were identified. The factors likely to influence the GH shift include: the quality and stability of

Licence CC BY-NC-ND 4.0

the refractive index matching oil (change of the oil's viscosity), and the holder used to press the SPR module.

II.6.2.1. Analysis of oil stability

Drifts can be caused by instabilities of the refractive index matching oil. These can be caused by:

- **Improper storage of the oil:** Long exposure to moisture or light will alter the viscosity of the oil, reducing its stability during measurements. When viscosity decreases, the oil is less resistant and will tend to escape from the assembly, especially under high pressure.
- **Oil quantity:** an excessive amount of oil can cause the SPR chip to slip inside the holder, introducing additional drifts if the holder system is not well conceived.

The following experiment clearly demonstrates how damaged oil sources can affect the stability of SPR measurements.

Two different Cargille oils sources with refractive index n=1.64 RIU were used. The first one (denoted as oil bottle 1) was stored at room temperature in the lab room in XLIM without air conditioning and without proper sealing. The bottle was left throughout the summer under uncontrolled conditions. The second one was stored in the clean room with accurate control on the ambient temperature and humidity (denoted as oil bottle 2).

Both experiments were performed using the commercial SPR chip coupled with SF11 prism (Figure 30), water as the surrounding environment, the reference platform (Figure 27), and the old holder (Figure 28 without the 3d printed v-groove). The experimental procedure is explained in II.3.2. The position x and power were measured for 1 minute (a total of 120 data points). The results are presented in Figures 59-60. Table 9 shows a comparison of oil bottles 1 and 2, based on their standard deviations in position and power.

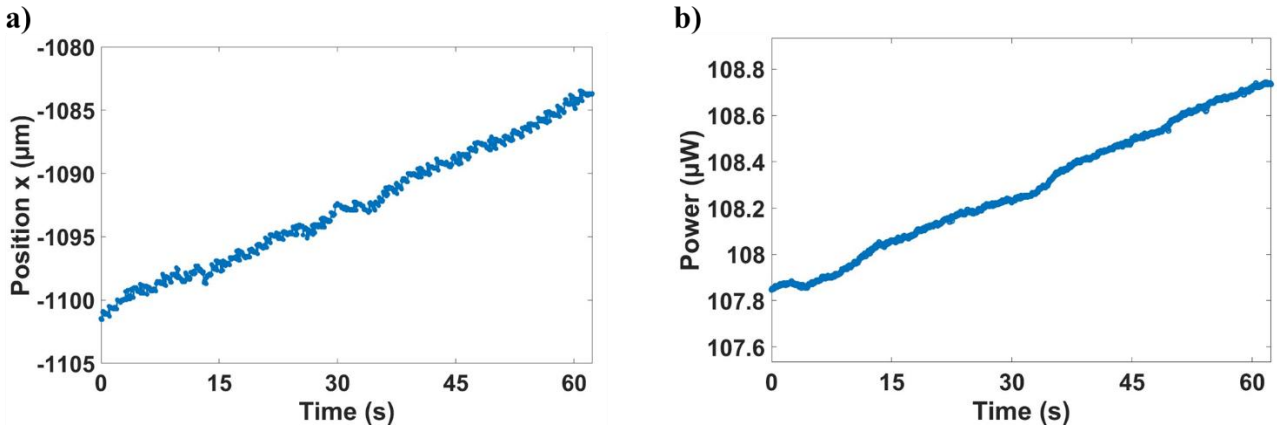


Figure 59 Measurement of the, a) Position x and b) Power using oil Bottle 1.

Licence CC BY-NC-ND 4.0

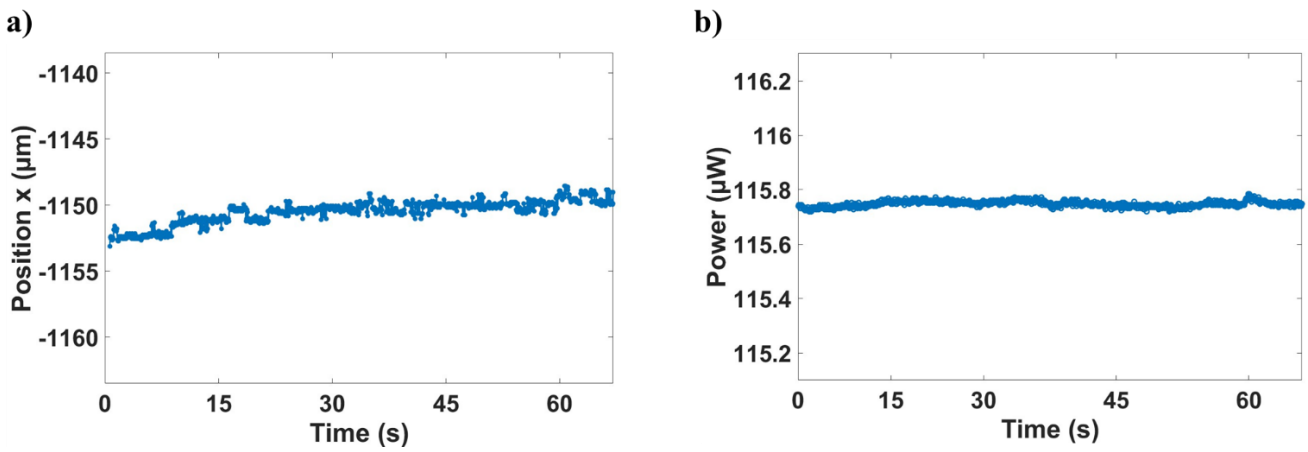


Figure 60 Measurement of the, a) Position x and b) Power using oil Bottle 2.

Table 9 Stability comparison of oil bottles 1 and 2 for a total of 120 data points per test.

Oil source	Standard deviation x position (µm)	Standard deviation Power (µW)
Bottle 2	1.1	0.01
Bottle 1	5.3	0.29

The measurements performed using oil bottle 2 (Figures 59- 60 and Table 9) produced stable results, with the beam position remaining consistent throughout the measurement. This result demonstrates that the oil bottle stored in the clean room retained its initial properties, including its viscosity value, enabling reliable SPR measurements. However, a decrease in stability was observed when measuring the stability of position and power using oil bottle 1. During the one-minute measurement, the position x exhibited significant drift, with a standard deviation of 5 µm. Meanwhile, power drifted by 1 µW. The high drift measured in x suggests that oil bottle 1 has lost its initial viscosity, most likely due to inappropriate storage conditions, namely long exposure to high humidity and moisture. The room temperature is not a contributing factor to oil degradation, as the oil can withstand temperature fluctuations between 18 and 32°C, according to the technical data sheet.

In conclusion, the instability experienced during the experiments was partly attributed to the use of poorly stored oil. The oil bottle had been stored for several months at room temperature without air conditioning and was not properly sealed, which altered its viscosity. To address this issue, a new bottle of oil was purchased, and its contents were divided into several small bottles to reduce the repeated exposure of the entire volume to moisture. In addition, a desiccator chamber was acquired to provide properly controlled storage conditions and avoid any further deterioration of the oil.

Licence CC BY-NC-ND 4.0

II.6.2.2. Analysis of the effect of the holder design

Although the holder is designed to keep the prism-SPR chip-fluidic channel assembly in place, its imprecise mechanical design could introduce drifts. The next experiment will demonstrate the importance of the holder design in ensuring stability.

The experiments were performed using the old holder with the 3d printed v-groove (Figure 28) for the first measurement and the newly developed holder (Figure 38) for the second one. In both cases, the position x and the power of the reflected beam were recorded under TM and TE polarizations over a 5-minute period (for a total of 600 measurement point for each test). The commercial chip coupled with SF11 prism (Figure 30) was tested in water. The results are shown in Figures 61-64.

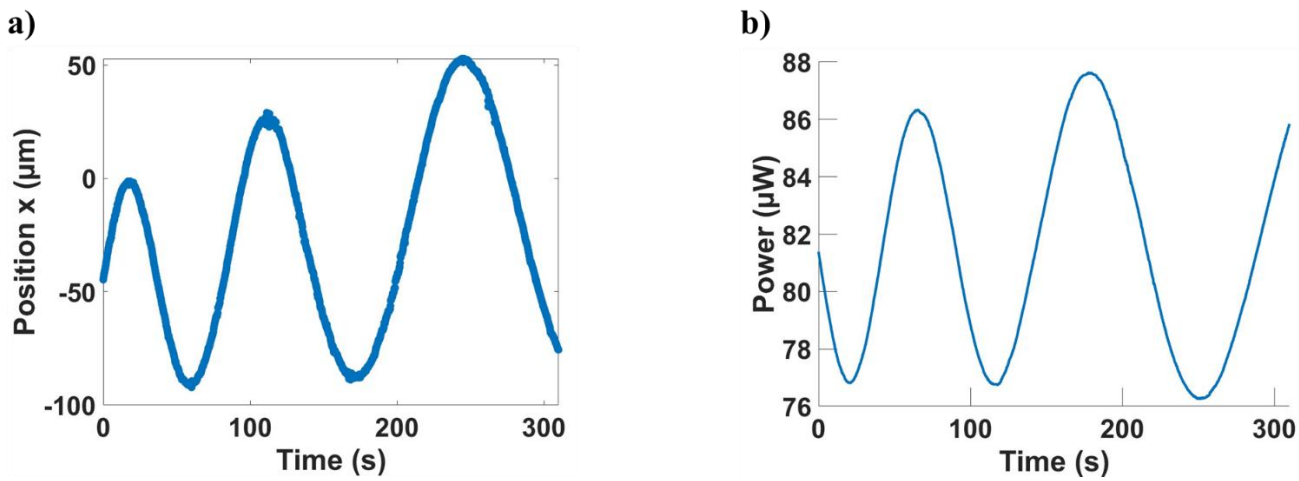


Figure 61 Measurement of, a) Position x and b) Power under TM polarization for 5 minutes and using the old holder.

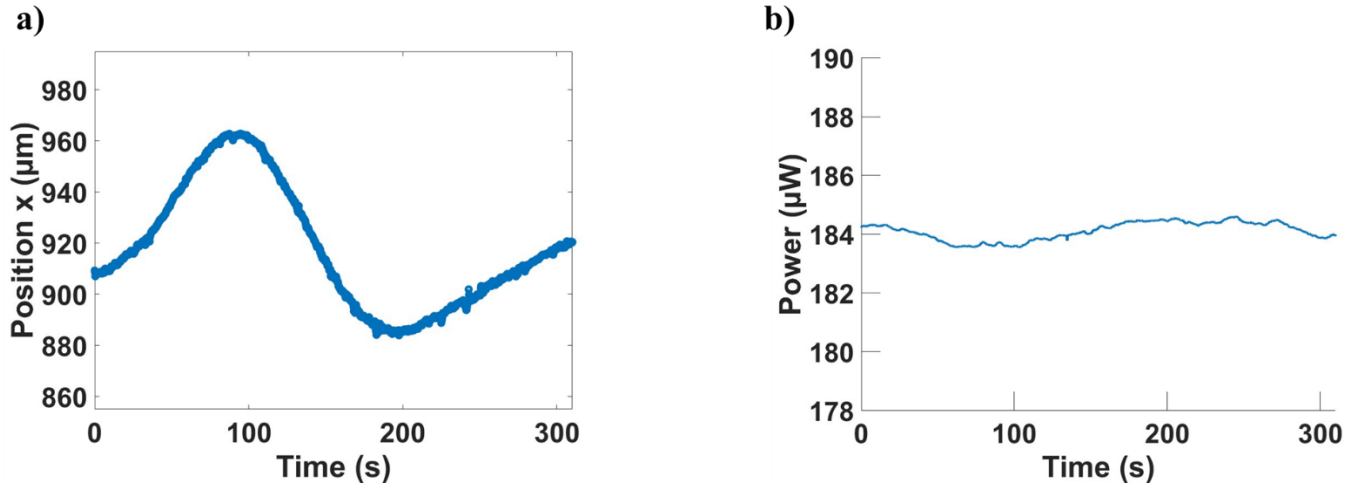


Figure 62 Measurement of, a) Position x and b) Power under TE polarization for 5 minutes and using the old holder.

The observed sinusoidal patterns in both TE and TM (Figures 61 -62) indicate rather mechanical instability introduced by the holder. The difference in position between the

Licence CC BY-NC-ND 4.0

maximum and minimum was 160 µm in TM and 90 µm in TE. Moreover, the large power fluctuations under TM polarization (approximately 10 µW) suggest that the incidence angle is not stable over the 5-minute acquisition period. In contrast, the reduced power variation under TE polarization implies that the mechanical drift is being amplified by SPR.

Drifts observed during this experiment was caused by the misalignment of the prism within the screw system. A 3D-printed groove pattern was placed on the holder to protect the prism from cracking. However, the printed pattern was not accurate enough in size, making it more difficult to align the prism. This caused the prism to tilt or pivot during the measurement resulting in large drifts in SPR measurements.

A new holder (Figure 38) was designed to improve mechanical stability and overcome these limitations.

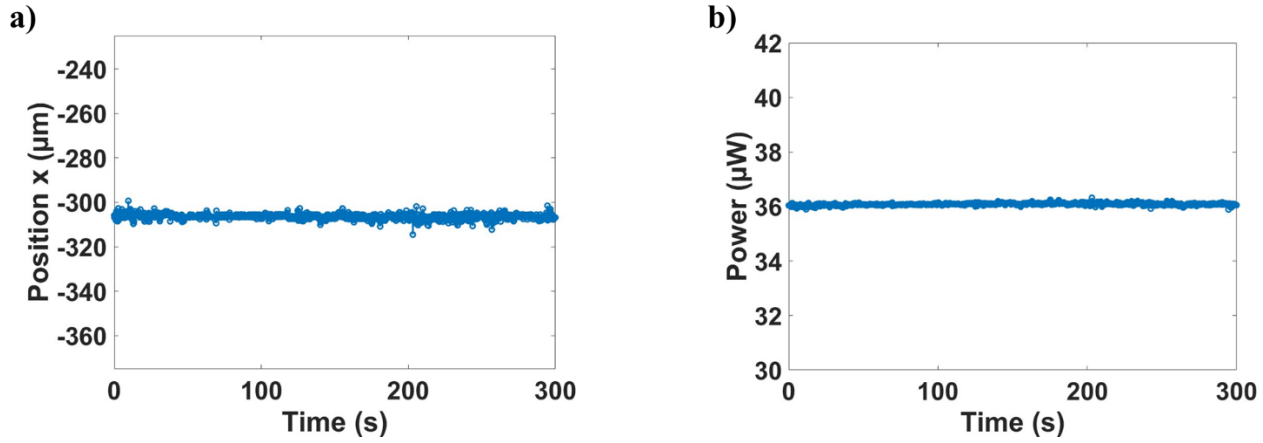


Figure 63 Measurement of, a) Position x and b) Power under TM polarization for 5 minutes and using the newly developed holder.

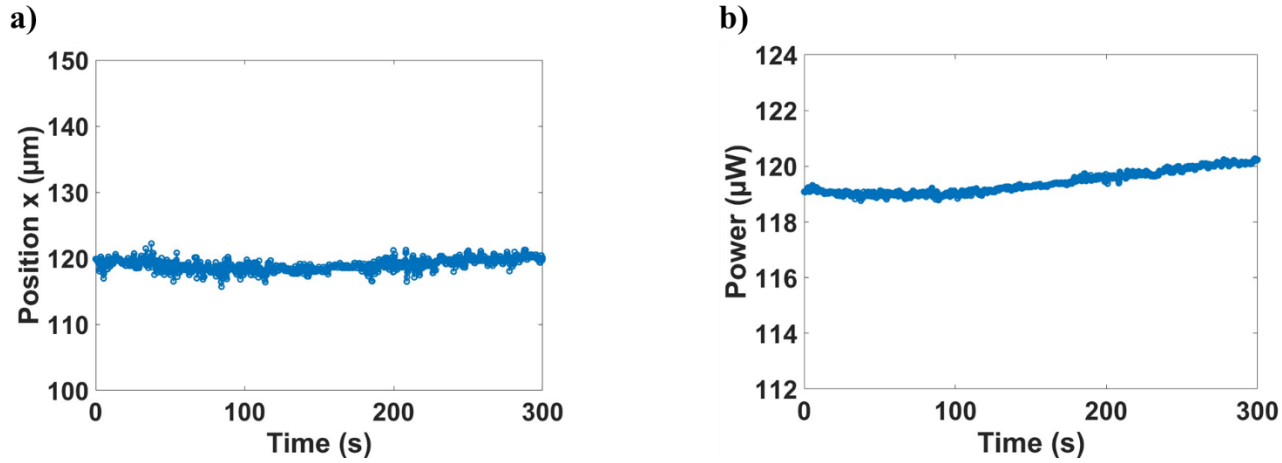


Figure 64 Measurement of, a) Position x and b) Power under TE polarization for 5 minutes and using the newly developed holder.

For TM and TE (Figures 63-64), the position x remained stable with standard deviations less than 1 µm for both polarizations. In parallel, no significant drift was shown in the power measured under TM polarization. However, fluctuations of 1 µW were shown in the power

Licence CC BY-NC-ND 4.0

under TE. The power drift was not translated into position drift meaning the centroid measured by the PSD was not drifting, suggesting a drift in the laser's overall power.

In conclusion, these results showed that it is possible to achieve high stability by redesigning the holder. The standard variations remained within the tolerable range for measuring the GH shift, validating the reliability of the newly developed holder for SPR measurements.

II.6.2.3. Analysis of the effect of polarization on the measured drift

When evaluating the stability of the prototype, the position was measured in the first place under TM polarization, as the phase changes at resonance are much more important in comparison to TE. Higher phase variation results in greater fluctuations in the position x of the reflected beam at TM. To validate the influence of polarization on the measured position drift, the experiment was conducted as follows.

The experiment was performed using the old holder (with 3d printed vgroove, Figure 28), the commercial chip coupled with a SF11 prism (Figure 30) and water as the surrounding environment. The position x of the reflected beam was recorded over a duration of 20 minutes, alternating between TM and TE. The sequence of acquisition consisted of 5 minutes in TM polarization, followed by 5 minutes in TE, then repeated once other time. The total measurement point for each measurement is 600 points. The results are shown in Figure 65 and Table 10.

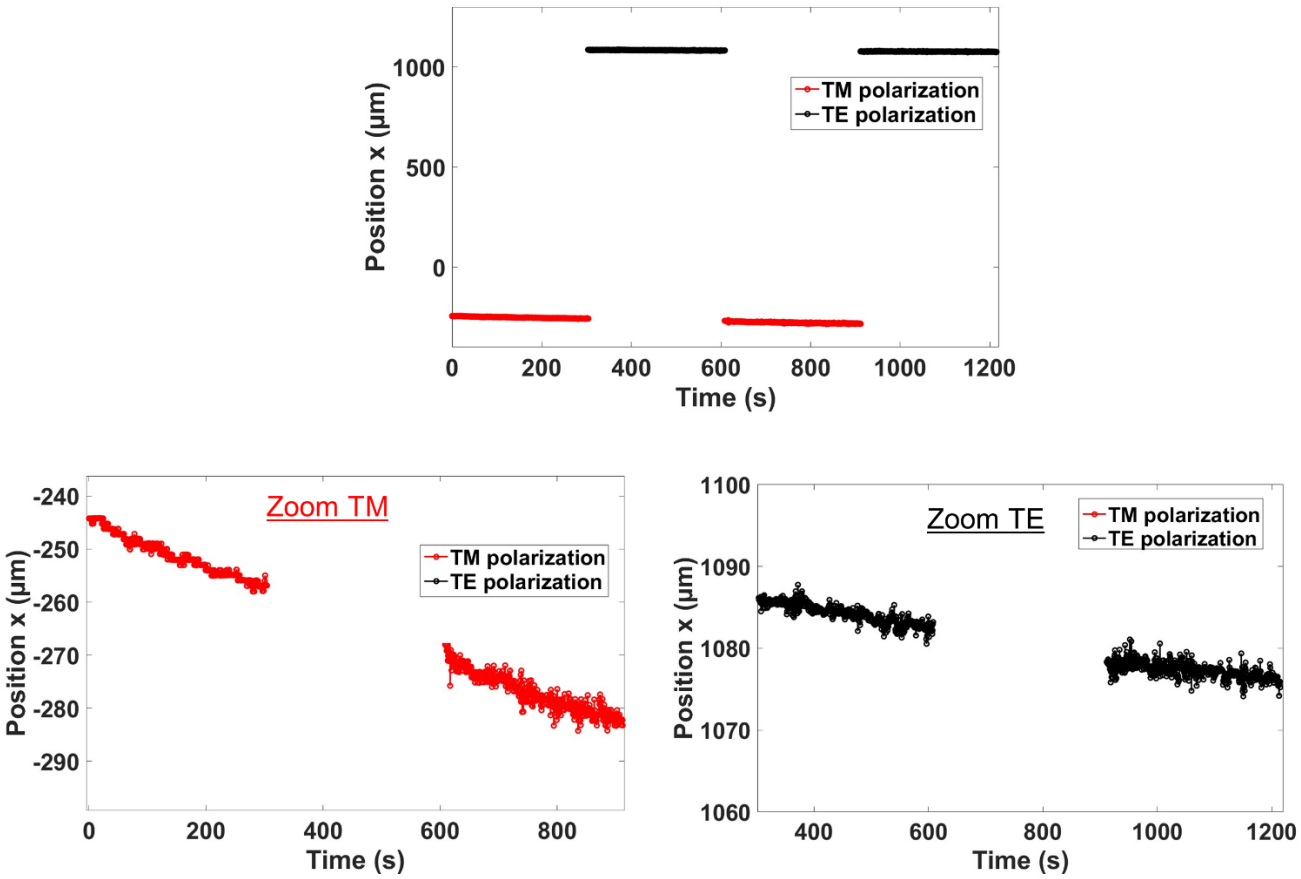


Figure 65 Measurement of the position x under alternating TM and TE polarizations.

Licence CC BY-NC-ND 4.0

Table 10 Stability of the position x of the reflected beam under TM and TE polarizations and over 20 minutes continuous measurements.

Polarization	Measurement number	Standard deviation (µm)
TM	1	3.8
TE	2	1.2
TM	3	3.7
TE	4	1.0

For TM polarization, position x shifted by 14 µm across two measurements (Figure 65). The standard deviation was 4 µm, indicating the instability of the tests. Under TE polarization, however, the reflected beam position was more stable. The x position drifted by 3 µm in the first measurement and by 1 µm in the second. These results confirm that the higher drift measured under TM polarization is primarily due to SPR. For this reason, stability measurements were always conducted under TM polarization first.

II.7. Conclusion

This chapter presented the development of a prototype for measuring the GH shift in SPR. Firstly, the reference platform was presented, along with its primary challenges, particularly with regard to its size and complexity of use. The prototype that we developed offered a simpler, more compact and easier-to-use design. Its essential components include a diode laser as the excitation source, a polarization filter with a half-wave plate mounted on a motorized rotary mount, and a newly developed holder to simplify the installation of the SPR module. A second polarization filter P2 was added in front of the detector to ensure the attenuation of the TM and TE components. The possibility of using a CCD camera as a detector was investigated, but further validation tests were required. Therefore, the detection system comprising the PSD was not altered.

The stability of the prototype was also rigorously analyzed to ensure precise and reliable GH measurements. Optical drifts from the optical elements were not found to be a source of instabilities. Conversely, SPR drifts were found to be key factors that significantly impacted the stability of the system. These were related to the poor storage of refractive index oil and the design of the holder. Consequently, the oil was preserved in small containers and isolated in a desiccator chamber. The newly developed holder solved previous mechanical instability issues by ensuring a tightly pressed SPR module.

Overall, we have validated the performance of our new prototype, enabling us to conduct further experiments for testing novel SPR chips to enhance sensitivity and eventually perform biodetection experiments for the detection of EVs.

Licence CC BY-NC-ND 4.0

Chapter III. Development and optimization of SPR chips

The enhancement of the sensitivity of a SPR biosensor not only depends on the interrogation method but also on the optimization of the SPR chip. This chapter is dedicated to the analysis, simulation and experimental testing of SPR chips developed during the course of this thesis. Based on the collaboration between several partners, we have developed two types of SPR chips. One type relies on the modification of the underlayer (layer below the metal or substrate), and the other upon changing the metallic layer. The chips were first simulated to maximize the GH sensitivity using the transfer matrix model (TMM). They were then fabricated and evaluated experimentally. The chapter is therefore divided into three main parts. The first one introduces the physical processes that occur inside the SPR structure, which cause an attenuation of the reflected light intensity. The second part focuses on VO_2 chips with metallic thin films fabricated by our XLIM colleagues. This part includes TMM simulations and experimental validation tests. The last part covers SPR chips with Ag NPs embedded in alumina and with an Au thin film on the top, developed by our IRCER partner. These chips were first designed using the TMM. Then, they were validated experimentally. Finally, they were simulated using the FDTD model to better understand the physical mechanisms occurring in these chips.

III.1. Introduction

III.1.1. Theoretical background

The GH shift is closely related to the phase changes and the depth of the reflectivity dip measured at the reflection. The phase of light usually exhibits interesting behavior when its intensity is near zero (point of darkness): it becomes undefined when light intensity is small. In SPR, the incident light is mostly attenuated by the plasmonic effect at the resonance angle, which corresponds to the point at which the coupling with the SPWs is maximized [55]. In this case, the incident light is attenuated by the SPR chip through several means.

To couple with SPWs, the phase matching conditions must be satisfied (Figure 66):

$$k_{SPR} = k_z \tag{17}$$

Where k_z is the wavevector component of the incident light parallel to the prism-metal interface and k_{SPR} is the wavevector of the SPWs also parallel to the interface.

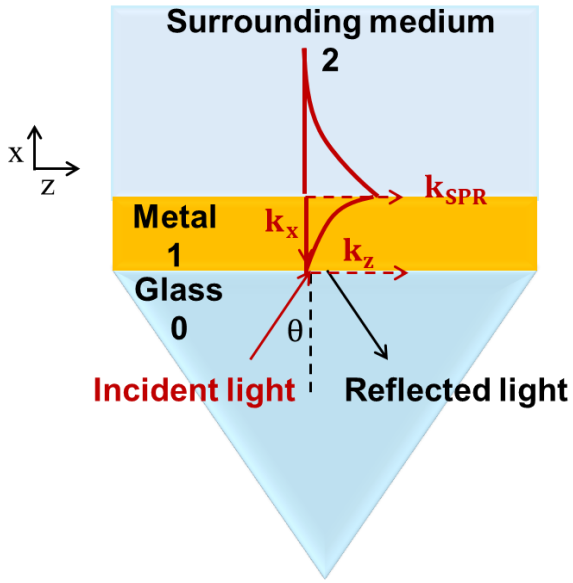


Figure 66 Schematic of the coupling of incident light to SPWs in the Kretschmann configuration.

For a simple Kretschmann configuration consisting of prism, metal and surrounding medium (Figure 66), k_{SPR} is defined by:

$$k_{SPR} = k_{light}\sqrt{\frac{\varepsilon_m \varepsilon_d}{\varepsilon_m + \varepsilon_d}} \tag{18}$$

Where k_{light} is the wavevector of light in vacuum, ε_m the permittivity of the metal and ε_d the permittivity of the surrounding medium. When SPWs are coupled, an evanescent field is created at the metal's interface. This field extends into both the metal and the surrounding medium, and it decays exponentially in the direction perpendicular to the interface [83]. The wavevector of the evanescent field inside the metal is defined by:

$$k_{x1} = \left[\varepsilon_1 \left(\frac{\omega}{c}\right)^2 - k_z^2\right]^{1/2} \tag{19}$$

Where: k_{x1} the wavevector normal to the metal-surrounding interface inside the metal (Figure 66), ω the angular frequency of light, c speed of light in vacuum and k_z the wavevector parallel to the metal-surrounding interface (In SPR, $k_{z0} = k_{z1} = k_{z2} = k_{SPR}$ meaning the parallel component of wavevector is conserved in all media 0,1 and 2). Since the real permittivity of the metal is negative ($\varepsilon_1 < 0$), k_{x1} has an imaginary component. This corresponds to the exponentially decaying evanescent field inside the metal. Since the metal is thin (usually between 45-50 nm), the evanescent field can penetrate the prism-metal interface and the normal wavevector component inside the prism k_{x0} becomes:

$$k_{x0} = \left[\varepsilon_0 \left(\frac{\omega}{c}\right)^2 - k_z^2\right]^{1/2} \tag{20}$$

License CC BY-NC-ND 4.0

From Equation 20, since the inequality $k_z \leq \sqrt{\varepsilon_0}\,\frac{\omega}{c}$ is satisfied, k_{x0} has a large real component. In this case, the evanescent field transforms in the prism into a propagating plane wave. This process is known as radiative damping, which means that the SPWs radiate light back into the coupling medium. In this case, prism-coupled SPWs are known as leaky waves.

The light radiated back into the prism, interferes with the reflected beam between prism and Au. The radiated wave is in antiphase (or undergoes a 180° phase shift) with the reflected wave. Both waves interfere destructively, minimizing the intensity of the reflected wave. In a simple Kretschmann configuration consisting of a prism, a metal layer, and a surrounding medium, the accumulated phase (and amplitude) inside the structure can be rearranged by adjusting the metal layer's thickness. To investigate experimentally this concept, our IRCER colleagues have deposited Au layers of thicknesses ranging from 15-110 nm on a BK7 substrate. The reflectivity curves of the SPR chips coupled with the BK7 prism were tested experimentally with air as the surrounding environment. The reference platform was used under TM polarization. The incident angle was varied in steps of 0.2° far from the resonance angle and 0.04° near the resonance angle. The intensity of the reflected light was measured at each step using a power meter (Figure 67).

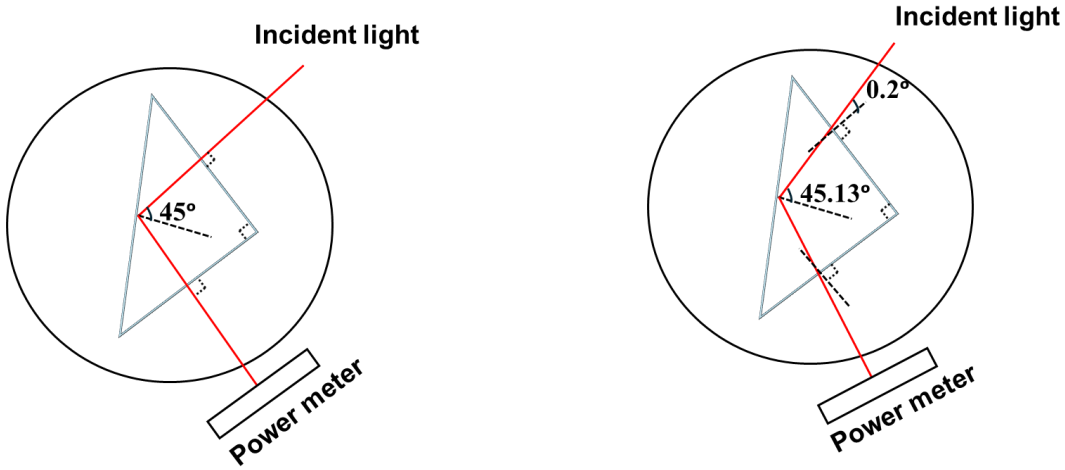


Figure 67 Schematic of the experimental procedure to measure the reflectivity curve illustrating the angular scanning of the incident light.

The results are shown in Figure 68.

License CC BY-NC-ND 4.0

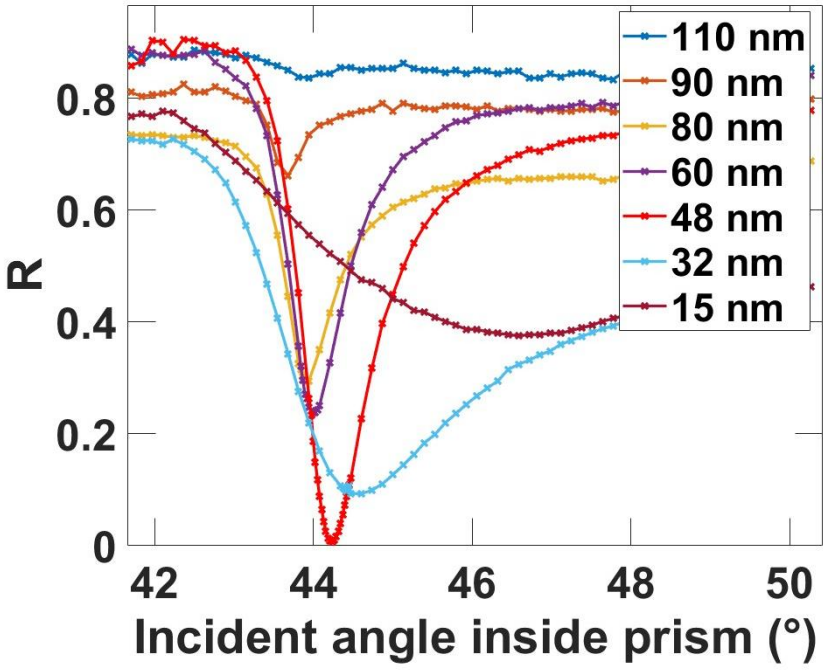


Figure 68 Reflectivity (R) versus the angle if incidence inside the prism for various Au thicknesses 15-110 nm. The SPR chips consist of a BK7 prism, Titanium adhesion layer of 2 nm, Au and air as the surrounding medium.

The optimal thickness for coupling SPWs was found to be around 48 nm, where destructive interferences dominate and deepen the reflectivity dip. For an Au thickness above 80 nm, radiative damping decreases significantly since the metal is too thick to allow the evanescent field created by the SPWs (on the metal's side) to penetrate the prism leaving the reflection coefficient closer to 1. Additionally, if the metal's layer is too thick, the evanescent field created between the prism and metal can no longer reach the Au-air interface and couple with SPWs. Conversely, with thinner Au films, radiative damping increases, and the phase-amplitude of the radiated field inside the prism cannot cancel out the effect of the incoming wave, resulting in a less pronounced reflectivity dip and a broader reflectivity curve width [83].

Additionally, during SPR, the electromagnetic field of SPWs excites electrons inside the metal above their Fermi level, leaving behind holes. Subsequent de-excitation produces phonons, resulting in the loss of energy through heating. This is defined as intrinsic damping ($\boldsymbol{\gamma_{int}}$). It is related to the imaginary part of the permittivity of the metal.

Overall, zero reflectivity (R = 0) occurs when the radiative and intrinsic losses are balanced (γ_{rad}=γ_{int}). The FWHM of the reflectivity curve is then defined by: FWHM= γ_{rad}+γ_{int} [83].

By targeting different layers in the SPR chip, the enhancement of the sensitivity can be achieved through these different routes:

1. **Optimization of the coupling conditions beneath the metal:** In a simple Kretschmann configuration consisting of a prism, metal and surrounding medium, modifying the refractive index of the prism beneath the metal re-adjusts the wave vector of the incident light (Equations 17 and 18). Although lower refractive index prisms are typically associated with higher angular sensitivities (Equation 21) [84–87],

License CC BY-NC-ND 4.0

higher refractive index prisms reduce the width of the reflectivity curve [84,87,88] and deepen the reflectivity dip due to the lower radiation damping [83,88].

$$\Delta\theta = \sin^{-1}\frac{\Delta k_{SPR}}{n_{prism}} \tag{21}$$

Where Δk_{SPR} is the variation of the SPW wavevector for with respect to $\Delta\varepsilon_d$.

2. **Decreasing the depth of the reflectivity dip inside the structure through intermediate layers:** At resonance, when the intensity of the reflected light decreases, the phase of the light becomes undetermined, resulting in a sudden phase shift (Figure 69). A sharper phase change at the resonance improves the GH sensitivity of the chip, meaning smaller variations of the refractive index could be detected. This can be achieved through a multilayer stack where the refractive indices and thicknesses of the various layers favor destructive interferences and decrease the reflectivity at resonance.

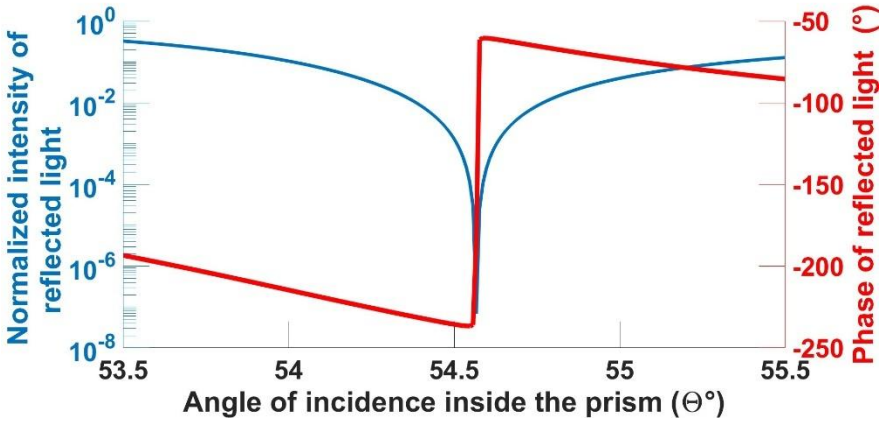


Figure 69 Reflectivity and phase vs incident angle inside the prism (simulated using the TMM explained in Section III.1.3).

3. **Amplification of the electric field in the vicinity of the metal:** improvement of the sensitivity by reengineering the coating layer above the metal. Coating materials as graphene are primary responsible for the enhancement of the electric field at the surface due to effective charge transfer from graphene to Au [89,90] . Additionally, the pi-stacking forces in graphene facilitate the adsorption of biomolecules onto its surface [91]. In fact, the enhancement of the electric field is related to the permittivity of the prism, surrounding medium and the overall transmission coefficient inside the structure [90,92,93].

$$\left|\frac{E\left(\frac{N}{N-1}\right)}{E\left(\frac{1}{2}\right)}\right|^2 = \frac{\varepsilon_1}{\varepsilon_N}|t|^2 \tag{22}$$

License CC BY-NC-ND 4.0

Where:

- $E\left(\frac{N}{N-1}\right)$: The electric field at the interface between the surrounding medium and the layer below it,
- $E\left(\frac{1}{2}\right)$: The electric field at the interface between layer 1 and 2,
- ε_N: The permittivity of the nth layer,
- t: The transmission coefficient in the multilayer structure,

While most commercial SPR systems rely on traditional bare Au structures, several studies in literature have demonstrated superior SPR sensitivities by modifying the nanomaterial's structure. The table below provides a summary of the structures used in literature to enhance sensitivity.

Table 11 Summary of SPR structures and their experimental sensitivities. (GST = $Ge_2Sb_2Te_5$, TNFα = Tumor Necrosis Factor alpha).

Structure	Experimental Sensitivity	Detection method	Reference
Au or Ag NPs in a close-packed array deposited on a glass prism	250 nm/RIU (normal incidence)	Spectral shift (Δλ/RIU)	[94]
Ag nanocomposite layer on Ag film	448.1°/RIU	Angular shift (Δθ/RIU)	[95]
Au NPs embedded in glass	1938 °/RIU	Phase shift (Δφ/RIU)	[96]
TiO_2/Au/Graphene	Maximum: 210 °/RIU	Angular shift (Δθ/RIU)	[97]
Au/graphene/Al_2O_3/Mxene	163.63 °/RIU	Angular shift (Δθ/RIU)	[98]
$BiFeO_3$ dielectric over Ag/Au	448.1°/RIU	Angular shift (Δθ/RIU)	[99]
Fe_2O_3/Au	2933.2 nm/RIU.	Spectral shift (Δλ/RIU)	[100]
Fused silica + Al thin film	149.9°/RIU	Angular shift (Δθ/RIU)	[101]
GST on Au	10^{-16} M for TNFα	GH shift (μm/RIU)	[102]
SF-10 glass prism/zinc oxide/Au/ MoS_2/graphene hybrid	101.58 °/RIU	Angular shift (Δθ/RIU)	[93]

License CC BY-NC-ND 4.0

Many structures have been explored to enhance the performance of SPR sensors, particularly by incorporating metallic NPs, intermediate dielectric layers, and two-dimensional materials such as graphene and molybdenum disulfide (MoS_2). These modifications enhance the SPR sensitivity by optimizing the coupling conditions, deepening the reflectivity dip, and enhancing the electromagnetic field at the metal-surrounding interface. As shown in Table 11, the obtained sensitivities vary considerably according to the structure and interrogation scheme (angular, spectral, phase or GH) employed. These results highlight the importance of designing the SPR chip to improve the sensor's performance.

III.1.2. Presentation of the TMM theoretical model

Before fabricating a new SPR chip, it is crucial to simulate its performance using a reliable theoretical model. In this regard, we have adopted the TMM.

A multilayer SPR chip can be accurately modelled using the TMM, which takes into consideration Fresnel equations for an N-layer multilayer medium [91,103]. When light travels through a multilayer system, it can be reflected or refracted multiple times, leading to constructive or destructive interferences. These contributions can be accounted for using a TMM approach, whereby each layer is defined in terms of its complex refractive index and thickness. The TMM is based on the continuity principle of the tangential component of electromagnetic field across the boundaries of a multilayered system, as defined by Maxwell's equations (Figure 70):

$$\mathrm{E}_{//}^{0} = \mathrm{E}_{//}^{1} \tag{23}$$

$$\mathrm{H}_{//}^{0} = \mathrm{H}_{//}^{1} \tag{24}$$

Where $\mathrm{E}_{//}^{0}$, $\mathrm{E}_{//}^{1}$, $\mathrm{H}_{//}^{0}$ and $\mathrm{H}_{//}^{1}$ are respectively the electric and magnetic fields (in TM polarization) parallel to the interface (z direction for E and y direction for H) in mediums 0 and 1 (Figure 70).

License CC BY-NC-ND 4.0

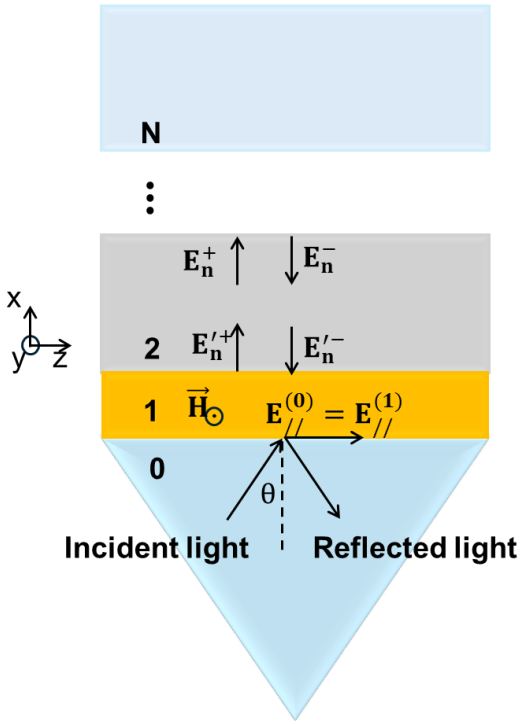


Figure 70 Schematic of a multilayer system showing an incident TM polarized light on a multilayer SPR chip. E^+ and E^- are defined as the forward and backward transmitted fields along the normal of the interfaces. E_n^+ and E_n^- represent the electric fields at the interface of layer n-n+1 and $E_n'^+$ and $E_n'^-$ at the interface of layer (n-1)-n (in this case n=2).

If the electromagnetic fields value is known at the initial boundary, it can be calculated at the final boundary via a matrix multiplication. Accordingly, E^+ and E^- (Figure 70) are defined as following:

$$\begin{bmatrix} E_{n-1}^+ \\ E_{n-1}^- \end{bmatrix} = I_{n-1,n} \begin{bmatrix} E_n^+ \\ E_n^- \end{bmatrix} \tag{25}$$

$$I_{n-1,n} = \frac{1}{t_{n-1,n}} \begin{bmatrix} 1 & r_{n-1,n} \\ r_{n-1,n} & 1 \end{bmatrix} \tag{26}$$

Where: $t_{n-1,n}$ and $r_{n-1,n}$ are the Fresnel transmission and reflection coefficients at the interface of (n-1)-n.

The field amplitudes (E_n^+ , E_n^-, $E_n'^+$ and $E_n'^-$) of the nth layer are then written as:

$$\begin{bmatrix} E_n'^+ \\ E_n'^- \end{bmatrix} = L_n \begin{bmatrix} E_n^+ \\ E_n^- \end{bmatrix} \tag{27}$$

$$L_n = \begin{bmatrix} e^{-i\Delta_n} & 0 \\ 0 & e^{i\Delta_n} \end{bmatrix} \tag{28}$$

License CC BY-NC-ND 4.0

$$\Delta_n = 2\pi\left(1/\lambda\right) n_n d_n \cos\theta_n \quad (29)$$

Where: λ, n_n, d_n and θ_n are respectively the incident wavelength, refractive index, thickness and incident angle of the nth layer.

The application of the above matrix transformations to the N layers and N + 1 interfaces gives:

$$\begin{bmatrix} E_0^+ \\ E_0^- \end{bmatrix} = I_{01} L_1 I_{12} L_2 \ldots . L_N I_{N,N+1} \begin{bmatrix} E_N^+ \\ E_N^- \end{bmatrix} \quad (30)$$

$$\begin{bmatrix} E_0^+ \\ E_0^- \end{bmatrix} = M \begin{bmatrix} E_N^+ \\ E_N^- \end{bmatrix} \quad (31)$$

The reflection coefficient can then be extracted from the matrix multiplication, and the intensity and phase of the reflected wave can be deduced:

$$M = \sum_{n=2}^{n=L-1} M_n \quad (32)$$

$$M_n = \begin{bmatrix} M_{11}\cos\beta_n & (-i\sin\beta_n)/\rho_n \\ -i\rho_n \sin\beta_n & \cos\beta_n \end{bmatrix} \quad (33)$$

$$\rho_n = \frac{\varepsilon_n - \varepsilon_1 \sin^2\theta_1}{\varepsilon_n} \quad (34)$$

$$\beta_n = \rho_n k_1 d_n \epsilon_n \quad (35)$$

$$r_{TM} = \frac{(M_{11} + M_{12}\rho_n)\rho_1 - (M_{21} + M_{22}\rho_n)}{(M_{11} + M_{12}\rho_n)\rho_1 + (M_{21} + M_{22}\rho_n)} \quad (36)$$

$$R_{TM} = |r_{TM}|^2 \quad (37)$$

$$\varphi_{TM} = \text{angle}(r_{TM}) \quad (38)$$

$$L_{GH} = -\frac{1}{k_0 n_0} \frac{\Delta\varphi_{TM}}{\Delta\theta} \quad (39)$$

Where:

- n: is the layer number,
- L: total number of layers,
- ε_n is the permittivity of the nth layer,
- ε_1 is the permittivity of the first layer,
- θ_1: is the angle of incidence at the base of the prism,
- k_1: wavevector inside the first layer, $k_1 = \frac{2\pi}{\lambda_0} n_1$, where:

License CC BY-NC-ND 4.0

    - λ_0: wavelength of the laser,
    - n_1: the refractive index of the first layer.
- r_{TM}: Fresnel reflection coefficient for TM polarisation,
- R_{TM}: Reflectivity for TM polarization,
- φ_{TM}: phase for TM polarization,
- L_{GH}: GH shift.

To validate the TMM, we applied it on a reference SPR chip consisting of bare 48 nm Au thin film deposited on BK7 with a 2 nm titanium adhesion layer. The experimental data are obtained as explained in Section III.1.1 above. The theoretical fit is represented in Figure 71.

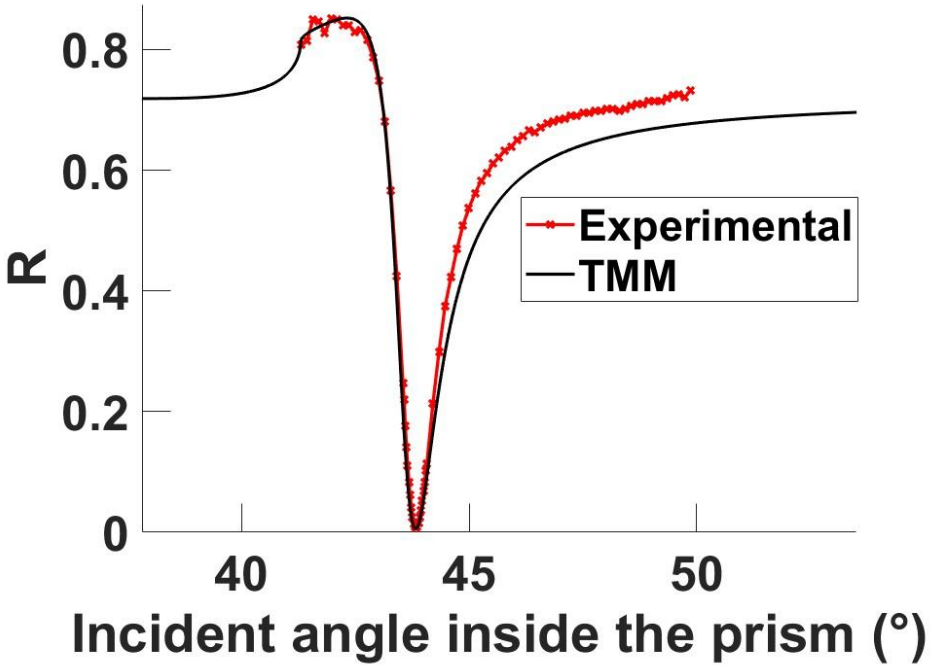


Figure 71 Experimental and theoretical reflectivity curves for a structure consisting of 48 nm Au, 2 nm Ti and BK7 prism tested in air as the surrounding medium.

It has been found that the reflectivity curve depth was correctly predicted by the TMM with a minimum value of 5.1×10^{-3} and an error of 1.5×10^{-3} obtained experimentally (Figure 71). The width of the reflectivity curve shows a slight discrepancy between the theoretical and experimental curves (a variation of 0.3° in the FWHM) especially away from the resonance angle, primarily due to experimental limitations: slight angular misalignments in the optical setup and fluctuations of the laser intensity measured with the detector.

After the theoretical model had been validated on a reference SPR chip, it had been adopted for the study of the novel SPR chips developed in this thesis.

III.2. Presentation of SPR chips based on Vanadium dioxide and gold

VO_2 is a phase change material that undergoes a reversible transition from insulator to metal when heated at 68°C, known as the metal-insulator transition temperature (MIT). This effect has been widely used in optical sensors, optical storage instruments and tunable devices.

License CC BY-NC-ND 4.0

Additionally, the properties of VO_2 have been exploited in plasmonic sensors for thermally tuning the plasmonic properties of Ag NPs [104] and of thin Au films (with 90 nm VO_2 nanocrystals [105]). This thesis focused on the insulator phase of VO_2 to enhance GH sensitivity. Exploiting the phase change properties of the material requires further investigation, namely with regard to heating the system.

Due to its high refractive index in the visible and near-infrared spectrum (detailed in the following section), VO_2 is considered as a promising candidate for enhancing the GH sensitivity. SPR substrates with a high refractive index material present many advantages (presented in Section III.1.1). The proposed new structure consists of a layer of VO_2 deposited on sapphire substrate with a thin layer of Au above (Figure 72).



Figure 72 Schematic of the proposed SPR chip composed of VO_2 layer deposited on sapphire substrate with an Au layer above.

We chose a sapphire substrate instead over BK7 for the following reasons:

1. Necessity to deposit VO_2 at high temperatures and the incapacity of the BK7 substrates to withstand high deposition temperatures,
2. The refractive index of sapphire is close to that of the SF11 prism. Therefore, there is almost no reflection between sapphire and SF11.

Indeed, the reflection coefficients between sapphire - VO_2 and between SF11 - BK7 at TM polarization were calculated at the resonance angle of each SPR structure. This corresponds to 54.2° for the commercial and 54.6° for the VO_2 chip (the SPR chip is presented in Section III.2.1 below). As can be seen in Figure 73, the reflection coefficient between SF11 and BK7 was found to be six times greater than that between sapphire-VO_2.

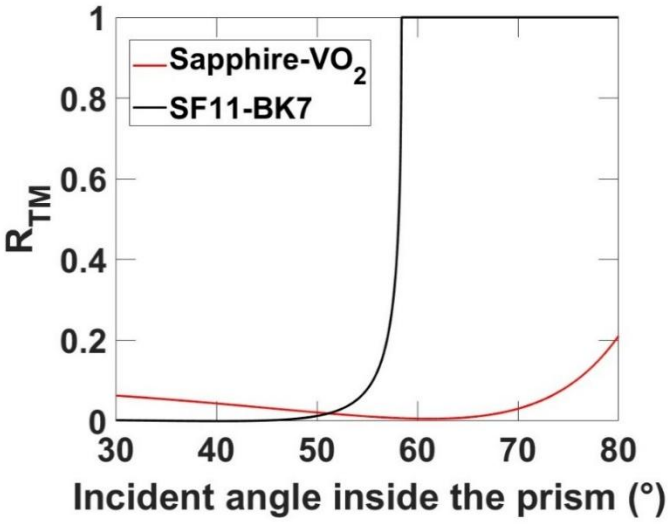


Figure 73 TM reflection coefficient calculated at the interface between sapphire-VO_2 and between SF11-BK7.

License CC BY-NC-ND 4.0

By reducing the intensity of the reflected beam between the prism and substrate, more field penetrates inside the structure and couples with SPWs. Additionally, with less intense secondary reflection spots, the PSD can measure the GH shift resulting from the SPR reflected beam with a greater accuracy (Figure 74).

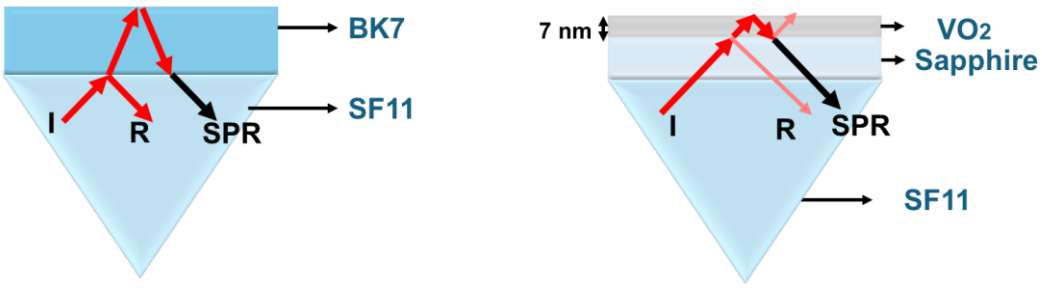


Figure 74 Schematics comparing the reflection between SF11-BK7 and sapphire-VO_2.

III.2.1. Simulation results of SPR chips based on VO_2 using the TMM

The complex refractive index of VO_2 was extracted by Dr. Jean-Christophe Orlianges (XLIM) using ellipsometry measurements (presented in Chapter 4). The results are shown in Figure 75.

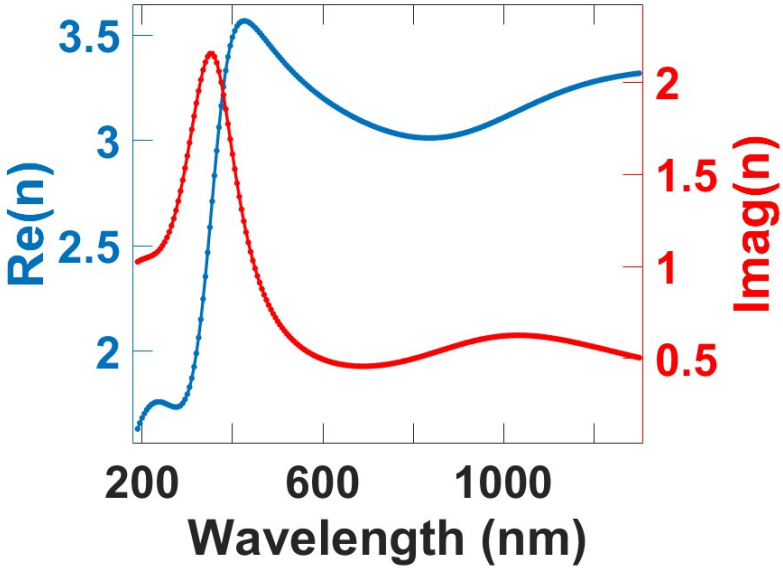


Figure 75 Complex refractive index of VO_2 vs wavelength at 20°C.

At 633 nm, the permittivity of VO_2 ($\varepsilon = n^2$) was found to be 9.7539 + 2.9904i. The large imaginary part of the permittivity indicates a high absorption (losses) of the incident light by the material. However, since the thickness is small (< 10 nm), this effect is less significant. This value was then incorporated into the TMM to simulate the response of the SPR chip.

To optimize the new SPR chip, the thicknesses of the Au, titanium and VO_2 layers were varied from 45 to 50 nm, 2 to 4 nm and 0 to 10 nm, respectively. The refractive indices of Au and titanium were extracted from the Johnson and Christy model [106].

License CC BY-NC-ND 4.0

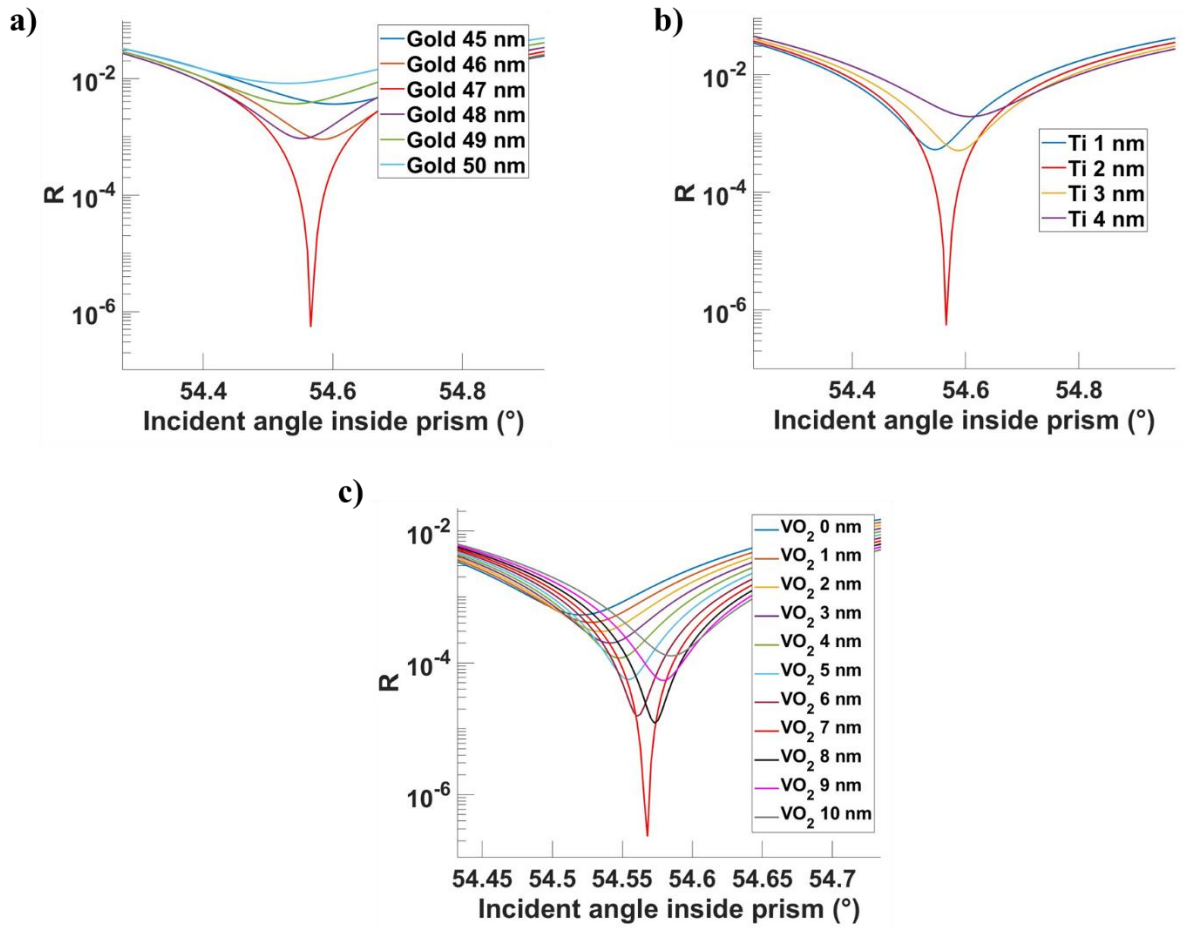


Figure 76 Reflectivity vs incident angle at the base of SF11 prism for a) Au: 45-50 nm, Ti: 2 nm and VO_2: 7 nm, b) Au: 47 nm, Ti: 1-4 nm and VO_2 7 nm and c) Au: 47 nm, Ti: 2 nm and VO_2 0-9 nm.

The optimal thickness of Au is found to be 47 nm (Figure 76-a). At this thickness, reflectivity is minimal, and the FWHM is the thinnest. This corresponds to maximum plasmonic coupling. When the Au thickness deviates from 47 nm, the reflectivity depth decreases by three orders of magnitude. Similarly, the optimal thickness of Ti was found to be 2 nm (Figure 76-b). Since titanium behaves as a metal at 633 nm (with ε_{Ti} = -3.9167 + 12.5888i), the effect of its thickness follows the same trend as that of Au (away from the optimal thickness of Ti, the reflectivity depth also decreases by a factor of 1000).

The deepest reflectivity dip occurs when the thickness of VO2 reaches 7 nm (Figure 76-c) which corresponds to the optimal thickness where destructive interferences lower the intensity of the reflected signal [83]. Additionally, since VO2 has a large absorption coefficient, a further increase in thickness will enhance the absorption of light by the substrate. This will ultimately attenuate the light before interacting with the Au-surrounding interface and coupling with SPWs.

License CC BY-NC-ND 4.0

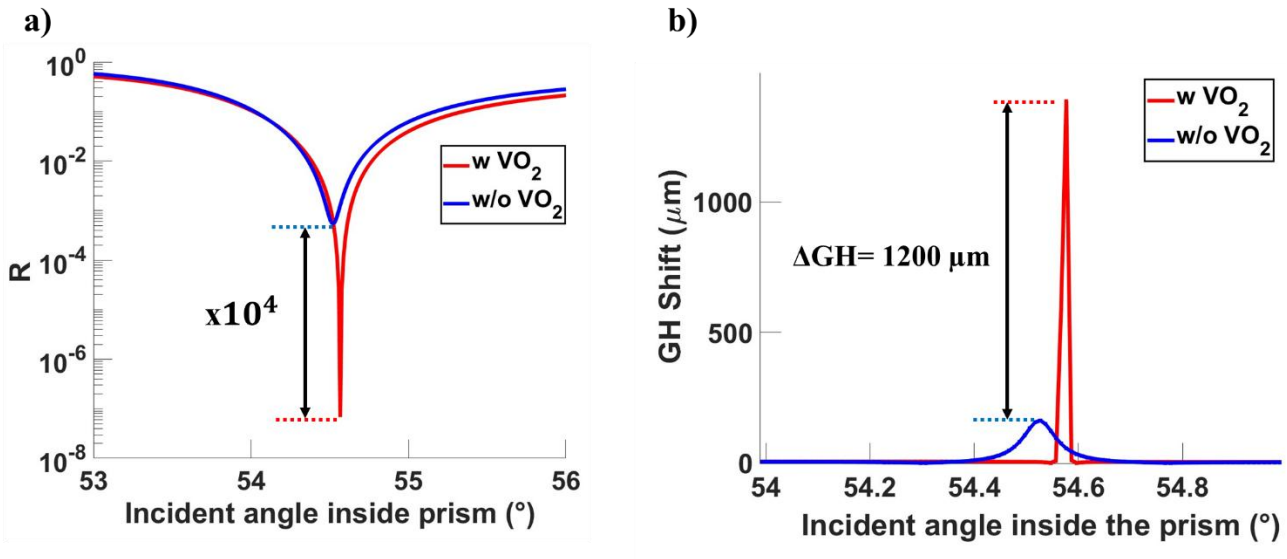


Figure 77 SPR curves comparing two chips with and without VO_2. a) Reflectivity vs incident angle and b) GH shift vs incident angle.

In conclusion, the addition of a 7 nm VO_2 layer under the Au generates a considerably sharper and shallower reflectivity minimum (Figure 77-a), which is four orders of magnitude higher than that of the bare Au structure. The deeper absorption in the reflected light leads to a more pronounced GH shift, with an improvement of 1200 µm in comparison to the bare Au structure (Figure 77-b).

After theoretically validating the high sensitivity of the VO_2-based SPR chips, the fabrication process took place according to the desired parameters: Au thickness of 47 nm, Titanium thickness of 2 nm and VO_2 thickness of 7 nm.

III.2.2. Experimental testing of the VO_2 based SPR chip

Our colleague at XLIM (Dr. Aurelian Crunteanu) fabricated the VO_2 chips using magnetron sputtering, a vapor phase deposition technique. It involves creating a plasma of argon in a vacuum chamber where ions bombard a vanadium target to extract atoms. These atoms are then deposited onto a sapphire substrate to form a uniform thin film (Figure 78). In reactive sputtering, a controlled flow of oxygen is introduced into the chamber enabling VO_2 to form with the correct stoichiometry. Magnetron sputtering enables the production of stoichiometric, homogeneous thin films over large areas [107]. The procedure is highly flexible: the addition of O_2 or N_2 enables the formation of oxides or nitrates, while co-sputtering multiple targets facilitates the production of doped materials and multilayer structures [108]. Another advantage of sputtering is the ability to control the film thickness with nanometer precision, which is necessary for adjusting the optical properties of VO_2 [109].

License CC BY-NC-ND 4.0

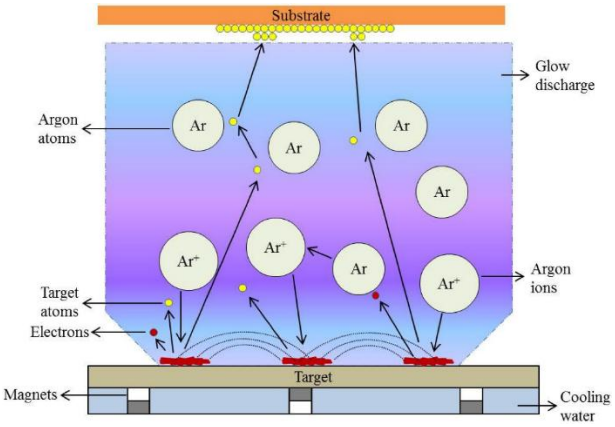


Figure 78 Illustration of the Magnetron sputtering process [110].

Before evaluating the GH sensitivity, the reflectivity curve of the chip was measured with water as the surrounding environment. Both chips were coupled with an SF11 prism and installed on the new holder. The reflectivity curve was subsequently compared with an identical structure without VO_2. The process is explained in section III.1.1. The results are presented in the Figure 79.

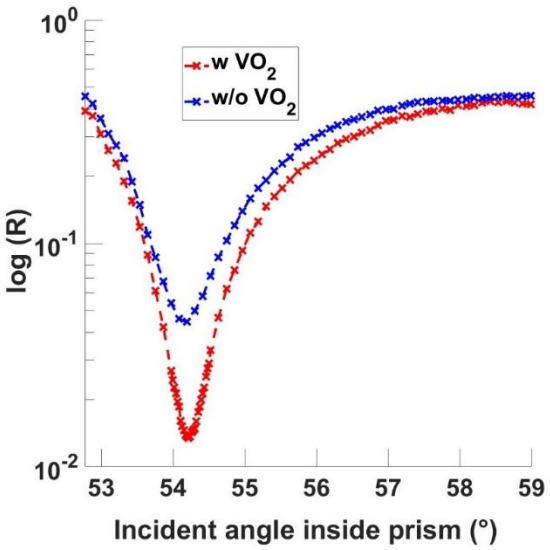


Figure 79 Measurements of the experimental reflectivity curve. The blue curve represents the SPR chip without VO_2 and the red with VO_2.

The addition of a 7 nm layer of VO_2 decreased the reflectivity dip by a factor of 4 (Figure 79). Consequently, a sharper phase change and stronger GH sensitivity is expected. From a theoretical perspective, the TMM determined that a thickness of 7 nm would produce the deepest reflectivity dip and the smallest FWHM. However, these experimental tests revealed a FWHM slightly higher than that of bare Au and a reflectivity dip shallower than calculated. This difference could be attributed to several factors. The reflectivity curve is highly sensitive to the thickness and permittivity of VO_2. The reflectivity curve is highly sensitive to the thickness and permittivity of VO_2. In practice, the permittivity used in the simulations were extracted from ellipsometric measurements performed on a 200 nm-thick VO_2. With very thin layers, it is quite

License CC BY-NC-ND 4.0

difficult to get an accurate estimate of the layers. Consequently, the actual permittivity of the deposited thin film may slightly differ from the values used in the TMM simulations. Additionally, for ultrathin films deposited by magnetron sputtering, the actual thickness may slightly differ from the target value.

The new VO_2 chip was then calibrated using diluted glycerin solutions and water. Glycerin is a useful calibrating agent because its refractive index is known. This will allow us to directly evaluate the sensor's sensitivity in terms of minimal detectable refractive index changes. Considering the refractive index of water (n=1.3320) and 100% glycerin (n=1.4707), the refractive indices of diluted glycerin were calculated by:

$$\Delta n = (n_{\text{glycerin } 100\%} - n_{\text{water}}). \text{concentration} \quad (40)$$

Table 12 Refractive index of diluted glycerin solutions.

Solution	n(solution)-n(water)
Water	0
0.05 % glycerin	6.6×10^{-5}
0.1 % glycerin	1.4×10^{-4}
0.5% glycerin	6.9×10^{-4}
1% glycerin	1.4×10^{-3}
2.5% glycerin	3.5×10^{-3}
5% glycerin	6.9×10^{-3}

The experiment was conducted as described in Section II.3.2 using the reference platform. The diluted glycerin solutions were injected into the fluidic channel successively starting from the lowest concentration.

Water was used as a reference to represent the results, and the subsequent shifts of the diluted glycerin solutions were subtracted from it (Figure 80).

License CC BY-NC-ND 4.0

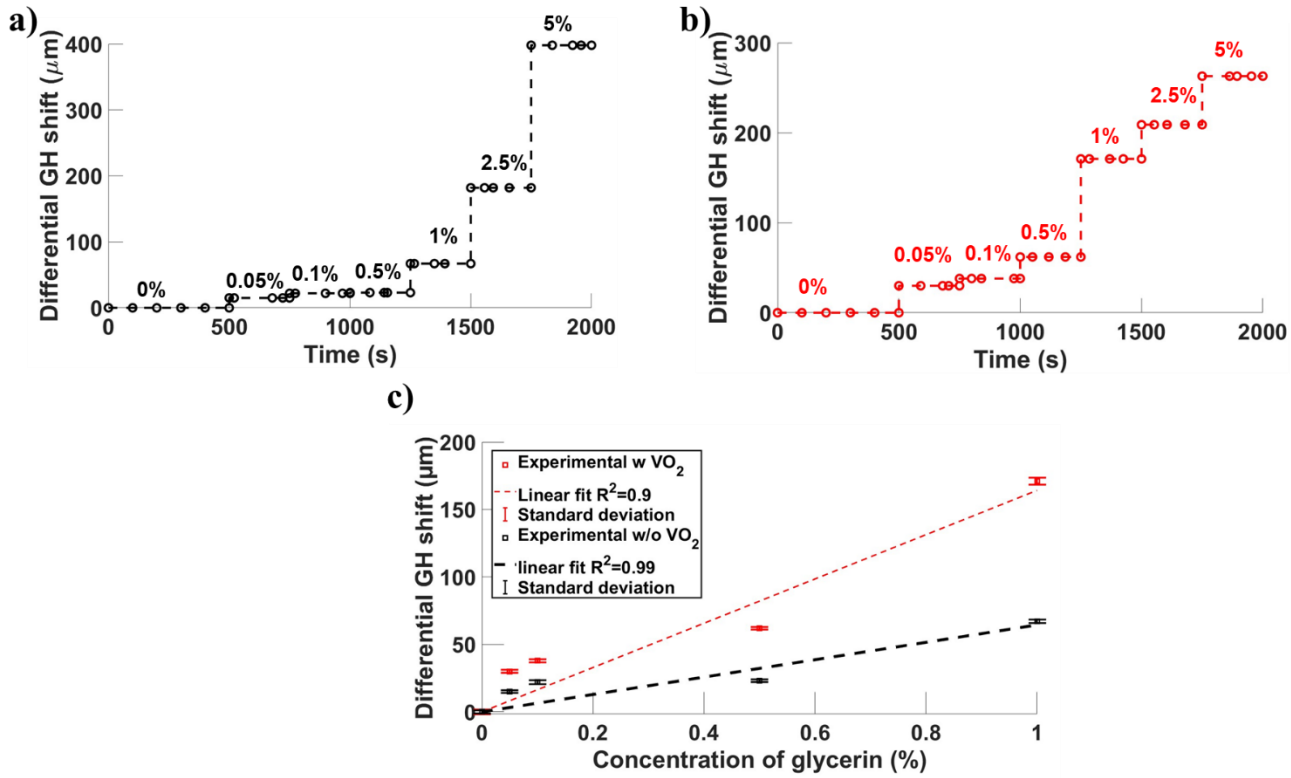


Figure 80, a) Measured differential GH shift for different glycerin concentrations for the SPR chip (a) without a VO_2 layer (b) with a VO_2 layer, c) Linear fit of the experimental data.

We detected a differential GH shift of 30 µm with the VO_2 chip for 0.05% glycerin (Figure 80) injected into the fluidic channel (in comparison with 15 µm without VO_2). As the concentration increases, the differential GH linearly rises, with a R^2 value of 0.9. The quasi-linear variation of the GH shift with respect to the refractive index can be explained by the linear variation of the resonance angle. For low changes in $\Delta\varepsilon_m$ (Figure 81), the shift of the resonance angle can be mathematically approximated by a first-order polynomial [111].

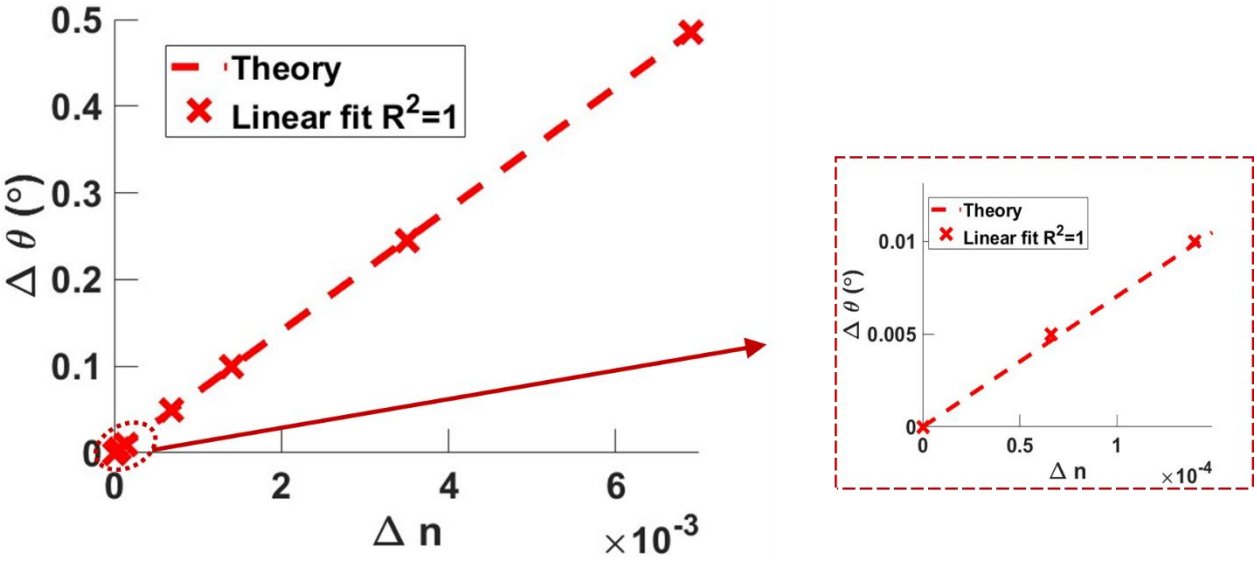


Figure 81 Variation of resonance (Δθ) angle calculated with respect to the refractive index of the surrounding medium.

License CC BY-NC-ND 4.0

As the GH shift is measured at a fixed incidence angle close to the resonance angle, it varies linearly with the glycerin concentration.

In conclusion, from these data, the sensitivity of the sensor can be estimated as 4.5×10^5 µm/RIU (Equation 41).

$$S = \frac{GH(water) - GH(0.05\%\ glycerin)}{n_{water} - n_{0.05\%\ glycerin}} \quad (41)$$

The limit of detection (LOD) can be determined by:

$$LOD = \frac{standard\ deviation \times 3}{S} \quad (42)$$

Given the standard deviation of the measurements ~0.7 µm, we estimate a LOD of 4.7×10^{-6} RIU.

The addition of a VO_2 layer enhanced the GH sensitivity by a factor of two in comparison with the structure without VO_2. The result demonstrates that incorporating VO_2 into the structure is an effective way to enhance the overall sensitivity, making it a promising material for use in SPR biosensing.

The chip was further tested for its ability to detect large biomolecules such as BSA (66.5 kDa). BSA molecules were diluted in PBS and injected successively into the fluidic channel starting from the lowest concentration. Since BSA was diluted in PBS, the resonance angle was found with PBS. To illustrate this concept, we present the simulated GH curves (Equation 39) for the VO_2 chip in three solutions: water, PBS and $n_{PBS}+10^{-4}$ RIU. The results are presented in Figure 82.

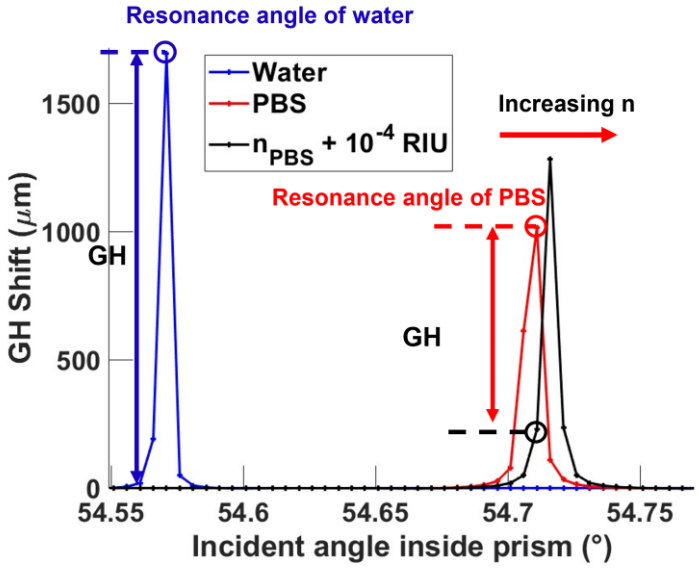


Figure 82 Calculated GH shift for three different solutions, Water, PBS and $n_{PBS}+10^{-4}$ RIU.

If the resonance angle is found with water, then the change in resonance angle between water and PBS corresponds to 0.14° and the GH shift becomes 1693 µm (Figure 82). Solutions diluted in PBS will introduce additional shifts in the resonance angle (example, $n_{PBS}+10^{-4}$ RIU). Hence, if the resonance angle is found with water, the chip will not be able to detect any

License CC BY-NC-ND 4.0

solution beyond PBS (saturation point). Whereas, if the resonance angle is found with PBS, a GH shift of 787 µm can still be found.

The results of BSA measurements are shown in Figure 83.

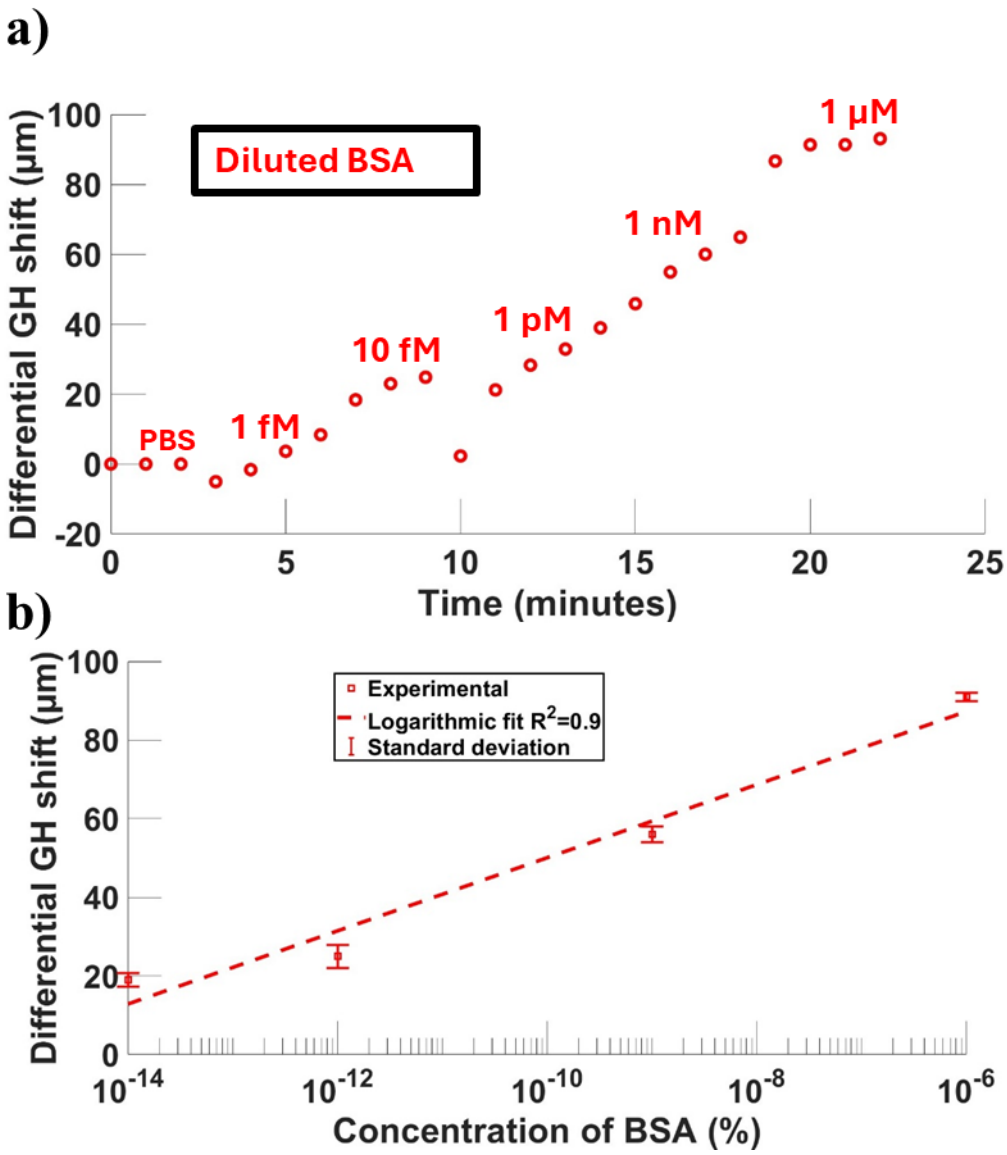


Figure 83 Measurement of the GH shift with diluted BSA solutions and the VO_2-based chip, a) Evolution of the GH shift during successive injections of BSA, b) logarithmic fit of the experimental data.

It has been shown that biomolecules tend to bind to the Au surface as the GH signal increases over time following the injection of BSA solutions (Figure 83). This is due to the high affinity of Au for the free thiol groups (-SH) present in BSA [112]. The minimal detectable concentration was in the order of 10 fM, with a GH shift of 25 µM with respect to PBS. The sensor shows a logarithmic trend when higher concentrations of BSA are injected, with an R^2 value of 0.9. The linearity in the log of the concentration can be explained by the Langmuir adsorption process where, in this case, the thiol groups (-SH) present in BSA can bind to Au molecules forming quasi-covalent Au-SH bonds [112]. The Langmuir model assumes that the available binding sites are identical, with each molecule occupying a single site. Furthermore, the ability of one

License CC BY-NC-ND 4.0

molecule to occupy a certain binding site is independent of the degree of occupation of neighboring sites [44,111,113,114]. Hence, the change in SPR response (here GH shift) follows a sigmoidal trend which can be approximated by linear function with respect to the logarithmic of the concentration.

In conclusion, this calibration step demonstrated the ability of the chip to detect BSA at concentrations as low as femtomolar and as high as 1 µM.

III.3. Presentation of SPR chips based on embedded silver NPs in alumina with a gold thin layer above

Ag and Au are both interesting metals for coupling SPWs, yet they present some disadvantages. A sharper and deeper resonance is achieved when a thin Ag layer is excited due to its low absorption losses. This is related to its smaller imaginary permittivity and larger real part of the permittivity compared to Au. However, Ag is not stable in a liquid environment and will corrode if exposed to air for extended periods [92].

Given the plasmonic properties of Ag and the chemical and biological stability of Au, the literature shows that combining their properties in a single nanocomposite increases the sensitivity compared to bare Au or Ag structures [92]. Directly embedding Ag NPs inside Au can suppress the NPs' LSPR, leading to damped plasmonic oscillations and reduced sensitivity to the surrounding medium. This is due to the fact that an electromagnetic field cannot be confined at a metal-metal interface. This causes the damping of the charge oscillations of the NPs by the surrounding metal [115]. Conversely, alumina is a transparent dielectric material that can support LSPR modes. Simultaneously, it forms a protective layer around Ag preventing it from deterioration and oxidation [116]. Additionally, since Au is chemically stable, depositing a thin layer above alumina can facilitate the functionalization of the SPR chip for biosensing applications [92]. The new chip investigated then consists of Ag NPs embedded in alumina with a thin layer of Au above (Figure 84).



Figure 84 Schematic of the SPR structure consisting of embedded Ag NPs in alumina with a thin layer of Au above.

Using pulsed laser deposition (PLD) in conjunction with a free cluster generator (FCG), our colleagues at IRCER can simultaneously fabricate metallic NPs and inject them into the alumina matrix [117]. PLD enables the deposition of pure, dense Al_2O_3 and Au thin films under vacuum, with nanometer-scale control of the thickness (Figure 85). For that, a target material (Au or alumina) is exposed to a pulsed excimer laser producing a plasma plume composed of ions, electrons and radicals. These species in their vapor phase then undergo an adiabatic expansion and condense onto the substrate placed at the proximity of the target (BK7 when depositing alumina or Alumina substrate when depositing Au).

License CC BY-NC-ND 4.0

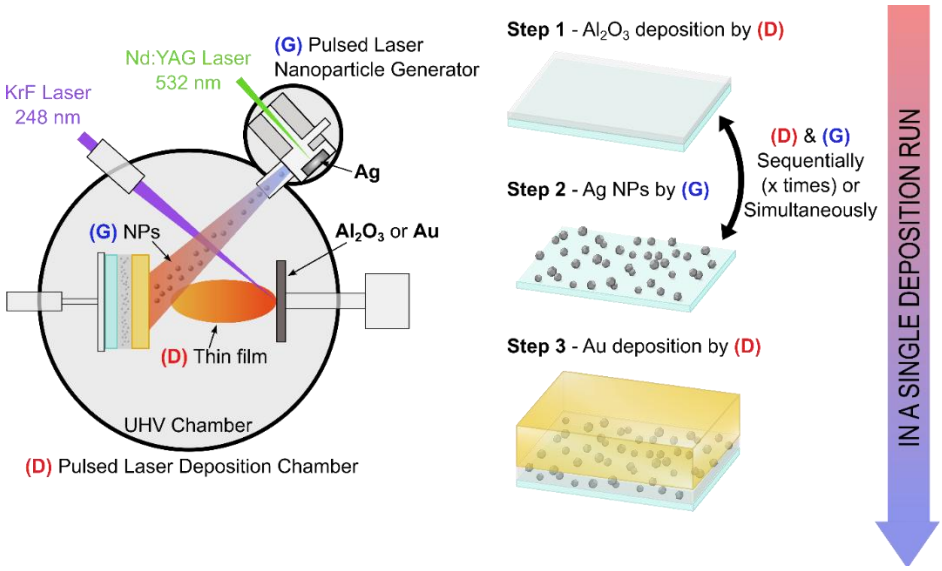


Figure 85 Schematic representation of the PLD chamber and Pulsed Laser NP generator chamber. The entire nanostructure is produced inside the reactor within a singular deposition process. Thin films are generated using PLD, while the Ag NPs are synthesized with the NP generator. The alumina oxide matrix and the Ag NPs are deposited by a combination of PLD and the NP generator, either sequentially or simultaneously. Finally, a Au top layer is deposited by PLD [117].

Meanwhile, Ag NPs can be synthesized using a FCG (Figure 86). Nd: YAG laser ablation of a target (Ag) creates a plasma plume expanding in the nucleation chamber. The cavity includes the target from one side and the laser on the other side. The laser pulses are synchronized with the opening of a pulsed valve for the introduction of high-pressure helium gaz. Helium gas allows the rapid cooling of the plasma plume and when supersaturated conditions are met, NPs start to grow. The mixture consisting of He gas and NPs is injected through a nozzle into the PLD chamber where it undergoes a supersonic expansion. The nozzle fixes the size and shape of the NPs before reaching the substrate. To produce homogenous NPs deposition, the substrate's holder can be rotated. In this case, since the kinetic energy of the NPs is lower than the cohesive energy of Ag, the formation of NPs clusters can be prevented [117].

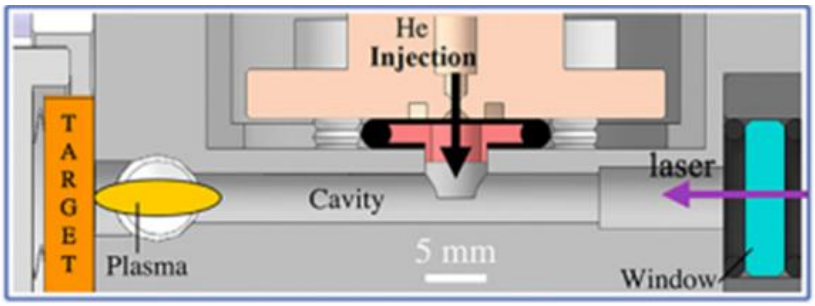


Figure 86 Schematic of the FCG.

Integrating PLD and FCG in the same reactor enables the fabrication of complex Ag-NP/Al_2O_3/Au nanocomposites along with multilayer NPs depositions without interface

License CC BY-NC-ND 4.0

contamination and with precise control over the architecture, concentration and size of the NPs [118]. As such, the size of NPs can be controlled with diameters ranging from 1-5 nm with a monodisperse distribution. This system is rather uncommon, unique and allows the simultaneous fabrication of multilayers of NPs and thin films.

III.3.1. Presentation of the analytical model to simulate SPR chips with embedded NPs in a matrix

Literature suggests different analytical models for simulating the effect of metallic spherical NPs embedded into a matrix. These are known as the effective medium approximations [119–125]. For our application, we consider three main approaches to simulate NPs embedded in a host matrix: Maxwell–Garnett (MG), Modified Maxwell–Garnett (MMG) and Bruggeman (Figure 87).

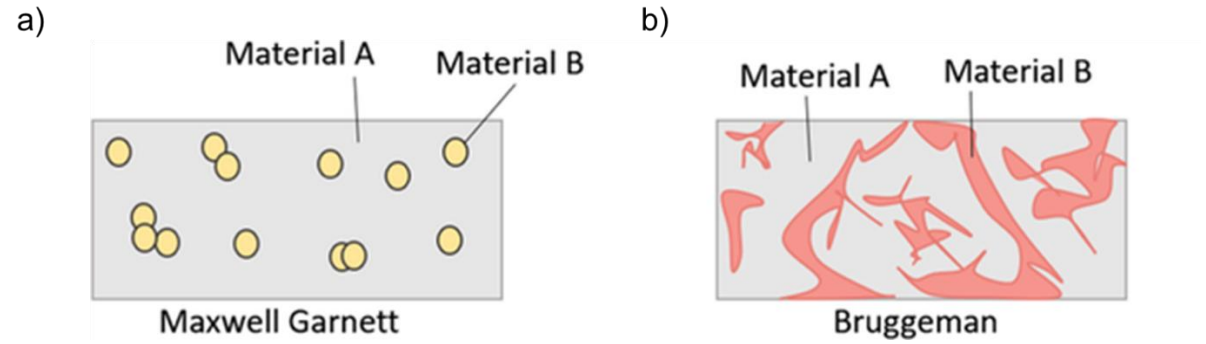


Figure 87 Illustration representing, a) Maxwell-Garnett and b) Bruggeman structures [126].

If the NPs are small in size (diameter < λ/2) and well diluted in the alumina matrix they can be modelled by Maxwell-Garnett effective medium theory. This theory treats the nanocomposite consisting of NPs incorporated inside alumina as a homogeneous medium, in which the effective permittivity is determined by the electromagnetic polarizability of the NPs within the matrix. The theory assumes that the NPs are spherical, dispersed randomly and uniformly inside the matrix. Additionally, it considers that the interparticle distance is large enough for only dipolar interactions to take place between the NPs. The effective permittivity of the nanocomposite (NPs and alumina) can be expressed by [127]:

$$\varepsilon_{eff} = \varepsilon_m \frac{2f(\varepsilon_s - \varepsilon_m) + \varepsilon_s + 2\varepsilon_m}{2\varepsilon_m + \varepsilon_s - f(\varepsilon_s - \varepsilon_m)} \quad (43)$$

Where:

- ε_m is the permittivity of the alumina matrix,
- ε_s is the permittivity of Ag NPs,
- f: is the concentration of the NPs.

The MG assumption becomes inaccurate at higher NP concentrations. In these cases, the distance between NPs decreases, leading to near-field coupling between the NPs. This modifies the resonance of the effective medium and the local field distribution. Thus, a modified version of the MG assumption, known as MMG theory, has been proposed to account for these

License CC BY-NC-ND 4.0

limitations. It assumes that NPs with different sizes are randomly dispersed within the matrix [125].

$$\frac{\varepsilon_{eff} - \varepsilon_m}{\varepsilon_{eff} + 2\varepsilon_m} = \frac{3i\lambda^3}{16\pi^3\varepsilon_m^{3/2}} \frac{f}{\overline{R}^3} \int P(R) a_1 \, dR \quad (44)$$

Where:

- λ: wavelength of the excitation source,
- $\overline{R}$: mean radius of the NPs,
- $P(R)$: NPs size distribution,
- $a_1(R)$: Electric Mie coefficient. $a_1(\varepsilon_s, R, \lambda)$.

Another approach proposed by Bruggeman (Figure 87-b) does not differentiate between the NPs and the matrix, treating them similarly. This approach is better suited to high concentrations, bigger NPs and disordered mixtures, where the matrix and NPs are interconnected [124].

$$f \frac{\varepsilon_s - \varepsilon_{eff}}{\varepsilon_s + 2\varepsilon_{eff}} + (1 - f) \frac{\varepsilon_m - \varepsilon_{eff}}{\varepsilon_m + 2\varepsilon_{eff}} = 0 \quad (45)$$

Our colleagues at IRCER can fabricate highly diluted NPs (f<20%) with diameters smaller than 5 nm. Therefore, we used the Maxwell-Garnett theory to simulate the SPR chip. The SPR chip consists of successive layers of NPs separated by layers of alumina. Then, to simulate the new chip using the TMM, we divide the alumina layer into four sublayers (Figure 88):

1. Alumina layer: with thickness d_1= 4 nm and permittivity ε_m,
2. Effective medium: with thickness d_2=2.r (where r is the radius of the NPs) and permittivity ε_{eff},
3. Alumina layer: with thickness d3= 4 nm and permittivity ε_m,
4. Effective medium: with thickness d4=2.r (where r is the radius of the NPs) and permittivity ε_{eff},

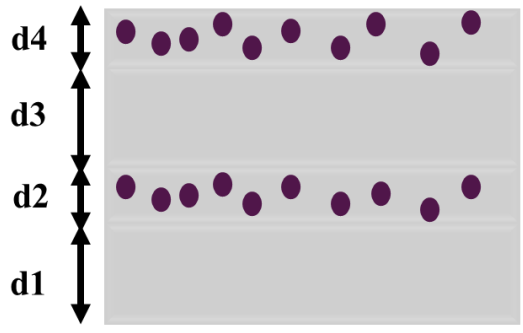


Figure 88 Schematic of the multilayer model used to represent the embedded Ag NPs in alumina in the TMM.

To simulate the new SPR chip, we first studied the effect of the concentration of the NPs. The Au thickness was fixed at 49 nm, the radius of the NPs at 1 nm and the thickness of alumina

License CC BY-NC-ND 4.0

at 12 nm (Figure 89). The refractive indices of Au and Ag were extracted from the Johnson and Christy model [106].

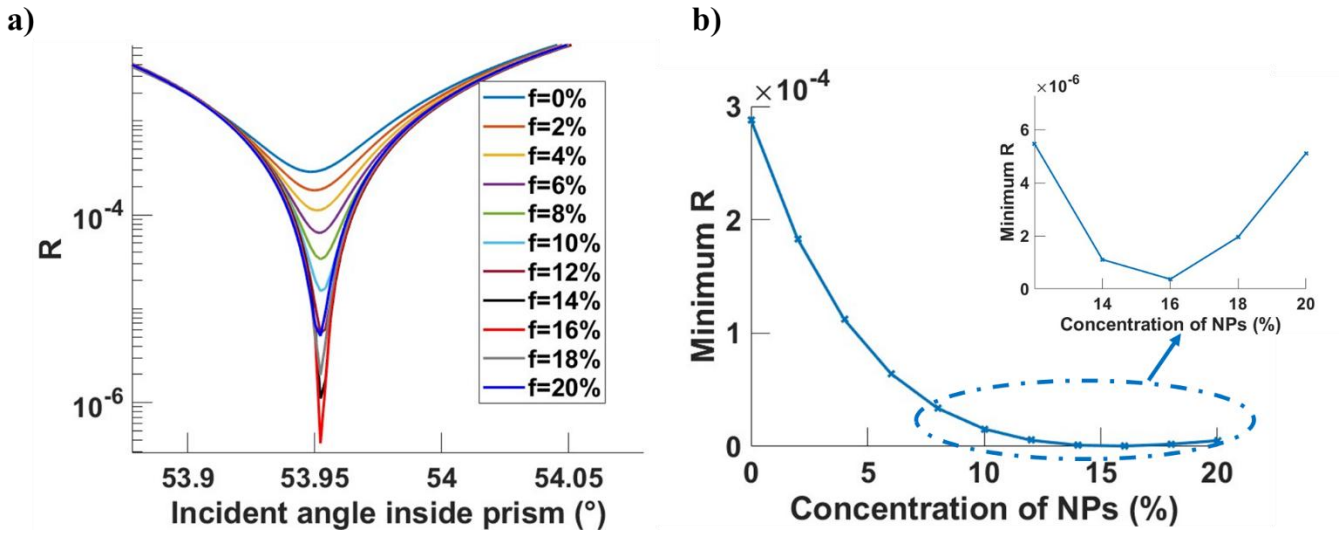


Figure 89 Calculated reflectivity curves for different NPs concentrations for a structure consisting of Ag NPs with a radius of 1 nm, embedded in an alumina matrix of 12 nm, with Au layer (t = 49 nm) on the top, a) Reflectivity vs incident angle and b) Minimum reflectivity vs concentration of NPs.

The deepest reflectivity occurs when the concentration of NPs in the alumina matrix is 16%. This value corresponds to a two-order-of-magnitude decrease in reflectivity compared to an alumina-Au chip without NPs. This preliminary result demonstrates the potential of the designed SPR chip to enhance sensitivity by achieving greater reflectivity, resulting in a steeper phase change and, consequently, a larger GH shift.

It is important to note that the SPR response of the chips depends on various parameters, including the thickness and radius of the metal, the concentration of the Ag NPs, and the thickness of the alumina, as shown in Figure 90.

License CC BY-NC-ND 4.0

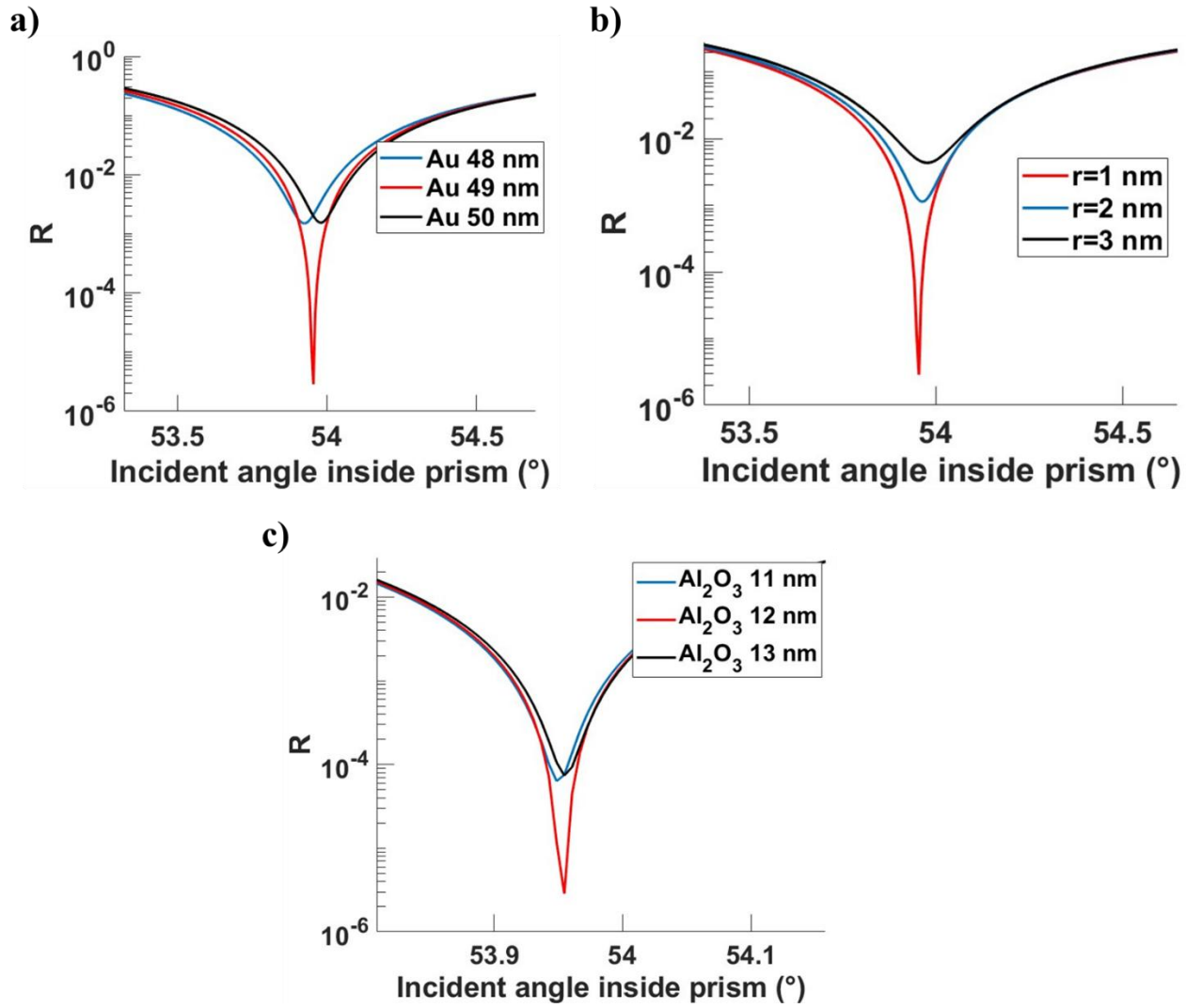


Figure 90 Reflectivity curves showing the effects of a) Au thickness with 12 nm alumina, r =1 nm and f=16%, b) radius of the NPs with alumina 12 nm, Au 49 nm and f=16%, c) effect of alumina thickness with r =1 nm, f=16% and Au 49 nm.

The thickness of the Au has the strongest influence (Figure 90-a) on the SPR reflectivity curve. A thickness of 49 nm leads to a deeper reflectivity dip due to the optimum balance between radiative and intrinsic losses. The radius of the NPs (Figure 90-b) is also an important parameter to consider, as it directly affects the nanocomposite's effective permittivity through MG theory. In this case, the smallest radius produced the deepest reflectivity dip. Conversely, the thickness of the aluminum layer (Figure 90-c) is shown to have a lesser influence since it is a non-absorbing layer. Its role involves modifying the accumulated phase inside the structure and thereby influencing the destructive interference process that determines reflectivity.

License CC BY-NC-ND 4.0

III.3.2. Experimental evaluation of the SPR chips with embedded NPs

Several chips were fabricated and tested to fine-tune the deposition parameters and adjust the concentration of the NPs. To evaluate the sensitivity of the chips, each of the samples was calibrated with diluted glycerin solutions. The experiments were performed according to the experimental procedure described in Section II.3.2 using the reference platform. Five different SPR chips were fabricated and measured: a commercial chip, three identical chips with Ag NPs in alumina and with a thin Au layer above (N1, N4, N5) and a reference chip composed of an alumina layer with Au (VAl8). Initially, the NPs concentration inside the chips was not identified: concentration of (N5)> (N4)>(N1). The NPs have a diameter of 4.4 ± 1.4 nm and the thickness of Au is 50 ± 1 nm. The results are represented in Figure 91.

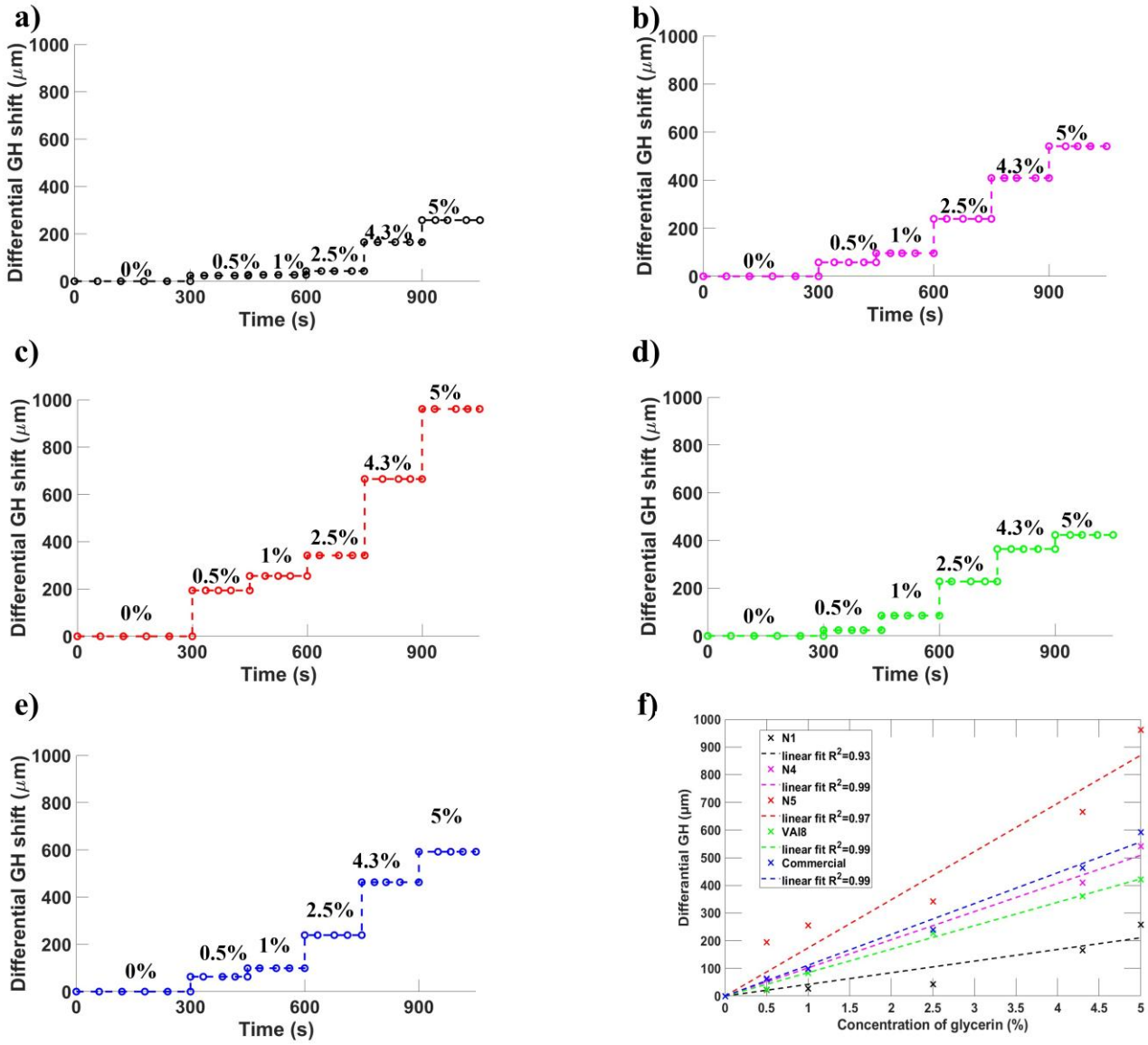


Figure 91 Measurement of the commercial, N1, VAl8, N4 and N5 chips with diluted glycerin. Au and alumina thicknesses are 48 and 12 nm respectively for all samples except the commercial. VAl8 is composed of a layer of alumina with NPs and N1, N4, N5 have Ag NPs embedded with concentrations ranging from the lowest (N1) to the highest (N5). Figures (a), (b), (c), (d),(e) show the differential GH shift for different glycerin concentrations, a) N1 chip, b) N4 chip, c) N5 chip, d) VAl8 chip, e) Commercial chip, and f) Linear fit of the experimental data.

License CC BY-NC-ND 4.0

The N1 chip (Figure 91) had the lowest sensitivity, followed by the VAl8 reference chip. The only chip that surpasses the sensitivity of the commercial chip was N5. This result clearly shows the importance of carefully adjusting the NP concentration to optimize GH sensitivity.

N5 was later tested in water to determine the experimental reflectivity curve. This curve was then compared to the commercial one (Figure 92). The experimental procedure is explained in Section III.2.2.

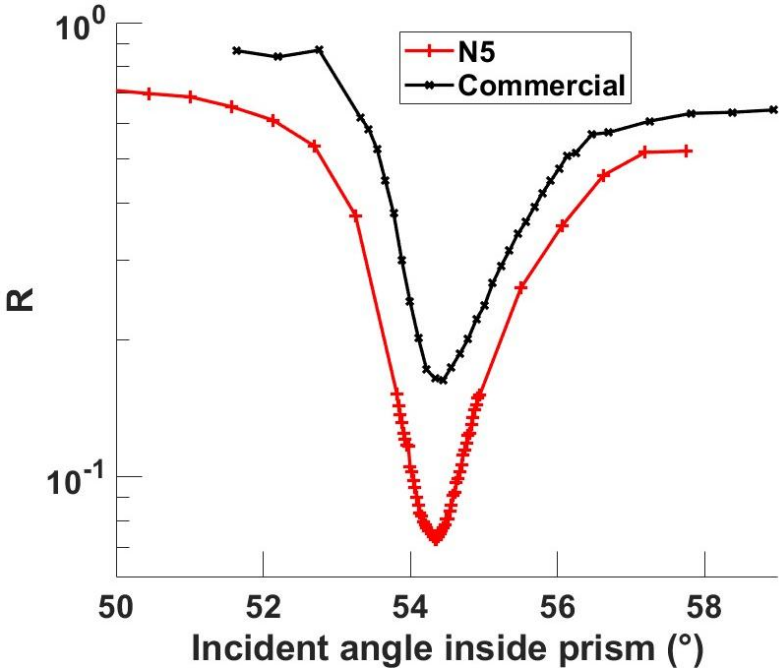


Figure 92 Measurement of the reflected intensity versus the incident angle for N5 and commercial chips tested in water.

A deeper reflectivity was obtained with N5 in comparison with the commercial: the reflectivity dip is about 2 times lower in comparison with the commercial chip (Figure 92). A deeper resonance peak indicates more efficient coupling of incident light inside the chip, a sharper phase change, and an improved GH shift.

After validating the N5 chip's higher sensitivity with glycerin calibration, the following stage involved evaluating its suitability for detecting biomolecules. To this end, the N5 was calibrated using diluted BSA solutions in PBS using the reference platform. Since the BSA was diluted in PBS, the resonance angle was determined using PBS. The results are shown in Figure 93 where each data point represents the average of a minute measurement.

License CC BY-NC-ND 4.0

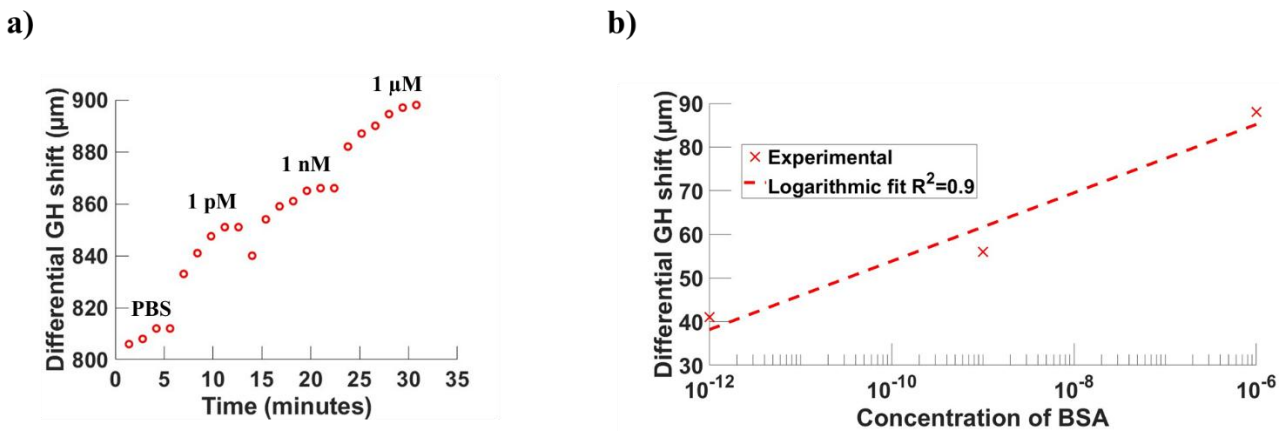


Figure 93 Measurement of the GH shift with diluted BSA solutions and the N5 chip, a) Evolution of the GH shift during successive BSA injections and b) Logarithmic fit of the experimental data.

The chip was able to detect molecules at the pM level with a GH shift of 38 µm relative to PBS (Figure 93). The linear fit in log scale suggests that concentrations down to 0.1 fM could be detected, with a predicted GH shift of around 7 µm.

Following confirmation of the enhanced sensitivity achieved with N5, a series of fabrication processes were initiated to refine the deposition parameters according to the simulation results. This resulted in the development of numerous chips leading to the optimized N24 chip. The N24 chip consists of NPs with a diameter of 2.3 ± 0.8 nm and an Au thickness of 48 ± 2 nm.

The new chip was hence tested and calibrated with diluted glycerin solutions to assess its sensitivity. The results are shown in Figure 94.

License CC BY-NC-ND 4.0

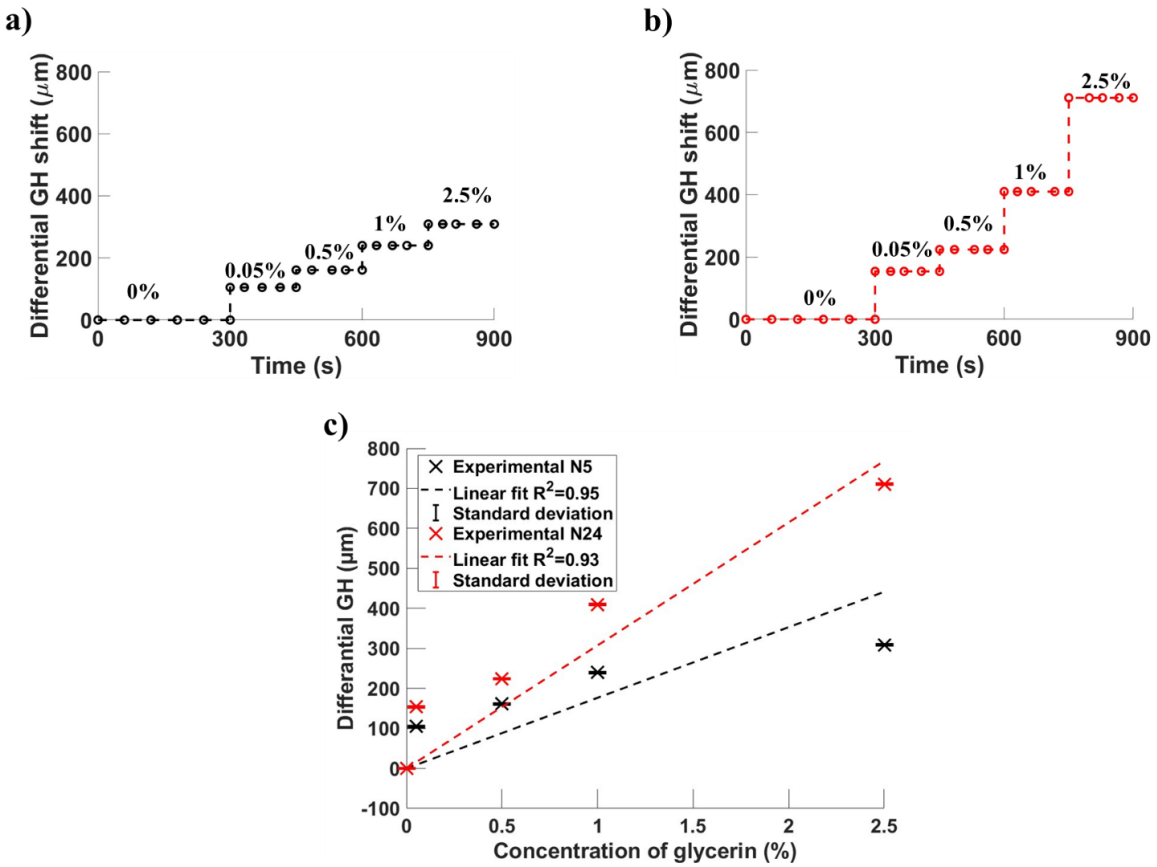


Figure 94 Measurement of, a) N5, b) N24 chips with diluted glycerin solutions and c) Linear fit of the experimental data.

The linear fit curve of N24 demonstrated a higher slope compared to N5, with an enhancement factor of two (Figure 94). We estimate the sensitivity S (Equation 41) of N24 at $2x10^7$ µm/RIU. Assuming a noise level of 0.7 µm (standard deviation of the position x in the measurements), we estimate a LOD of 1.10^{-7} RIU (Equation 42).

In conclusion, the N24 chip was selected for future biodetection experiments due to its superior sensitivity.

A material characterization study was conducted (by IRCER researchers) to determine the composition of the chips [117]. NPs were first deposited on copper grids covered with a carbon membrane. As shown in Figure 95-a, Ag NPs were visualized using high resolution transmission electron microscope (HR-TEM) to deduce their size, distribution and shape. A statistical analysis performed on the HR-TEM images revealed a particle diameter of 2.3±0.8 nm ensuring a fine control level over the NPs in the N24 chip. The shape factor F $\left(F = \frac{\sqrt{4\pi A}}{P^2}\right.$, where A is the area and P is the perimeter of the NP) was analyzed in order to evaluate the degree of circularity (where F=1 indicates a perfect circle). The analysis yielded a value of 0.8, thus suggesting a 3D spherical shape. These TEM images are of great importance as the properties of the NPs are related to their shape and size. Additionally, the thickness of the Au layer in N24 was measured by atomic force microscopy (AFM), yielding a value of 48± 2 nm. A cross-section of the structure was then obtained using a Focused Ion beam (FIB) and observed by HRTEM. The images reveal amorphous glass and Ag NPs embedded in12 nm Al_2O_3 thick layer with a thin Au layer above. The deposition is shown to be free of

License CC BY-NC-ND 4.0

contamination, with no signs of porosity between the interfaces. This ensures effective LSPR coupling and demonstrates that PLD combined with CG enables the effective and flexible design of complex nanocomposites [117].

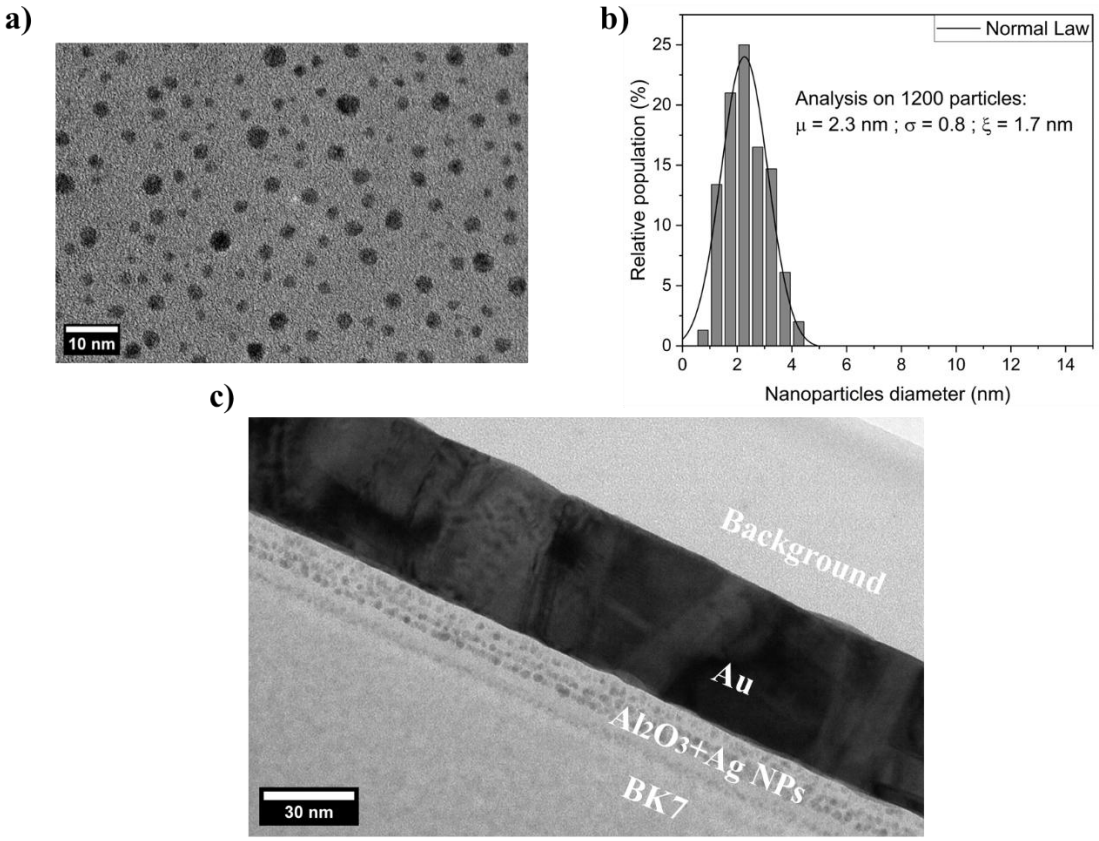


Figure 95 Cross-sectional images of N24 chip taken using HRTEM. a) HR-TEM image of Ag NPs deposited on a TEM grid, 200000× magnification. b) The corresponding statistical analysis over the diameter of the particles. The center of the distribution and mean diameter is μ = 2.3 nm, the standard deviation is σ = 0.8 and the FWHM is ξ = 1.7 nm. c) HR-TEM cross section image presents the architecture of the nanocomposite, 100000× magnification. Images from [117].

III.3.3. Finite-Difference Time-Domain simulations of the N24 SPR chip

After validating the superior sensitivity of the newly fabricated chips containing NPs, it became important to understand the underlying physical mechanism. To gain further insights into the dual effects of Ag NPs and thin Au layers, a simulation method based on Finite-Difference Time-Domain (FDTD) was proposed.

FDTD is a powerful tool for modelling the interaction between light and nano-scale structures. It solves Maxwell's equations directly within a mesh and computes the electric and magnetic fields inside. The advantage of this method is that it allows for the derivation of both spatial and temporal electromagnetic field parameters, which makes tracking phase evolution feasible. The only limitation is the computational power required for large-scale calculations.

License CC BY-NC-ND 4.0

III.3.3.1. Presentation of the FDTD model

The FDTD simulations were performed using Ansys Lumercial computational software. In order to learn how to use the software, we began by simulating a SPR chip based on the simple case of an Ag film on glass, with air as the surrounding medium. Ansys proposed this structure as an example to illustrate SPR modeling (Figure 96).

The boundary conditions along x were defined as PML (perfectly matched layer) so that the scattered light along the structure could be absorbed. Bloch boundary conditions (BBCs) were applied along the y-axis. These conditions are designed for situations in which light is injected at a specific angle. The simulation system typically represents one unit cell, but the actual physical system corresponds to a unit cell repeated infinitely. When light is injected at a certain angle, the electromagnetic field from one period to the other is out of phase. At the boundary of the FDTD, BBC are introduced to copy the field and reinject it on the other side with a phase shift.

The mesh size was set to 0.25 nm, and the meshing around the Ag is 5 nm, which corresponds to one-tenth of the metal's thickness, as specified in the tutorial. The plane wave source was injected 150 nm from the surface. In order to obtain the SPR reflectivity curve, the power of the reflected wave is measured using a power monitor placed behind the source to capture the intensity of the reflected light only, thus avoiding interferences with the incident beam.

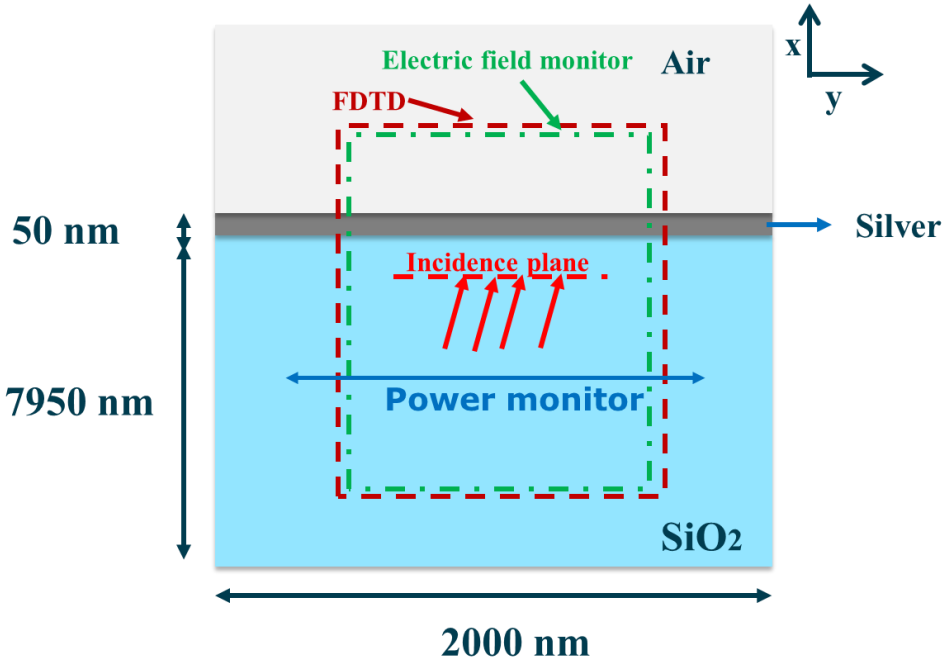


Figure 96 Illustration of the FDTD model for coupling the incident light to SPWs excited between Ag and air.

The incident and reflected beams are usually captured on the same side (both inside prism). Hence, the power monitor is placed at a certain distance from the source. Therefore, we investigated the influence of the position power monitor on the SPR reflection curve. We placed the power monitor at a fixed distance of 750 nm from the glass-Ag interface. Then, we varied the position of the plane of incidence, starting at 200 nm from the Ag-air interface and moving to 400 and 600 nm. Next, we extracted the reflectivity curve by performing an angular sweep around the resonance angle (42-52°) with steps of 0.2° (Figure 97). The position of the source

License CC BY-NC-ND 4.0

was found not to have a significant effect on the reflected wave, as neither the width of the curve nor value of the dip was affected.

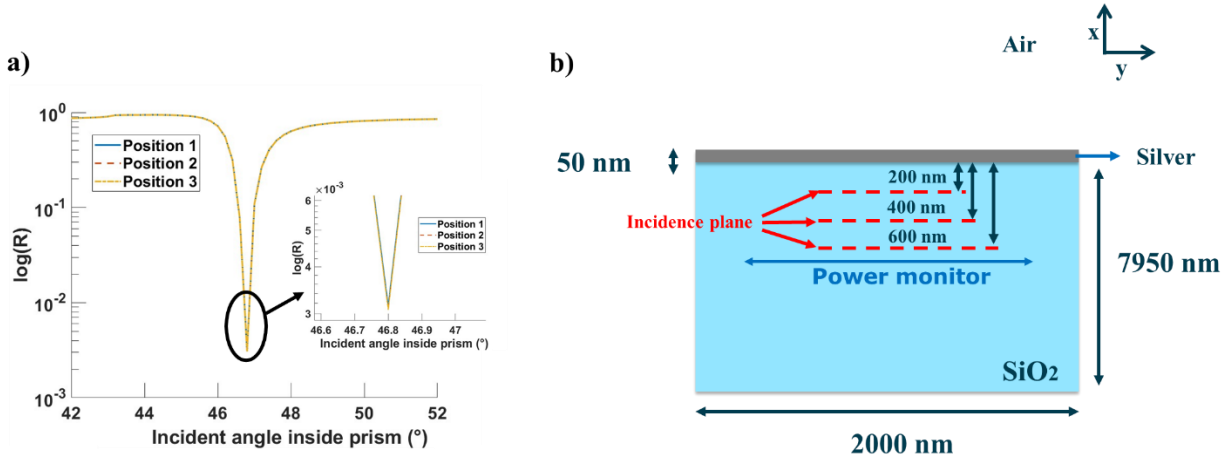


Figure 97 SPR reflection curve obtained by varying the position of the source with respect to the glass-metal boundary. Position 1 at 200 nm, Position 2 at 400 nm and Position 3 at 600 nm from the interface.

Additionally, it is important to note that the source cannot be injected directly at the interface between glass and Ag. Indeed, as illustrated in Figure 98, there is an absence of a reflection dip, which indicates an inability to couple the incident light to SPWs at the Ag-air interface.

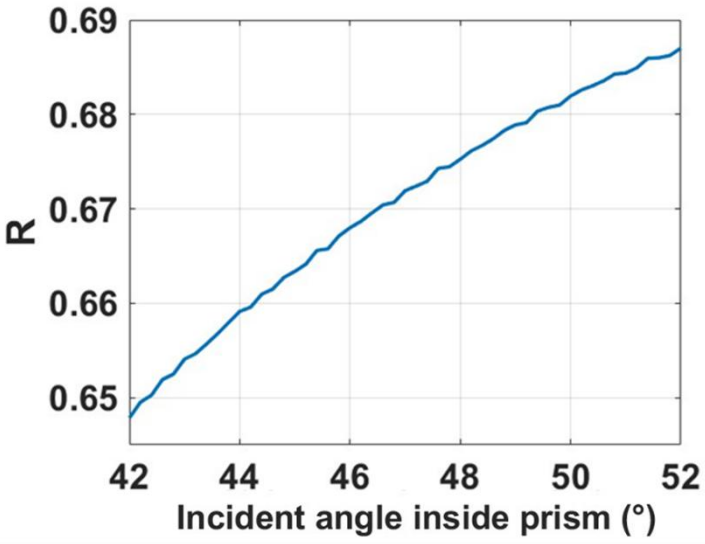


Figure 98 Reflectivity curve of a glass-Ag-air SPR chip computed with FDTD. In this case, the source is positioned at the glass-Ag boundary.

To better understand how the simulation works, we visualized the electric field amplitude and phase of the bare Ag chip using the 2D electric field monitor. Because the incident and reflected beams are measured on the same side, the amplitude and phase of the electric field exhibit interference patterns in the area between the plane of incidence and the prism-metal interface. The results are shown in Figure 99.

License CC BY-NC-ND 4.0

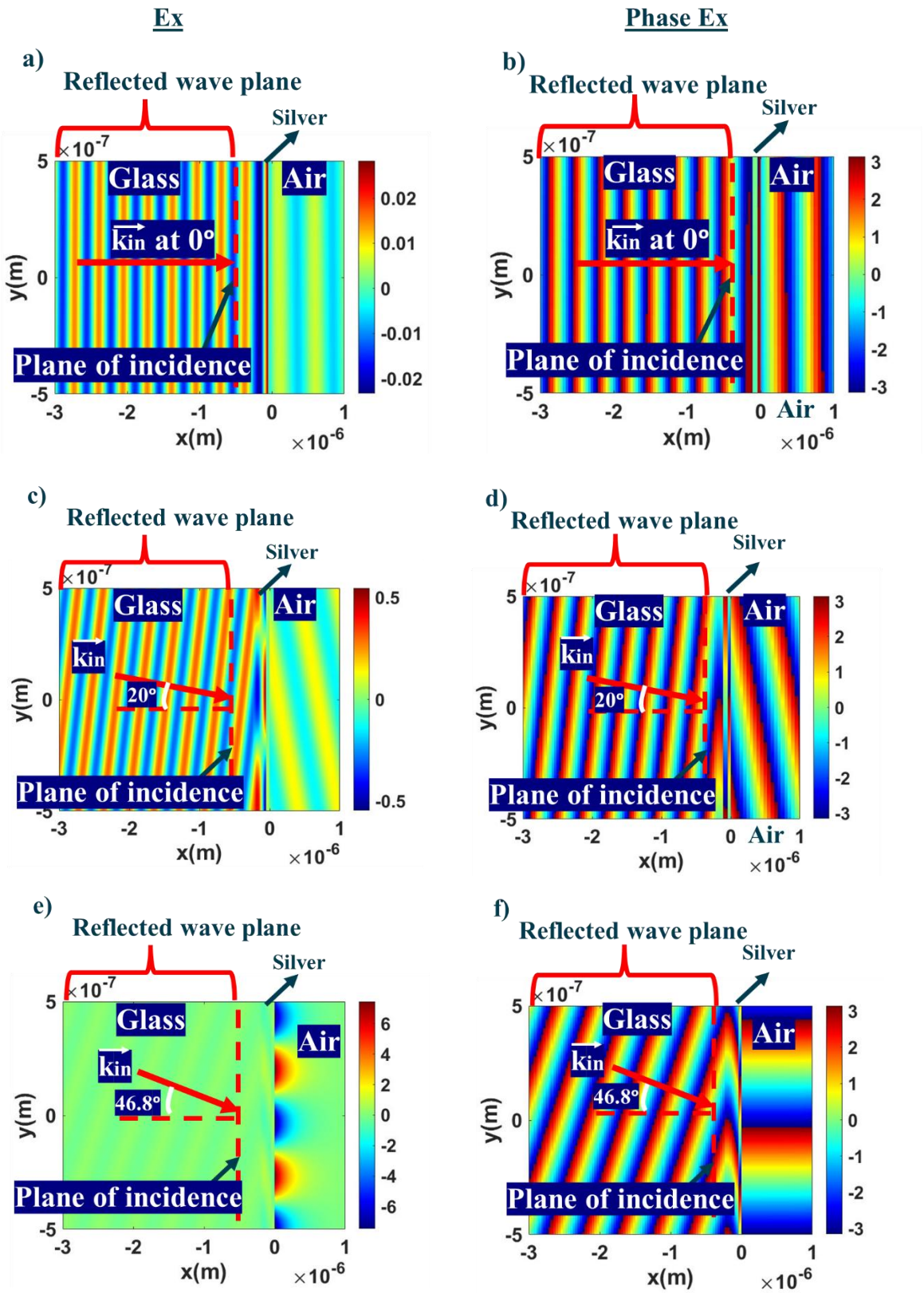


Figure 99 Electric field map, normalized amplitude Re (Ex) and phase Imaginary (Ex), a-b) for normal incidence, c-d) at 20° incidence and e-f) at the SPR resonance angle (46.8°).

License CC BY-NC-ND 4.0

Far from the resonance angle (Figure 99 a-d), we find a case of a simple Fresnel reflection, where light is partially reflected and refracted inside the structure. Figures e-f) represent the SPR case where plasmonic waves are excited at the boundary between Ag and air. We observe light coupling to SPWs, visible as an alternating pattern of dark blue and red in the electric field amplitude. This corresponds to SPWs propagating along the Ag-air interface. Additionally, the electric field amplitude in SPR is greater than in the other two cases (6 for the SPR compared to ~0 for normal incidence). Furthermore, we observe light attenuation by SPWs in the amplitude of the electric field map. In the SPR case, the amplitude of the reflected light's electric field is much smaller than in the normal and 20° incidence cases.

III.3.3.2. Validation of the FDTD simulation model with a commercial SPR chip

The objective of this section is to validate the simulation model with a reference chip, the commercial chip in water. For this purpose, the reflectivity and phase curves obtained with the FDTD, were compared with the TMM.

The commercial chip consists of 0.7 mm BK7 sublayer, 2.5 nm Ti and 50 nm Au. For testing liquid environments, the chip is experimentally coupled with SF11 prism to find the resonance angle at a convenient incident angle (~54°). To optimize the computational time in FDTD simulations and since the BK7 layer is too thick for a fine mesh (of 0.25 nm), the incident light was coupled directly into the BK7 substrate and refracted back to the SF11 prism (Figure 100). Fresnel equations can then be used to calculate the reflection and transmission coefficient at the interface between SF11 and BK7.

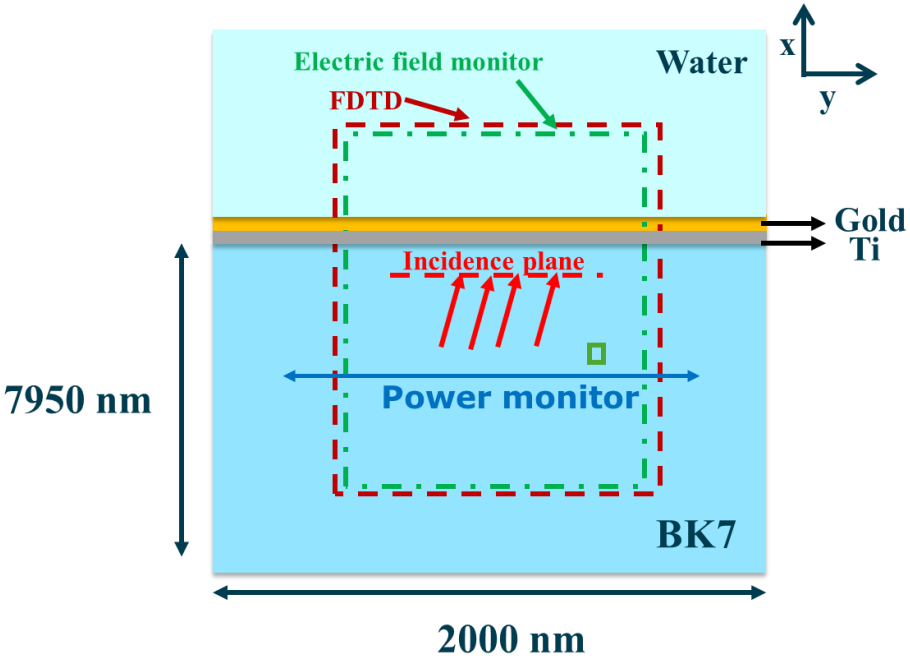


Figure 100 Schematic of the FDTD model used to simulate the commercial chip in water. The green rectangle represents a mesh point that can be used to extract phase data.

Then, the reflectivity curve was obtained by performing an angular sweep of the incident light and measuring the light intensity from the power monitor. In parallel, the phase was obtained by scanning the electric field monitor's and by collecting data at each mesh point. Since the SPWs exponentially decay along the x axis, the phase value was defined by angle (Ex) and

License CC BY-NC-ND 4.0

then extracted from a mesh point positioned on the reflection side (Figure 100). The reflectivity and phase curves are plotted in Figure 101, with the ones calculated by the TMM.

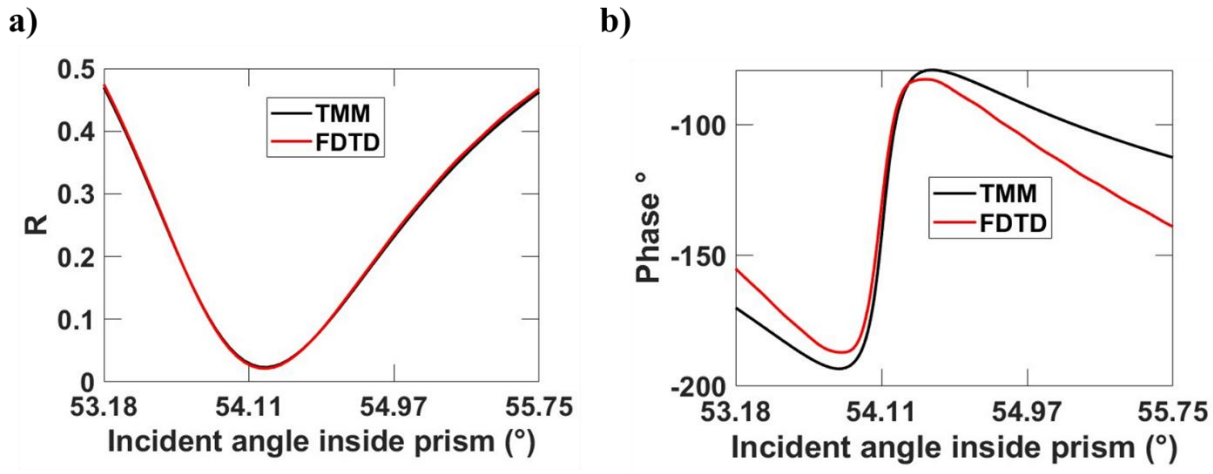


Figure 101 SPR curves for a commercial chip computed by the TMM and by FDTD, a) Reflectivity vs incident angle inside the prism and b) Phase vs incident angle inside the prism.

The reflectivity curve (Figure 101-a) shows a perfect match between the two methods. The resonance angle, reflectivity dip value, and FWHM are all consistent. On the other side, the phase curve reveals slight variations. The phase jump around the resonance angle obtained from the TMM corresponds to 114°, while that computed from FDTD gives 104°. This corresponds to a 9% variation from the TMM. The error difference remains relatively small, validating the use of FDTD model to predict phase changes.

III.3.3.3. FDTD simulation of the N24 SPR chip

Having validated the simulation model, this section aims to simulate the N24 chip to gain further insight into the origin of the enhanced sensitivity observed in experiments. Ag spherical NPs were randomly positioned into the alumina matrix (Figure 102).

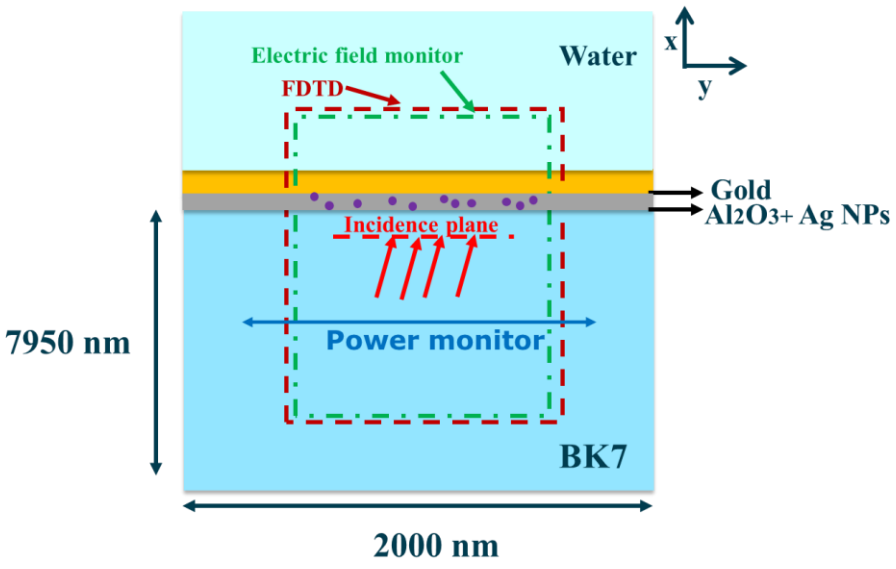


Figure 102 Schematic of the FDTD model used for simulating the N24 sample.

License CC BY-NC-ND 4.0

The NP concentration (f) was defined and the number of NPs required to be added in the alumina matrix was calculated using the following formula:

$$\text{Number of NPs} = \frac{\text{f} \times \text{Volume of alumina}}{\text{Volume of 1 NP}} \quad (46)$$

To prevent particles overlapping, a spatial constraint was applied, ensuring that the distance between neighboring NPs (d) was always larger than twice the NP radius (d>2 x 1.15 nm). The mesh size was set at 0.25 nm, while the mesh size surrounding the metal (alumina matrix+Au) at 2.3 x 10^{-3} nm (corresponding to the diameter of NPs/1000).

To analyze the effect of Ag NPs in an alumina matrix compared to a chip without them, we extract the power map using the 2D electric field monitor (Figure 103). The resonance angle was determined as the angle corresponding to the minimum reflected intensity, as measured by the power monitor.

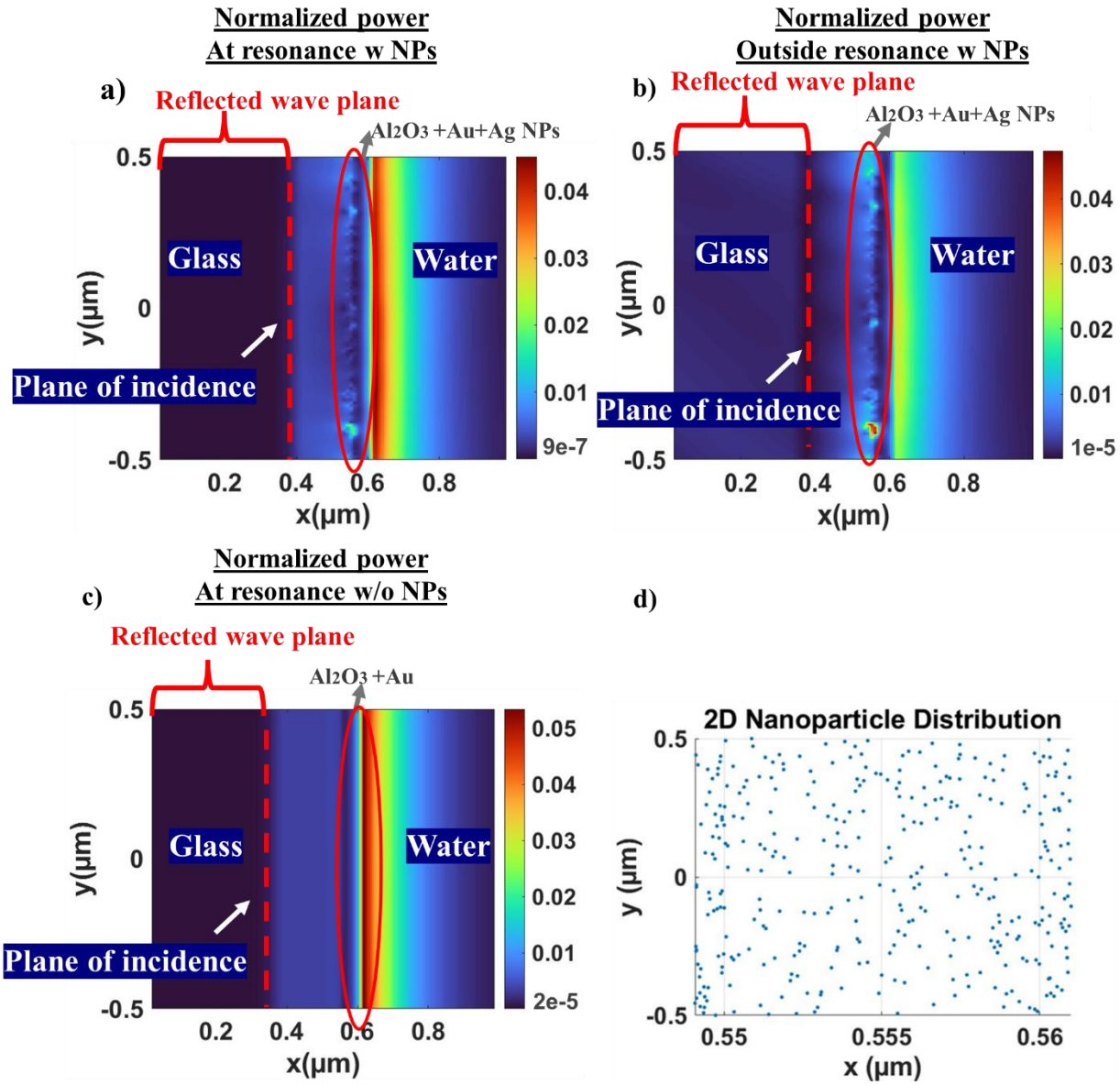


Figure 103 Normalized power map for a chip with NPs, a) at resonance θ=54.09°, b) outside resonance θ=52.93°, c) Without NPs at resonance θ=54.12° and d) represents the 2D distribution of the NPs inside alumina.

License CC BY-NC-ND 4.0

At plasmonic resonance, most of the incident light is coupled with SPWs, with a smaller amount interacting with the NPs (Figure 103-a). Outside of resonance (Figure 103-b), a higher portion of the incident light is interacting with the Ag NPs, and the remainder is being reflected by the chip. Additionally, the introduction of 16% NPs within the alumina reduced the reflectivity by a factor of 10 compared to the chip without NPs (Figure 103-c). The 2D NPs distribution reveals a unform distribution of the NPs with no clustering occurring at a specific location (Figure 103-d).

To better understand the interactions between the incident light and the NPs in N24, our colleagues in IRCER [117] performed transmittance measurements . They deposited 16% Ag NPs within a 12 nm alumina layer on a glass substrate. Broadband light in the ultraviolet and visible spectrum is incident on the chip, and the transmitted intensity is measured as a function of wavelength. The results are shown in Figure 104.

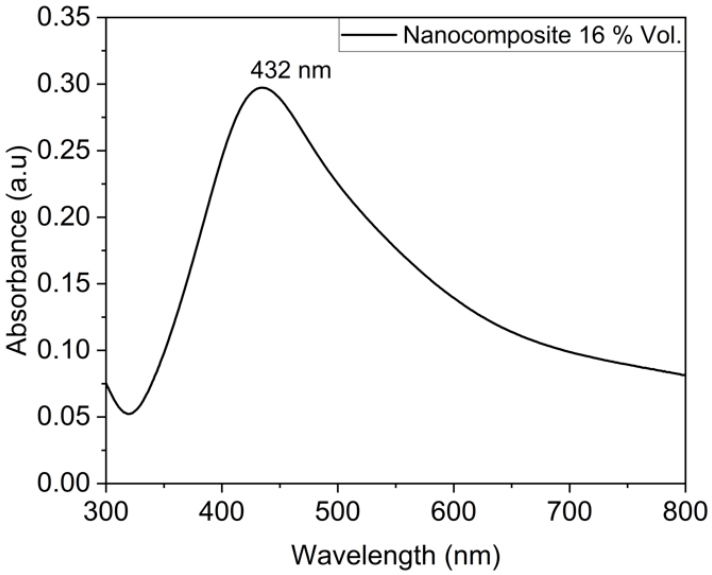


Figure 104 Optical absorption spectrum of N24 (without an Au layer).

The transmittance measurements (Figure 104) revealed an absorption peak at 432 nm corresponding to the LSPR of Ag NPs embedded in alumina. According to Mie theory, LSPR occurs when the $\mathrm{Re}(\varepsilon_i) = -2\varepsilon_m$ [128,129], where ε_i is the permittivity of the NP (for Ag NPs, $\mathrm{Re}(\varepsilon_i)$= -18.281 at 633 nm form the Johnson and Christy model) and ε_m is the permittivity of the matrix (for Al_2O_3 , $\mathrm{Re}(\varepsilon_i)$ = 3.118 at 633 nm). LSPR conditions can hence be satisfied when the wavelength of the incident light is in the blue range (~400 nm) rather than near infrared. These results suggest the absence of strong LSPR resonance modes but rather a weaker coupling of the incident light with NPs leading to the redistribution of the field between the SPR and LSPR modes.

As the GH shift is directly related to phase changes at resonance, phase analysis provides an alternative means of assessing the influence of the NPs in the N24 chip. In this context, the phase was calculated by considering the angle of the Ex-vector as explained in Section III.3.3.2 above. The results are represented in Figure 105 below.

License CC BY-NC-ND 4.0

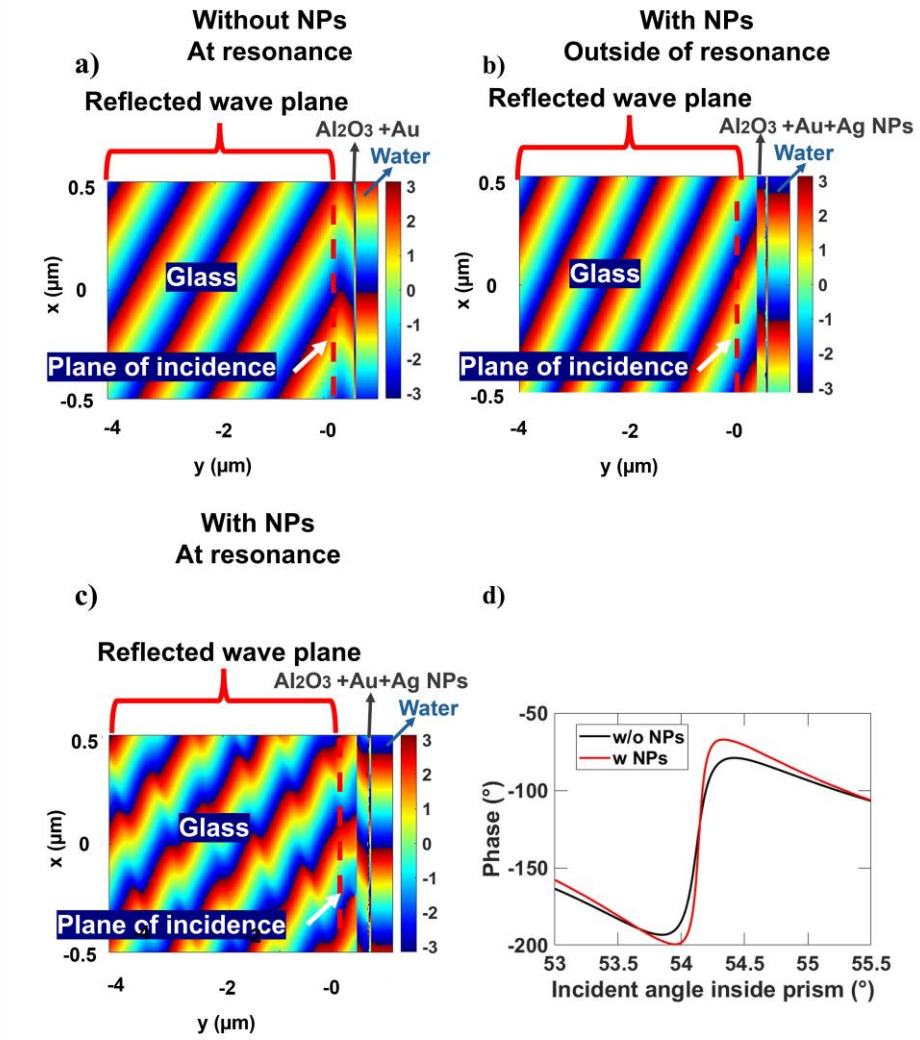


Figure 105 2D phase map of, a) Chip without NPs at resonance, b) Chip with NPs outside of resonance, c) Chip with NPs at resonance, d) phase shift with respect to incident angle at the base of the prism for both chips with and without NPs. The curves were extracted from a mesh point in the reflection region.

The resonance angle was determined for all three cases (Figures 105 a-c) after plotting the FDTD SPR reflectivity curve. It was identified as the angle with minimal reflection. Without NPs (Figure 105-a), the phase presents a normal distribution related to the propagation of the reflected plane wave. When NPs are introduced, far from resonance (Figure 105-b), the phase distribution remains similar to the case without NPs. However, at resonance (Figure 105-c), the phase distribution becomes highly deformed highlighting the impact of NPs. Compared to the reference structure without NPs, the chip with NPs exhibits a steeper phase change (Figure 105-d). The phase shift was computed over an angular increment of 0.01◦ close to the resonance angle for the two chips. The chip containing NPs exhibits a phase shift that is twice higher than that of the chip without NPs. This indicates an increase in phase sensitivity and a larger GH shift in the NP-incorporated chip.

Due to experimental limitations encountered in the course of the thesis (drift problems presented in chapter 2), part of the experiments was performed by our colleagues in Troyes

License CC BY-NC-ND 4.0

using the reference platform. The laser used is operating at 785 nm. Therefore, additional simulations have been carried out at 785 nm. In particular, the impact of the chosen NPs material on the SPR response, were studied by considering Au or Ag NPs embedded in alumina. In both cases (Ag and Au NPs), the NPs distribution remains unchanged, with only the material being altered. The corresponding phase maps are shown in Figure 106.

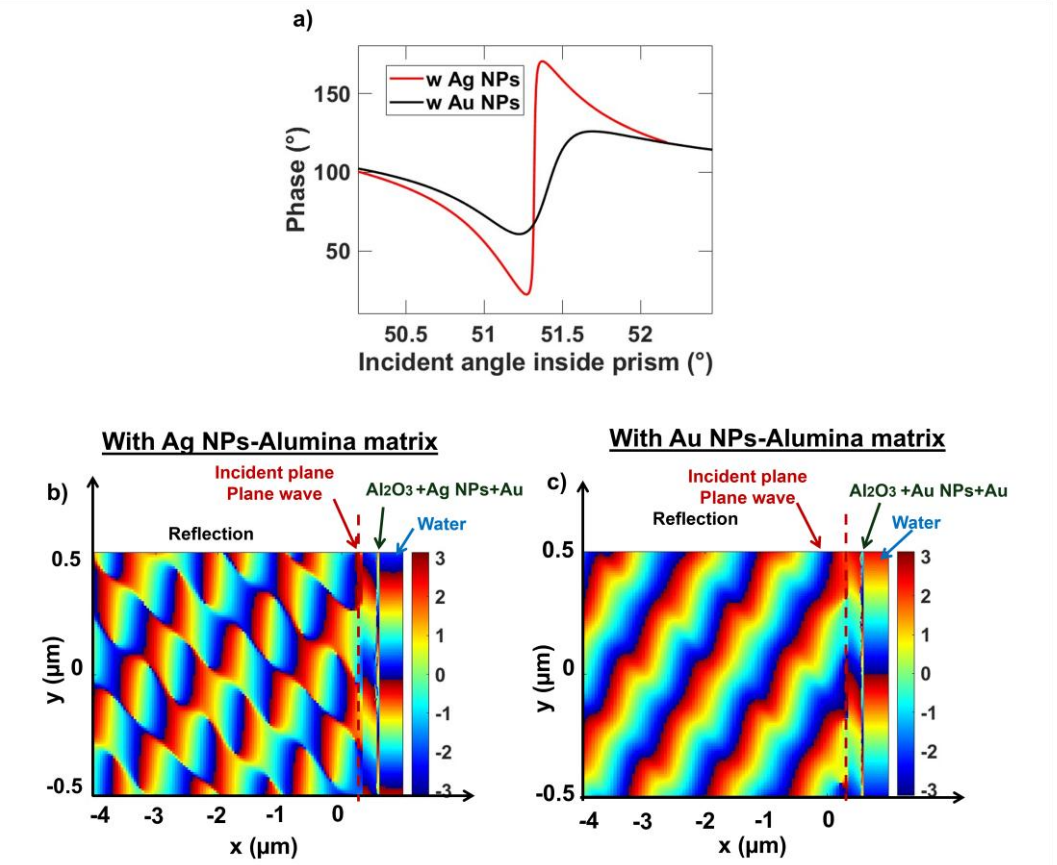


Figure 106 Phase maps of SPR chips with two types of NPs: Ag NPs and Au NPs, both of which are embedded in alumina. (a) Phase vs incident angle incident prism obtained with FDTD for Ag NPs (red) and Ag NPs (black) embedded in Al_2O_3. (b) Phase map at the resonance angle with Ag NPs embedded in a 12 nm alumina. (c) Phase map at the resonance angle with Au NPs embedded in 12 nm alumina.

The SPR phase curves (Figure 106-a) reveal a steeper phase change with Ag NPs instead of Au NPs. The chip with Ag NPs exhibited a phase variation 12 times higher than that of the chip with Au NPs. A comparison of these phase maps (Figures b and c) shows a stronger modulation of the phase with Ag NPs. This result highlights the importance of choosing the NPs material to optimize the coupling of incident light to SPWs.

Ag's higher performance compared to Au is usually linked to the ratio of the real part of the permittivity to the imaginary part. For Ag, this ratio is 79, compared to 16 for Au (at 785 nm). A higher ratio is usually associated with deeper reflection and a narrower FWHM of the reflectivity curve, highlighting the higher sensitivity of the structure with Ag NPs.

Additionally, the effect of the embedding material on the SPR response was simulated to validate the choice of alumina as the dielectric host for Ag NPs. The corresponding phase maps are shown in Figure 107.

License CC BY-NC-ND 4.0

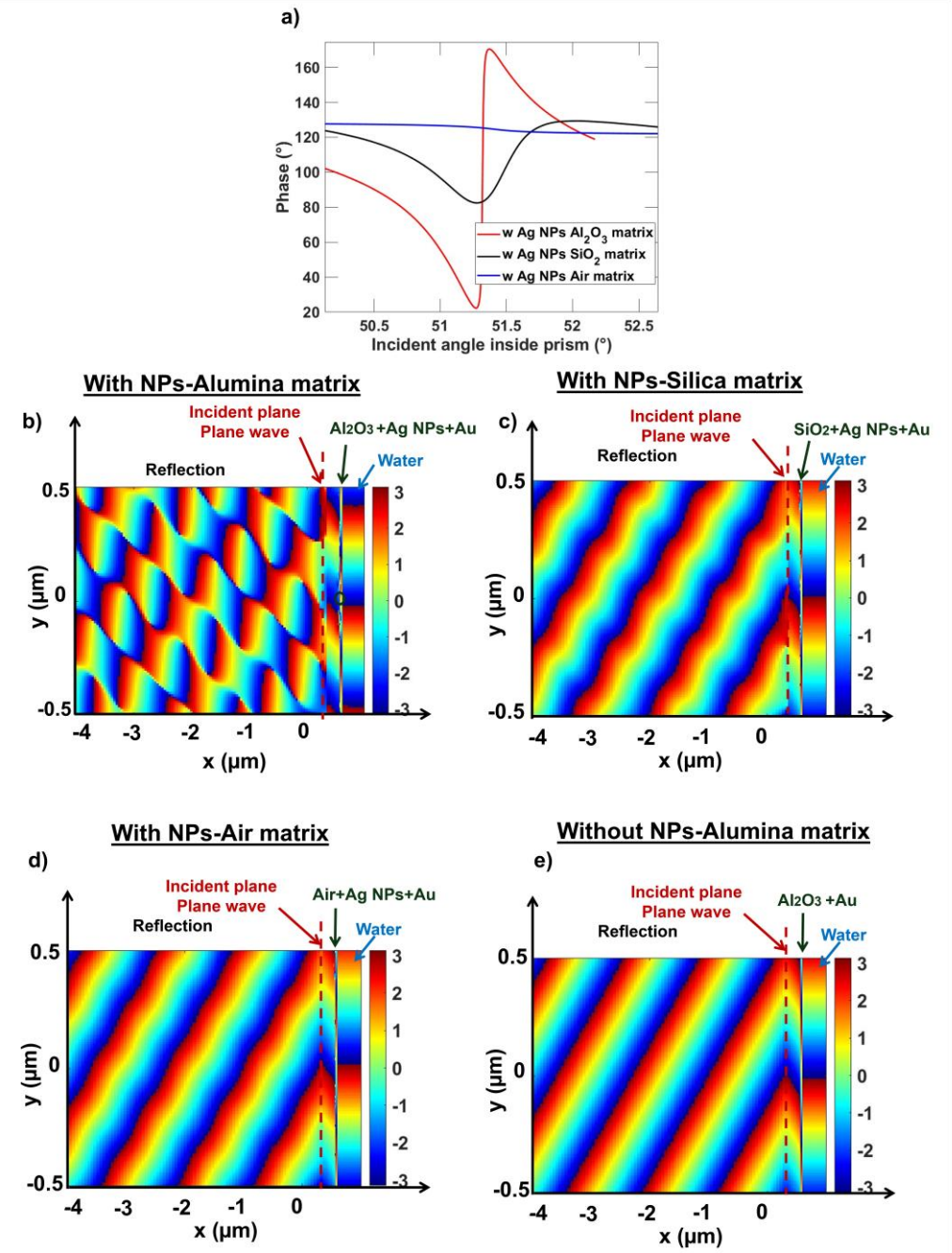


Figure 107 Comparison of the effects of different dielectric matrixes with Ag NPs, a) Phase vs incident angle incident prism obtained with FDTD for Alumina matrix (red), silica matrix (black) and Air matrix (blue). b) Phase map at the resonance angle with Ag NPs embedded in a 12 nm alumina. (c) Phase map at the resonance angle with Ag NPs embedded in 12 nm Silica matrix. (d) Phase map at the resonance angle with Ag NPs embedded in 12 nm Air matrix.

The SPR phase curves (Figure 107-a) show a steeper and greater phase change for Ag NPs in alumina matrix rather than in silica or in air matrix. The chip with an alumina matrix exhibited a phase variation 12 times higher than that of the chip with a silica matrix.

According to Mie theory [128,129], the LSPR resonance of NPs embedded in a host matrix is achieved when $\mathrm{Re}(\varepsilon_i) = -2\varepsilon_m$ is satisfied ($\mathrm{Re}(\varepsilon_i)$=-29.7897 for Ag NPs, $\mathrm{Re}(\varepsilon_m)$ = 3.1184 for

License CC BY-NC-ND 4.0

Al_2O_3, $\mathrm{Re}(\varepsilon_m)$ = 2.1130 for SiO_2 and $\mathrm{Re}(\varepsilon_m)$ = 1 for air). The mismatch between $\mathrm{Re}(\varepsilon_i)$ and $-2\varepsilon_m$ is the lowest for alumina, followed by silica than air. Consequently, the interaction between the incident light and NPs is the highest when NPs are embedded in a high refractive material. In this case, a higher fraction of the incident field interacts with the NPs and the rest is coupled with SPWs at the Au-water interface.

To visualize the effect of the embedding materials, phase maps were plotted for each material based on the resonance angle associated with it (Figures b-c). The results show higher modulation of the phase map with the alumina matrix. Conversely, the phase map perturbations are smallest with silica and air, highlighting the limited interactions between the incident field and NPs.

These results emphasize the importance of selecting the host material to optimize the sensitivity. The use of alumina led to the highest phase modulation, deeper reflectivity, and ultimately higher GH sensitivity.

III.4. Conclusion and perspectives

This chapter begins by reviewing the physical phenomena that occur inside an SPR chip. The reflectivity dip at resonance can be lowered by balancing radiative and intrinsic losses. This can be accomplished through the re-engineering of the multilayer system's structure (underlayer, intermediate layer, and overlayer). A lower reflection coefficient is related to a steeper phase change and higher GH shift.

For designing SPR chips, the well-known TMM was employed to simulate innovative SPR chips: the integration of a thin VO_2 film below Au, and the use of a nanocomposite containing Ag NPs embedded in alumina, with a thin Au film above.

Firstly, the analysis of the SPR chip incorporating VO_2 revealed the critical importance of the material's optical properties and the need to control its thickness at the nanometer scale. Due to the high real and imaginary parts of its permittivity, even a thin VO_2 film will modify the coupling conditions of SPWs and therefore influence the depth of the reflectivity minimum. VO_2 modifies the accumulated phase of light inside the SPR structure to promote destructive interferences and amplify the fraction of light transmitted between the prism and VO_2 towards Au. An optimized chip was obtained by introducing a 7 nm VO_2 layer below 47 nm Au with an enhancement of GH sensitivity with a factor of two in comparison with the bare Au. The new chip was able to detect BSA molecules with a LOD of 10 fM with a LOD of 4.6×10^{-6} RIU.

By taking into consideration the advantages of plasmonic materials like Au and Ag, an Ag NP/Al_2O_3/Au chip was designed and fabricated by our colleagues at IRCER, using an original system combining PLD with FCG. Preliminary simulations based on the Maxwell-Garnett theory, revealed maximum sensitivity when 1 nm NPs are incorporated into 12 nm alumina with a 49 nm Au above. The simulations additionally emphasized the influence of radius and concentration of the NPs, thickness of alumina and Au on the SPR reflectivity curves. Experimental testing showed a sensitivity of 2×10^7 µm/RIU and a LOD of 10^{-7} RIU when testing the N24 chip consisting of 2.3 ± 0.8 nm Ag NPs incorporated inside a transparent 12 nm alumina layer with a 48 ± 2 nm Au layer above. FDTD simulations highlighted the role of NPs in disrupting the phase map of the reflected wave and improving phase singularity at resonance, which leads to improved GH sensitivity. Additionally, the choice of metallic NP (Au or Ag) and embedding material type (alumina, silica or air) was validated through 2D simulations, which highlighted that Ag NPs embedded in alumina were the most effective at

License CC BY-NC-ND 4.0

improving sensitivity. Finally, FDTD simulations with different embedding materials (Al_2O_3, SiO_2 and air) highlighted the importance of choosing the ideal material to enhance the LSPR effect of the NPs and optimize sensitivity. These results, which have been validated through numerous calibration tests, will enable us to use the N24 chip to detect EVs in the following chapter.

License CC BY-NC-ND 4.0

Chapter IV. Analysis of the GH Shift in SPR under rotating incident polarization

IV.1. Introduction and context

In the initial stage of this thesis, we measured the GH shift at the TM polarization and subtracted it from the TE. TM was identified as the angle of polarization that produced the minimum reflected power at resonance. This angle was determined by rotating the waveplate in 1° increments and recording the intensity via a power meter at each step (Figure 108). The TE polarization was then deduced by setting:

$$Angle_{TE} = Angle_{TM} + 45° \quad (47)$$

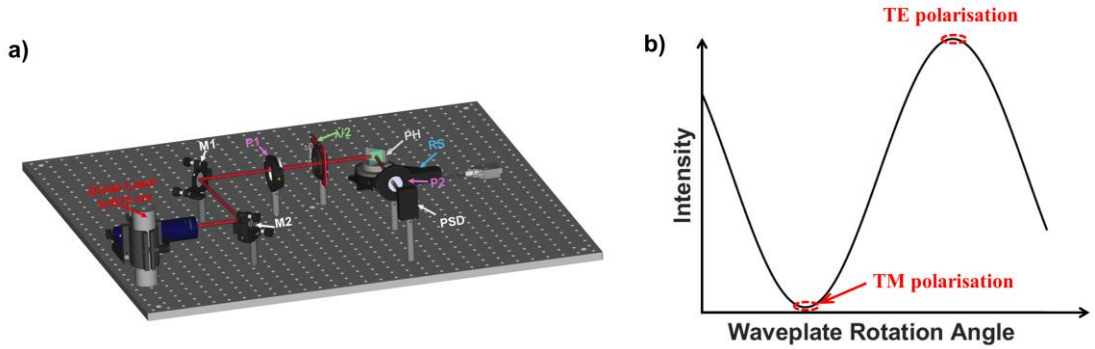


Figure 108 Identification of TM polarization using a waveplate. a) Illustration of the setup consisting of a diode laser at 633 nm, mirrors (M1 and M2), polarization filters 1 and 2 (P1 and P2), half-waveplate (λ/2) on a rotational mount, rotational stage (RS), prism holder (PH) and PSD. b) Reflected intensity vs polarization angle of the waveplate. TM is identified as the polarization angle with the minimal reflected power at resonance.

To eliminate the uncertainty regarding the orientation of the waveplate (TM / TE polarization), and to remove the need to determine the TM polarization angle prior to each experiment, a new interrogation method involving a continuous and rapid rotation of the waveplate was proposed. The advantage of this approach is the ability to access the GH shift at several polarization angles in a short timescale. On the other hand, a cheap DC motor can be obtained, making this approach inexpensive and simple to implement.

By analogy, the analysis of the polarization state of light is widely used in ellipsometry as a way of determining the refractive index and thickness of unknown materials [130]. Ellipsometry is also a method used in SPR for retrieving the phase shift at the resonance [131]. Likewise, in our prototype, the GH shift would be measured as a function of the polarization angle through a continuous rotation of the waveplate.

This chapter begins by introducing the concept of ellipsometry, its associated theory and applications in SPR. Then, we present a simulation model based on Jones matrices to evaluate this new interrogation method. Finally, we will test this new method on the commercial and N24 chips using diluted glycerin solutions.

License CC BY-NC-ND 4.0

IV.2. Fundamentals of ellipsometry

Ellipsometry is a very powerful, non-invasive, label-free measurement technique often used to estimate the complex refractive index and thickness of an unknown material by analyzing the polarization state of light upon reflection or transmission [132]. When a linearly polarized light (oriented at 45° with respect to TM / TE) interacts with a multilayer system, the TM component acquires a phase and amplitude shift with respect to the TE component causing the reflected light to be elliptically polarized (Figure 109) [133].

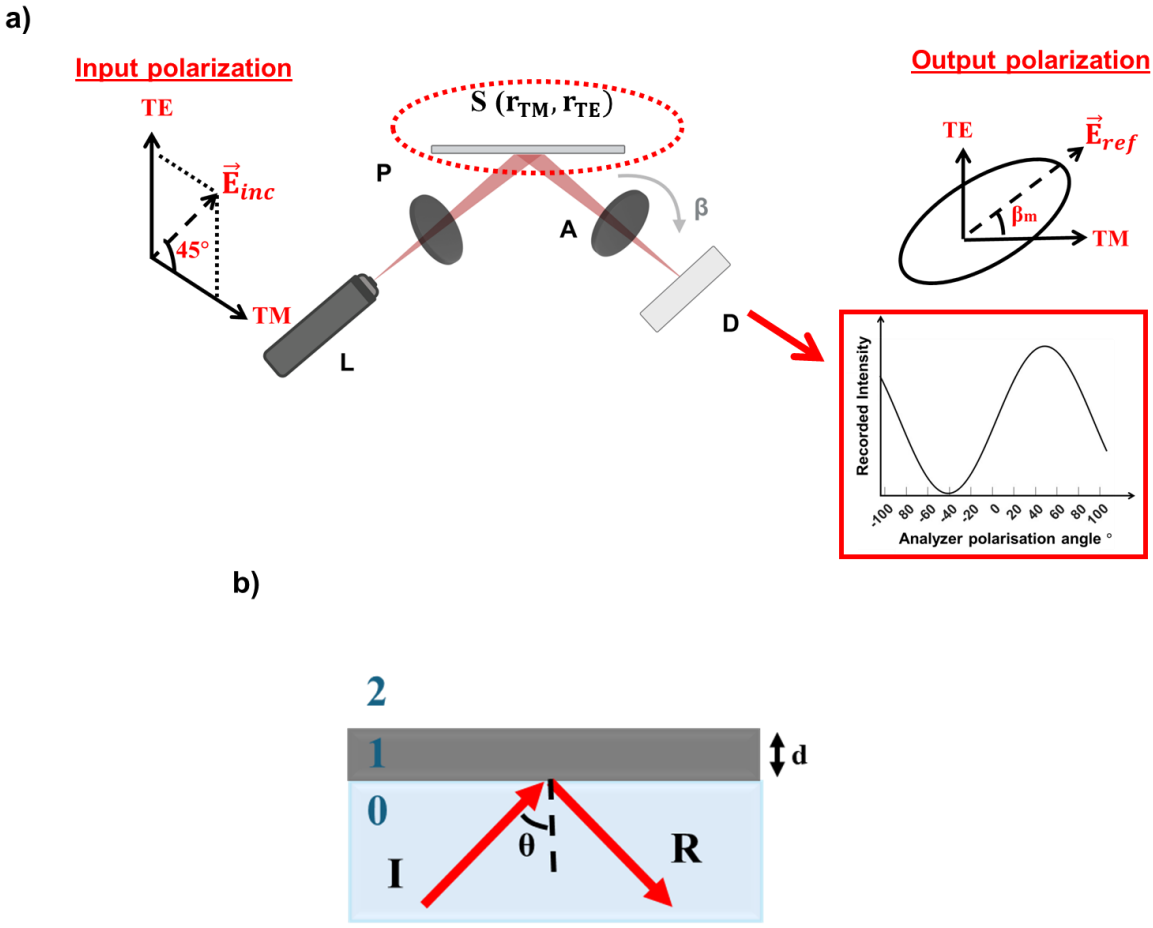


Figure 109 Schematic illustration of the principles of ellipsometry measurements showing (a) a laser (L), polarization filter (P), sample (S), analyzer (or A, rotating polarization filter) and detector (D). β is the rotation angle of the analyzer and β_m is the azimuth of the polarization ellipse of the reflected beam. r_{TM} and r_{TE} are the Fresnel reflection coefficients for TM and TE polarization. b) Schematic illustration of a sample three-layers structure tested in ellipsometry where I and R respectively represent the incident and reflected lights, θ the angle of incidence and d the thickness of layer 1.

The experimental setup illustrated in Figure 109 is typically composed of:

- A light source,
- A polarization filter (P) oriented at 45° [5, 6] producing a linear polarization where the TM and TE components are equal to optimize the sensitivity of the setup,

License CC BY-NC-ND 4.0

- Sample material (S) with unknown properties: thickness (d) and refractive index ($n=n_r+in_i$ where n_r and n_i are respectively the real and imaginary components of the refractive index),
- A rotating polarization filter (analyzer A) to scan the polarization ellipse of the reflected light,
- A light detector (photodetector or CCD camera) [132].

In order to describe the modification of the polarization state of light upon reflection, the electric field components are expressed in complex notation. This representation takes into account both the amplitude and phase of the TM and TE components.

We consider a monochromatic incident wave with a linear polarization that can be decomposed into two orthogonal components TM and TE. The total electric field can be written as the sum of these two components. After reflecting from a surface, each component is modified by a complex reflection coefficient (r_{TM} or r_{TE}), introducing a modification of amplitude and phase.

$$E_{TM}^{inc}(t) = E_{0TM}e^{i\omega t} \tag{48}$$

$$E_{TE}^{inc}(t) = E_{0TE}e^{i\omega t} \tag{49}$$

$$E_{TM}^{ref}(t) = r_{TM}E_{0TM}e^{i\omega t} \tag{50}$$

$$E_{TE}^{ref}(t) = r_{TE}E_{0TE}e^{i\omega t} \tag{51}$$

$$r_{TM} = |r_{TM}|e^{i\Delta_{TM}} \tag{52}$$

$$r_{TE} = |r_{TE}|e^{i\Delta_{TE}} \tag{53}$$

$$E^{ref}(t) = E_{TM}^{ref}(t) + E_{TE}^{ref}(t) = e^{i(\omega t+\Delta_{TE})}\begin{pmatrix} |r_{TM}|E_{0TM}e^{i(\Delta_{TM}-\Delta_{TE})} \\ |r_{TE}|E_{0TE} \end{pmatrix} \tag{54}$$

Where E_{TM}^{inc} and E_{TE}^{inc} are the incident electric field components at respectively TM and TE polarizations, E_{0TM} and E_{0TE} are the amplitudes of the electric field, ω is the angular frequency, t the time, E_{TM}^{ref} and E_{TE}^{ref} are the reflected electric fields, $|r_{TM}|$ and $|r_{TE}|$ are the amplitudes of the reflection coefficients, Δ_{TM} and Δ_{TE} are the phase values of the reflected wave.

Equations 48-54 reveal that the polarization state of the reflected light depends on $|r_{TM}|$, $|r_{TE}|$, Δ_{TM} and Δ_{TE}:

1. If Δ_{TM}-$\Delta_{TE} = 0$ or π, the resulting polarization is linear,
2. If Δ_{TM}-$\Delta_{TE} = \pm\frac{\pi}{2}$ and $|r_{TM}|E_{0TM}=|r_{TE}|E_{0TE}$, the resulting polarization is circular,
3. Otherwise, if $\Delta_{TM} \neq \Delta_{TE}$ and $|r_{TM}|E_{0TM} \neq |r_{TE}|E_{0TE}$, the resulting polarization is elliptical.

The complex refractive index and thickness of an unknown material can be determined by comparing the complex reflection coefficients obtained experimentally and theoretically using

License CC BY-NC-ND 4.0

the TMM model. In practice, the reflection coefficient depends on the thickness and refractive indices of the multilayer system.

To explain the principles of ellipsometry, we consider a three layers system (Figure 109-b). By analogy, in ellipsometry layer 1 is considered to be the unknown material, whereas in SPR, layer 1 is the metallic layer. To determine the complex reflection coefficients experimentally (Equations 52 and 53), we need first to extract the intensity profile of the reflected beam. This is obtained as described below.

After reflecting from the material, the beam passes through A. The transmitted electric field is written as [131]:

$$T = r_{TM} \cos\beta + r_{TE} \sin\beta \tag{55}$$

The intensity measured by the photodetector (defined by I = T T*) corresponds to:

$$I = |r_{TM}|^2 \cos^2\beta + |r_{TE}|^2 \sin^2\beta + 2|r_{TM}||r_{TE}| \cos\beta \sin\beta \cos\Delta \tag{56}$$

With $\Delta = \Delta_{TM} - \Delta_{TE}$, the phase difference between TM and TE.

From Equation 56, it can be observed that the reflected intensity measured by the detector depends on many factors: the amplitudes of the reflection coefficients of the sample material ($|r_{TM}|$ and $|r_{TE}|$), the rotation angle (β) of A and the phase difference between TM and TE (Δ). The intensity profile versus the polarization angle of the analyzer is represented in Figure 110.

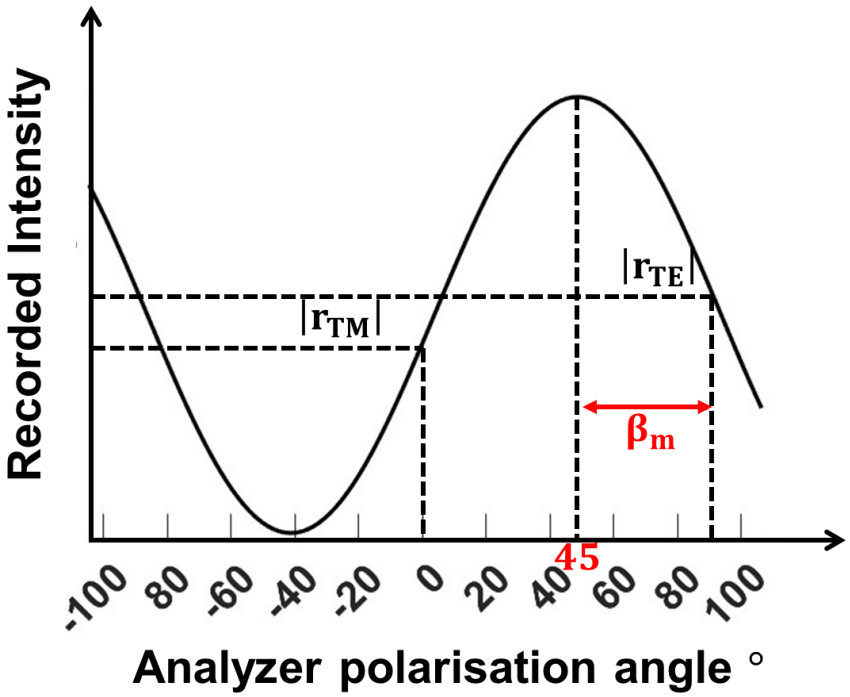


Figure 110: Typical intensity vs polarization angle obtained in ellipsometry. $|r_{TM}|$ and $|r_{TE}|$ respectively represent the amplitudes of measured at TM (0°) and TE (90°) polarizations and β_m represents the azimuth of the polarization ellipse defined as the analyzer angle at which the detected intensity is maximal.

License CC BY-NC-ND 4.0

$|r_{TM}|$ and $|r_{TE}|$ are obtained from the intensity profile of the reflected beam. They refer to the intensity values measured at TM and TE polarizations where the polarization filter angle is 0^o for TM and 90^o for TE (Figure 110).

We cannot determine the phase difference directly from the intensity profile but rather the azimuth of the polarization ellipse β_m. β_m is defined as the angle between the TM polarization direction and the major axis of the ellipse. The major axis corresponds to the polarization angle where the intensity of the reflected light is maximum (extrema of the intensity curve) [130].

To find the analytical expression of β_m, we set the derivative of the intensity with respect to the polarization angle to 0 (dI/dβ=0) [131]:

$$\tan 2\beta_m = \frac{2|r_{TM}||r_{TE}|.\cos\Delta}{(|r_{TM}|^2 - |r_{TE}|^2)} \tag{57}$$

We can now determine the phase expression from Equation 57:

$$\Delta = \cos^{-1}\left(\frac{(|r_{TM}|^2 - |r_{TE}|^2)\tan 2\beta_m}{2|r_{TM}||r_{TE}|}\right) \tag{58}$$

Experiments cannot directly provide Δ_{TM} Δ_{TE} individually but rather the phase difference Δ (Equation 58). Additionally, the amplitude reflection coefficients $|r_{TM}|$ and $|r_{TE}|$ are sensitive to fluctuations in the laser intensity. We therefore define a complex ellipsometric ratio ρ_{exp} (Equation 59):

$$\rho_{exp} = \tan\psi_{exp} e^{i\Delta_{exp}} = \frac{r_{TM,exp}}{r_{TE,exp}} \tag{59}$$

$$\psi = \frac{|r_{TM}|}{|r_{TE}|} \tag{60}$$

ψ take into consideration the amplitude ratio and make the experiments more robust and insensitive to laser variations.

In parallel, we need to determine a theoretical ellipsometric ratio ρ_{theo} . The complex reflection coefficients can also be obtained theoretically through the TMM model for a three-layers system (Figure 109-b):

$$r = \frac{r_{12} + r_{23}e^{2ikd}}{1 + r_{12}r_{23}e^{2ikd}} \tag{61}$$

$$k = \frac{2\pi}{\lambda}\sqrt{n_1^2 - n_0^2\ \sin^2\theta} \tag{62}$$

$$\rho_{theo} = \frac{r_{TM}}{r_{TE}} \tag{63}$$

License CC BY-NC-ND 4.0

Where:

- r_{12}: Fresnel reflection coefficient at the interface of layer 1-2,
- r_{23}: Fresnel reflection coefficient at the interface of layer 2-3,
- λ: Wavelength of the incident light,
- n_1: refractive index of layer 1 (unknown),
- n_0: refractive index of layer 0,

.

Now we define an error function f_{error} to determine the refractive index and thickness from the experimental and theoretical ellipsometric ratios [136]:

$$f_{error} = \left[\mathrm{Re}(\rho_{exp}) - \mathrm{Re}(\rho_{theo})\right]^2 + \left[\mathrm{Imag}(\rho_{exp}) - \mathrm{Imag}(\rho_{theo})\right]^2 \quad (64)$$

The main advantage of ellipsometry lies in its high sensitivity: in the order of sub-nanometer in terms of thickness [137] and a precision in the order of 10^{-3}-10^{-4} RIU [134,135,138–140]. Many materials have been characterized by ellipsometry, including : phase change materials such as VO_2 films (Chapter 3, [141]), 2d materials (graphene and WSe2) [140], liquid solutions (deionized water, refractive index matching oils, ethanol) [139], organic solvents: (isopropyl acetate, dimethyl sulfoxide, P-Xylene, and ethyl acetate) [138], semiconductors (Silicon [142], GaN [143], InN [143]) and metallic NPs (Au [144], Ag [145], gallium [146]). Ellipsometry has been additionally used for biosensing applications mainly for immunosensing of immunoglobulin G proteins with a LOD of 15 ng/mL [132] as well as for determining the concentration of ovalbumine solutions [139].

Therefore, it can be concluded that ellipsometry offers a way to indirectly determine the phase value from the measured intensity [147]. For this reason, ellipsometry has mainly been applied to metallic films in SPR as a method for measuring the phase with simpler detection benches compared to optical setups based on bulk interferometers and optical heterodyne setups. Using commercial ellipsometers with SPR Au chips, SPR-assisted ellipsometry (SPRE) has demonstrated high sensitivity for biosensing and chemical applications. The reported LODs are 3 pM for BSA proteins [148], 1 nM for SARS-CoV-2 RdRp–Hel oligonucleotide sequences [149], 0.8 nM for brevetoxin [150] and 41 nM for mercury ions [151].

In this context, the high sensitivity of phase in SPR, extracted through ellipsometric measurements, has led to the development of different approaches to further improve performance. Particularly, the GH shift which is related to the first order derivative of the phase constitutes an alternative approach to measure and optimize phase sensitivity. In our prototype, the continuous rotation of the waveplate enables us to access GH values at intermediate polarization states. By analogy to the basic SPR ellipsometry setup, our prototype could also provide access to the phase value. However, this potential is not directly demonstrated in our work.

IV.3. Theoretical modelling of the prototype using Jones formalism

To gain further insight into the operation of the prototype, a theoretical model based on Jones calculus was implemented [130]. In this regard, the electric field of the laser beam can be represented by a Jones vector, while each optical element corresponds to a 2D Jones matrix (Figure 111). The interaction of the laser beam with the optical setup can be modelled by

License CC BY-NC-ND 4.0

multiplying the Jones matrices for each optical element by the incident beam. This approach enables the estimation of the reflected intensity, polarization state, and phase difference before the detector, as a function of the incident polarization and the refractive index of the surrounding medium. It is important to note that the angle of P2 is oriented close to TM direction to attenuate the TE beam, but not to extract the phase related data.

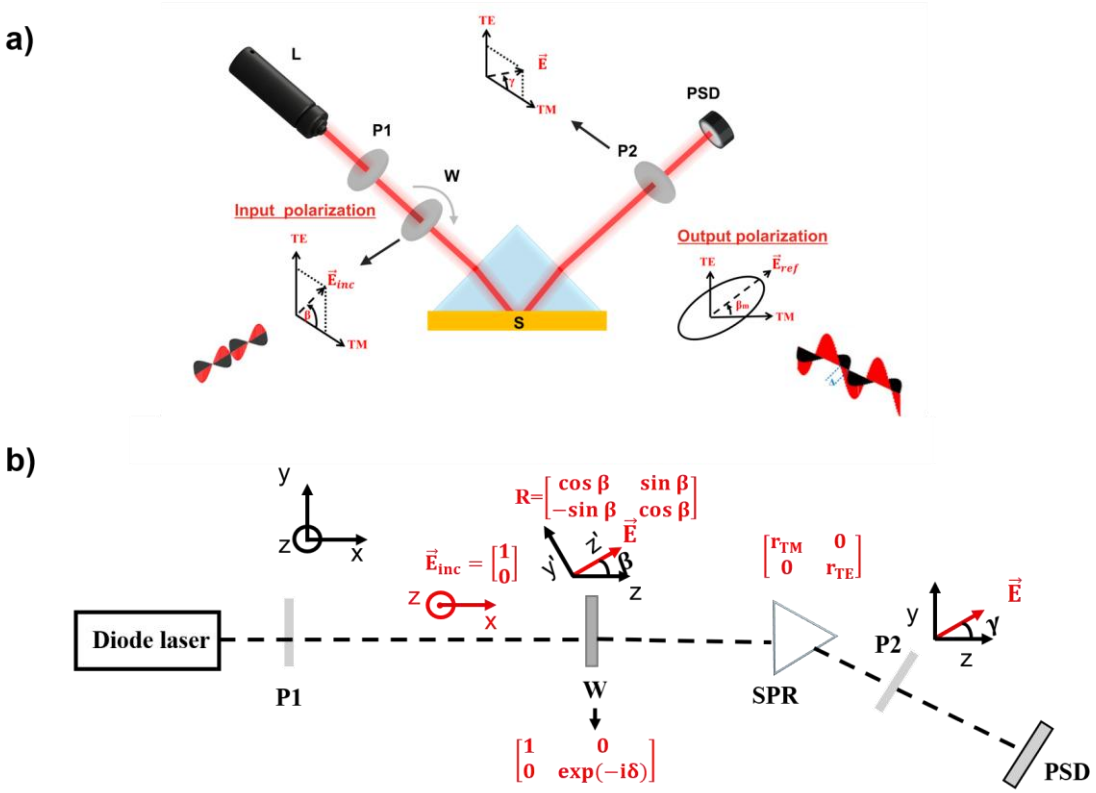


Figure 111 a) Representation of the prototype with a rotating waveplate showing a laser (L), polarization filters 1 and 2 (P1 and P2), rotating waveplate (W), sample (S), and PSD. (b) Representation of the prototype with Jones matrices. In this configuration, the z axis represents the TM polarization and y the TE polarization.

The optical elements in the setup (Figure 111) are each represented by a Jones matrix:

- $E_{inc} = \begin{bmatrix} 1 \\ 0 \end{bmatrix}$: the incident electric field after P1 (assumed to be TM polarized).
- β: rotation angle of the waveplate with respect to the z axis of the system (the z axis is assumed to be the axis of the TM polarization directly after the laser).
- γ: the angle of P2 with respect to the original coordinate system of the laser (y-z axis).
- $R(\theta) = \begin{bmatrix} \cos(\theta) & \sin(\theta) \\ -\sin(\theta) & \cos(\theta) \end{bmatrix}$: The waveplate matrix W is defined in its own axes (fast and slow axes, waveplate frame). When the waveplate is rotated by β, the incident electric field is rotated in the waveplate frame using R(β). After applying W, the electric field is rotated back to the original frame using R(-β). The overall transformation is $R(-\beta)WR(\beta)$.
- $W = \begin{bmatrix} 1 & 0 \\ 0 & \exp(-i\delta) \end{bmatrix}$: matrix of the waveplate where δ is the waveplate retardance (δ=π for a half-waveplate).

License CC BY-NC-ND 4.0

- $S=\begin{bmatrix} r_{TM} & 0 \\ 0 & r_{TE} \end{bmatrix}$: corresponds to the matrix of light reflection after the sample where r_{TM} and r_{TE} as calculated by the TMM at resonance.

The electric field before P2 can be expressed by (Figure 111):

$$E_{ref}(\beta) = SR(-\beta)WR(\beta)E_{inc} \tag{65}$$

As a result:

$$E_{ref}(\beta) = \begin{bmatrix} r_{TM}\cos(2\beta) \\ r_{TE}\sin(2\beta) \end{bmatrix} E_{inc} \tag{66}$$

Upon reaching P2, the transmitted electric light (T) can be expressed by [131]:

$$T=r_{TM}\cos(2\beta)\cos(\gamma) + r_{TE}\sin(2\beta)\sin(\gamma) \tag{67}$$

The intensity (I=TT*, where T* is the conjugate of T) is then defined by:

$$I = |r_{TM}|^2\cos^2\gamma\cos^2 2\beta + |r_{TE}|^2\sin^2\gamma\sin^2 2\beta + 2|r_{TM}||r_{TE}|\cos 2\beta\sin 2\beta\cos\gamma\sin\gamma\cos(\Delta_{TM}-\Delta_{TE}) \tag{68}$$

From Equation 68 it is shown that the intensity profile depends on the amplitudes of the TM and TE lights ($|r_{TM}|$ and $|r_{TE}|$ respectively), the angle of P2 (γ) and the phase difference $\Delta_{TM} - \Delta_{TE}$. By analogy from ellipsometry theory, the phase difference $\Delta = \Delta_{TM} - \Delta_{TE}$ is typically constant during one polarization rotation (incorporating one maxima and one minima, 180°) as it related to the azimuth of the polarization ellipse. As a result, we cannot determine the expression of the GH shift with respect to the waveplate polarization angle using the first order derivative of the phase. To this end, we need a different analytical approach, which was not completed in the scope of this thesis.

Analytically the phase can be derived by setting the derivative of the intensity equal to 0 ($\frac{dI}{d\beta}$=0) [131]:

$$\Delta = \cos^{-1}\left(\frac{|r_{TM}|^2\cos^2\gamma - |r_{TE}|^2\sin^2\gamma}{2|r_{TM}||r_{TE}|\cos\gamma\sin\gamma}\tan(4\beta_m)\right) \tag{69}$$

In classical ellipsometry, the incident polarization (at 45°) is fixed and P2 is rotating to measure the polarization ellipse. In contrast, in our case, the incident polarization is rotating, while P2 before detector is fixed. As a result, we obtain a different elliptical polarization with a distinct azimuth for each incident polarization. Since P2 is fixed, it does not permit the scanning of the polarization ellipse to access its azimuth. Instead, it projects the field into a single polarization axis (defined by γ).

In order to understand the physical influence of P2, the setup was simulated without P2. This preliminary step is essential to establish a reference model in which the detector directly

License CC BY-NC-ND 4.0

measures the effect of rotating the waveplate without P2. In this case, the detector measures the reflected intensity of the TM and TE components directly.

Conditions of the simulations:

- The resonance angle was found from the TMM model with water. The complex Fresnel coefficients r_{TM} and r_{TE} were extracted accordingly.
- To simulate the effect of changing the surrounding environment at the gold's surface, 1% and 5% glycerin were simulated with their coefficients r_{TM} and r_{TE} extracted at the resonance angle of water.
- In this case, when $\beta = 0^o,90^o,180^o,270^o,360^o$ the beam is purely TM polarized. Likewise, when $\beta = 45^o,135^o,225^o,315^o$ the beam is purely TE polarized.

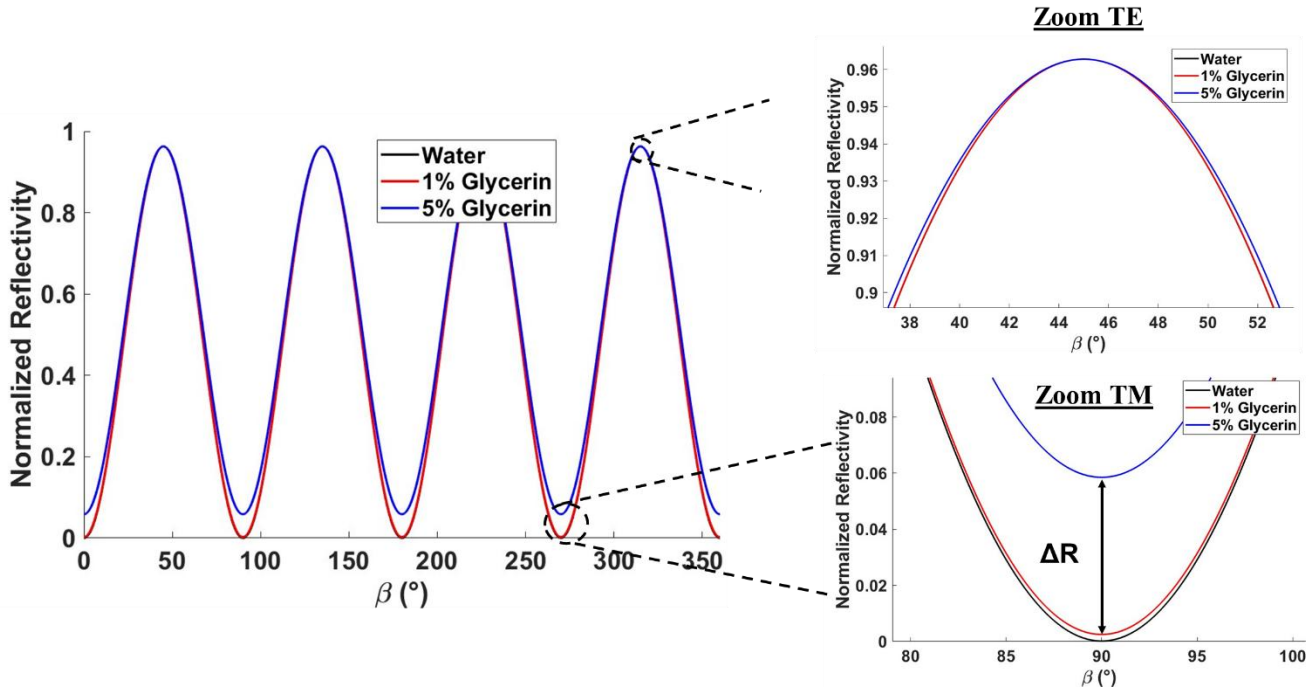


Figure 112 Simulated SPR reflectivity curves versus the angle (β) of the waveplate, for water, 1% glycerin and 5% glycerin.

In this case, the intensity of the reflected light is defined by:

$$I=|r_{TM}|^2 \cos(2\beta) + |r_{TE}|^2 \sin(2\beta) \quad (70)$$

As expected, the three curves represent a sinusoidal variation with respect to β with four maxima and minima. There is no variation of the intensity (between water, 1% and 5% glycerin) at the TE polarization. For TM polarization, the changes in reflectivity are 2.5×10^{-3} and 5.8×10^{-2} between water and 1% glycerin and between water and 5% glycerin, respectively. Furthermore, as expected, the positions of the minima and maxima are not modified with the variation of the refractive index of the surrounding environment. For all curves the position of the maxima occurs at $45^o,135^o,225^o,315^o$ and the position of the minima at $0^o,90^o,180^o,270^o$. Equation 70 shows that, in this configuration (without P2 before the PSD), the detected intensity depends only on the reflection coefficients of the SPR chip ($|r_{TM}|$ and $|r_{TE}|$). The phase information associated with SPR is inaccessible via simple intensity measurements. This corresponds to the previous measurement method specified in Chapters 2and 3.

License CC BY-NC-ND 4.0

Next, we simulated the prototype using the same analytical model but with P2 positioned before the PSD (Figure 111). We set γ as 90° (P2 oriented at TE direction), 20°, 10°, 1° and 0° (P2 oriented at TM direction). The results are presented in Figures 113-114.

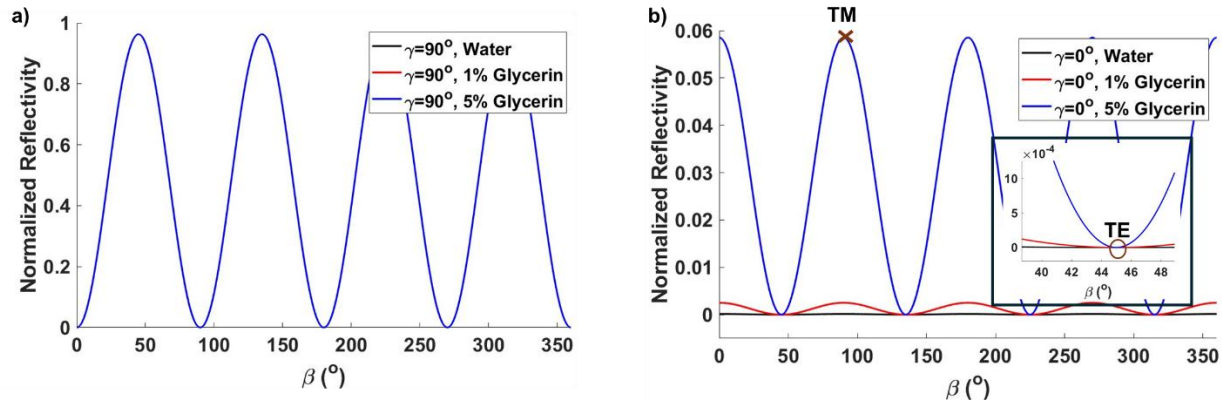


Figure 113 Simulated SPR reflectivity curves versus the angle of the waveplate for water, 1% glycerin and 5%. a) γ=90° (P2 oriented parallel to TE polarization, meaning it transmits all TE polarized light), and b) γ=0° (P2 oriented parallel to the TM polarization, meaning it transmits all TM polarized light). The intersection of the three curves is marked by a circle.

When P2 is oriented parallel to either the TM or TE polarization, the angular positions of the minima and maxima values remain the same for all three curves. From Equation 68, the interference term $(\cos\gamma \sin\gamma \cos(\Delta_{TM} - \Delta_{TE}))$ cancels when $\gamma = 0°$ and $\gamma = 90°$ making the phase parameter inaccessible. In these two cases, the transmitted polarization after P2 is linearly polarized (either TM or TE).

When P2 is oriented parallel to the TE polarization (Figure 113-a), we notice an absence of an intensity change, shown by the superimposed curves. In parallel, when P2 is oriented parallel to the TM polarization (Figure 113-b), we see a maximum sensitivity and intensity change. The three curves intersect at a single angular point. This corresponds to the TE polarization where the change of surrounding medium does not affect the change of reflectivity at resonance. In this case, the TE polarization is located at 45°. In parallel, the maximum intensity change occurs at 90° which corresponds to the TM polarization ($Angle_{TM}=Angle_{TE}+45°$).

License CC BY-NC-ND 4.0

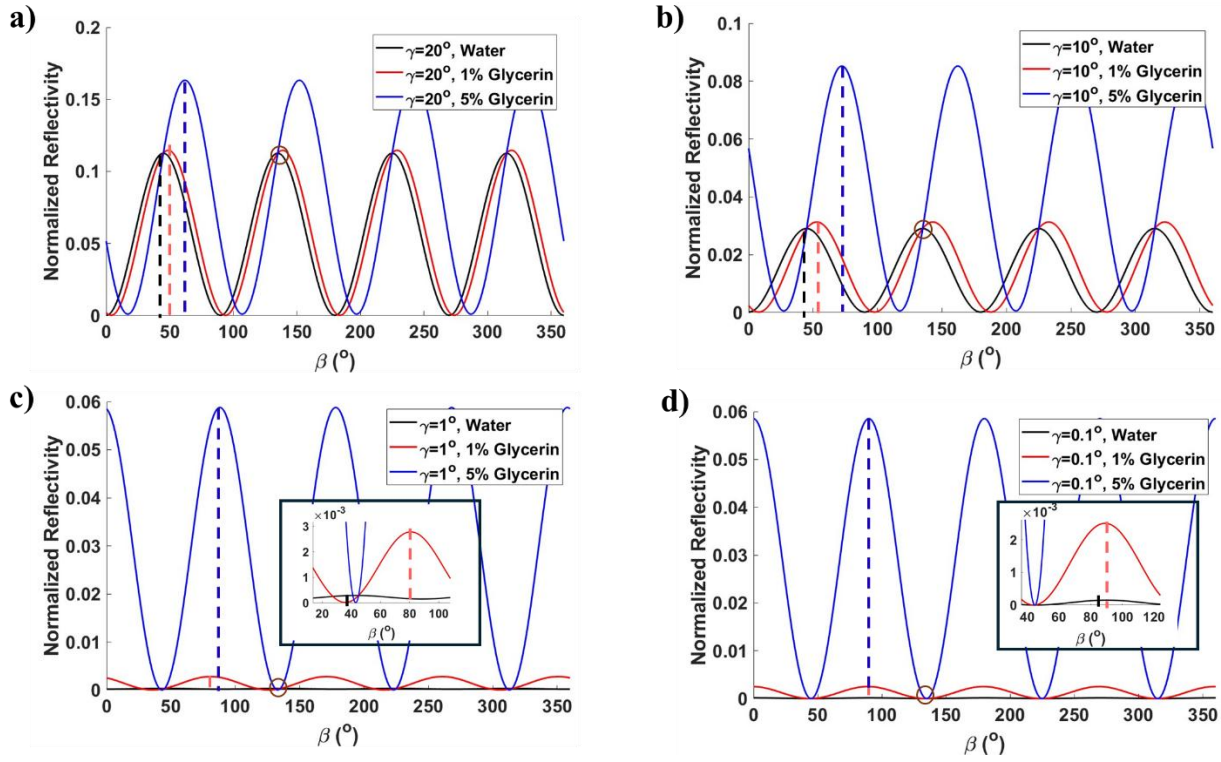


Figure 114 Simulated SPR reflectivity curves versus the waveplate polarization angle for water, 1% glycerin and 5% glycerin. a) γ=20°, b) γ=10°, c) γ=1° and d) γ=0.1°. In all four cases γ<45° meaning P2 transmits more TM polarized light and attenuates TE. The dashed lines in black, red and blue respectively represent the angular position of the first maximum. The circle represents the intersection points of the three curves.

The curves in Figure 114 still present a sinusoidal shape with four maxima and minima. However, the angular positions of the minima and maxima depend on the angle of P2. As explained in Section IV.2, these positions are related to the azimuth of the polarization ellipse β_m. From Equation 69, we extract β_m:

$$\beta_m = \frac{1}{4}\tan^{-1}\left(\frac{2|r_{TM}||r_{TE}|\cos\gamma\sin\gamma}{|r_{TM}|^2\cos^2\gamma - |r_{TE}|^2\sin^2\gamma}\cos(\Delta)\right) \quad (71)$$

It is shown from Equation 71, that the positions of the minima and maxima depend on the amplitude of the reflection coefficients, phase difference after SPR and the angle of P2 γ. Additionally, these positions shift with respect to the glycerin solutions. The shift between water and 1% glycerin is the greatest when γ = 1° (37°) and the smallest when γ = 0.1° (1°).

For all cases, the three curves intersect at a single angular position. This corresponds to the TE polarization where the intensity of light is not affected by the change in the refractive index of the surrounding medium. The angular position of this intersection is located at 45°,135°,225°,315°.

It is important to highlight that the highest intensity variation is not located at the TM polarization (180°) but rather at an intermediate polarization angle (163°, Figure 115).

License CC BY-NC-ND 4.0

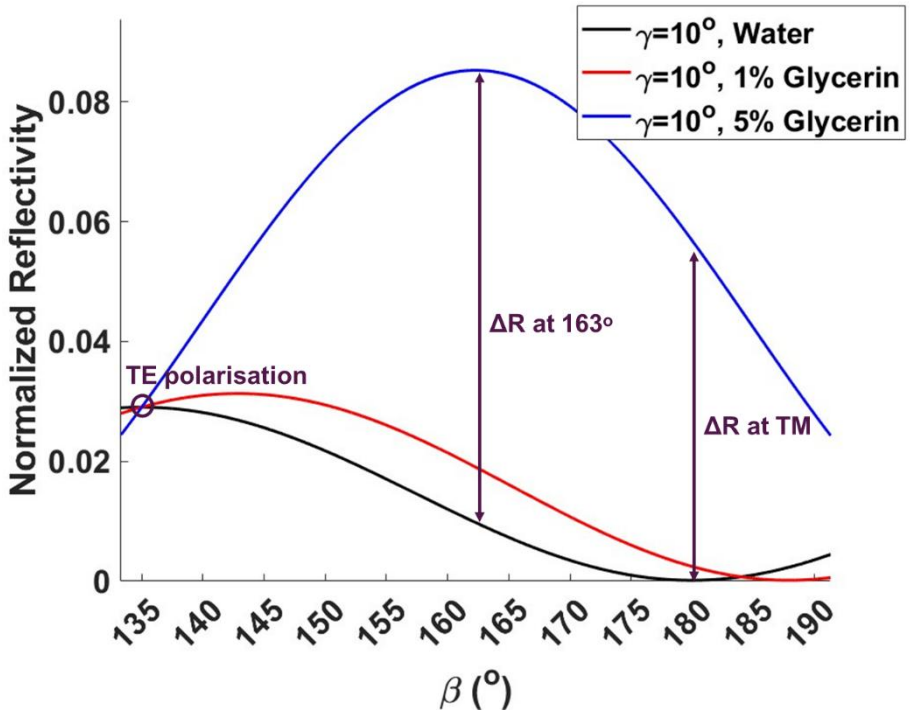


Figure 115 Simulated SPR reflectivity curves versus the angle of the waveplate for water, 1% glycerin and 5% glycerin. The polarization angle of P2 is 10°. TE polarization is located at 135° and TM at 180°.

These preliminary simulation results show that the angular shift is caused by the presence of P2 before the PSD. Its magnitude is affected by the angle of P2. Taking these findings into account, experimental studies were conducted to measure the GH shift with respect to the waveplate's polarization angle.

IV.4. Experimental tests to measure the GH shift under rotating incident polarization

A commercial SPR chip was tested with glycerin solutions to evaluate the new method. The waveplate was rotated over 180° with steps of two degrees using the piezoelectric motor. The angle of P2 was adjusted to be close to TM so that it would transmit most of TM and attenuate TE. The position x and the power of the reflected beam on the PSD were recorded at each step. This approach enables a direct assessment of the dependence of the GH shift with respect to the polarization state.

Before conducting any long experiment, the stability of the system is evaluated by recording the x-position and the power of the reflected beam for 10 minutes at the TM polarization. The results are shown in Figure 116.

License CC BY-NC-ND 4.0

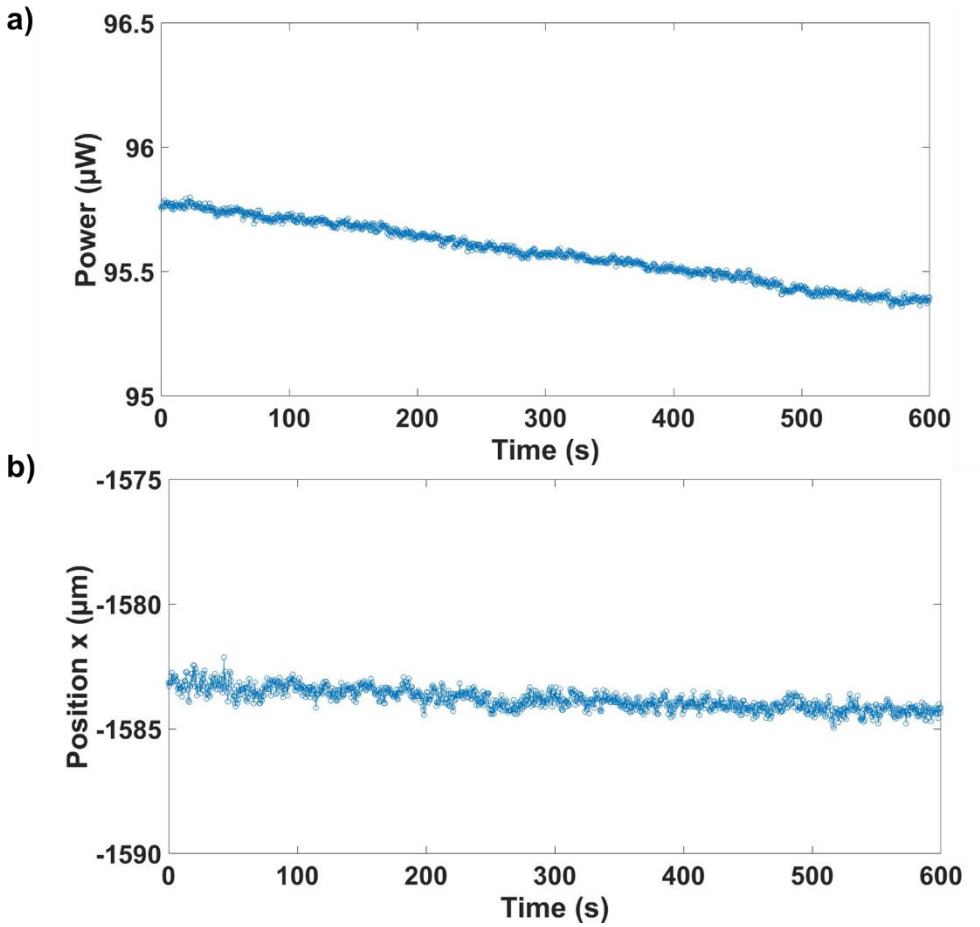


Figure 116 Stability measured over 10 minutes using the commercial chip at the TM polarization and with water as the surrounding environment. (a) Power and (b) x Position on the PSD.

The position x and power were shown to be stable with standard deviations of 0.4 µm and 0.12 µW respectively. Then, these variables were recorded by rotating the waveplate in two degrees increments, followed by a 5-seconds pause, over a total rotation of 180°. The results are shown in Figure 117.

License CC BY-NC-ND 4.0

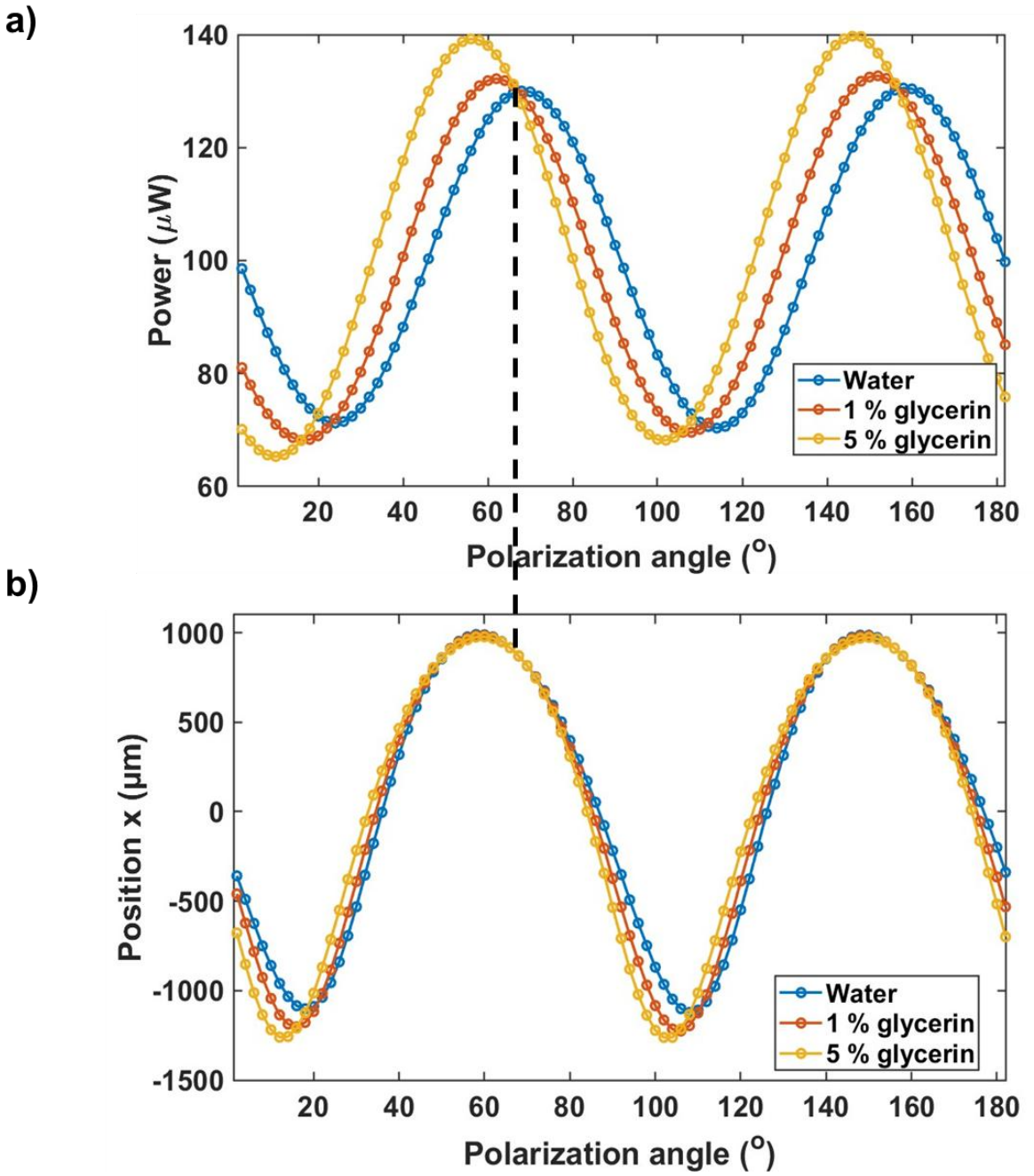


Figure 117 Measurement of (a) x Position and (b) Power with respect to the angle of the waveplate for 3 solutions: water, 1% and 5% glycerin.

We notice a sinusoidal-like pattern with two minima and two maxima over a rotation of 180° of the waveplate (Figures 117 a-b).

The amplitude, or the difference between the minimum and maximum, corresponds to 60, 64, and 73 μW for water, 1% glycerin, and 5% glycerin, respectively (Figure 10a). In addition, the angular position of the minima and maxima shifts by the same amount upon the injection of glycerin solutions. Specifically, it varies by ~6° between water and 1% glycerin, and by ~12° between water and 5% glycerin. This change follows a similar trend as seen in the theory (Section IV.3). Furthermore, the three curves (water and glycerin solutions) intersect at one position (~68°). This angle represents TE polarization, in which the intensity of the reflected

License CC BY-NC-ND 4.0

beam remains constant regardless of the surrounding medium. The corresponding TM polarization then occurs at 23 or 113°.

From the other side, the amplitude (shift in position x, Figure b) corresponds to 2098, 2195 and 2236 µm for water, 1% glycerin, and 5% glycerin respectively. We notice only a variation of the angular position of the minima. The first minimum is located at 108°, 106°, and 102° for water, 1% and 5% glycerin respectively. The maximum of all the curves occurs at 60°, which represents an eight-degree difference from the TE. This result implies that the maxima does not represent TE polarization but rather an intermediate polarization between TM and TE but closer to TE.

In order to quantitatively evaluate the sensitivity of this SPR setup, we subtracted the glycerin curves from that of water (position curves of Figure b). The results are shown in Figure 118 below.

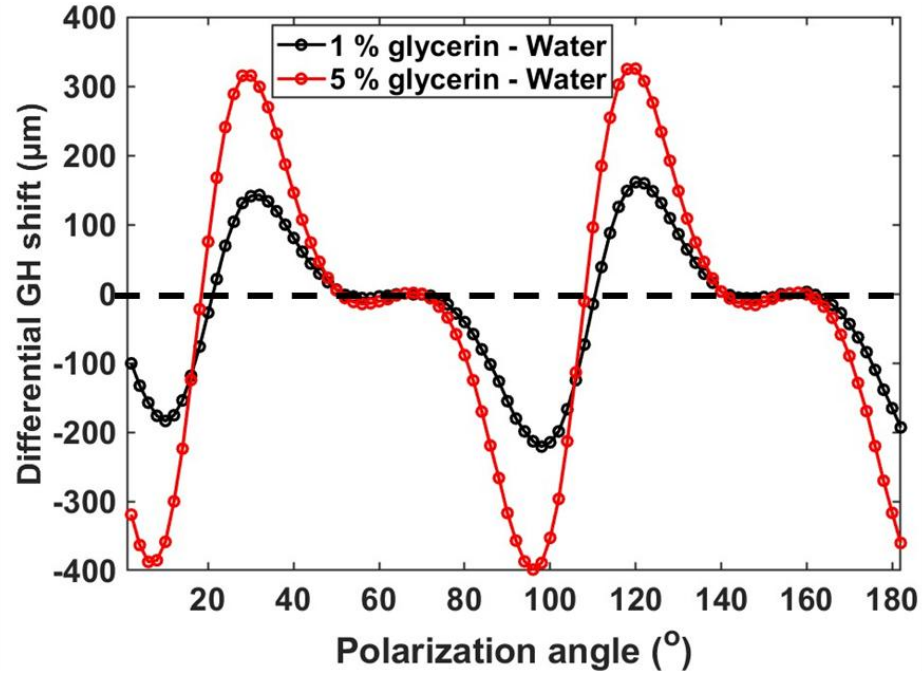


Figure 118 Differential GH shift between glycerin solutions and water as a function of the polarization angle.

We observe a sinusoidal pattern in the differential GH shift curves, with two minima and two maxima. A quasi-horizontal line of 0 µm was observed close to TE. The differential GH alternates in sign (positive GH shift between 20 and 40° and negative between 80 and 100°). The shift is significantly larger for 5% glycerin than for 1%, indicating increased sensitivity with respect to changes in the refractive index of the surrounding environment. These results are consistent with those presented in Chapter 3.

It is important to note that the highest sensitivity (highest GH shift between water and diluted glycerin solutions) was not obtained at the minimum of the water curve, 108° and neither at the TM polarization (113°), but rather at 96°.

In summary, measuring the GH shift at multiple polarization angles allows us to carefully select the optimal polarization angle to maximize the sensitivity of SPR. Additionally, the analysis of the GH curves vs the polarization angle highlighted an asymmetry in the sinusoidal shape. This asymmetry could be attributed to the polarization angle of P2 (γ) which is responsible for

License CC BY-NC-ND 4.0

attenuating a portion of the TM and TE polarizations. Follow-up measurements were conducted to assess the influence of γ on the shape of the GH curve. Instead of γ, the power ratio $\left(\mathrm{r} = \frac{\text{Power at maximum}}{\text{Power at minimum}}\right)$ was used because it directly reflects the relative contributions of the TM and TE components. The closer r is to 0, the greater the contribution of TM contribution and the higher the attenuation of TE.

Influence of r on the position x curves under rotating incident polarization:

To evaluate the influence of r on measured GH shifts, experiments were performed at the same resonance angle with varying r achieved by slightly rotating P2. The position x of the reflected beam was measured by rotating the waveplate with steps of 4°.

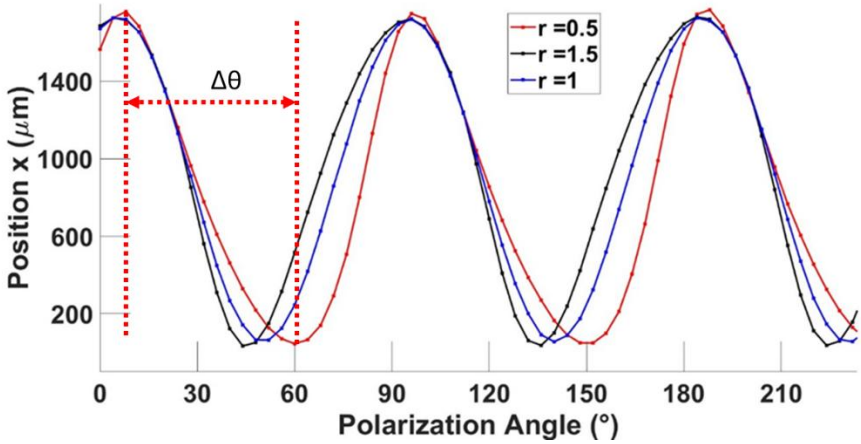


Figure 119 Measurement of the position x of the reflected beam versus the angle of the waveplate. The curves were obtained at the resonance angle of the commercial SPR chip with water as the surrounding environment. The curves were acquired at r =0.5,1 and 2.5. Δθ represents the difference between the angles of the first maximum and the first minimum.

Overall, the curves preserve a quasi-sinusoidal shape (Figure 119), and the amplitudes are identical. The main differences between these curves are Δθ and the angular position of the minima (Table 13).

Table 13 Angular distance between first maximum and first minimum for 3 different r values.

Curve	Value (°)
Red, r =0.5	Δθ: 52°
	Angular position of the first minimum: 60°
Black, r =1.5	Δθ: 36°
	Angular position of the first minimum:44 °
Blue, r=1	Δθ:40 °
	Angular position of the first minimum:48 °

License CC BY-NC-ND 4.0

When r is the lowest, Δθ is the highest (red curve). On the other hand, when r is the highest, Δθ is the lowest (black curve). These observations confirm that the shape of the position x curves depends on the ratio r which controls the power transmitted at TM and TE. Additional work is hence required to assess the influence of r on the GH sensitivity. This work was not completed in the scope of this thesis.

IV.5. GH measurements with fast and continuous rotation of the incident polarization

In the previous sections, the GH shift was measured by adjusting the polarization angle in small increments using the piezoelectric motor. Overall, the 180° rotation of the waveplate took around 450 seconds. In actual biodetection experiments, a large amount of data must be acquired over a short period of time to monitor the binding of molecules to their targets. It is then preferable to acquire a full rotation of 360° in less than 30 seconds. Therefore, we replaced the piezoelectric motor with a Brushed DC Servo Motor (Annex S8) that permits continuous and fast rotation of the waveplate.

Considering the difficulty of synchronizing the PSD with the fast rotation of the waveplate (the former was controlled using a LabVIEW program developed previously, and the latter was controlled using Thorlabs' Kinesis software) the data processing was performed as described in this section.

At first, the velocity profile of the motor was derived from a python code by measuring the motor position with respect to time for a total 1080° rotation (Figure 120). Velocity and acceleration are set at 20°/s and a=25°/s^2 and the sampling time was set to 250 ms (a total of 220 data points). Even though the original velocity was set to be uniform at 20°/s, the profile obtained showed big variations with an average of 20°/s and a standard deviation of 4°/s around the mean. It is important to note that a variation of 4°/s in velocity will ultimately lead to a variation of polarization up to 8°/s leading to further uncertainties concerning the polarization angle measured.

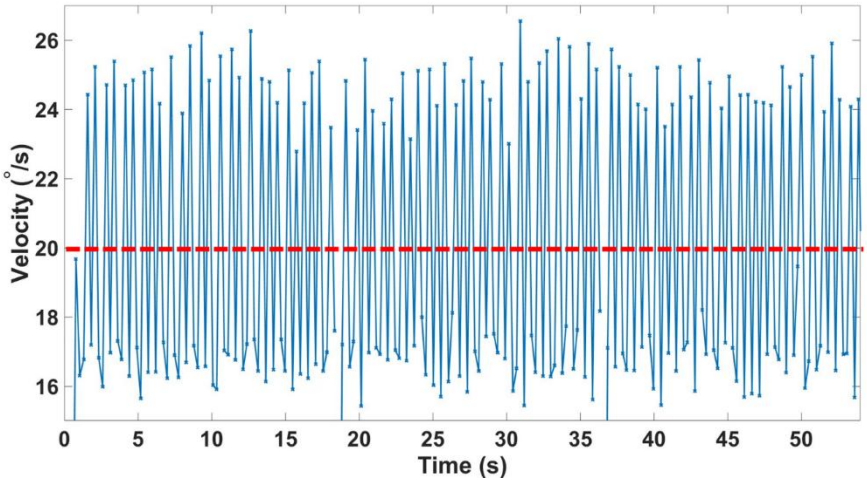


Figure 120 Measurement of the velocity profile of the brushed DC servo motor. The blue curve represents the actual velocity profile obtained and the red dashed line represents the expected velocity profile.

To evaluate the noise induced by the inhomogeneity of the motor's rotation, the system was evaluated using water as the sensing medium and a commercial SPR chip. Using water as a

License CC BY-NC-ND 4.0

reference enables a stable baseline to be established, which is necessary for interpreting the results. The motor's velocity and acceleration were set to 20 m/s and 25 m/s², respectively, and the motor was rotated by 3,600° (10 cycles of 360°). An extract of the results is presented in Figure 121.

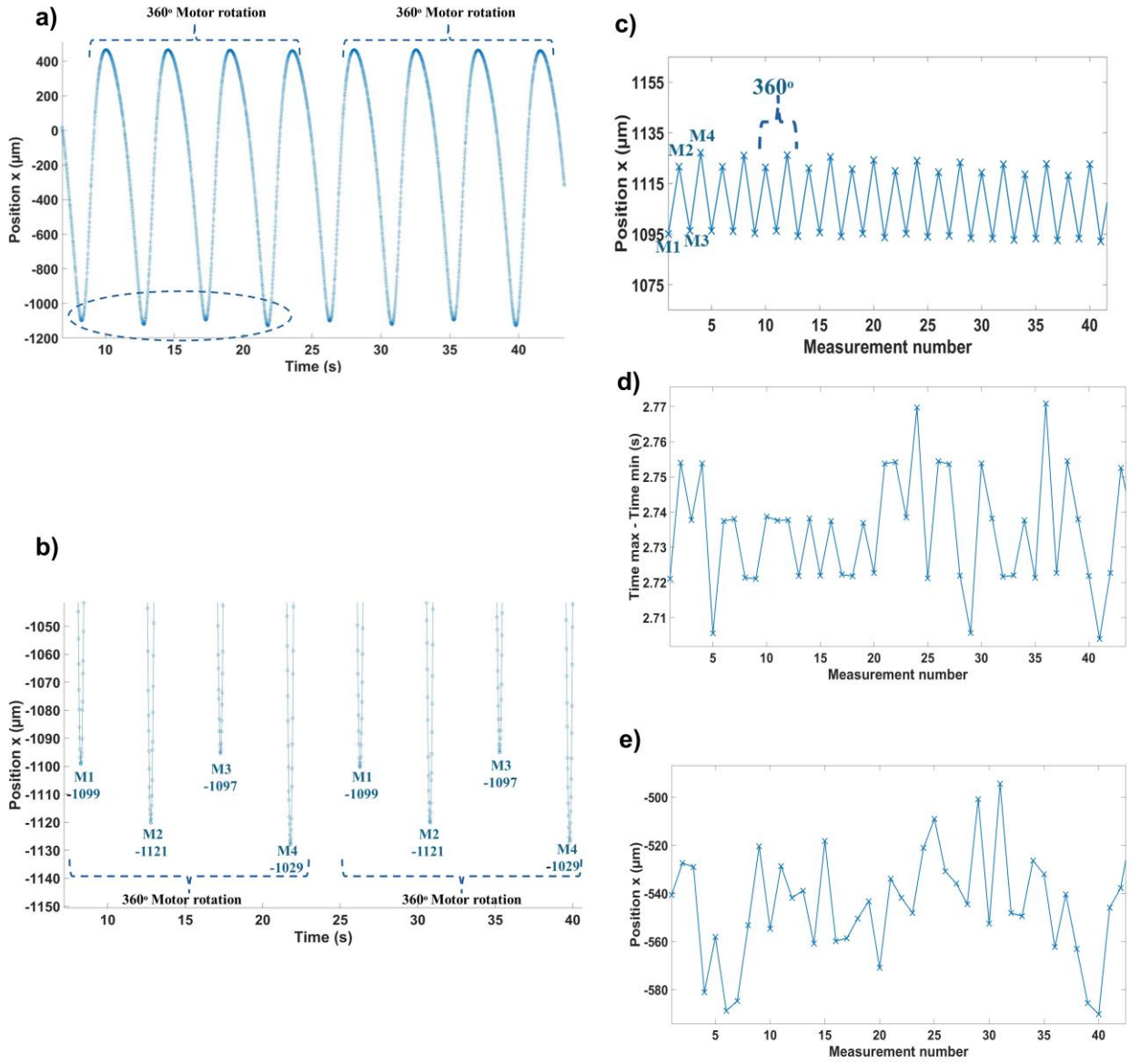


Figure 121 Measurement of the position x of the reflected beam for 10 cycles (10x360°) of the waveplate rotation. Evolution of a) the position x, b) zoom in section of (a), c) the position of the minima, d) the time difference bewteen 2 consecutives mimuma and maxima, e) the exctracted position at a fixed polarization angle of 100°.

Since the waveplate multiplies the polarization angle by a factor of 2, a rotation of 360° by the motor induces a polarization angle change of 720° (4 minima and 4 maxima positions). For every 360° rotation, the position x of the peaks (M1, M2, M3, M4) repeat itself. The average position of M1, M2, M3, M4 was found to be reproducible with a standard deviation of 0.9 µm for 10 cycles (Figure c). The low standard deviation indicates a low noise level, which suggests that this method of evaluation is adequate for determining the GH shift.

License CC BY-NC-ND 4.0

Two consecutives maxima generally correspond to a cycle of 180° (or a time difference of 9 seconds if the motor velocity is 20°/s). To determine the change in the angular position of the minima, we calculate the time difference between two consecutive maxima and minima and multiply it by the average velocity of the motor. An average difference of 2.735 s (T_{max} -T_{min}), with a standard deviation of 0.016 s is obtained in Figure d. This corresponds to an angle of 54.7° with a variation of 0.314°, calculated at a motor velocity of 20°/s. This suggests that variations faster than 0.016 s (0.314°) cannot be detected with precision from the current system.

Moreover, the polarization measured at an angle other than the minimum or maximum typically resulted in significant fluctuations around the mean with standard deviation of 23 µm calculated at 100°. This influences the sensitivity of the system to detect smaller position shifts.

In conclusion, we present three possibilities for retrieving the GH shift:

- **Case 1 (C1)-**By tracking the position shift of each minimum and subtracting it from TE (Figure 122-b):

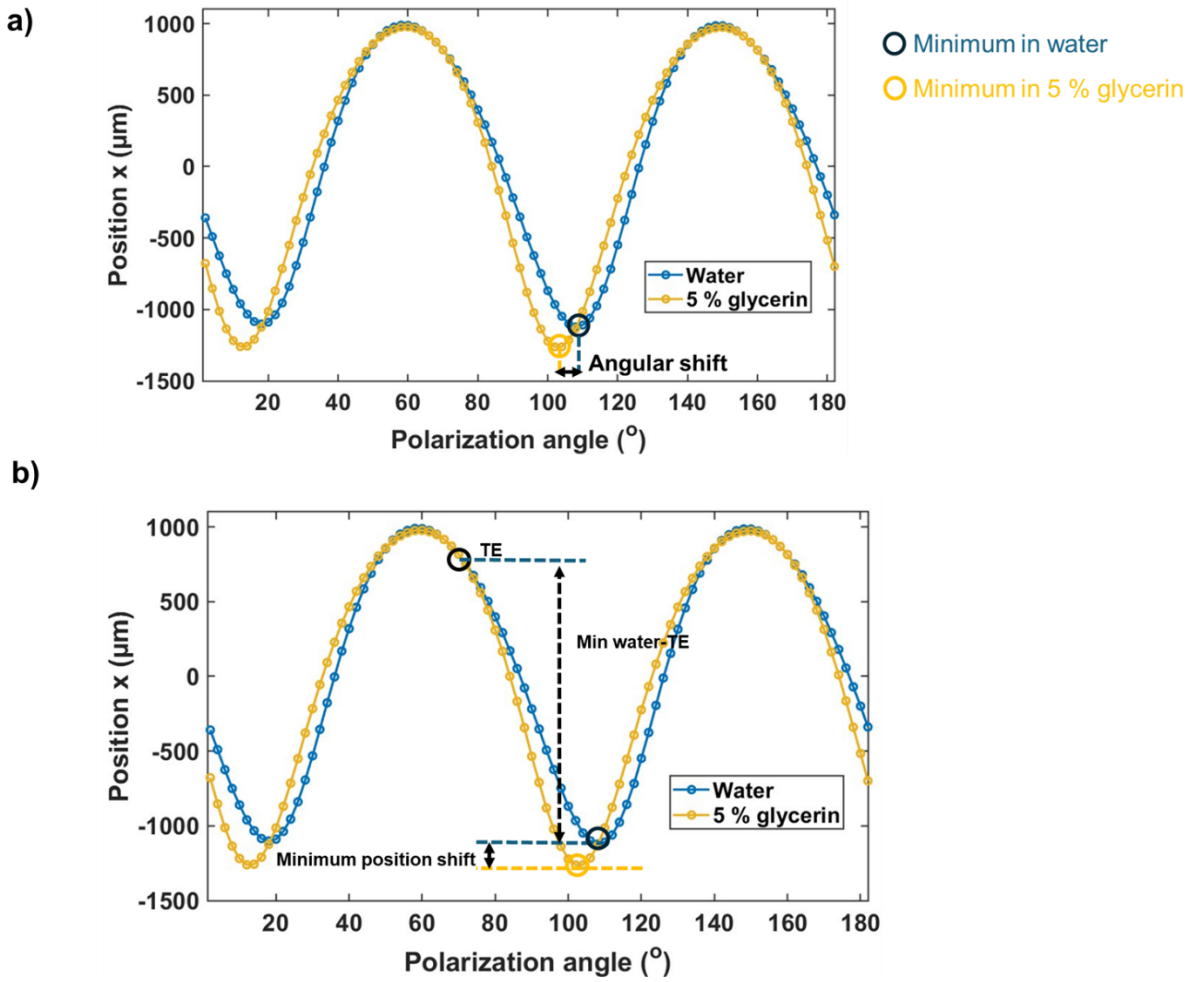


Figure 122 Illustration showing the angular position shift and the minimum position shift between water and 5% glycerin.

- **Case 2 (C2)-**By tracking the polarization angle shift (Figure 122-a).
- **Case 3 (C3)-** By extracting the position at an optimized polarization angle for each cycle of minimum -maximum. This corresponds to the polarization angle that produces the maximum GH shift between two solutions. This position is later subtracted from TE.

License CC BY-NC-ND 4.0

In the previous measurement, the waveplate was rotated in two-degree increments (Section IV.4). Therefore, we had access to the position x at each polarization angle with high precision and low noise. In this case, we have additional variation coming from the lack of synchronization between PSD and motor. Hence, we can directly extract the position shift of the minima and maxima with high precision. Regardless of the high noise level at intermediate polarization states, the fast rotation of the motor (360 ° rotation in 20 s) allows us to access a high amount of data in a short timescale with noise that could be eventually subtracted via a proper data processing algorithm.

IV.6. Comparison of the GH sensitivity obtained at TM polarization and that at an optimized polarization under continuous rotation

The prototype was then tested in order to compare the new interrogation method with the previous one (presented in Chapters 2 and 3). For our first measurement, we use the commercial chip.

First, the commercial chip was installed on the newly developed holder. Then, the resonance angle was then found with water as the surrounding environment. The TM polarization was determined as described in Section IV.1. Next, the GH shift between water and 1% glycerin was measured at TM polarization. This value was then subtracted from the TE polarization value. The chip was rinsed with water, after which the experiment was repeated. For each solution, the waveplate was rotated through nine 360° cycles. We determined the GH shift using case 3 (described in Section IV.5 above). This value was then subtracted from the value obtained at the TE polarization. The TE polarization corresponds to the angle that produces the minimum GH shift between water and 1% glycerin. The results are presented in Figure 123.

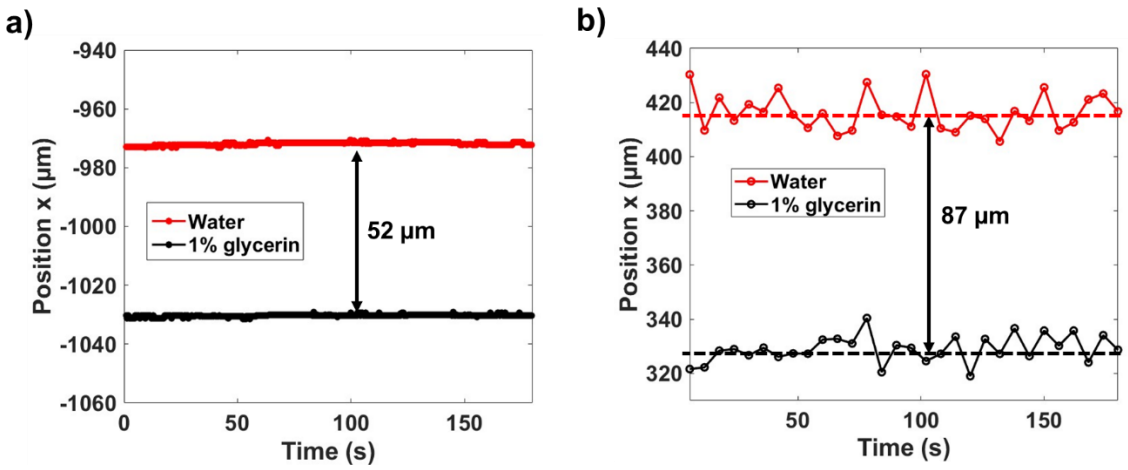


Figure 123 Measurement of the GH shift between water and 1% glycerin measured at, a) the TM polarization subtracted from TE and b) at the optimized polarization angle subtracted from TE.

To evaluate the stability of the measurements, the standard deviations of the measurements in water and 1% glycerin were calculated. The standard deviation was approximately 0.4 µm for the first test (Figure 123-a, with 600 measurement points for each test) and 6 µm for the second test (Figure 123-b, with 30 measurement points for each solution). The GH shift was found to be 52± 0.4 µm for the first test, and 87± 6 µm for second test. We found a significant

License CC BY-NC-ND 4.0

difference of 35 ± 6 µm between the two measurements. This emphasizes the increased sensitivity achieved by measuring the GH shift at an optimized polarization angle.

IV.7. Measurement of the GH sensitivity of the N24 chip with a rotating incident polarization

After testing the new interrogation method with the commercial chip, we re-tested it with the N24 chip. This will enable us to evaluate any improvement in sensitivity that the new method might have provided.

Similarly, the N24 chip was installed on the newly developed holder, and the resonance angle was found with water as the surrounding medium. Diluted glycerin solutions (0.5, 1 and 2.5%) were then successively injected into the fluidic channel. By analogy with the previous measurement (Figure 117), the maxima of the GH curves were positioned in the same location. The angular position of the TE polarization can be determined by identifying the polarization angle that experiences the least variation in position with respect to changes in the surrounding medium. Then, the GH shifts are subtracted from the TE polarization. The GH shift is evaluated according to C1, C2 and C3. The evolution of the position with respect to the rotation of the waveplate is represented in Figure 124.

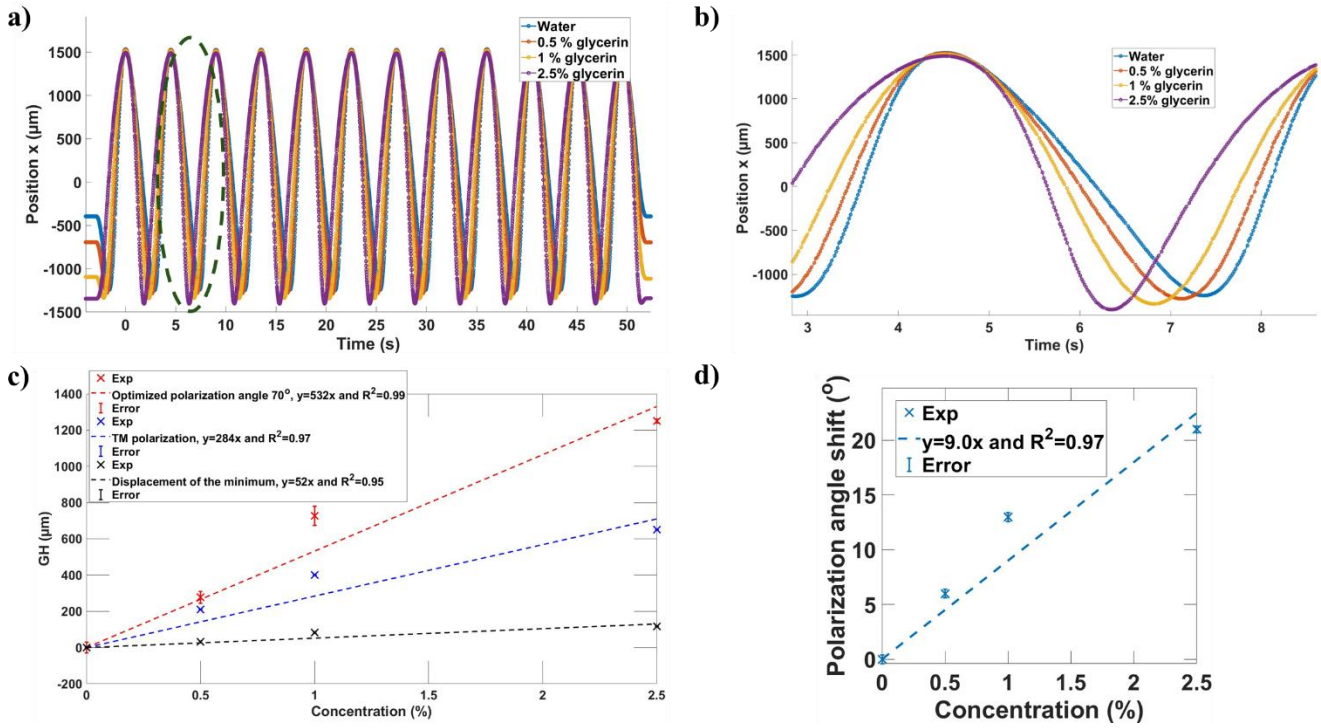


Figure 124 Evaluation of the N24 chip under rotating incident polarization, a) Position x of the reflected beam measured by the PSD vs waveplate rotation, b) zoom in section of a), c) Linear fit of the GH shift extracted for 3 different configurations: Displacement of the minimum, GH shift at TM polarization (extracted from Chapter 3, Section III.3.2) and GH shift at the optimized polarization angle 70°, d) shift of the polarization angle, experimental and linear fit.

The GH shift was evaluated at an optimized polarization angle (method C3) of 70° (Figure 124). This produced a GH shift of 728 µm for 1% glycerin. Meanwhile, a GH shift of 83 µm was observed using method C1. Additionally, a GH shift of 211 µm was obtained at TM polarization (extracted from Chapter 3, Section III.3.2). The sensitivity was also evaluated using method

License CC BY-NC-ND 4.0

C2 (Figure d). The high R^2 value (0.97) suggests a linear variation of the polarization angle for small changes in the refractive index.

In conclusion, these results show that choosing the polarization angle improves the GH sensitivity when compared to the previous method described in Chapter 3.

IV.8. Conclusion

This chapter focused on the analysis of the prototype in a configuration involving the rotation of the polarization of the incident beam. Although our approach does not involve phase detection using SPR ellipsometry, a thorough understanding of the theory was necessary to gain further insight into the effects of the rotating the polarization on the measurements. The theoretical part involved extracting the intensity profile with respect to the polarization angle calculated using Jones matrices. The experimental results showed a shift in the polarization angle near the TM zone only, as well as an improvement in sensitivity when the polarization angle was selected. The setup was later assessed with two SPR chips, commercial and N24, both of which produced greater sensitivity when properly selecting the polarization angle.

The originality of our experimental setup relies on the fact that the prototype no longer depends on the uncertainty of the waveplate's position for defining TM and TE, eliminating the need for searching for TM polarization before each experiment.

Compared to SPR setups with phase interrogation using ellipsometry, the GH shift — being the first-order derivative of the phase — provides a sharp and pronounced GH shift at resonance, resulting in greater sensitivity. Evaluating the GH shift as the first order derivative of the phase is shown to be insufficient to predict the effect of the waveplate polarization angle on the GH shift. As such, a comprehensive theoretical model to advance our understanding of the underlying physical processes is still needed. Further experimental tests are also required to assess the influence of P2 on sensitivity. A data processing algorithm should also be implemented to reduce noise produced by the inhomogeneous rotation of the motor.

License CC BY-NC-ND 4.0

Chapter V. Application of the SPR sensing platform for the detection of EVs

V.1. Introduction and Context

The collaboration between CAPTuR and XLIM involves testing and verifying the prototype, particularly for detecting EVs. Following the validation, the prototype will be used to detect cancer-related biomarkers. In this context, our collaborators in CAPTuR specialize in studying EVs that contain glioblastoma biomarkers.

Glioblastoma brain cancer (GBM), is the most common type of brain tumors (around 50% of cases of brain tumors [152]) known for its aggressiveness and malignance. It is classified as a grade IV glioma by the World Health organization due to its severity, high mortality rate, and low survival span [153]. It is known to be highly resistive to traditional treatments such as chemo and radiation therapy making it especially difficult to cure and highly prone to remissions [154]. Hence, the need for a sensitive tool to monitor the progression of the disease and its response to treatments is urgent.

To gain a better understanding and assess the interest in developing the prototype, it is important to review the various methods employed for diagnosing and monitoring glioblastoma in research and clinical practice.

When a patient starts to experience some symptoms related to glioblastoma, he is generally recommended to undergo some imaging tests such as magnetic resonance imaging (MRI) or computed tomography (CT) scan to assess the presence/absence of a tumor [155]. These techniques are primarily used to get information about the tumor size, shape and location but cannot directly reveal the type of the tumor [155]. For this reason, and in case of a tumor has been spotted, the clinician recommends a biopsy (Figure 125). This is an invasive surgical procedure to extract a part of the tumor for examination under a microscope to assess its type [156].

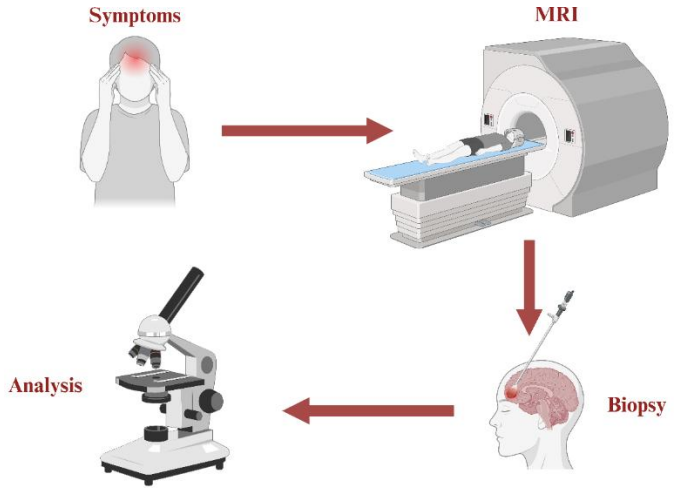


Figure 125 Illustration showing the glioblastoma detection procedure.

If the tumor has been identified as cancerous, the treatment begins. In parallel, several techniques can be adopted to track the evolution of the disease and its response to treatment. The ability to perform regular tests with high sensitivity is often valued since it will allow the

License CC BY-NC-ND 4.0

clinician to adapt the treatment plan according to the evolution of the disease. For this reason, several methods can be adopted:

- **Imaging techniques such as MRI and CT scan:** these techniques show some disadvantages as they primarily lack of resolution for early detection (with a maximal spatial resolution between 0.5 - 1 mm [157,158]. They are not often repeatable where the patient must wait for a period of 2-3 months between each scan [159].
- **Biopsies:** Repeated biopsies cannot be performed frequently as it is an invasive surgical procedure.

In order to overcome the challenges posed by these methods, researchers are starting to consider tests based on liquid biopsies (Figure 126). These are non-invasive detection methods that can identify biomarkers (e.g. circulating tumor cells CTCs, circulating tumor DNA ctDNA, EVs, tumor-educated platelets TEPs and circulating free RNA cfRNA) associated with cancer in biological fluids such as saliva, blood and urine [160] .

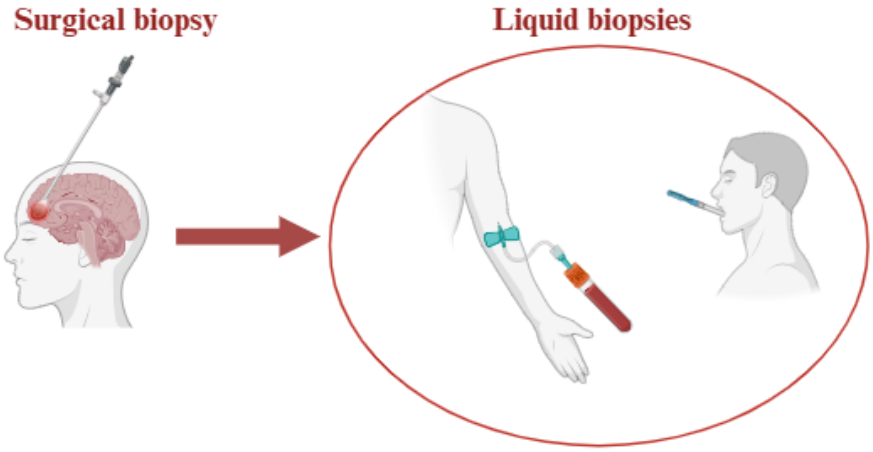


Figure 126 Illustration of surgical and liquid biopsies.

In this regard, our collaborators in CAPTuR are specialized in the study of EVs produced by tumor cells (Figure 127). EVs are types of lipid bilayer nano-sized particles secreted by all types of cells into the extracellular medium. They can be widely found in biological fluids such as blood (10^8-10^{12} EVs/ml [161]), saliva and urine [162]. Their main role is to transport biological information (protein, DNA fragments, mRNA and microRNA) between cells. Specifically, in the case of cancer, these messengers will affect the development of healthy cells facilitating the spreading of the cancer [162].

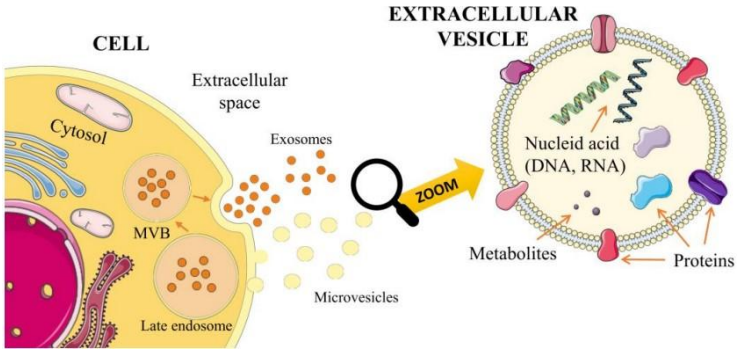


Figure 127 Illustration showing the composition of EVs [163].

License CC BY-NC-ND 4.0

In the context of glioblastoma, EVs are secreted by cancerous cells, cross the blood-brain barrier (BBB), and are found in the blood [164]. The identification of these EVs is of great clinical importance as it carry information about the progression of the tumor during treatment [161]. Different techniques have been developed for detecting biomarkers present in EVs. These include :

- **Western blotting (WB):** First, proteins are separated according to their molecular weight through gel electrophoresis. Then, they are transferred onto a polyvinylidene fluoride membrane and treated with a primary antibody that recognizes the protein of interest. This is followed by a labelled fluorescent secondary antibody that attaches to the primary antibody and emits a detectable light signal [165].
- **ELISA (Enzyme-Linked Immunosorbent Assay)**: In this approach, the protein of interest is first immobilized on a solid surface and then detected using an enzyme-labelled antibody. The enzyme reaction produces a colorimetric signal proportional to the amount of analyte (protein) present [166].
- **Flow cytometry (FC)**: FC is used to analyze the physical and biochemical properties of individual cells in suspension. Cells labelled with fluorescent antibodies are sequentially injected through a laser beam path, where light scattering and fluorescence emissions are detected [167].

Table 14 provides a comparison of these techniques for detecting cancer biomarkers, highlighting their respective applications and limitations.

License CC BY-NC-ND 4.0

Table 14 Comparison of commonly used techniques for the detection of EVs.

Method	Applications	Limitations	Reference
WB	- Confirming the presence of some proteins (CD63, CD81, EGFRvIII), - Determining the molecular weight of proteins.	- Not quantitative, - Long protocol, - No possibility for real-time monitoring.	[165]
ELISA	- Quantifying the amount of a specific protein (measuring the concentration of circulating biomarker in blood),	- Requires labeling tags (enzymes), - No possibility for real-time monitoring.	[166]
FC	-Analyzing cells individually (thousands of cells per second), -Identifying cell populations, -Determining the presence and abundance of some proteins on cells (CD81, EGFRvIII),	-Requires fluorescent labeling, -Long protocol, -Requires high concentration of cells, - Complex and heavy instrumentation.	[167]
SPR	- Studying biomolecular interactions in real-time and without labelling, -Confirming the presence of some proteins (confirming EV protein markers: CD63, CD81, EGFRvIII).	-Sensitive to experimental conditions, -Bulky instrumentation.	XLIM, [67]

Although these methods (WB, ELIZA, and FC; Table 1) are widely used in cancer research, they present some limitations. Most of them require additional fluorescent or enzymatic labelling, which adds extra steps to the sample preparation process. Additionally, some methods, such as ELISA and WB, do not allow for real-time monitoring of biological interactions. In this context, SPR emerges as a promising alternative. It offers several advantages, such as eliminating the need for additional labeling or sample preparation steps, providing higher sensitivity, and making it easy to use in clinical applications. SPR demonstrated an approximately 2500-fold improvement in sensitivity compared to Western blot [168], with a shorter analysis time (about 2 hours for SPR versus 1 day for Western blot) for the detection of the glycoprotein E2 of the swine fever virus. Additionally, a comparative study of ELISA and SPR for detecting Mycoplasma hyopneumoniae bacteria revealed that SPR could detect solutions that were 10 times more diluted than with ELISA [169]. Another

License CC BY-NC-ND 4.0

experiment showed that SPR detected Ractopamine in swine urine at a limit of 0.09 ng/ml, compared to 0.21 ng/ml for ELISA. The analysis also indicated a shorter surface functionalization time for SPR (18 minutes) than for ELISA (overnight) [170]. The high sensitivity of the SPR sensor is particularly interesting for detecting cancer biomarkers at low concentrations. One study showed that an SPR chip incorporating gold NP amplification tags could detect EVs originating from MCF-7 breast cancer cells. This resulted in a limit of detection 10^4 times lower than that obtained with ELISA [5].

In the context of our work, we are using EVs extracted from two glioblastoma cell lines:

- **U87-MG (wild-type EGFR Epidermal Growth Factor Receptor)**: based on the standard glioblastoma model and widely used in research. It expresses the wild-type EGFR receptor and serves as the reference for validating and adjusting the prototype [171].
- **U87-MG modified with EGFRvIII** (**Epidermal Growth Factor Receptor variant III**): this represents a mutation form of EGFR, genetically engineered by biologists from U87-MG cell line to express a more aggressive form of EGFR. It is found in about 30% of cases with glioblastoma and is often associated with shorter survival rates [172].

EV solutions representing the two cell lines are prepared by our colleagues in CAPTuR. U87-MG cells are grown at a concentration of 10 000 cells/cm² in Dulbecco's Modified Eagle Medium (DMEM) containing 10% fetal bovine serum (FBS), 1% non-essential amino acids (NEAA), 1% sodium bicarbonate and 1% antibiotics (100 Units/mL penicillin and 100 µg/mL streptomycin). For U87-EGFRvIII, the cells are grown in a MEM medium containing 10% FBS, 0.2% gentamicin, 200 µg/mL G412 and 1% antibiotics. To study EVs, the cells are cultured in an identical medium containing FBS from which exosomes have been removed. EVs contained in FBS are removed by ultracentrifugation at 120 000xg for 17 hours, creating an 'exo-free' culture medium.

After 72 hours of culture, the cell supernatant is collected, and differential centrifugation steps are performed to sort the vesicles based on their density. This process isolates the EVs contained in the supernatant (cell culture medium). First, the supernatant is centrifuged for 10 minutes at 300 g to remove dead cells. Then, cellular debris is removed by centrifuging for a further 10 minutes at 2000 g. The resulting supernatant is then filtered using a 0.2 µm filter before being ultracentrifuged twice for two hours at 120,000 g (using an Optima XPN-80 Ultracentrifuge, Beckman Coulter) to collect and wash the EVs.

Our work focuses on validating the prototype by verifying the presence of CD81 markers on the EVs. CD81 is a transmembrane tetraspanin protein that is expressed in many different types of cells. It is present in normal cells, including immune and haematopoietic cells. In cancer, CD81 is associated with tumor progression, angiogenesis, and metastasis. It is present in acute myeloid leukemia and multiple myeloma. Therefore, CD81 is not considered a cancer-specific biomarker, but rather a general surface marker [173]. EVs derived from the U87-MG cell line naturally express CD81 proteins. Those derived from EGFRvIII carry both CD81 and EGFRvIII biomarkers. Additionally, we performed a control experiment to confirm that the measured signals originate from specific interactions rather than non-specific binding.

License CC BY-NC-ND 4.0

V.2. First bio-detection test with the commercial chip

This section presents the results of bio-detection experiments conducted to identify the presence of CD81 on EGFRvIII EVs. For this, the commercial chip was coupled with a SF11 prism and installed on the newly developed holder. The experiments were performed on the prototype by measuring the GH shift at the TM polarization and subtracting it from the TE (as Specified in Chapters 2 and 3).

At the beginning of each experiment, the stability of the prototype is tested using water as surrounding medium. This ensures that there is no additional drift that could interfere with the measurements. To achieve this, the position x of the reflected beam is measured at resonance for 10 minutes under TM polarization. The results are shown in Figure 128.

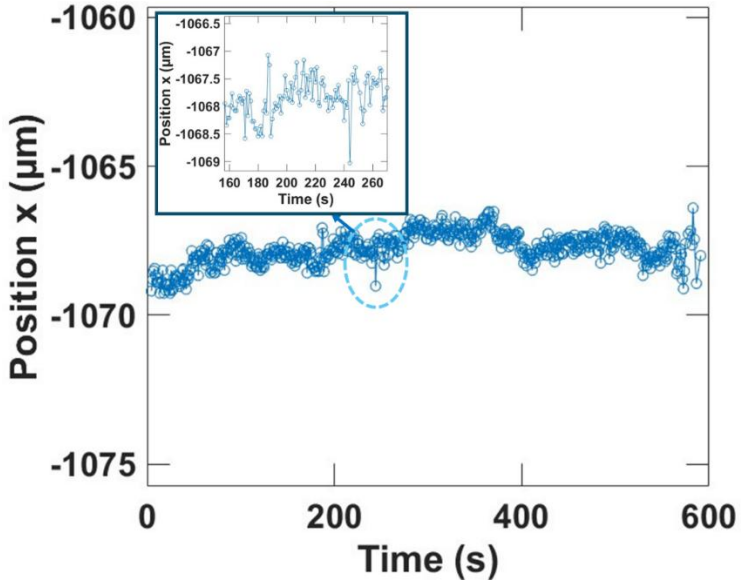


Figure 128: Position x measured for 10 minutes at the resonance angle under TM polarization and with water as the surrounding environment.

No significant position drift was measured. Over 10 minutes, the signal showed fluctuations of about 2 µm and a standard deviation of 0.7 µm.

After this measure, PBS is injected into the fluidic channel, and the resonance angle is found accordingly. In bio-detection experiments, the resonance angle is found with PBS since all solutions (EVs, antibodies) are diluted with PBS. The system is then calibrated using water and diluted glycerin solutions (0.5,1 and 2.5%) to measure the sensitivity of the system and to validate the system's linearity and reliability before starting the bio-experiment. The calibration experiments were conducted according to the experimental procedure described in Section II.3.2. The system is subsequently rinsed with water, and PBS. A new PBS baseline is then established (Figure 129).

License CC BY-NC-ND 4.0

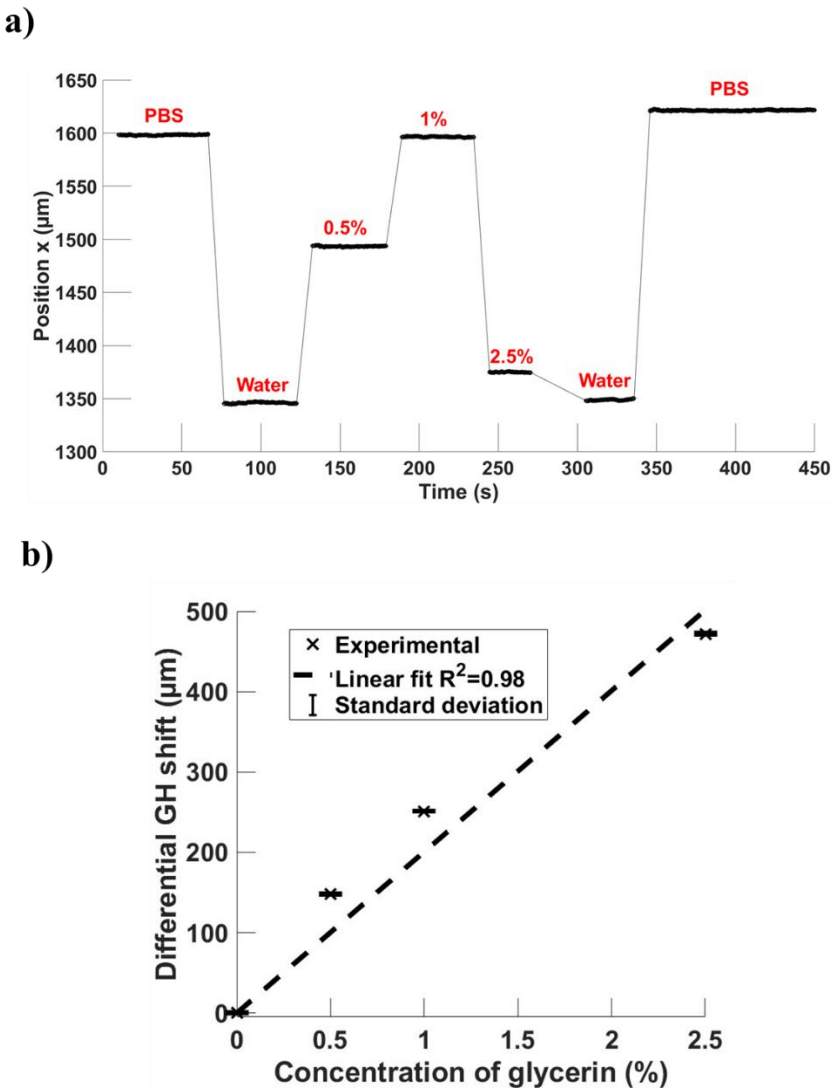


Figure 129 Calibration of the commercial chip before biodetection, a) GH shift for Water, PBS and different glycerin concentrations, b) Linear fit.

It is noticeable that the GH shifts of water and PBS are close in value before and after rinsing (Figure 129-a). The GH shifts return to their original levels with respective errors of 1.4% (PBS) and 0.1% (water). In addition, we observe a change of sign after injecting 2.5% glycerin: GH (1% glycerin-water) > GH (2.5% glycerin-water). To better understand the evolution of the GH response with increasing glycerin concentration, theoretical GH curves are presented around the resonance angle (Figure 130). These illustrations explain how choosing the resonance angle (measurement angle) experimentally influences the measured GH shift.

License CC BY-NC-ND 4.0

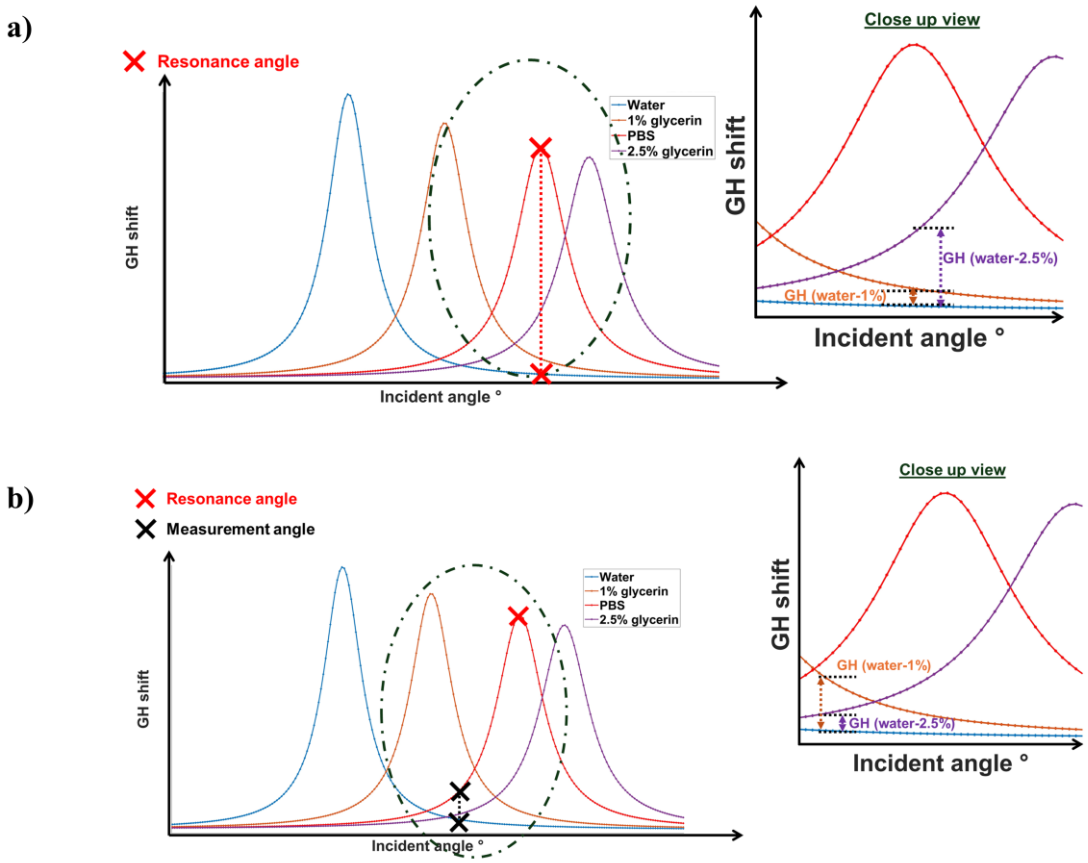


Figure 130 Illustration showing the effect of the choice of the measurement angle (measurement angle is the resonance angle found experimentally) on the measured GH shift, a) The measurement angle found is exactly at the resonance angle of the PBS GH curve and b) The measurement angle is far from the resonance angle of the PBS GH curve.

If the measurement angle (measurement angle is the resonance angle found experimentally) is exactly located at the resonance angle of PBS (Figure 130-a), the GH shift evolution must be linear: GH shift (water-1% glycerin) < GH (water- 2.5% glycerin). In other cases where the measurement angle is far from the actual resonance angle of PBS (Figure 130-b), the GH evolution is no longer linear: GH (water-1% glycerin) > GH (water- 2.5% glycerin). To plot the linear fit curve (Figure 129-b), the differential GH shift (water- 2.5% glycerin) was computed and added to the GH shift of 1% glycerin-water. This produced a high R^2 value of 0.98 and hence suggests a linear trend.

In conclusion, we have shown that the choice of the resonance angle experimentally affects the measured GH shift. Slight deviations from the actual resonance angle can lead to variations in the GH shift measured.

Following the calibration process, the bio-experiments were conducted according to the following procedure:

1. Injection of CD81 antibodies diluted from PBS at 1mM (~20 KDa [174]) with an incubation time around 1 hour,
2. PBS rinse with a new baseline established for 5 minutes measurements,
3. Injection of EGFRvIII EVs diluted with PBS with an incubation time of around 30 minutes,

License CC BY-NC-ND 4.0

4. PBS rinse with a new baseline established for 5-minute measurements.

In this section of the thesis, the antibodies were injected directly onto gold. Gold is widely known for its biocompatibility and its ease of functionalization. It has a high affinity for thiol groups present in some proteins forming quasi-covalent Au-SH bonds (Figure 131) [175]. Consequently, the potential presence of free thiol groups within the antibodies enables direct functionalization of the gold surface.

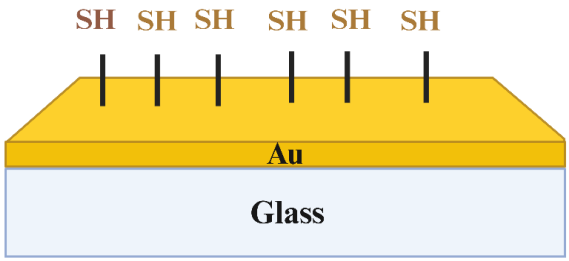


Figure 131 Illustration of the functionalization procedure of the gold's surface based on Au-SH semi-covalent bonds.

The antibodies were first injected on the gold's surface and incubated for approximately 1 hour. The measured GH shift is presented in Figure 132.

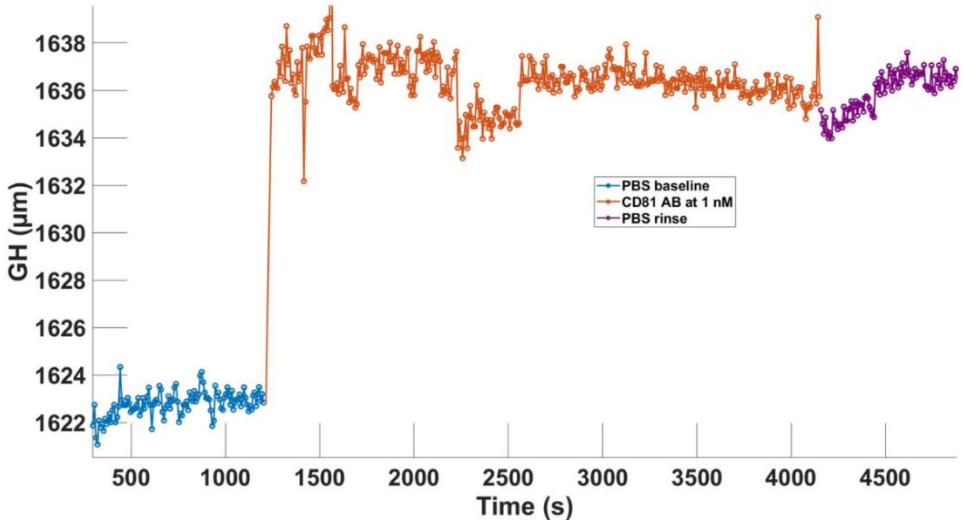


Figure 132 Measurement of the GH shift as a function of time for successive injections of PBS, CD81 AB and PBS to rinse antibodies.

The injection of 1 nM of CD81 antibodies (Figure 132) induced a GH shift of 12 µm with respect to the PBS baseline. The fluidic channel was later rinsed with PBS and the GH signal did not change following the washing step. This confirms the attachment of ABs to the gold's surface.

Following this step, EGFRvIII EVs were injected into the fluidic channel. The evolution of the GH shift is represented in Figure 133.

License CC BY-NC-ND 4.0

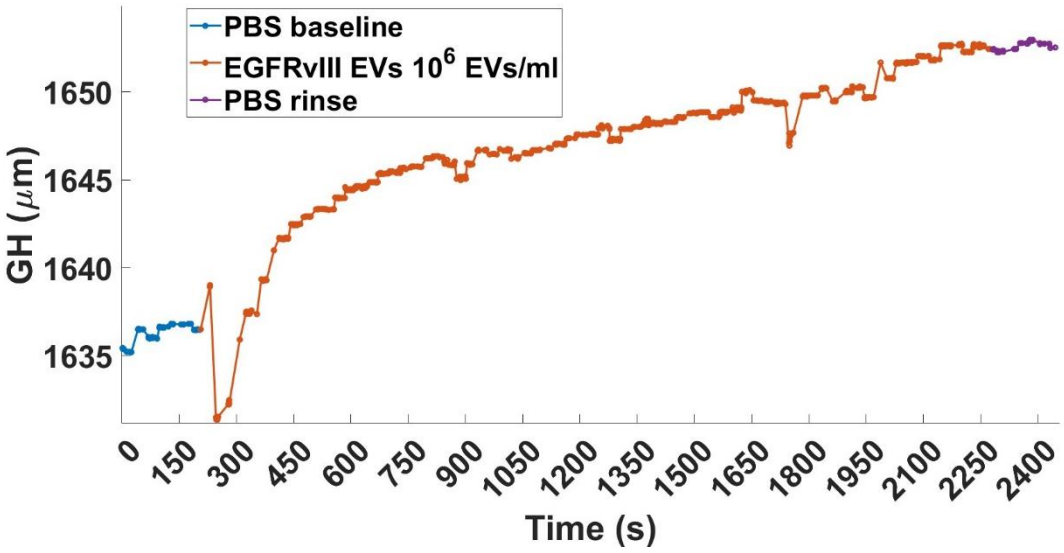


Figure 133 Measurement of the GH shift as a function of time for successive injections of PBS, EGFRvIII EVs diluted at 10^6 EVs/ml and PBS.

The blue curve corresponds to the original PBS baseline, which was measured to demonstrate the stability of the system prior to the injection of the analyte (Figure 133). Injecting EGFRvIII EVs (10^6 EVs/mL) induced a progressive GH shift due to the EVs binding to the antibody. This evolution is caused by a modification of the effective refractive index at the metal-surrounding interface, which introduces a measurable GH shift. The observed trend indicates a rapid increase in the GH shift after injection, followed by smaller variations towards a plateau. Following the PBS rinse, the signal remains stable, confirming the binding of EVs to the antibodies with a GH shift of 15 µm with respect to the initial PBS baseline.

In conclusion, these preliminary results confirm the presence of CD81 biomarkers on EGFRvIII EVs.

To validate the previous result, the binding of EGFRvIII EVs to CD81 antibodies was re-measured on another commercial chip (from the same batch). This time, the experiment was conducted using the prototype with the rotating waveplate. All previous steps remain the same: stability measurements and glycerin calibration.

To illustrate the following processes, we represent the change in position x relative to the rotation of the waveplate. We show a zoomed-in view of the results at a time t. This corresponds to an interval at the end of each measurement. As validated in each Chapter 4, we also positioned the maxima of each measurement at the same position t. We use three methods to evaluate the results (Section IV.5): C1, C2, and C3. To display the evolution of the GH shift, we plot the displacement of the minimum subtracted from TE polarization (C1). Each data point represents the average of four consecutive minima. C2 represents the change in the angular position of the minima, which is computed for each cycle of minima and maxima. C3 indicates the position x measured at an intermediate polarization angle for each cycle of one minimum and one maximum. It was then subtracted from position x at TE. First, we injected ABs directly onto gold. The results are shown in Figure 134.

License CC BY-NC-ND 4.0

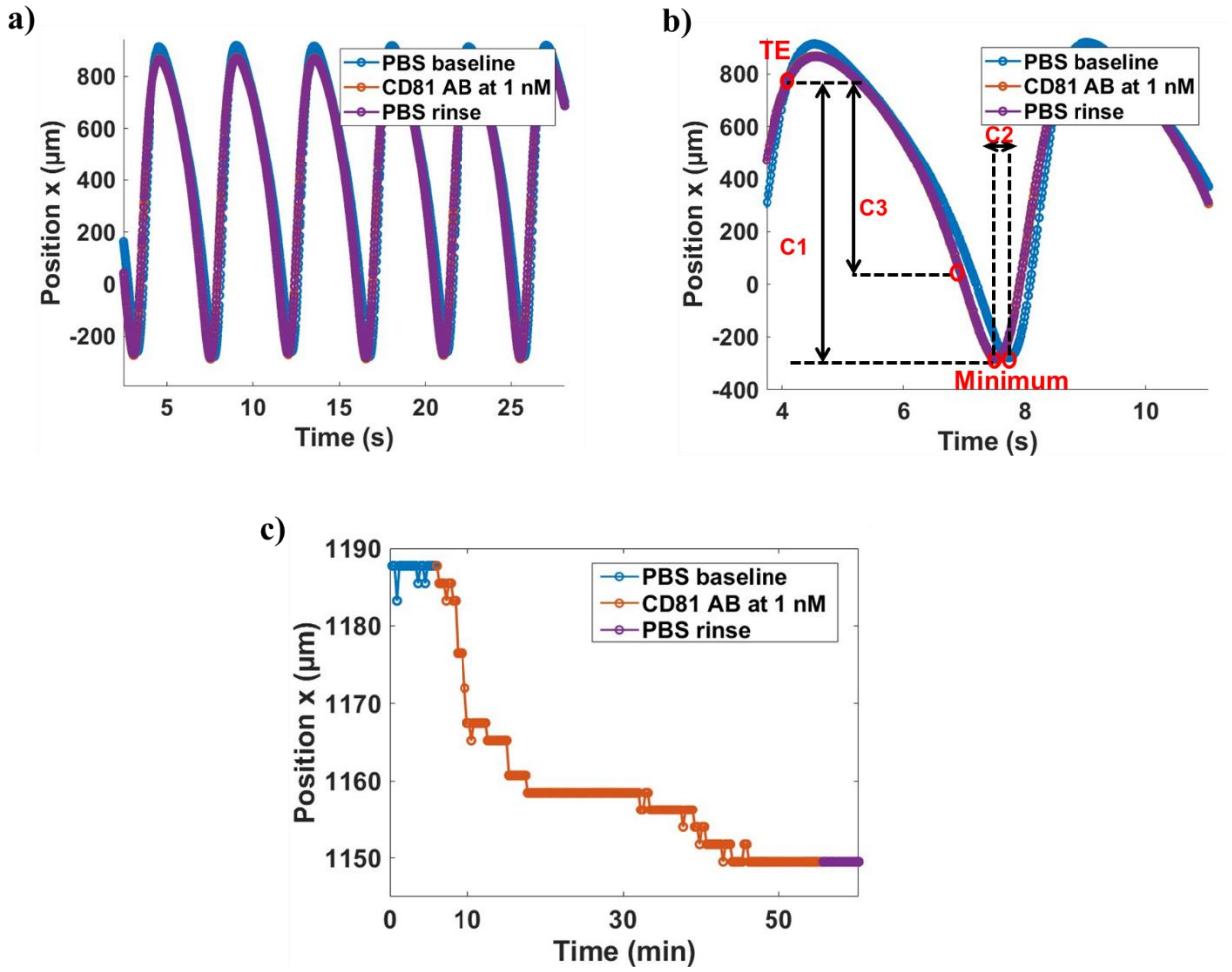


Figure 134 Functionalization of gold with CD81 antibodies. a) Position x with respect to the waveplate rotation, b) zoom in of (a) and c) GH shift of the minima subtracted from TE.

CD81 antibody induced a displacement of the position x curve with respect to the baseline (Figures 134-a and b). This corresponds to a polarization angle shift (C2) of approximately 4°. After rinsing with PBS, the curve remains in its previous position. Additionally, we obtained a GH shift of 40 µm with respect to the PBS baseline measured by C1 (Figure 134-c). The GH signal did not change following the rinsing step. This confirms the attachment of ABs to the gold's surface. It is important to note that the sign of the obtained shift depends on the measurement angle and is not significant for evaluating the binding process.

Next, we present the results of EGFRvIII EVs binding to ABs (Figure 135).

License CC BY-NC-ND 4.0

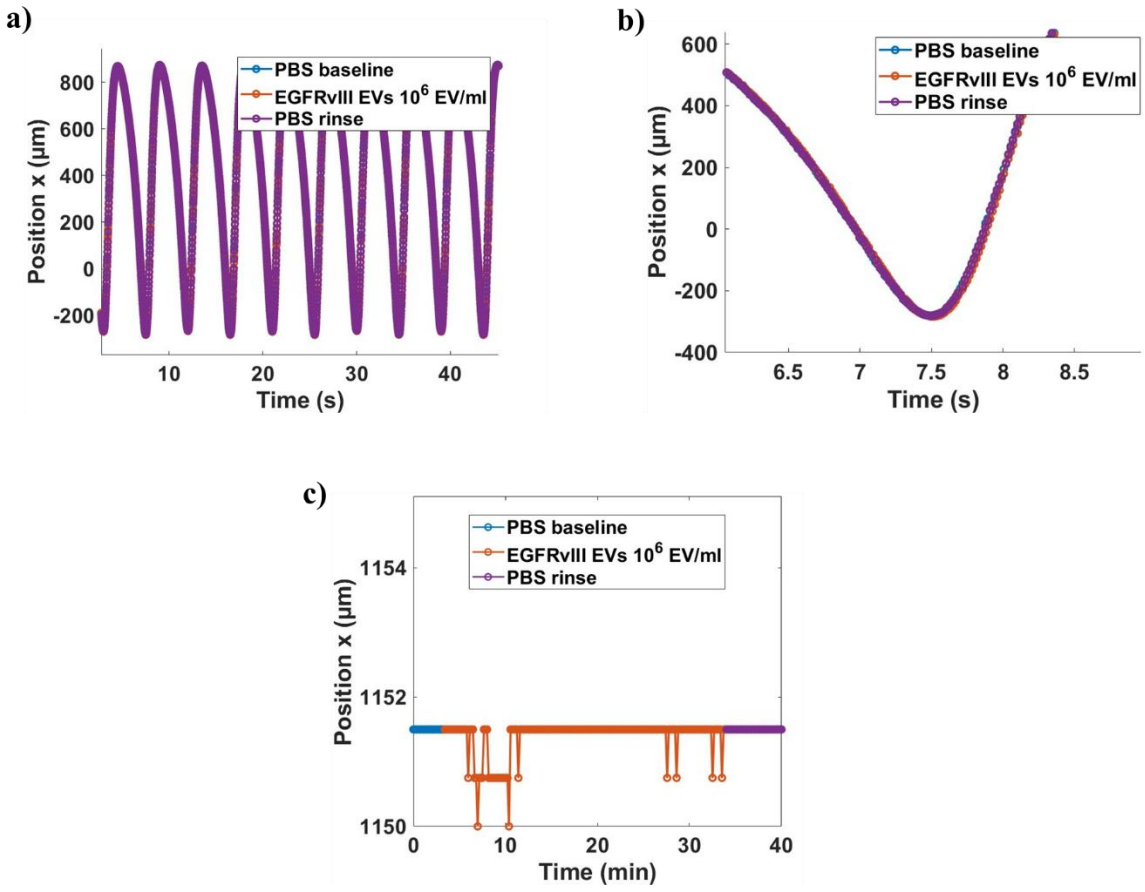


Figure 135 Attachment of EGFRvIII EVs at 10^6 EVs/ml to CD81 ABs. a) Position x with respect to the waveplate rotation, b) zoom in of (a) and c) GH shift of the minima subtracted from TE.

Following the injection of EVs, there was no shift in the position x curve with respect to the baseline. The three curves are shown to be overlapping (Figures 135 a and b). Additionally, there was no shift in the position of the minima (C1). This indicates that the EVs did not bind to the CD81 ABs. This result suggests that there were no available binding sites in the antibody structure, leading us to reconsider our functionalization protocol.

V.3. Analysis of the protocol of gold surface functionalization

The aim of this section is to present the various protocols used in literature to functionalize the gold's surface for biodetection experiments. This can be achieved by either modifying the antibody structure or the gold's surface through the use of additional linkers.

V.3.1. Functionalization protocol based on the modification of the antibody's structure

Gold generally has a high affinity for thiol groups present in some proteins forming quasi-covalent bonds (Au-SH). In parallel, antibodies naturally contain disulfide bonds (S-S bonds) that hold together their inner structure (Figure 136). Additionally, antibodies possess free carboxyl (COOH) and amine (NH_2) groups [176].

License CC BY-NC-ND 4.0

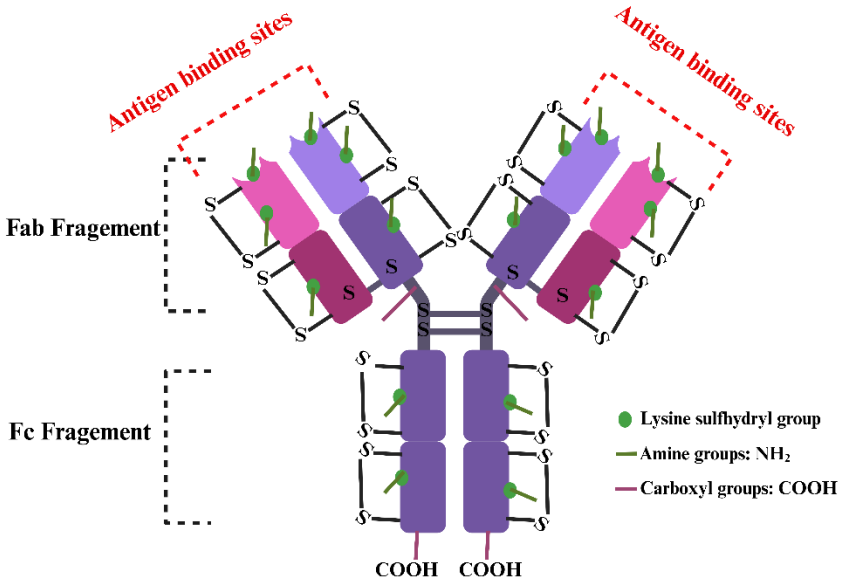


Figure 136 Schematic of the antibody's structure.

One way to functionalize gold is to link it to a thiol group. According to literature, the disulfide bonds inside the ABs are not free to bound with gold. In order to liberate thiol groups, these links must be broken. This can be done through reduction agents such as Tris(2-carboxyethyl)phosphine TCEP (Figure 137-a) [177].

License CC BY-NC-ND 4.0

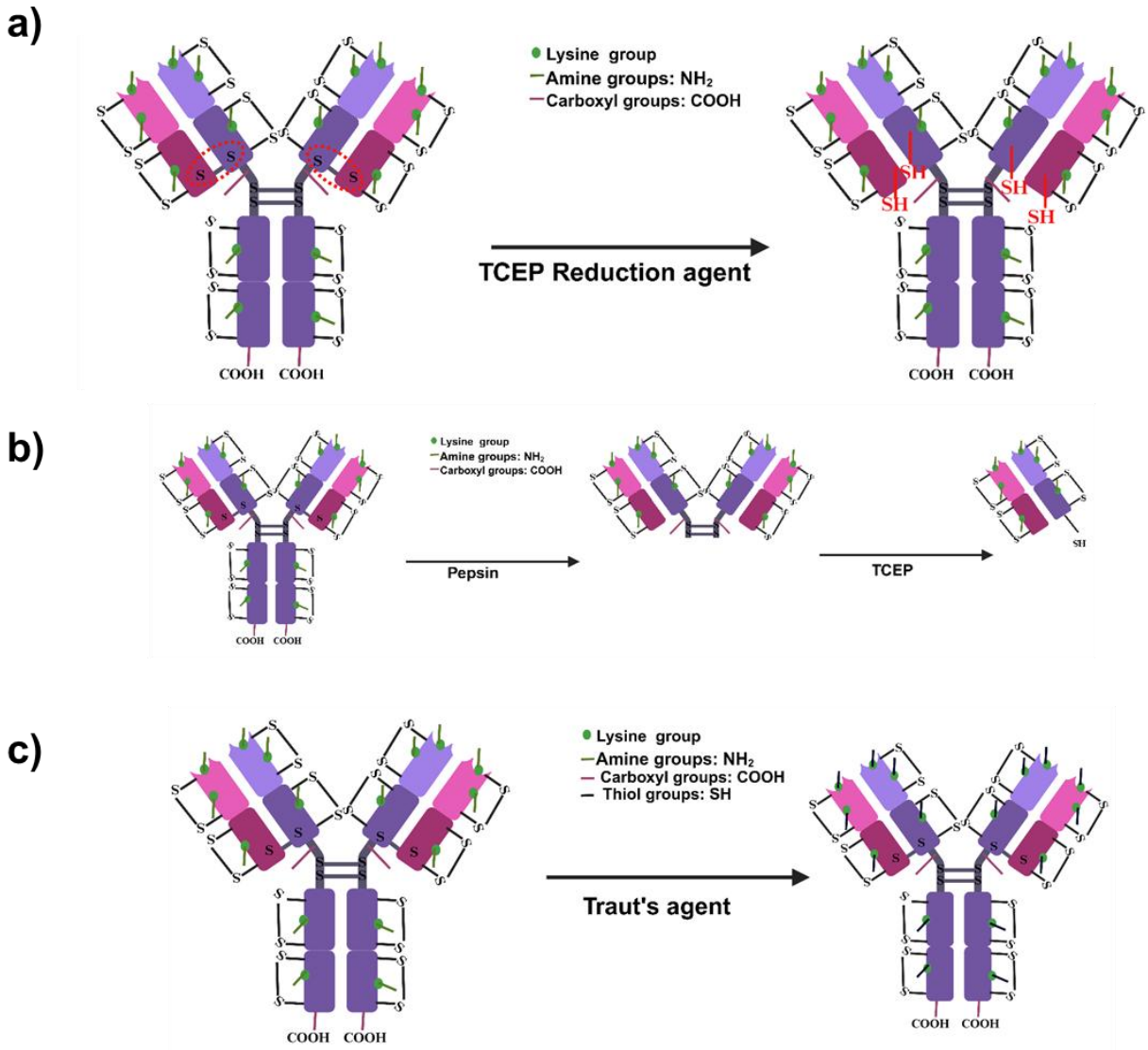


Figure 137 Illustrations showing the modification of the antibody structure by (a) partial reduction of AB using TCEP. The disulfide bridges (marked in red) are broken and free -SH groups are liberated. (b) The creation of free thiol groups. First, the structure of the antibody is broken using Pepsin. Then, the disulfide bonds are broken through TCEP reduction agent. (c) The thiolation of the AB using Traut's agent. Free amine molecules on lysine groups (represented by green lines) are replaced by thiol groups (represented by black lines).

Additionally, literature suggests the breaking of the antibody structure also through agents as Pepsin, Bromelain or Ficin [178]. TCEP reduction solutions then cut disulfide bridge and create free thiol groups (Figure 137-b). This method improves the orientation of the antibody on the surface, thereby allowing the antigen to bind more easily. Another method relies on the addition of SH- groups on lysine residues. This can be done using Traut's reagent (Figure 137-c) [179].

The modification of the antibody using Traut's agent was disregarded, as this approach would present thiol groups throughout the antibody structure. This could potentially block the antigen binding sites. Additionally, the reduction of the antibody was not considered due to the complexity of its implementation. Instead, a functionalization approach based on intermediate linkers was chosen.

License CC BY-NC-ND 4.0

V.3.2. Functionalization of the gold's surface through intermediate linkers

Instead of altering the antibody's structure, some research relies on the addition of thiolated linkers directly on the gold's surface. This can be achieved using 11-mercaptoundecanoic acid (MUA). The thiol groups bind to the gold from one side. On the other side, the free carboxyl groups (COO-) form electrostatic bonds with the positively charged amine of the antibody, as illustrated in Figure 138 [180].

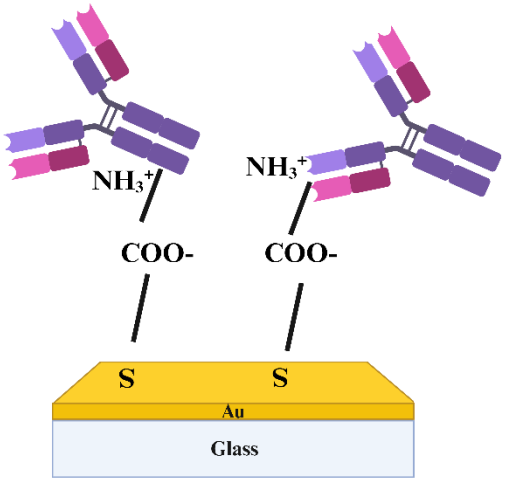


Figure 138 Illustration showing the functionalization of gold with MUA (11-Mercaptoundecanoic acid).

The main disadvantage of this method is the random orientation of ABs on the surface, since free amine groups are present in all regions of the antibody (Figure 138).

On the other hand, the binding of antibodies via their COOH groups favors the adsorption of the antibodies via their Fc regions leaving the antigen binding sites (Fab arms) free [181]. To this extent, molecules such as APTES (3-Aminopropyl)triethoxysilane contain positively charged amine groups in their structure. Once diluted in PBS, they can electrostatically bind to the negatively charged carboxyl groups of the antibody. Attaching APTES to the gold can be achieved through:

- **Electrostatic interactions:** Electrostatic interactions can contribute to the adsorption of APTES on gold when the experiments are realized with solutions diluted in PBS. Phosphate anions present in PBS can naturally adsorb on the metal, producing a negatively charged surface [182]. Free amine groups of APTES become positively charged in an aqueous medium and can electrostatically adhere to the negatively charged gold. This interaction is considered noncovalent, reversible and can break after strong rinsing procedures. Simultaneously, APTES molecules undergo condensation reactions between their silanol (Si-OH) groups. These reactions lead to the formation of siloxane links (Si-O-Si) between neighboring molecules, developing a partially polymerized chain at the interface. This process is known as vertical polymerization and can take place when the concentration of APTES is high. In this configuration, a portion of amine groups remain free to attach to the carboxyl groups of antibodies (Figure 139) [181,183].

License CC BY-NC-ND 4.0

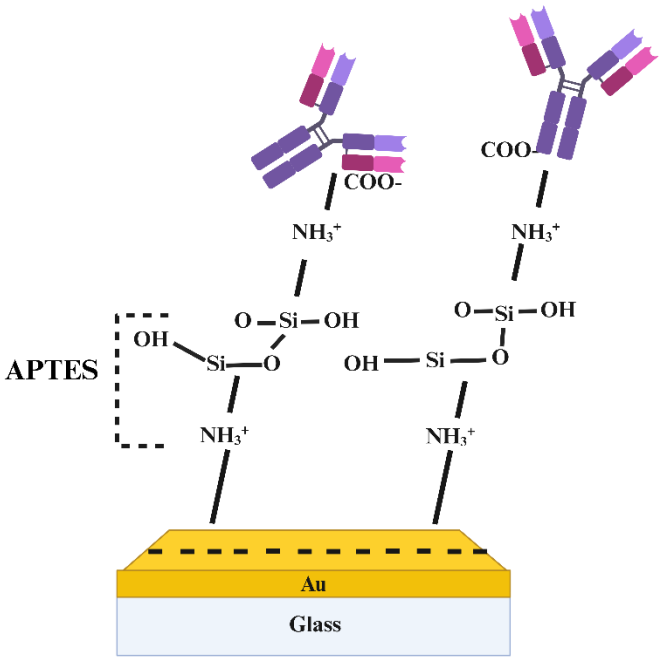


Figure 139 Illustration showing the binding of antibodies to gold through their COO- groups, and with an intermediate layer of APTES.

- **Covalent interaction:**
  - By oxidizing the metal's surface with -OH groups (using acid solutions such as KOH or NaOH), covalent bounds can be formed between OH and Si atoms present in APTES. This leaves the amine groups free to attach antibodies via their COO- groups (Figure 140) [181].

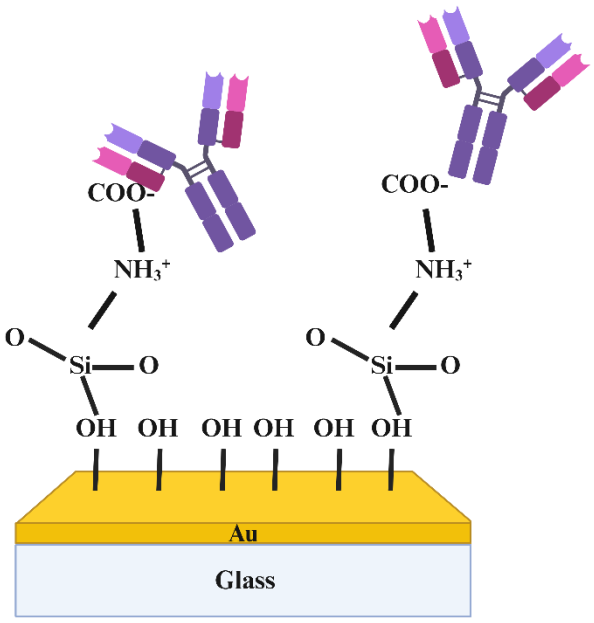


Figure 140 Illustration showing the attachment of antibodies with an intermediate layer of APTES and an oxidized gold surface.

License CC BY-NC-ND 4.0

- Using an intermediate layer of 3-Mercaptopropyl)trimethoxysilane (MPTMS): MPTMS attaches to the gold layer due to the natural affinity of the metal for thiol groups present in the molecule. Silane groups of MPTMS remain free for further reaction and hydrolyze into silanols (Si-OH). The injection of APTES induces condensation reactions between silanol groups present in both APTES and MPTES leading to the formation of (Si-O-Si) links. In this configuration, amine groups present in APTES are free to bind to carboxyl groups present in antibodies (Figure 141) [184].

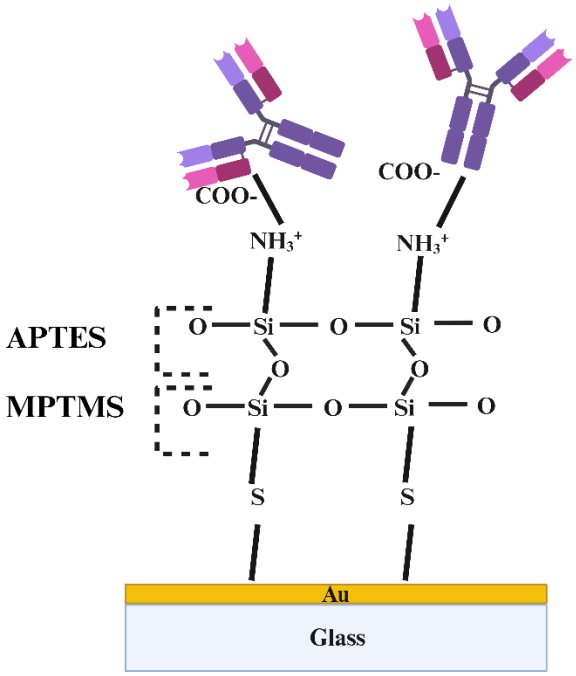


Figure 141 Illustration of the binding of AB on gold with intermediate layers of MPTMS and APTES.

Literature additionally suggests the functionalization of the surface with protein A, G or A/G to control the orientation of the antibody. In this case, antibodies are forced to attach by their Fc region [181]. Gold's surface can be first functionalized with a thiolated linker (such as MUA) to create free carboxyl groups. Protein A possesses free amine groups that can later bind with carboxyl groups (Figure 142).

License CC BY-NC-ND 4.0

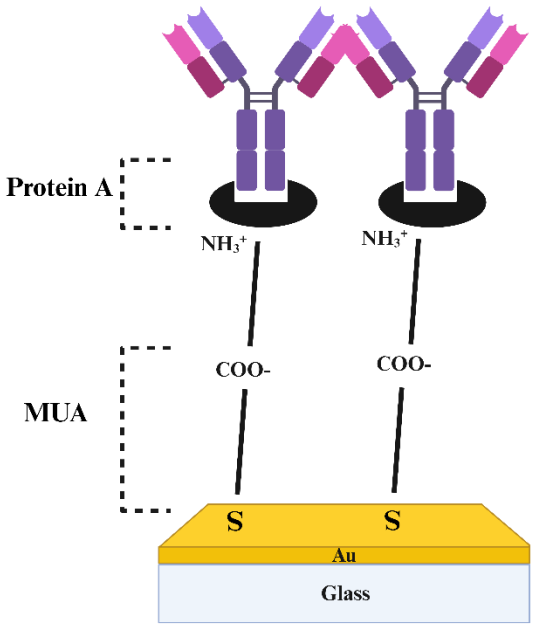


Figure 142 Illustration of the binding of AB on gold with intermediate layers of MUA and protein A (oriented immobilization of AB).

Since SPR chips are generally reused for several tests and due to the lack of time to study different regeneration protocols, it was decided that the surface should be electrostatically functionalized to facilitate its cleaning. The use of protein A to improve the orientation of AB was identified as a potential approach. However, protein A is a relatively large molecule (~42 KDa), which introduces an additional intermediate layer on the gold limiting the measurement range. Hence, this but was not realized within the scope of this thesis.

To validate the functionalization protocol, several surface treatments were realized on different commercial chips (from the same batch). First, the primary CD81 antibody was injected onto a pre-functionalized surface (treated with/without KOH and with/without APTES). It was then rinsed with PBS to remove unbound antibodies. The secondary antibody can bind to the primary antibody, emitting a fluorescent signal. The mixture was subsequently rinsed with PBS. This signal was observed under a microscope. It is proportional to the quantity of secondary antibodies present on the surface after PBS rinse. A control test was conducted simultaneously, where secondary antibodies were injected directly onto the gold surface. This step accounts for non-specific binding of the secondary antibody to the gold. The experiments were done with CAPTuR and five conditions were investigated:

1. Untreated gold surface + CD81 antibody (incubated for 1 hour and diluted with PBS at 1 nM) + PBS rinse + secondary fluorescent antibody (incubated for 1 hour and diluted with PBS at 1 nM) + PBS rinse.
2. KOH treatment (incubated for 5 minutes and diluted with water at 1%) + Injection of water (5 minutes) + CD81 antibody (incubated for 1 hour and diluted with PBS at 1 nM) + PBS rinse+ secondary fluorescent antibody (incubated for 1 hour and diluted with PBS at 1 nM) + PBS rinse.
3. KOH treatment (incubated for 5 minutes and diluted with water at 1%) + Injection of water (5 minutes) +APTES (incubated for 1 hour and diluted with PBS at 1 mM) + PBS rinse+ CD81 antibody (incubated for 1 hour and diluted with PBS at 1 nM) + PBS rinse+

License CC BY-NC-ND 4.0

secondary fluorescent antibody (incubated for 1 hour and diluted with PBS at 1 nM) + PBS rinse.

4. No treatment + secondary fluorescent antibody (incubated for 1 hour and diluted with PBS at 1 nM) + PBS rinse.
5. APTES (incubated for 1 hour and diluted with PBS at 1 mM) + PBS rinse + CD81 antibody (incubated for 1 hour and diluted with PBS at 1 nM) + PBS rinse+ secondary fluorescent antibody (incubated for 1 hour and diluted with PBS at 1 nM) + PBS rinse.

The results are shown in Figure 143 below.

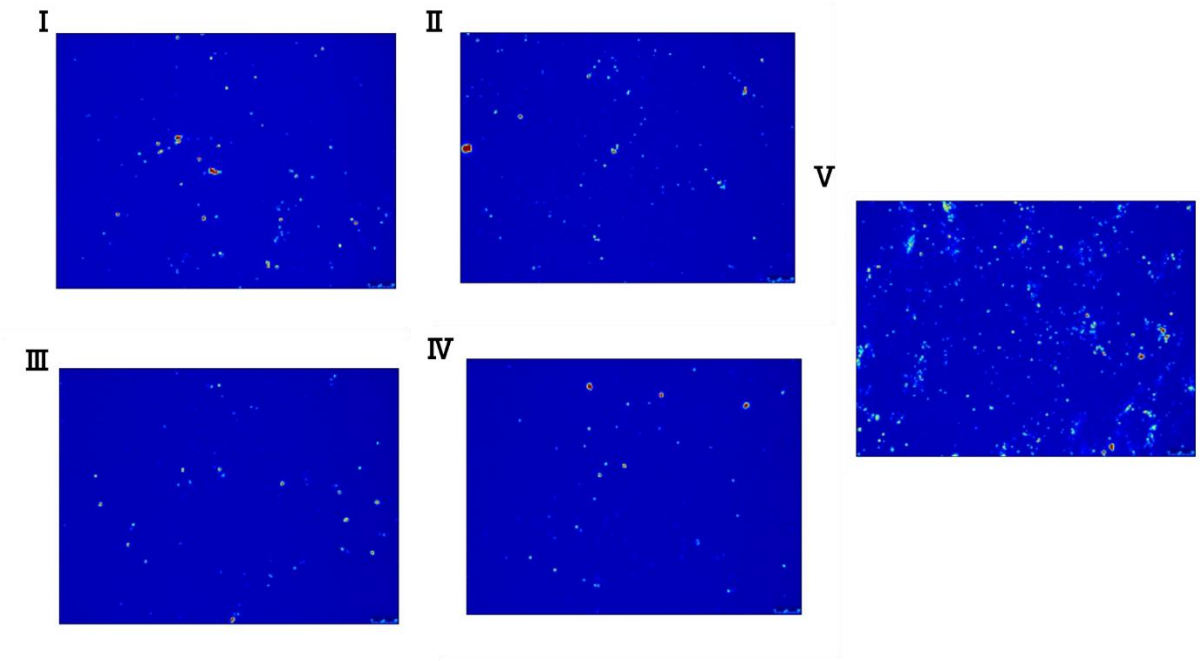


Figure 143 Visualization of the commercial chips treated with secondary fluorescent CD81 antibodies, I) No treatment+ fluorescent antibody, II) No treatment + CD81 antibody +fluorescent antibody, III) KOH+ water + CD81 antibody + fluorescent antibody, IV) KOH + water + APTES+ CD81 antibody+ fluorescent antibody, and V) APTES+ CD81 antibody+ fluorescent antibody.

We observed a small fluorescent signal in the control condition (Case I), which indicates that the secondary antibody bound to the gold to some extent. A similar fluorescent signal was obtained in case II, revealing the antibody's limited binding to gold. Following KOH treatment, the fluorescence signal remains the same (Case III), implying that the KOH pretreatment is ineffective. This suggests the inability to actively oxidize the gold surface with a 1% KOH solution. Hence, limited -OH groups were created, and APTES can no longer adsorb to the gold surface.

The highest fluorescent signal was obtained when APTES was used to functionalize the gold surface. In this case, APTES directly absorbs onto the gold surface via electrostatic interactions. The primary antibody binds to APTES via electrostatic interactions between its negatively charged carboxyl group and the positively charged amine groups of the APTES.

In conclusion, we demonstrated the difficulty of functionalizing the surface of gold directly with antibodies. Additionally, oxidizing the gold surface with 1% KOH was deemed ineffective. The optimal functionalization protocol involved injecting APTES into the gold surface. It was adopted for all our future biodetection tests.

License CC BY-NC-ND 4.0

V.4. Biodetection tests using APTES-functionalized gold surfaces

The experiments presented in this section are focused on measuring the binding of EVs to antibodies. This is achieved by employing the selected APTES-based functionalization protocol. These tests were conducted using the rotating waveplate interrogation method. The N24 chip coupled with SF11 prism was used for all tests.

To assess the stability of the system, the position x of the reflected beam was measured using water as the surrounding medium and under TM polarization. The results are shown in Figure 144.

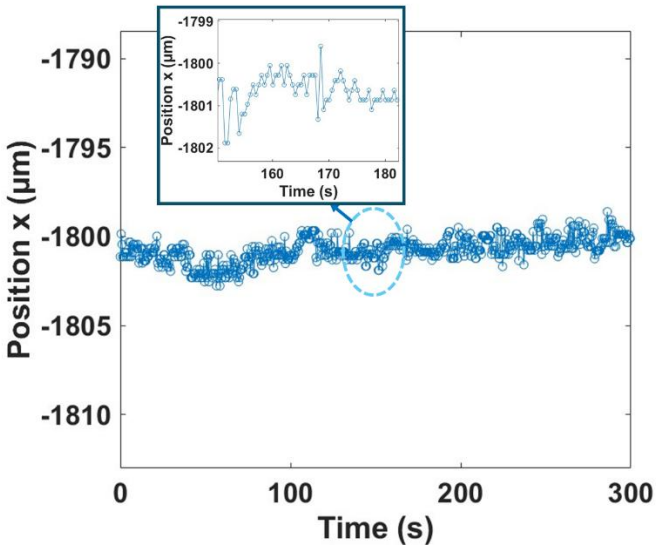


Figure 144 Position x measured for 5 minutes at the resonance angle of water under TM polarization.

No drift was recorded in the position x measurements. The noise accounted for a standard deviation of approximately 0.7 µm, with fluctuations of up to 2 µm.

Following this, PBS was introduced into the fluidic channel, and the resonance angle was determined. We then calibrated the system using water and diluted glycerin solutions. The chip was rinsed with water, and a new PBS baseline was established. We represent the data as explained in Section V.2. The results are shown in Figure 145.

License CC BY-NC-ND 4.0

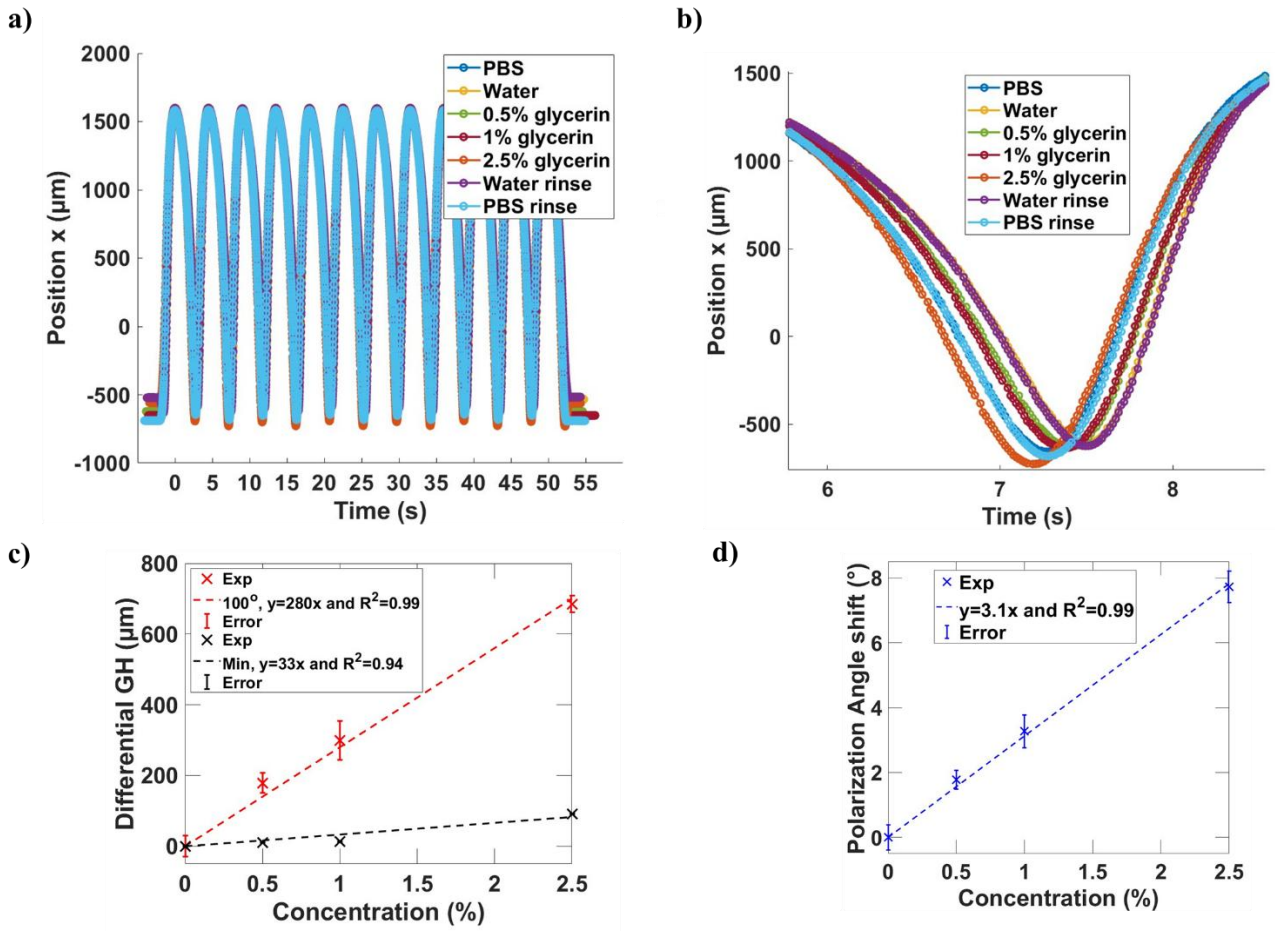


Figure 145 Calibration curves of the N24 chip with the rotation waveplate interrogation method, a) Position x of the reflected beam vs waveplate rotation, b) zoom in section of (a), c) Differential GH shift extracted for 2 different configurations: GH shift at the optimized polarization angle 100° and average displacement of the minima and, d) shift of the polarization angle (experimental and linear fit).

We observed a shift in the position x curves between PBS, water, and diluted glycerin solutions. After a water or PBS rinse, the curves return to their respective initial positions before glycerin (Figures 145 a and b).

The GH shift obtained using C1 was low (30 µm between PBS and water, Figure 145-c). However, the shift at the polarization angle of 100° (C3) was found to be 11 times larger. The noise induced by the inhomogeneity of the motor produced large standard deviations which makes this approach unsuitable to measure smaller GH shifts for the time being. As expected, the polarization angle shift shows a linear progression trend with respect to the concentration of glycerin (C2, Figure 145-d).

The bio-experiments were conducted according to the functionalization protocol described below. It is important to note that the fluids injections were performed manually via syringes:

- Functionalization with APTES diluted from PBS at 1 mM (221.37 Da [185]) with an incubation time around 1 hour,
- PBS rinse. A new stable baseline was established for 5 minutes,
- The previous solution was removed and antibodies diluted from PBS at 1mM (~20 KDa [174]) where injected with an incubation time around 1 hour,

License CC BY-NC-ND 4.0

- PBS was used to rinse unbound molecules. A new baseline was established for 5 minutes,
- Injection of EVs diluted with PBS directly in the fluidic channel with an incubation time of around 30 minutes,
- PBS was used to rinse unbound molecules. A new baseline was established for 5 minutes.

The binding curves of the different analytes (binding of APTES to gold, antibody to APTES and EVs to antibody) are plotted by tracking changes in the position of the minima subtracted from the position of TE.

In the following section, two measurements are presented using the same N24 chip:

- Reference experiment: Binding of U87-MG EVs to CD81 ABs,
- Control experiment: Binding of EGFRvIII EVs to c-MET antibodies.

V.4.1. Detection of CD81 with U87-MG EVs

After validating the linearity and stability of the system, the SPR chip was tested for the detection of U87-MG EVs with CD81 antibodies. We first begin by functionalizing the gold surface with APTES. We represent the data as explained in Section V.2. The results are shown in Figure 146.

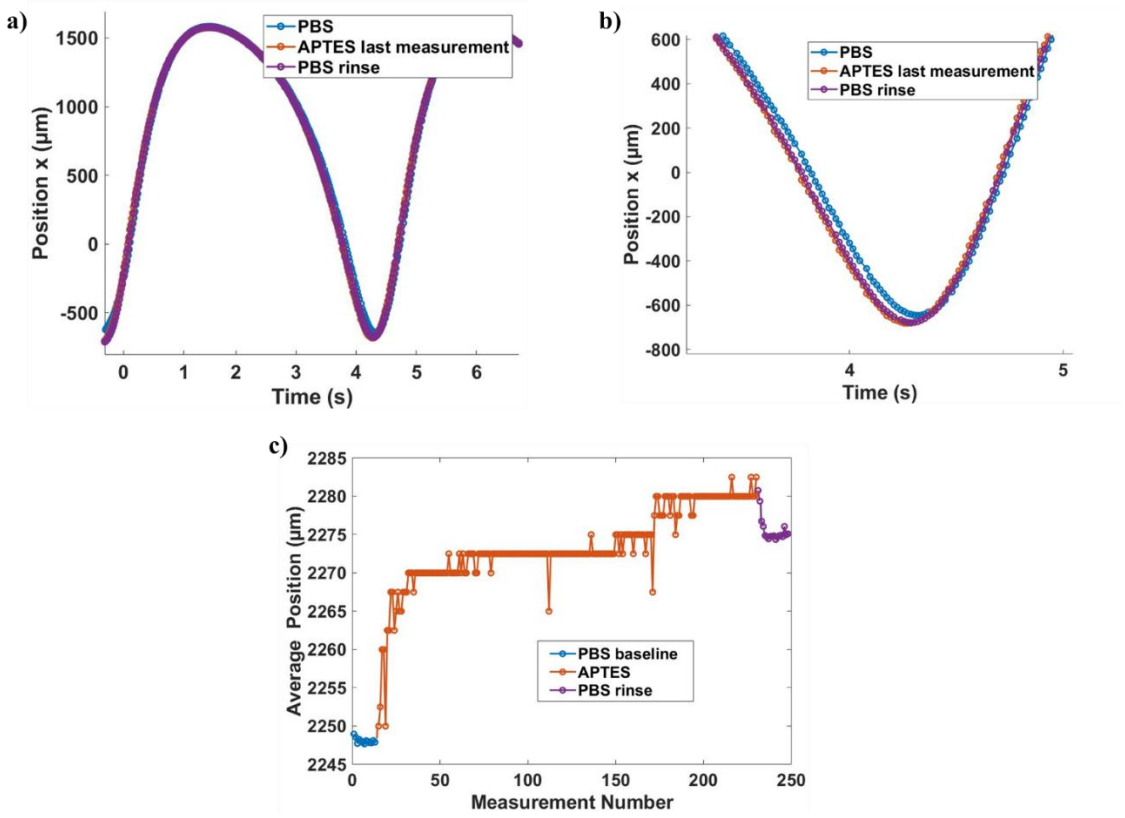


Figure 146 Functionalization of gold with APTES, a) Position x with respect to the waveplate rotation, b) zoom in of (a) and c) GH shift of the minima subtracted from TE.

License CC BY-NC-ND 4.0

APTES adsorption on gold surface induces shift in the position x curve with respect to the PBS baseline (Figures 146-a and b). A PBS rinse leaves the curve in the same position. The GH shift measured using C1 (Figure 146-c) corresponds to 33 µm. PBS rinse removed some unbound molecules. The remaining GH shift accounts for 28 µm, indicating that some APTES molecules remain attached to the gold surface.

The GH shift measured by the displacement of the minima remains low. Therefore, additional methods to evaluate sensitivity are introduced in the following Table 15. The standard deviations are computed over the last 5 minutes of the measurement (once the signal has stabilized).

Table 15 PBS baseline-APTES GH shift after PBS rinse measured with C1, C2 and C3.

Calculation method	Shift	Standard deviation (µm)
Min (C1)	**33 µm**	**0.7**
Optimized polarization angle (C3)	**105 µm**	**37.5**
Polarization angle shift (C2)	1.0°	0.5°

We measured a GH shift value of 105± 38 µm using C3. The higher GH shift is however counterbalanced by the high noise (38 µm). This result highlights the importance of choosing the correct polarization angle to improve the sensitivity of the measurement. The attachment of APTES is also evident through C2 with a polarization angle shift of 1.0°± 0.5°.

After attaching APTES to gold, we inject the antibodies into the fluidic channel and monitor their binding for 1 hour. The results are presented in Figure 147.

License CC BY-NC-ND 4.0

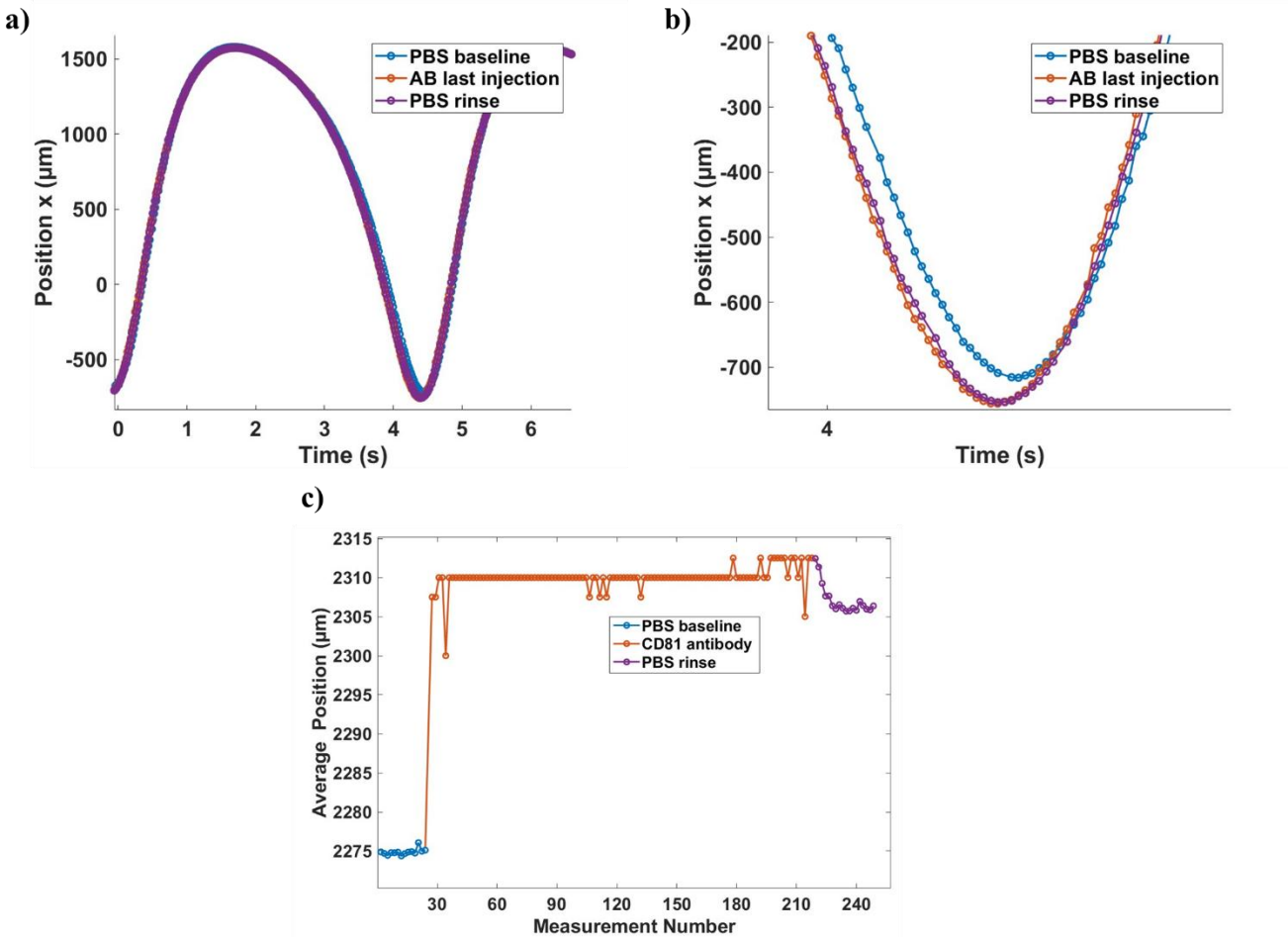


Figure 147 Attachment of CD81 AB to APTES, a) Position x with respect to the waveplate rotation, b) Zoom-in of a) and c) Evolution of the position of the minima (each point represents the average of 4 minima) within 1 hour incubation of the AB.

We noticed a shift in the position x curves between PBS baseline and ABs (Figures 147 a-b). Following PBS rinse, the curve remains in its position. Additionally, we measured a GH shift of 35 µm with respect to the PBS baseline (C1, Figure 147-c). A subsequent rinse removed unattached antibodies. The remaining GH shift accounts for 28 µm with respect to the baseline. This indicates that some APTES molecules remain bound to APTES.

Similarly, the GH shift was additionally extracted using C1, C2 and C3. The results are presented in Table 16).

Table 16 PBS baseline-AB GH shift after PBS rinse measured with C1,C2 and C3.

Calculation method	Shift	Standard deviation (µm)
Min (C1)	**35 µm**	**0.4**
Optimized polarization angle (C3)	**126 µm**	**13.7**
Polarization angle shift (C2)	1.4°	0.5°

License CC BY-NC-ND 4.0

We observed a GH shift of 126±14 µm between PBS and AB using C3. Additionally, a remaining polarization angle shift of 1.4° (C2) was observed after PBS rinsing, validating the attachment of ABs to the APTES functionalized surface.
After binding the antibodies to APTES, we successively inject EVs solution starting from the lowest concentration 10^2 EVs/ml. The fluidic channel has a volume of 500 µL, meaning there are approximately 500 EVs inside the channel. The results are shown in Figure 148.

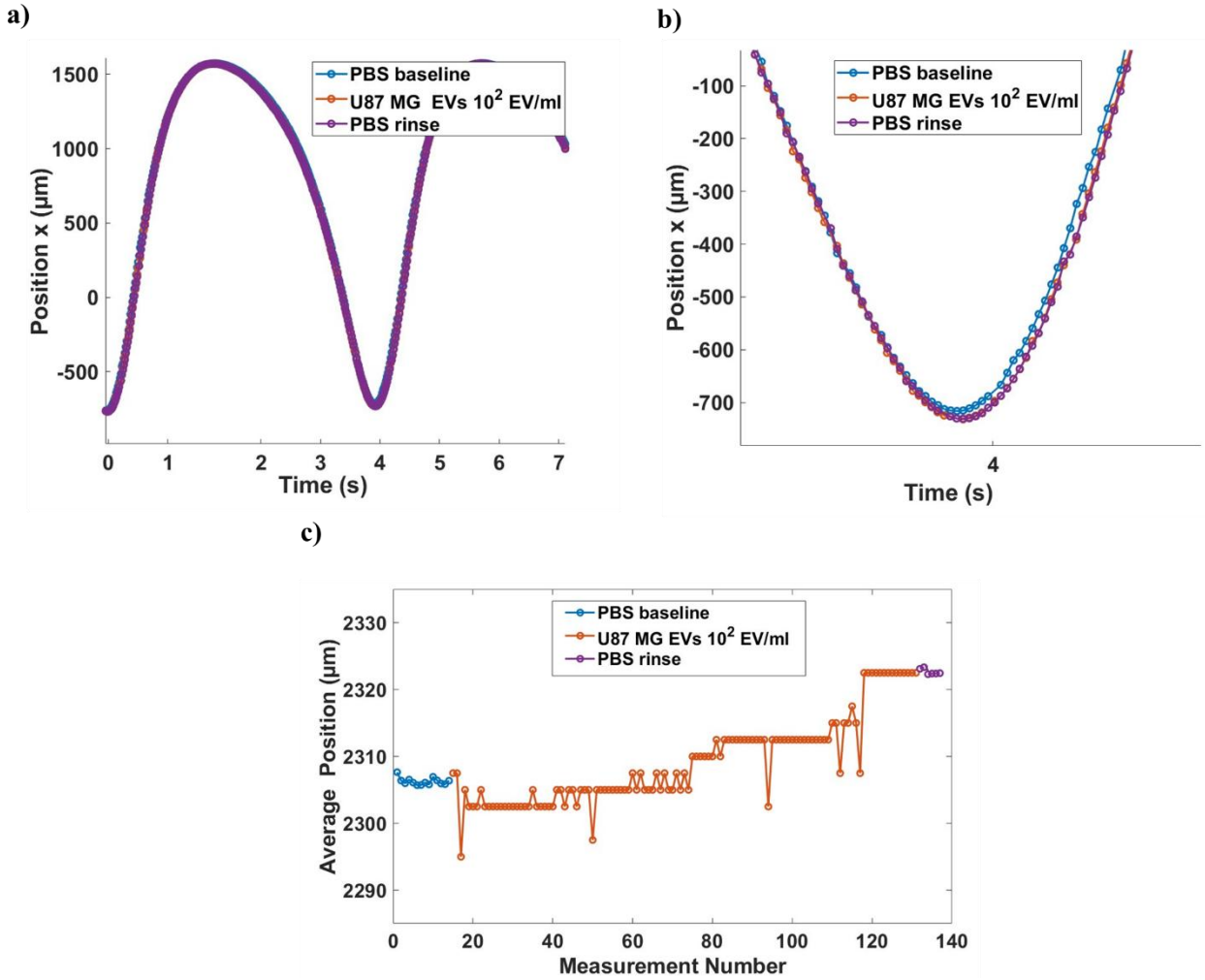


Figure 148 Attachment of U87 MG EVs diluted at 10^2 EVs/ml to CD81, Position x measured with respect to the waveplate rotation, b) Zoom-in of a) and c) Evolution of the position of the minima (each point represents the average of 4 minima) within 1 hour incubation of the EVs.

As expected, we observe a shift in the position x curve of the EVs relative to the baseline. Additionally, the EVs and PBS rinse curves overlap (Figures 148 a-b). Furthermore, we detected a 16 µm GH shift caused by the EVs. This value remained unchanged following the PBS rinse, proving that the EVs were firmly bound to the ABs. The GH shift was additionally obtained with C1, C2 and C3. The results are presented in Table 17.

License CC BY-NC-ND 4.0

Table 17 PBS baseline-U87 MG EVs (at 10^2 EV/ml) GH shift after PBS rinse measured with C1, C2 and C3.

Calculation method	Shift	Standard deviation (µm)
Min (C1)	**16 µm**	**0.9**
Optimized polarization angle (C3)	**9 µm**	**57.1**
Polarization angle shift (C2)	0.4 °	0.5°

The GH shift we measured with C3 was smaller (9 µm) than the value from C1. Additionally, we obtained a 0.4° shift in polarization angle. These results validate the N24 chip's ability to detect small concentrations of EVs.

The SPR chip functionalized with APTES and CD81 antibodies was incubated with an additional solution of U87-MG EVs (10^4 EVs/ml). The results are presented in Figure 149.

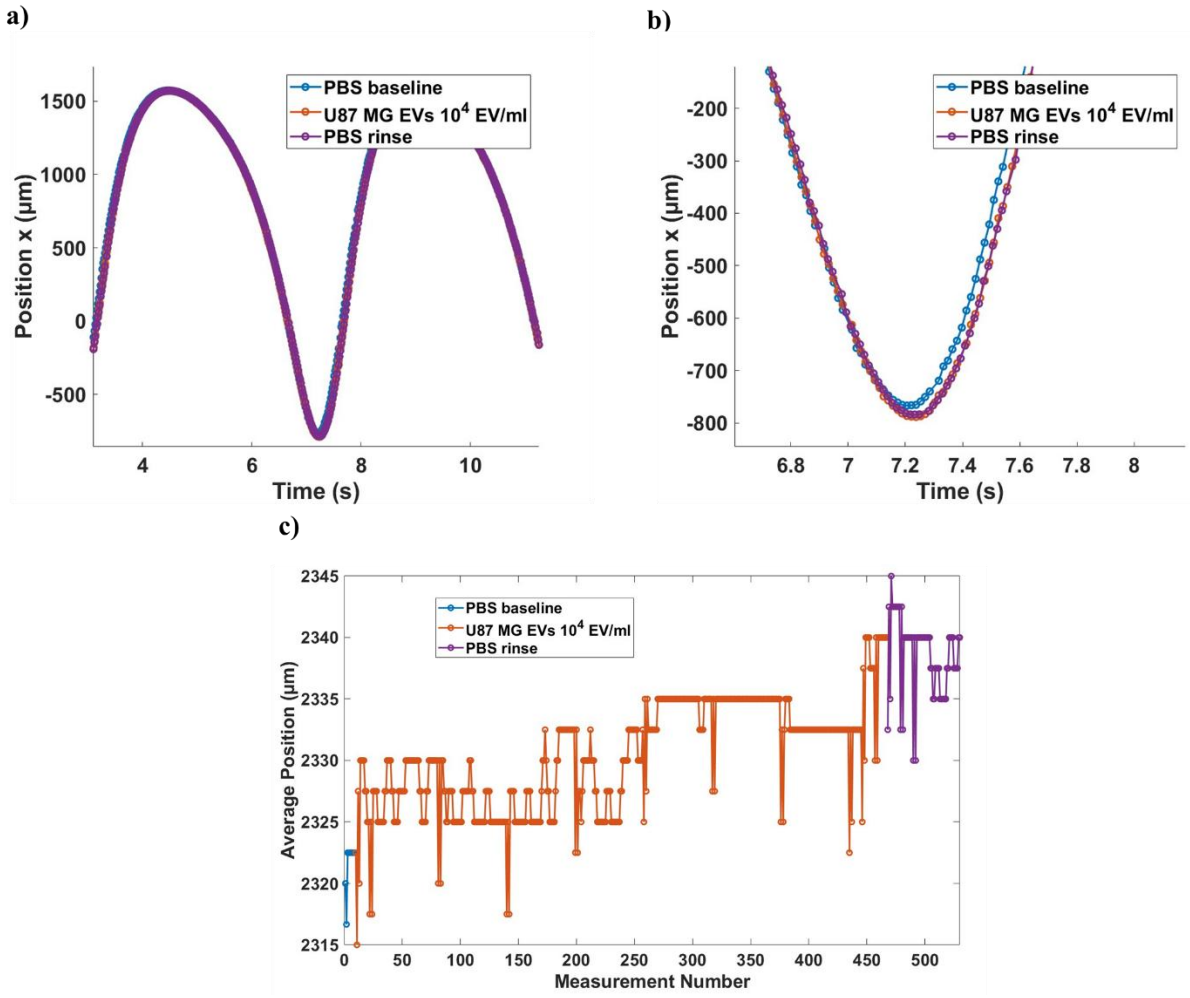


Figure 149 Attachment of U87 MG EVs diluted at 10^4 EVs/ml to CD81, Position x with respect to the waveplate rotation, b) Zoom-in of a) and c) Evolution of the position of the minima (each point represents the average of 4 minima) within 1 hour incubation of the EVs.

License CC BY-NC-ND 4.0

As previously observed, injecting additional EVs resulted in a shift of the position x curve (Figures 149 a-b). As shown before, the EV and PBS rinse curves coincide. On the other hand, the GH signal increased by 17 µm compared to the original PBS baseline using C1 (Figure 149-c). This value remained consistent after rinsing, further proving the EVs' binding to the antibodies.

In conclusion, we demonstrated the prototype's reliable functioning. EVs were detected down to the concentration of 10^2 EV/ml (or 500 EVs for our 500 µl fluidic channel). However, an additional control experiment is needed to validate the specificity of the binding.

V.4.2. Control experiment: binding of EGFRvIII EVs to c-MET antibodies

The objective of this section is to conduct a control experiment to confirm the specific binding of EVs to antibodies and validate the previous result. Our team previously conducted control experiments on the reference platform to verify the specificity of the interactions. This was done using HSC-70 antibodies. U87 MG EVs are known to lack HSC-70 proteins [174]. Therefore, the EVs failed to bind to the antibodies, and the signal was completely rinsed off after washing with PBS. In this section, we will conduct an additional control experiment by testing c- EGFRvIII EVs with MET antibodies.

c-MET are types of receptor proteins, that after binding to their specific ligand, hepatocyte growth factor (HGF), activate a chain of cellular signaling pathways including cell migration, proliferation, and motility. Under normal conditions, this protein regulates cell growth required during tissue repair. During cancerous cases, this protein is turned on in an abnormal and uncontrolled way, highly influencing cancer cells growth and invasion [186]. According to literature, the presence of c-MET has been proven inside EGFRvIII EVs, which are considered to play a major role in tumor recurrence after a period of remission [187,188]. However, the presence of c-MET at the surface of EGFRvIII has not been demonstrated therefore EGFRvIII EVs are not expected to bind to c-MET antibodies during SPR bio-experiments. The following control experiment validated this concept.

The functionalization procedure is the same as that described in the previous section. We present the data as explained in Section V.2. First, the gold surface is functionalized with 1 mM APTES for one hour. The results are shown in Figure 152.

License CC BY-NC-ND 4.0

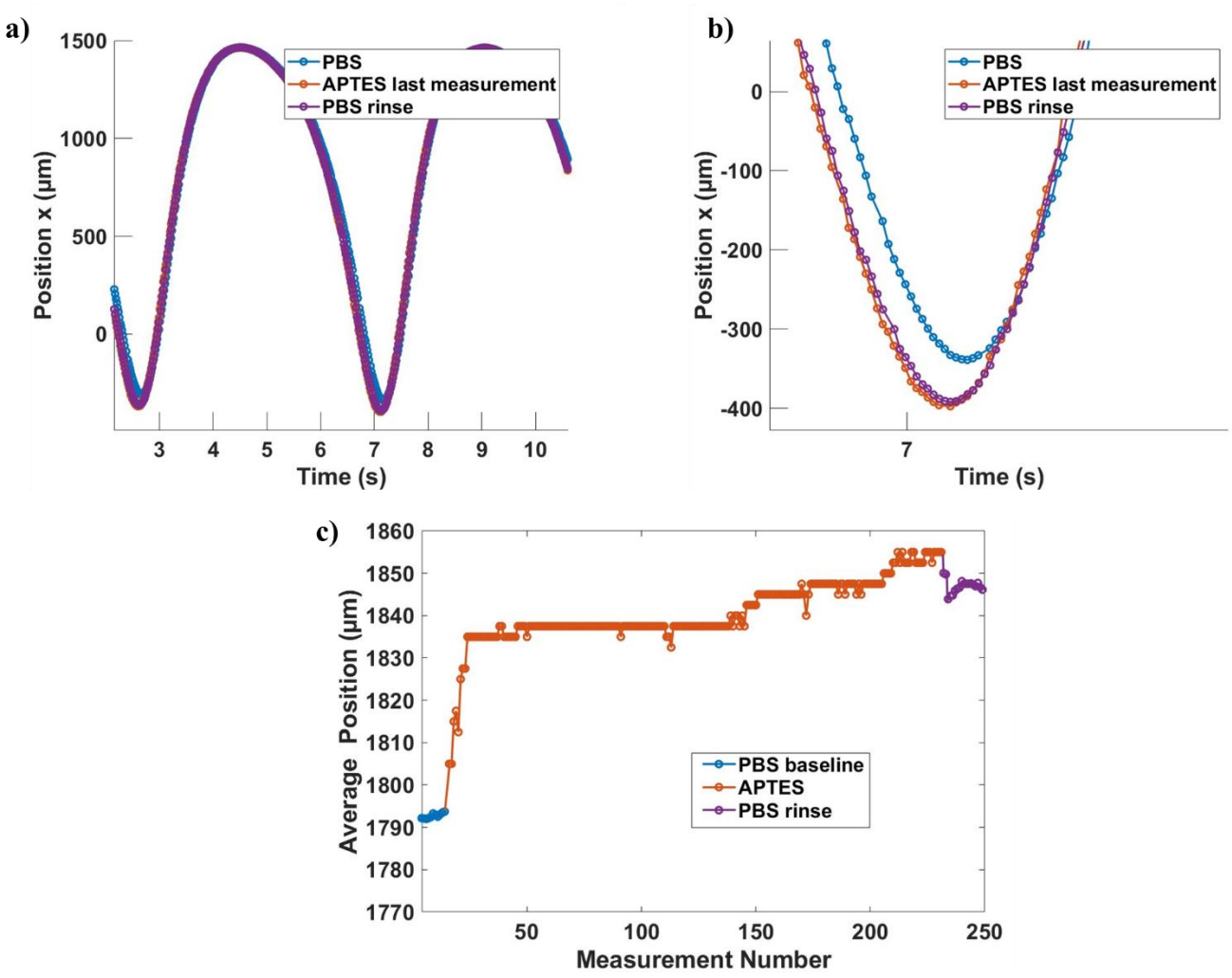


Figure 150 Functionalization of gold with APTES, a) Position x with respect to the waveplate rotation, b) zoom in of (a) and c) GH shift of the minima subtracted from TE.

As previously noted, we observe a shift in the position x curves between PBS and APTES (Figures 150 a and b). Additionally, the PBS rinse and APTES curves are shown to overlap. We then measured a GH shift of 62 µm with respect to the PBS baseline using C1. PBS rinsing removes unbound molecules. The GH shift remaining accounts for 55 µm, showing that APTES molecules are still bound to the gold.

After APTES, c-MET antibodies were incubated for one hour. The results are shown in Figure 153.

License CC BY-NC-ND 4.0

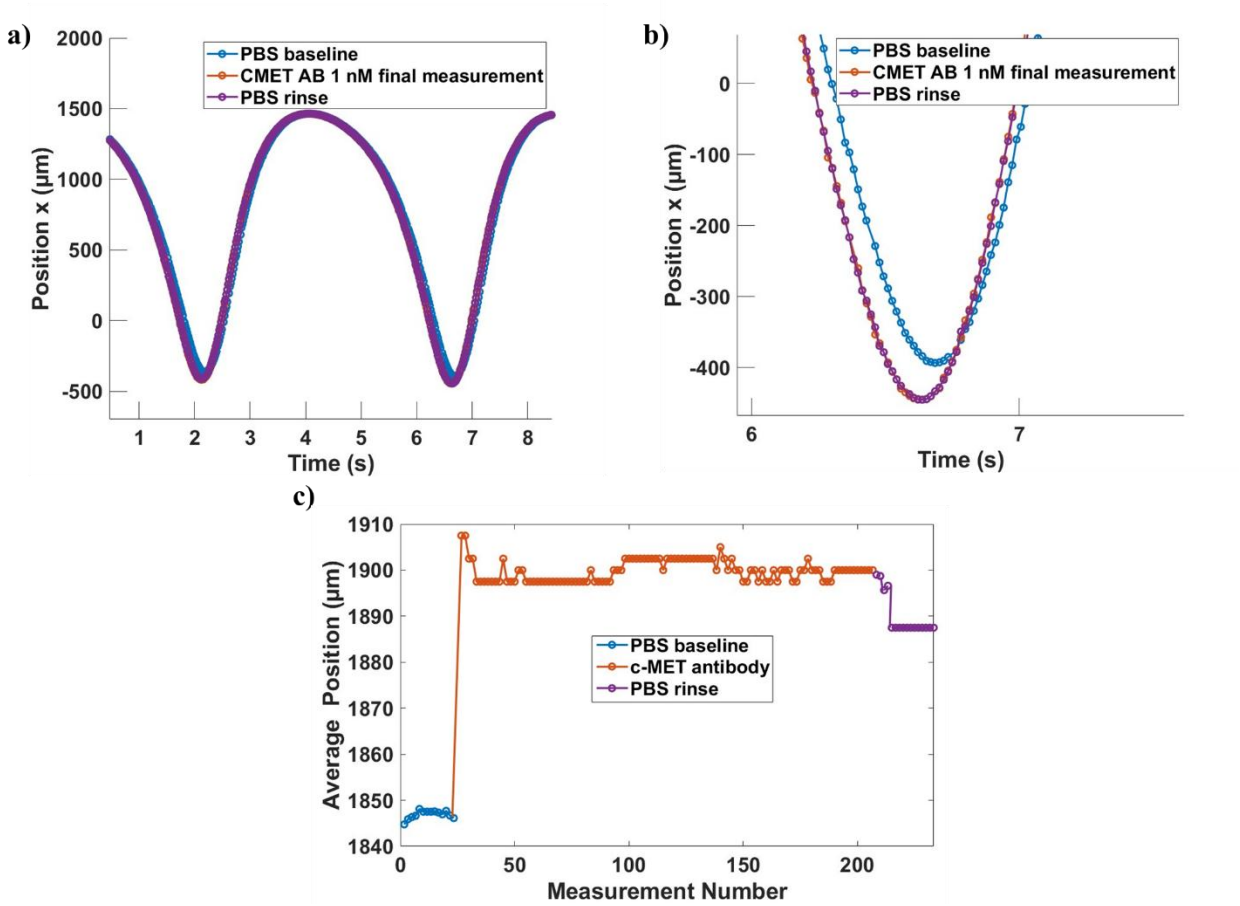


Figure 151 Attachment of c-MET ABs to APTES, a) Position x measured with respect to the waveplate rotation, b) zoom in of (a) and c) GH shift of the minima subtracted from TE.

As previously noted, we detected a shift in the position x following the introduction of the antibodies (Figures 151 a and b). After PBS rinsing, the AB and PBS rinse curves appear to overlap.

The injection of c-MET antibodies resulted in a GH shift of 55 µm measured using C1 (Figure 151-c). The GH shift remaining after the PBS rinse is 44 µm, which further validates the antibodies' binding to APTES.

Following this step, EGFRvIII EVs at 10^6 EVs/ml were injected into the fluidic channel. The results are shown in Figure 152.

License CC BY-NC-ND 4.0

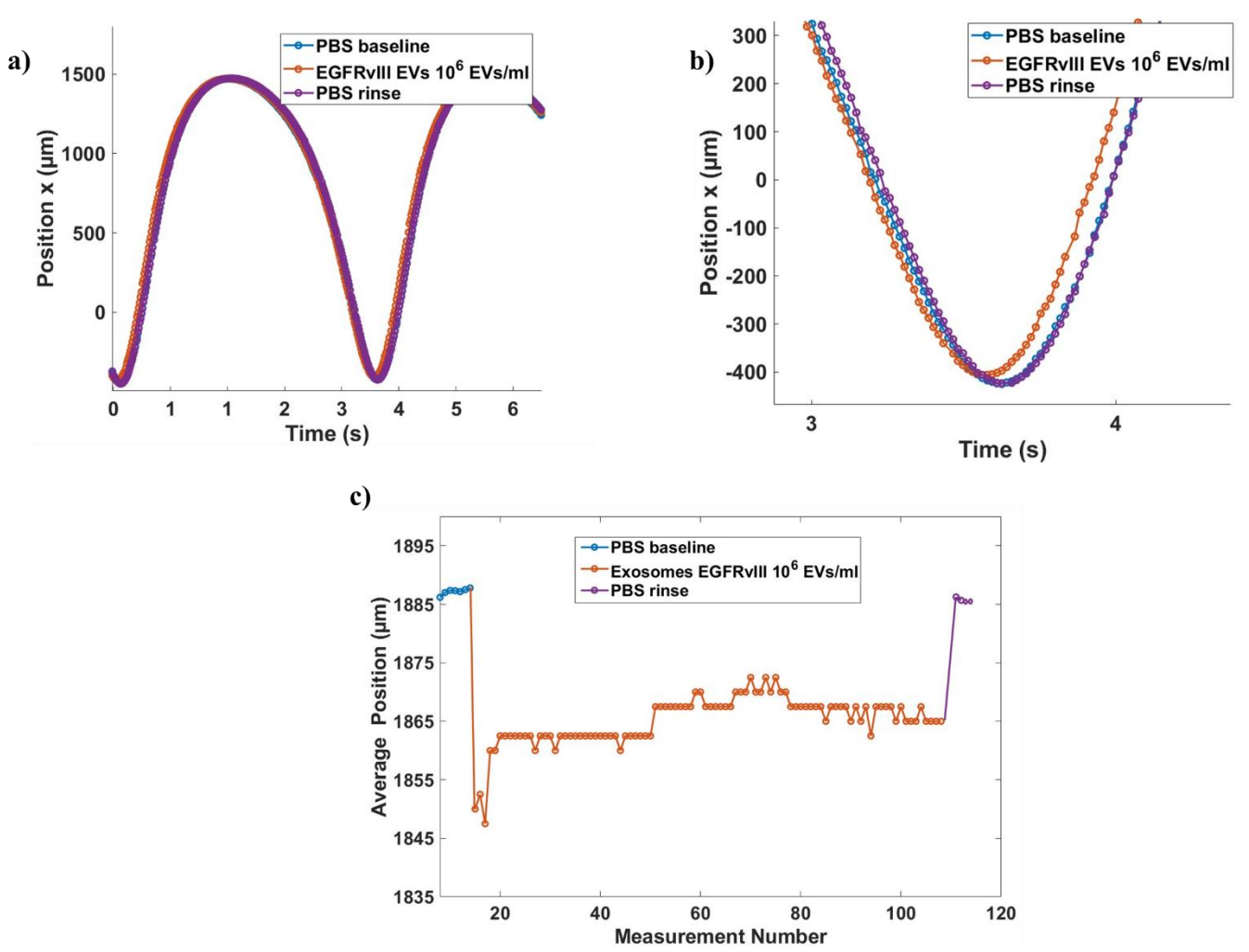


Figure 152 Attachment of EGFRvIII EVs to c-MET ABs, a) Position x of the reflected beam measured with respect to the waveplate rotation, b) zoom in of (a) and c) GH shift of the minima subtracted from TE.

The EVs induced a shift in position x curve with respect to the baseline (Figures 152 a and b). The presence of EVs in the fluidic channel increases the effective refractive index near the metal. Following the washing step, the PBS rinse curve overlaps with the baseline. Additionally, EVs produced a 20 µm GH shift measured using C1 (Figure 152 c), which was completely washed away with PBS. This result confirms the absence of c-MET markers on the surface of EGFRvIII. As such, the control experiment has been validated, indicating the specificity of our measured interactions.

V.5. Optimization of experimental parameters

Throughout this project, the experimental parameters were gradually adjusted to improve the stability, precision and repeatability of the measurements. Initially, the solutions were injected manually using syringes. Also, the fluidic channel was not cleared of solution prior to the next injection. Later on, the experimental protocol was modified, and the fluidic channel was cleared each time before the next solution is injected. This approach reduces the effect of any residual solution in the injection tube. To improve the reproducibility of our measurements we started using a pump syringe. This reduces user errors and injection instabilities resulting from

License CC BY-NC-ND 4.0

hydrodynamic perturbations, such as air bubble problems and inconsistent injection speeds associated with manual injections. Since the flow rate influences the biological interactions inside the fluidic channel, it was necessary to determine the optimal flow rate for injecting the solutions. We conducted additional experiments on two different commercial chips with two injection flow rates (500 µl/min and 1000 µl/min). The functionalization protocol remained the same (we begin by injecting APTES followed by the ABs). The binding curves of CD81 ABs to APTES for the two injection flow rates are shown in Figure 153.

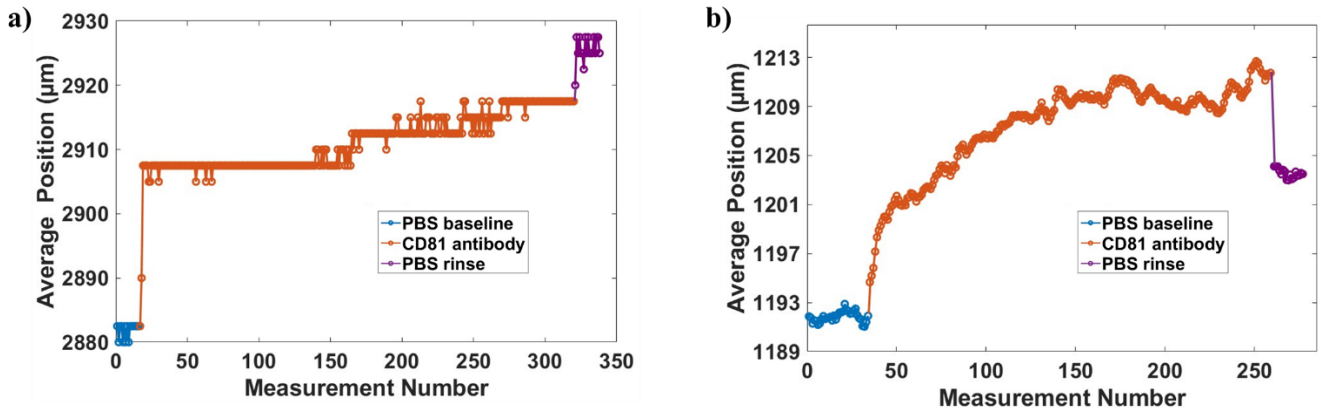


Figure 153 Binding curve of CD81 to APTES adsorbed on a commercial gold chip, a) PBS rinse with a 500 µl/min flow rate and b) PBS rinse with a 1000 µl/min flow rate.

Stronger PBS rinsing flow rates (Figure 153-b, 1000 µl/min) remove weakly bound antibodies. Whereas slower flow rates (Figure a, 500 µl/min) produce an additional shift, rather than rinsing unattached antibodies. Therefore, an injection flow rate of 1000 µl/min was selected for the following experiments to ensure the complete removal of unbound molecules.

Another issue noted during the experiments is that SPR chips were not reusable for more than 4–5 times. Exceeding this limit prevents molecules from attaching due to a lack of available binding sites on the surface of gold. Figure 154 shows the absence of a GH shift between PBS baseline and APTES after using the N24 chip around 7 times.

License CC BY-NC-ND 4.0

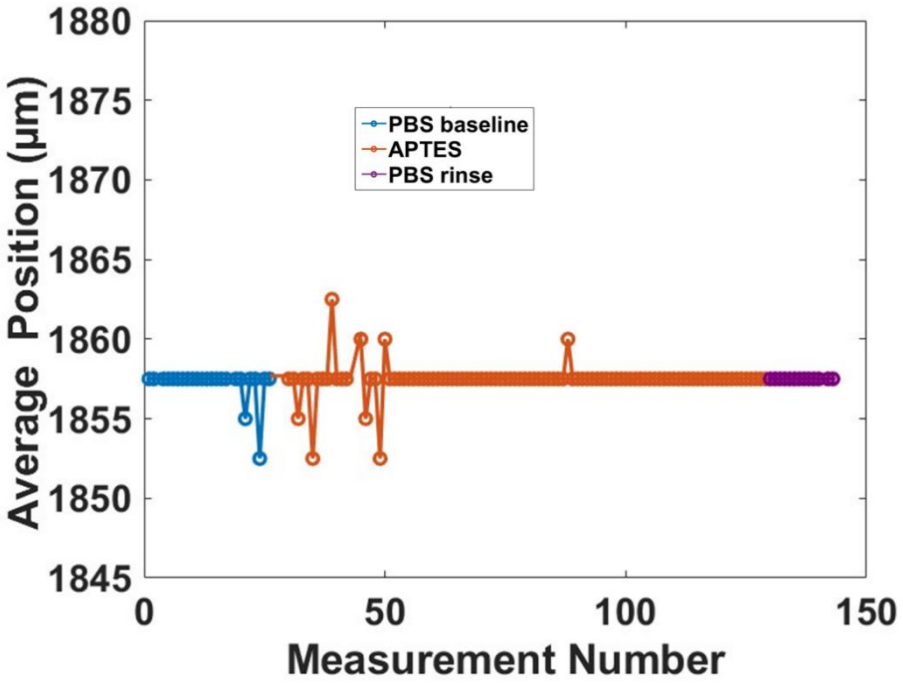


Figure 154 Binding of APTES to gold after using the N24 chip 7 times.

However, by properly adjusting the regeneration protocol, literature suggests that SPR chips could be reused up to 10 times [189]. Additionally, our IRCER colleagues have suggested the possibility of etching the gold surface and redepositing a new one as an alternative to cleaning the gold surface of N24. This approach would be particularly beneficial for chips with NPs, given the significant time required for their fabrication.

V.6. Conclusion

Gold-based SPR chips are biocompatible, making them ideal for bioexperiments and facilitating surface functionalization. It has high affinity for thiol groups which were presumed to be abundant in antibodies. However, it has been proven through fluorescence tests that antibodies have limited free thiol groups. For this reason, a functionalization procedure based on APTES has been proposed. This provides amine groups that electrostatically bind to the negatively charged carboxyl group of the AB. As a result, we have greater control over the orientation of the antibodies, and the Fab antigen-binding sites are left free for binding to EVs.

The prototype with the rotating waveplate configuration, combined with the new N24 SPR chip, could detect U87 MG EVs at concentrations as low as 100 EVs/ml (or 50 particles per 500-µl fluidic channel). Additionally, control experiments proved the absence of c-MET proteins on EGFRvIII antibody surfaces, thus validating the specificity of our experiments.

License CC BY-NC-ND 4.0

Conclusion

This thesis focuses on developing an SPR-based biosensing prototype using the GH detection method. The work performed resulted in a more compact, stable, and easier-to-use version of the reference platform. We presented several theoretical and experimental developments aimed at improving the sensitivity and reliability of our prototype. These findings are summarized in the following paragraphs.

In the first chapter, we presented a general theoretical and bibliographical framework related to SPR. We began by introducing the fundamentals of SPR, followed by the various interrogation methods that can be used to excite SPWs. In our project, we employed the Kretschmann configuration due to its high sensitivity and ease of operation. We then presented classical interrogation methods based on angular, spectral, intensity and phase. Particular attention was given to phase interrogation methods and to the GH shift due to their high sensitivity potential. The GH shift offers an alternative approach to phase, providing a simpler and easier-to-use experimental setup. This chapter concluded by presenting the various commercial SPR platforms available on the market, highlighting their diverse applications, multiplexing capabilities, and automated operation. We highlighted the importance of developing a novel SPR prototype that enhances sensitivity compared to current platforms.

The second chapter was dedicated to the development of the SPR prototype. Firstly, we presented the reference platform originally used in XLIM and highlighted its limitations in terms of bulkiness, instability, and the difficulty of usage. To address these issues, we introduced the new prototype. The new elements include a more compact excitation source, an automatic polarization switching module, controlled attenuation and an easy-to-use SPR module. We also presented the possibility of replacing the PSD-based detection module with a larger, cheaper CCD camera in the future. The second part of this chapter involved studying the stability of the prototype, which was classified into two main categories: mechano-optical and SPR drifts. Optical drifts could be caused by the optical mounts themselves but were not found to affect the stability of the system. Conversely, we found that SPR-related drifts were a significant contributor to the instability of the prototype. These include the deterioration of the refractive index matching oil and the unsuitable holder design. These issues were resolved by ensuring proper storage and sealing of the oil and by designing a new holder. From this perspective, we can propose the use of more stable refractive index matching polymers instead of oil. We also suggested an improved holder design to facilitate the installation of the SPR module. Further miniaturization, automation and integration of the prototype are important future prospects. The prototype is intended to be transportable and easy to use by non-specialists, such as trained biologists and doctors, for cancer detection applications.

The third part of this thesis was dedicated to studying novel SPR chips to enhance GH sensitivity. These chips were first designed using TMM-based simulations and then tested experimentally. Two approaches were analyzed in this regard. The first targets the modification of the substrate by introducing a thin layer of VO_2 deposited on sapphire. With this chip, we obtained a LOD of 4.7×10^{-6} RIU. The second approach involved altering the metallic layer by incorporating Ag NPs inside alumina, with a thin gold layer above. After testing many chips experimentally, we achieved a LOD of 10^{-7} RIU using the optimized N24 chip. Additionally, we performed Lumerical FDTD simulations to better understand the physical mechanisms

License CC BY-NC-ND 4.0

occurring inside the chip. Incorporating Ag NPs in alumina was found to disrupt and modulate the phase map. This resulted in a phase variation that was twice as high compared to the chip without NPs. We also studied the effect of changing the embedding material on the phase response, finding that alumina produced the highest phase sensitivity compared to SiO_2 (with a 12-fold higher phase variation) and air. Finally, we studied the effect of changing the metal of the NPs from Ag to Au. This study validated the choice of Ag NPs due to the higher phase change at resonance (with a variation 12 times higher with Au NPs). Further optimization of the NPs concentration, geometry and surrounding materials could lead to additional improvements in GH sensitivity.

The fourth chapter outlined an improvement to the prototype made at the end of the thesis. This involved the continuous rotation of the waveplate and the simultaneous measurement of the position of the reflected light. In this case, the sensitivity we measured was independent of the uncertainty of TM. We were also able to access the GH shift at multiple polarization angles, which improved the sensitivity of the prototype. Using Jones formalism, we presented a theoretical model to simulate the effect of rotating incident polarization. This involved obtaining intensity curves (of the reflected light) with respect to the incident polarization. We observed changes in the angular positions of the minima and maxima in the intensity curves. The magnitude of this shift was found to depend on the position of P2. However, we were unable to develop a theoretical approach to calculate the GH shift with respect to the incident polarization by setting the GH shift as the first-order derivative of the phase. Therefore, further work is required to achieve this. Experimentally, we tested commercial and N24 chips using a rotating incident polarization configuration. By incrementally rotating the polarization, we found an angular shift in the position of the minima (close to TM) but no shift in the angular position of the maxima (near TE). The TE position was identified as the polarization angle yielding the smallest GH shift and does not correspond to the maxima. After validating this concept, we performed measurements with the polarization in continuous rotation. The sensitivity at intermediate polarization angles was found to be limited by high noise levels due to a lack of synchronization between the PSD and the motor. We also demonstrated the higher sensitivity of this method by comparing it with the GH shift measured at TM polarization. Additional technical work is needed in this regard to develop processing algorithms that can remove noise. A theoretical model must also be established to simulate the effect of the GH shift with respect to the polarization angle.

In the final chapter, these developments were applied to biodetection experiments conducted in collaboration with Captur. The work focused on detecting EVs issued from two glioblastoma cell lines. A surface functionalization protocol was implemented to improve the fixation of ABs on gold and the binding of EVs. The initial results confirmed the ability of the prototype, along with the N24 chip, to detect U87-MG EVs at concentrations as low as 10^2 EVs/ml (or 500 EVs in a 500 µl fluidic channel) using CD81 antibodies. Additionally, a control test based on the detection of EGFRvIII EVs using c-MET antibodies validated the reliability of the prototype and the specificity of the interactions. These findings pave the way for the detection of the glioblastoma biomarker EGFRvIII at low concentrations. Furthermore, future work will focus on detecting glioblastoma biomarkers from actual patient samples. This step is important because it will enable biologists and doctors to monitor the progression of glioblastoma and adjust the course of treatment according to the evolution of the disease. Finally, the prototype could be adjusted to detect other types of cancer that are prevalent in biomedical applications. Further

License CC BY-NC-ND 4.0

research will involve establishing regeneration protocols to effectively clean the gold's surface and improve the SPR chip reusability.

In the end, this thesis contributed to the development of novel SPR approaches based on the GH shift under rotating incident polarization. It also presented an optimized SPR chip, combining theoretical, instrumental and experimental aspects. The results obtained confirm the potential of our method for the realization of ultrasensitive SPR sensors that are compact and adaptable to biodetection applications outside the traditional laboratory environment.

License CC BY-NC-ND 4.0

Bibliography

[1] Generation X and Millennials in U.S. Have Higher Risk of Developing 17 Cancers Compared to Older Generations, New Study Suggests. Am Cancer Soc MediaRoom n.d. https://pressroom.cancer.org/higherriskGenXandMillennials (accessed January 5, 2026).

[2] Global cancer burden growing, amidst mounting need for services n.d. https://www.who.int/news/item/01-02-2024-global-cancer-burden-growing--amidst-mounting-need-for-services (accessed January 5, 2026).

[3] Bhalla N, Jolly P, Formisano N, Estrela P. Introduction to biosensors. Essays Biochem 2016;60:1–8. https://doi.org/10.1042/EBC20150001.

[4] Yoo E-H, Lee S-Y. Glucose Biosensors: An Overview of Use in Clinical Practice. Sensors 2010;10:4558–76. https://doi.org/10.3390/s100504558.

[5] Das S, Devireddy R, Gartia MR. Surface Plasmon Resonance (SPR) Sensor for Cancer Biomarker Detection. Biosensors 2023;13:396. https://doi.org/10.3390/bios13030396.

[6] Khan MZH, Hasan MR, Hossain SI, Ahommed MS, Daizy M. Ultrasensitive detection of pathogenic viruses with electrochemical biosensor: State of the art. Biosens Bioelectron 2020;166:112431. https://doi.org/10.1016/j.bios.2020.112431.

[7] Wang C, Liu M, Wang Z, Li S, Deng Y, He N. Point-of-care diagnostics for infectious diseases: From methods to devices. Nano Today 2021;37:101092. https://doi.org/10.1016/j.nantod.2021.101092.

[8] Zuber AA, Klantsataya E, Bachhuka A. Biosensing. Compr. Nanosci. Nanotechnol., Elsevier; 2019, p. 105–26. https://doi.org/10.1016/B978-0-12-803581-8.10410-2.

[9] Qazi S, Raza K. Smart biosensors for an efficient point of care (PoC) health management. Smart Biosens. Med. Care, Elsevier; 2020, p. 65–85. https://doi.org/10.1016/B978-0-12-820781-9.00004-8.

[10] Vigneshvar S, Sudhakumari CC, Senthilkumaran B, Prakash H. Recent Advances in Biosensor Technology for Potential Applications – An Overview. Front Bioeng Biotechnol 2016;4. https://doi.org/10.3389/fbioe.2016.00011.

[11] Wood RW. On a Remarkable Case of Uneven Distribution of Light in a Diffraction Grating Spectrum. Proc Phys Soc Lond 1902;18:269–75. https://doi.org/10.1088/1478-7814/18/1/325.

[12] Strutt JW. On the dynamical theory of gratings. Proc R Soc Lond Ser Contain Pap Math Phys Character 1907;79:399–416. https://doi.org/10.1098/rspa.1907.0051.

[13] Hessel A, Oliner AA. A New Theory of Wood's Anomalies on Optical Gratings. Appl Opt 1965;4:1275. https://doi.org/10.1364/AO.4.001275.

[14] Palmer CH. Parallel Diffraction Grating Anomalies*. J Opt Soc Am 1952;42:269. https://doi.org/10.1364/JOSA.42.000269.

[15] Palmer CH. Diffraction Grating Anomalies II Coarse Gratings*. J Opt Soc Am 1956;46:50. https://doi.org/10.1364/JOSA.46.000050.

[16] Fano U. The Theory of Anomalous Diffraction Gratings and of Quasi-Stationary Waves on Metallic Surfaces (Sommerfeld's Waves). J Opt Soc Am 1941;31:213. https://doi.org/10.1364/JOSA.31.000213.

[17] Bohm D, Pines D. A Collective Description of Electron Interactions. I. Magnetic Interactions. Phys Rev 1951;82:625–34. https://doi.org/10.1103/PhysRev.82.625.

License CC BY-NC-ND 4.0

[18] Pines D, Bohm D. A Collective Description of Electron Interactions: II. Collective vs Individual Particle Aspects of the Interactions. Phys Rev 1952;85:338–53. https://doi.org/10.1103/PhysRev.85.338.

[19] Bohm D, Pines D. A Collective Description of Electron Interactions: III. Coulomb Interactions in a Degenerate Electron Gas. Phys Rev 1953;92:609–25. https://doi.org/10.1103/PhysRev.92.609.

[20] Ritchie RH. Plasma Losses by Fast Electrons in Thin Films. Phys Rev 1957;106:874–81. https://doi.org/10.1103/PhysRev.106.874.

[21] Ferrell RA. Predicted Radiation of Plasma Oscillations in Metal Films. Phys Rev 1958;111:1214–22. https://doi.org/10.1103/PhysRev.111.1214.

[22] Powell CJ, Swan JB. Effect of Oxidation on the Characteristic Loss Spectra of Aluminum and Magnesium. Phys Rev 1960;118:640–3. https://doi.org/10.1103/PhysRev.118.640.

[23] Otto A. Excitation of nonradiative surface plasma waves in silver by the method of frustrated total reflection. Z Für Phys Hadrons Nucl 1968;216:398–410. https://doi.org/10.1007/BF01391532.

[24] Kretschmann E. Die Bestimmung optischer Konstanten von Metallen durch Anregung von Oberflächenplasmaschwingungen. Z Für Phys Hadrons Nucl 1971;241:313–24. https://doi.org/10.1007/BF01395428.

[25] Nylander C, Liedberg B, Lind T. Gas detection by means of surface plasmon resonance. Sens Actuators 1982;3:79–88. https://doi.org/10.1016/0250-6874(82)80008-5.

[26] Boriskina SV, Cooper TA, Zeng L, Ni G, Tong JK, Tsurimaki Y, Huang Y, Meroueh L, Mahan G, Chen G. Losses in plasmonics: from mitigating energy dissipation to embracing loss-enabled functionalities 2018. https://doi.org/10.48550/ARXIV.1802.01469.

[27] Greffet J-J. Introduction to Surface Plasmon Theory. In: Enoch S, Bonod N, editors. Plasmonics, vol. 167, Berlin, Heidelberg: Springer Berlin Heidelberg; 2012, p. 105–48. https://doi.org/10.1007/978-3-642-28079-5_4.

[28] Raether H. Surface Plasmons on Smooth and Rough Surfaces and on Gratings. vol. 111. Berlin, Heidelberg: Springer Berlin Heidelberg; 1988. https://doi.org/10.1007/BFb0048317.

[29] Lamprecht B, Krenn JR, Schider G, Ditlbacher H, Salerno M, Felidj N, Leitner A, Aussenegg FR, Weeber JC. Surface plasmon propagation in microscale metal stripes. Appl Phys Lett 2001;79:51–3. https://doi.org/10.1063/1.1380236.

[30] Kretschmann E, Raether H. Notizen: Radiative Decay of Non Radiative Surface Plasmons Excited by Light. Z Für Naturforschung A 1968;23:2135–6. https://doi.org/10.1515/zna-1968-1247.

[31] Schasfoort RBM, editor. Front Matter. Handb. Surf. Plasmon Reson. 2nd ed., Cambridge: Royal Society of Chemistry; 2017, p. P001–4. https://doi.org/10.1039/9781788010283-FP001.

[32] Shukla N, Chetri P, Boruah R, Gogoi A, Ahmed GA. Surface Plasmon Resonance Biosensors Based on Kretschmann Configuration: Basic Instrumentation and Applications. In: Biswas R, Mazumder N, editors. Recent Adv. Plasmonic Probes, vol. 33, Cham: Springer International Publishing; 2022, p. 191–222. https://doi.org/10.1007/978-3-030-99491-4_6.

[33] Lee Y, Kim J, Sim S, Llamas-Garro I, Kim J. Air-Gap Interrogation of Surface Plasmon Resonance in Otto Configuration. Micromachines 2021;12:998. https://doi.org/10.3390/mi12080998.

License CC BY-NC-ND 4.0

[34] Fontana E, Kim J, Llamas-Garro I, Oliveira Cavalcanti G. Microfabricated Otto Chip Device For Surface Plasmon Resonance Based Optical Sensing 2015. https://doi.org/10.5281/ZENODO.45548.

[35] Cullen DC, Brown RGW, Lowe CR. Detection of immuno-complex formation via surface plasmon resonance on gold-coated diffraction gratings. Biosensors 1987;3:211–25. https://doi.org/10.1016/0265-928X(87)85002-2.

[36] Popescu A, Savastru D. Efficient Diffraction Grating Coupling of Light with Surface Plasmon Polariton Waves. 2024 Adv. Top. Meas. Simul. At., Constanta, Romania: IEEE; 2024, p. 105–8. https://doi.org/10.1109/ATOMS60779.2024.10921621.

[37] Murugan D, Tintelott M, Narayanan MS, Vu X, Kurkina T, Rodriguez-Emmenegger C, Schwaneberg U, Dostalek J, Ingebrandt S, Pachauri V. Recent Advances in Grating Coupled Surface Plasmon Resonance Technology. Adv Opt Mater 2024;12:2401862. https://doi.org/10.1002/adom.202401862.

[38] Popescu A, Savastru D. Planar Surface Plasmonic Resonance Light Coupling via Transmission Diffraction Gratings for Chemical Optical Sensors. Plasmonics 2025;20:9217–23. https://doi.org/10.1007/s11468-025-02976-8.

[39] Chen L. Optical Devices Based on Symmetrical Metal Cladding Waveguides. In: Xi P, editor. Opt. Devices Commun. Comput., InTech; 2012. https://doi.org/10.5772/48146.

[40] Jorgenson RC, Yee SS. A fiber-optic chemical sensor based on surface plasmon resonance. Sens Actuators B Chem 1993;12:213–20. https://doi.org/10.1016/0925-4005(93)80021-3.

[41] Homola J, Yee SS, Gauglitz G. Surface plasmon resonance sensors: review. Sens Actuators B Chem 1999;54:3–15. https://doi.org/10.1016/S0925-4005(98)00321-9.

[42] Su R, Pei Z, Huang R, Qi W, Wang M, Wang L, He Z. Polydopamine-assisted fabrication of fiber-optic localized surface plasmon resonance sensor based on gold nanoparticles. Trans Tianjin Univ 2015;21:412–9. https://doi.org/10.1007/s12209-015-2693-4.

[43] Maguis S, Laffont G, Ferdinand P, Carbonnier B, Kham K, Mekhalif T, Millot M-C. Biofunctionalized tilted Fiber Bragg Gratings for label-free immunosensing. Opt Express 2008;16:19049. https://doi.org/10.1364/OE.16.019049.

[44] Schasfoort RBM, editor. Front Matter. Handb. Surf. Plasmon Reson. 2nd ed., Cambridge: Royal Society of Chemistry; 2017, p. P001–4. https://doi.org/10.1039/9781788010283-FP001.

[45] Devanarayanan VP, Manjuladevi V, Gupta RK. Surface plasmon resonance sensor based on a new opto-mechanical scanning mechanism. Sens Actuators B Chem 2016;227:643–8. https://doi.org/10.1016/j.snb.2016.01.027.

[46] Thadson K, Sasivimolkul S, Suvarnaphaet P, Visitsattapongse S, Pechprasarn S. Measurement precision enhancement of surface plasmon resonance based angular scanning detection using deep learning. Sci Rep 2022;12:2052. https://doi.org/10.1038/s41598-022-06065-2.

[47] Thadson K, Sasivimolkul S, Suvarnaphaet P, Visitsattapongse S, Pechprasarn S. Measurement precision enhancement of surface plasmon resonance based angular scanning detection using deep learning. Sci Rep 2022;12:2052. https://doi.org/10.1038/s41598-022-06065-2.

[48] Li C-T, Yen T-J, Chen H. A generalized model of maximizing the sensitivity in intensity-interrogation surface plasmon resonance biosensors. Opt Express 2009;17:20771. https://doi.org/10.1364/OE.17.020771.

[49] Hma Salah N, Pal A, Rasul HM, Uniyal A. Sensitivity enhancement of the surface plasmon resonance sensor based on gallium-doped zinc oxide and silicon for cancer detection: A

License CC BY-NC-ND 4.0

wavelength interrogation approach. Micro Nanostructures 2024;186:207736. https://doi.org/10.1016/j.micrna.2023.207736.

[50] Chen Z, Liu L, He Y, Ma H. Resolution enhancement of surface plasmon resonance sensors with spectral interrogation: resonant wavelength considerations. Appl Opt 2016;55:884. https://doi.org/10.1364/AO.55.000884.

[51] Huang YH, Ho HP, Wu SY, Kong SK. Detecting Phase Shifts in Surface Plasmon Resonance: A Review. Adv Opt Technol 2012;2012:1–12. https://doi.org/10.1155/2012/471957.

[52] Huang YH, Ho HP, Kong SK, Kabashin AV. Phase-sensitive surface plasmon resonance biosensors: methodology, instrumentation and applications. Ann Phys 2012;524:637–62. https://doi.org/10.1002/andp.201200203.

[53] Kabashin AV, Patskovsky S, Grigorenko AN. Phase and amplitude sensitivities in surface plasmon resonance bio and chemical sensing. Opt Express 2009;17:21191. https://doi.org/10.1364/OE.17.021191.

[54] Deng S, Wang P, Yu X. Phase-Sensitive Surface Plasmon Resonance Sensors: Recent Progress and Future Prospects. Sensors 2017;17:2819. https://doi.org/10.3390/s17122819.

[55] Kravets VG, Schedin F, Jalil R, Britnell L, Gorbachev RV, Ansell D, Thackray B, Novoselov KS, Geim AK, Kabashin AV, Grigorenko AN. Singular phase nano-optics in plasmonic metamaterials for label-free single-molecule detection. Nat Mater 2013;12:304–9. https://doi.org/10.1038/nmat3537.

[56] Kabashin AV, Kravets VG, Grigorenko AN. Label-free optical biosensing: going beyond the limits. Chem Soc Rev 2023;52:6554–85. https://doi.org/10.1039/D3CS00155E.

[57] Ho AH-P, Wu S-Y, Kong S-K, Zeng S, Yong K-T. SPR Biosensors. In: Ho AH-P, Kim D, Somekh MG, editors. Handb. Photonics Biomed. Eng., Dordrecht: Springer Netherlands; 2017, p. 123–45. https://doi.org/10.1007/978-94-007-5052-4_38.

[58] Sohrabi F, Saeidifard S, Hamidi SM. Plasmonic structures for phase-sensitive ellipsometry biosensing: a review. Opt Quantum Electron 2021;53:710. https://doi.org/10.1007/s11082-021-03356-2.

[59] Wu C-M, Jian Z-C, Joe S-F, Chang L-B. High-sensitivity sensor based on surface plasmon resonance and heterodyne interferometry. Sens Actuators B Chem 2003;92:133–6. https://doi.org/10.1016/S0925-4005(03)00157-6.

[60] Li Y-C, Chang Y-F, Su L-C, Chou C. Differential-Phase Surface Plasmon Resonance Biosensor. Anal Chem 2008;80:5590–5. https://doi.org/10.1021/ac800598c.

[61] Ho HP, Lam WW, Wu SY. Surface plasmon resonance sensor based on the measurement of differential phase. Rev Sci Instrum 2002;73:3534–9. https://doi.org/10.1063/1.1502016.

[62] Kashif M, Bakar A, Arsad N, Shaari S. Development of Phase Detection Schemes Based on Surface Plasmon Resonance Using Interferometry. Sensors 2014;14:15914–38. https://doi.org/10.3390/s140915914.

[63] Kabashin AV, Nikitin PI. Interferometer based on a surface-plasmon resonance for sensor applications. Quantum Electron 1997;27:653–4. https://doi.org/10.1070/QE1997v027n07ABEH001013.

[64] Ho HP, Lam WW, Wu SY. Surface plasmon resonance sensor based on the measurement of differential phase. Rev Sci Instrum 2002;73:3534–9. https://doi.org/10.1063/1.1502016.

License CC BY-NC-ND 4.0

[65] Renard RH. Total Reflection: A New Evaluation of the Goos–Hänchen Shift. J Opt Soc Am 1964;54:1190. https://doi.org/10.1364/JOSA.54.001190.

[66] Wild WJ, Giles CL. Goos-Hänchen shifts from absorbing media. Phys Rev A 1982;25:2099–101. https://doi.org/10.1103/PhysRevA.25.2099.

[67] Wang Y, Zeng S, Crunteanu A, Xie Z, Humbert G, Ma L, Wei Y, Brunel A, Bessette B, Orlianges J-C, Lalloué F, Schmidt OG, Yu N, Ho H-P. Targeted Sub-Attomole Cancer Biomarker Detection Based on Phase Singularity 2D Nanomaterial-Enhanced Plasmonic Biosensor. Nano-Micro Lett 2021;13:96. https://doi.org/10.1007/s40820-021-00613-7.

[68] Schasfoort RBM, editor. Front Matter. Handb. Surf. Plasmon Reson. 2nd ed., Cambridge: Royal Society of Chemistry; 2017, p. P001–4. https://doi.org/10.1039/9781788010283-FP001.

[69] Capelli D, Scognamiglio V, Montanari R. Surface plasmon resonance technology: Recent advances, applications and experimental cases. TrAC Trends Anal Chem 2023;163:117079. https://doi.org/10.1016/j.trac.2023.117079.

[70] Hinman SS, McKeating KS, Cheng Q. Surface Plasmon Resonance: Material and Interface Design for Universal Accessibility. Anal Chem 2018;90:19–39. https://doi.org/10.1021/acs.analchem.7b04251.

[71] Ho AH-P, Wu S-Y, Kong S-K, Zeng S, Yong K-T. SPR Biosensors. In: Ho AH-P, Kim D, Somekh MG, editors. Handb. Photonics Biomed. Eng., Dordrecht: Springer Netherlands; 2017, p. 123–45. https://doi.org/10.1007/978-94-007-5052-4_38.

[72] Multi-Parametric Surface Plasmon Resonance. BioNavis n.d. https://bionavis.com/products/mp-spr/ (accessed January 8, 2026).

[73] Korhonen K, Granqvist N, Ketolainen J, Laitinen R. Monitoring of drug release kinetics from thin polymer films by multi-parametric surface plasmon resonance. Int J Pharm 2015;494:531–6. https://doi.org/10.1016/j.ijpharm.2015.08.071.

[74] Surface Plasmon Resonance | Bruker n.d. https://www.bruker.com/en/products-and-solutions/surface-plasmon-resonance.html (accessed January 9, 2026).

[75] OpenSPR-XT. Nicoya n.d. https://nicoyalife.com/products/spr-instruments/openspr-xt/ (accessed January 9, 2026).

[76] Alto. Nicoya n.d. https://nicoyalife.com/products-overview/alto-digital-spr/ (accessed January 9, 2026).

[77] Overview of Digital Microfluidics | Alto™ Digital SPR. Nicoya Lifesciences Inc n.d. https://nicoyalife.com/blog/digital-microfluidics-integration-with-spr/ (accessed March 24, 2026).

[78] Staff B. Technical Note 101: Principle of SPR Detection: Intensity profile and shift of the SPR angle - Biosensing Instrument 2015. https://biosensingusa.com/technical-notes/technical-note-101-principle-spr-detection-intensity-profile-shift-spr-angle/ (accessed March 24, 2026).

[79] Biosensing Instrument - Biosensing Instrument n.d. https://biosensingusa.com/ (accessed January 9, 2026).

[80] Campbell CT, Kim G. SPR microscopy and its applications to high-throughput analyses of biomolecular binding events and their kinetics. Biomaterials 2007;28:2380–92. https://doi.org/10.1016/j.biomaterials.2007.01.047.

[81] SPR-Advantages n.d. https://www.reichertspr.com/SPR Systems/Technology/SPR-Advantages (accessed March 24, 2026).

[82] Hedhly M, Wang Y, Brunel A, Beffara F, Akil H, Verdier M, Bessette B, Crunteanu A, Ho H-P, Humbert G, Lalloue F, Zeng S. Ultra-sensitive real-time detection of cancer-derived

License CC BY-NC-ND 4.0

exosomes directly from cell supernatants by a large Goos–Hänchen signal generation on plasmonic sensing interface. Biosens Bioelectron X 2023;15:100391. https://doi.org/10.1016/j.biosx.2023.100391.

[83] Raether H. Surface Plasmons on Smooth and Rough Surfaces and on Gratings. vol. 111. Berlin, Heidelberg: Springer Berlin Heidelberg; 1988. https://doi.org/10.1007/BFb0048317.

[84] Brahmachari K, Ray M. Effect of prism material on design of surface plasmon resonance sensor by admittance loci method. Front Optoelectron 2013;6:185–93. https://doi.org/10.1007/s12200-013-0313-2.

[85] Levy D, Camley RE. Enhancement of sensitivity in surface plasmon resonance. AIP Adv 2025;15:035036. https://doi.org/10.1063/5.0245116.

[86] Shalabney A, Abdulhalim I. Electromagnetic fields distribution in multilayer thin film structures and the origin of sensitivity enhancement in surface plasmon resonance sensors. Sens Actuators Phys 2010;159:24–32. https://doi.org/10.1016/j.sna.2010.02.005.

[87] Gupta G, Kondoh J. Tuning and sensitivity enhancement of surface plasmon resonance sensor. Sens Actuators B Chem 2007;122:381–8. https://doi.org/10.1016/j.snb.2006.06.005.

[88] Micheletto R, Hamamoto K, Fujii T, Kawakami Y. Tenfold improved sensitivity using high refractive-index substrates for surface plasmon sensing. Appl Phys Lett 2008;93:174104. https://doi.org/10.1063/1.3005584.

[89] Zain HA, Batumalay M, Harith Z, Rahim HRA, Harun SW. A Graphene/Gold-Coated Surface Plasmon Sensor for Sodium Nitrate Detection. Photonics 2022;9:588. https://doi.org/10.3390/photonics9080588.

[90] Maharana PK, Padhy P, Jha R. On the Field Enhancement and Performance of an Ultra-Stable SPR Biosensor Based on Graphene. IEEE Photonics Technol Lett 2013;25:2156–9. https://doi.org/10.1109/LPT.2013.2281453.

[91] Zeng S, Hu S, Xia J, Anderson T, Dinh X-Q, Meng X-M, Coquet P, Yong K-T. Graphene–MoS2 hybrid nanostructures enhanced surface plasmon resonance biosensors. Sens Actuators B Chem 2015;207:801–10. https://doi.org/10.1016/j.snb.2014.10.124.

[92] Ong BH, Yuan X, Tjin SC, Zhang J, Ng HM. Optimised film thickness for maximum evanescent field enhancement of a bimetallic film surface plasmon resonance biosensor. Sens Actuators B Chem 2006;114:1028–34. https://doi.org/10.1016/j.snb.2005.07.064.

[93] Kushwaha AS, Kumar A, Kumar R, Srivastava SK. A study of surface plasmon resonance (SPR) based biosensor with improved sensitivity. Photonics Nanostructures - Fundam Appl 2018;31:99–106. https://doi.org/10.1016/j.photonics.2018.06.003.

[94] Borah R, Ninakanti R, Bals S, Verbruggen SW. Plasmon resonance of gold and silver nanoparticle arrays in the Kretschmann (attenuated total reflectance) vs. direct incidence configuration. Sci Rep 2022;12:15738. https://doi.org/10.1038/s41598-022-20117-7.

[95] Sayed FA, Elsayed HA, Al-Dossari M, Eissa MF, Mehaney A, Aly AH. Angular surface plasmon resonance-based sensor with a silver nanocomposite layer for effective water pollution detection. Sci Rep 2023;13:21793. https://doi.org/10.1038/s41598-023-48837-4.

[96] Moirangthem RS, Yaseen MT, Wei P-K, Cheng J-Y, Chang Y-C. Enhanced localized plasmonic detections using partially-embedded gold nanoparticles and ellipsometric measurements. Biomed Opt Express 2012;3:899. https://doi.org/10.1364/BOE.3.000899.

License CC BY-NC-ND 4.0

[97] Mostufa S, Akib TBA, Rana MdM, Islam MdR. Highly Sensitive TiO2/Au/Graphene Layer-Based Surface Plasmon Resonance Biosensor for Cancer Detection. Biosensors 2022;12:603. https://doi.org/10.3390/bios12080603.

[98] Khodaie A, Heidarzadeh H. Ultra-sensitive surface plasmon resonance sensor integrating MXene (Ti3C2TX) and graphene for advanced carcinoembryonic antigen detection. Sci Rep 2025;15:13571. https://doi.org/10.1038/s41598-025-97853-z.

[99] Sayed FA, Elsayed HA, Al-Dossari M, Eissa MF, Mehaney A, Aly AH. Angular surface plasmon resonance-based sensor with a silver nanocomposite layer for effective water pollution detection. Sci Rep 2023;13:21793. https://doi.org/10.1038/s41598-023-48837-4.

[100] Wang J, Xu Y, Song Y, Wang Q. Surface Plasmon Resonance Sensor Based on Fe2O3/Au for Alcohol Concentration Detection. Sensors 2024;24:4477. https://doi.org/10.3390/s24144477.

[101] He C, Li Y, Yang Y, Fan H, Li D, Han X. Sensitive Aluminum SPR Sensors Prepared by Thermal Evaporation Deposition. ACS Omega 2023;8:43188–96. https://doi.org/10.1021/acsomega.3c06855.

[102] Zhu S, Jaffiol R, Crunteanu A, Vézy C, Chan S-T, Yuan W, Ho H-P, Zeng S. Label-free biosensing with singular-phase-enhanced lateral position shift based on atomically thin plasmonic nanomaterials. Light Sci Appl 2024;13:2. https://doi.org/10.1038/s41377-023-01345-6.

[103] Troparevsky MC, Sabau AS, Lupini AR, Zhang Z. Transfer-matrix formalism for the calculation of optical response in multilayer systems: from coherent to incoherent interference. Opt Express 2010;18:24715. https://doi.org/10.1364/OE.18.024715.

[104] Xu G, Chen Y, Tazawa M, Jin P. Surface Plasmon Resonance of Silver Nanoparticles on Vanadium Dioxide. J Phys Chem B 2006;110:2051–6. https://doi.org/10.1021/jp055744j.

[105] Jostmeier T, Mangold M, Zimmer J, Karl H, Krenner HJ, Ruppert C, Betz M. Thermochromic modulation of surface plasmon polaritons in vanadium dioxide nanocomposites. Opt Express 2016;24:17321. https://doi.org/10.1364/OE.24.017321.

[106] Johnson PB, Christy RW. Optical Constants of the Noble Metals. Phys Rev B 1972;6:4370–9. https://doi.org/10.1103/PhysRevB.6.4370.

[107] Borowski P, Myśliwiec J. Recent Advances in Magnetron Sputtering: From Fundamentals to Industrial Applications. Coatings 2025;15:922. https://doi.org/10.3390/coatings15080922.

[108] De Oliveira GHI, Escote MT, Nantes IL, Criado D. Versatile r.f. magnetron sputtering doping method to produce aluminum-doped zinc oxide films. J Am Ceram Soc 2024;107:4729–37. https://doi.org/10.1111/jace.19753.

[109] Colin J, Jamnig A, Furgeaud C, Michel A, Pliatsikas N, Sarakinos K, Abadias G. In Situ and Real-Time Nanoscale Monitoring of Ultra-Thin Metal Film Growth Using Optical and Electrical Diagnostic Tools. Nanomaterials 2020;10:2225. https://doi.org/10.3390/nano10112225.

[110] Maurya D, Sardarinejad A, Alameh K. Recent Developments in R.F. Magnetron Sputtered Thin Films for pH Sensing Applications—An Overview. Coatings 2014;4:756–71. https://doi.org/10.3390/coatings4040756.

[111] Jung LS, Campbell CT, Chinowsky TM, Mar MN, Yee SS. Quantitative Interpretation of the Response of Surface Plasmon Resonance Sensors to Adsorbed Films. Langmuir 1998;14:5636–48. https://doi.org/10.1021/la971228b.

[112] Bhatt N, Mehata MS. A Sustainable Approach to Develop Gold Nanoparticles with Kalanchoe fedtschenkoi and Their Interaction with Protein and Dye: Sensing and

License CC BY-NC-ND 4.0

Catalytic Probe. Plasmonics 2023;18:845–58. https://doi.org/10.1007/s11468-023-01814-z.

[113] Svirelis J, Andersson J, Stradner A, Dahlin A. Accurate Correction of the “Bulk Response” in Surface Plasmon Resonance Sensing Provides New Insights on Interactions Involving Lysozyme and Poly(ethylene glycol). ACS Sens 2022;7:1175–82. https://doi.org/10.1021/acssensors.2c00273.

[114] Saftics A, Kurunczi S, Peter B, Szekacs I, Ramsden JJ, Horvath R. Data evaluation for surface-sensitive label-free methods to obtain real-time kinetic and structural information of thin films: A practical review with related software packages. Adv Colloid Interface Sci 2021;294:102431. https://doi.org/10.1016/j.cis.2021.102431.

[115] Thapa DK, Saha SK, Bhattacharyya B, Rajasekar GP, Mahadevu R, Pandey A. Unconventional Optical Response in Engineered Au-Ag Nanostructures 2019. https://doi.org/10.48550/ARXIV.1906.05342.

[116] Zhang H, Xue X. The research progress on corrosion and protection of silver layer. SN Appl Sci 2019;1:464. https://doi.org/10.1007/s42452-019-0495-3.

[117] Du F, Gireau M, Youssef J, Humbert G, Vergnole S, Dumas-Bouchiat F, Champeaux C, Zeng S. Extreme sensitivity label-free biosensing platform based on topologically disruptive phase nano-optics. Microsyst Nanoeng 2026;12:106. https://doi.org/10.1038/s41378-026-01222-3.

[118] Gaudin M, Carles P, Laborde E, Champeaux C, Dumas-Bouchiat F. A dual nanosecond-pulsed laser setup for nanocomposite synthesis—Ag nanoparticles in Al2O3/VO2 matrix. J Appl Phys 2019;125:054301. https://doi.org/10.1063/1.5058107.

[119] Braun MM, Pilon L. Effective optical properties of non-absorbing nanoporous thin films. Thin Solid Films 2006;496:505–14. https://doi.org/10.1016/j.tsf.2005.08.173.

[120] Garahan A, Pilon L, Yin J, Saxena I. Effective optical properties of absorbing nanoporous and nanocomposite thin films. J Appl Phys 2007;101:014320. https://doi.org/10.1063/1.2402327.

[121] Navid A, Pilon L. Effect of polarization and morphology on the optical properties of absorbing nanoporous thin films. Thin Solid Films 2008;516:4159–67. https://doi.org/10.1016/j.tsf.2007.10.117.

[122] Hutchinson NJ, Coquil T, Richman EK, Tolbert SH, Pilon L. Reflectance of surfactant-templated mesoporous silica thin films: Simulations versus experiments. Thin Solid Films 2010;518:2134–40. https://doi.org/10.1016/j.tsf.2009.08.006.

[123] Hutchinson NJ, Coquil T, Navid A, Pilon L. Effective optical properties of highly ordered mesoporous thin films. Thin Solid Films 2010;518:2141–6. https://doi.org/10.1016/j.tsf.2009.08.048.

[124] Niklasson GA, Granqvist CG, Hunderi O. Effective medium models for the optical properties of inhomogeneous materials. Appl Opt 1981;20:26. https://doi.org/10.1364/AO.20.000026.

[125] Battie Y, Resano-Garcia A, Chaoui N, Zhang Y, En Naciri A. Extended Maxwell-Garnett-Mie formulation applied to size dispersion of metallic nanoparticles embedded in host liquid matrix. J Chem Phys 2014;140:044705. https://doi.org/10.1063/1.4862995.

[126] Li ATB, Bakar MAA, Omar AF, Saheed MSM, Taib NAM, Mohammad SM, Krishnan G, Abdullah M. 3rd order optical nonlinearity enhancement of halochromic phenol red dye immobilized in PVA/silica hybrid host matrix. J Sol-Gel Sci Technol 2023;107:523–35. https://doi.org/10.1007/s10971-023-06153-3.

[127] Keita A-S, Naciri AE, Battie Y, Delachat F, Carrada M, Ferblantier G, Slaoui A. Determination of the optical properties and size dispersion of Si nanoparticles within a

License CC BY-NC-ND 4.0

dielectric matrix by spectroscopic ellipsometry. J Appl Phys 2014;116:103520. https://doi.org/10.1063/1.4894619.

[128] Kelly KL, Coronado E, Zhao LL, Schatz GC. The Optical Properties of Metal Nanoparticles: The Influence of Size, Shape, and Dielectric Environment. J Phys Chem B 2003;107:668–77. https://doi.org/10.1021/jp026731y.

[129] Hang Y, Wang A, Wu N. Plasmonic silver and gold nanoparticles: shape- and structure-modulated plasmonic functionality for point-of-caring sensing, bio-imaging and medical therapy. Chem Soc Rev 2024;53:2932–71. https://doi.org/10.1039/D3CS00793F.

[130] Fujiwara H. Spectroscopic Ellipsometry: Principles and Applications. 1st ed. Wiley; 2007. https://doi.org/10.1002/9780470060193.

[131] Hooper IR, Sambles JR. Sensing using differential surface plasmon ellipsometry. J Appl Phys 2004;96:3004–11. https://doi.org/10.1063/1.1778218.

[132] Li K, Wang S, Wang L, Yu H, Jing N, Xue R, Wang Z. Fast and Sensitive Ellipsometry-Based Biosensing. Sensors 2017;18:15. https://doi.org/10.3390/s18010015.

[133] Homola J, Yee SS. Novel polarization control scheme for spectral surface plasmon resonance sensors. Sens Actuators B Chem 1998;51:331–9. https://doi.org/10.1016/S0925-4005(98)00208-1.

[134] Losurdo M, Bergmair M, Bruno G, Cattelan D, Cobet C, De Martino A, Fleischer K, Dohcevic-Mitrovic Z, Esser N, Galliet M, Gajic R, Hemzal D, Hingerl K, Humlicek J, Ossikovski R, Popovic ZV, Saxl O. Spectroscopic ellipsometry and polarimetry for materials and systems analysis at the nanometer scale: state-of-the-art, potential, and perspectives. J Nanoparticle Res 2009;11:1521–54. https://doi.org/10.1007/s11051-009-9662-6.

[135] En Naciri A, Broch L, Johann L, Kleim R. Fixed polarizer, rotating-polarizer and fixed analyzer spectroscopic ellipsometer: accurate calibration method, effect of errors and testing. Thin Solid Films 2002;406:103–12. https://doi.org/10.1016/S0040-6090(01)01777-1.

[136] Ma Z, Lian J, Wang Q-P, Guan W-L, Wu S-L, Gao S, Song P, Wang X. Spectroscopic ellipsometry measurements on an anisotropic crystal: 6H-SiC. Optik 2012;123:1609–12. https://doi.org/10.1016/j.ijleo.2011.09.010.

[137] Arwin H. Application of ellipsometry techniques to biological materials. Thin Solid Films 2011;519:2589–92. https://doi.org/10.1016/j.tsf.2010.11.082.

[138] Li X, Wang C, Ma L, Liu L. Ellipsometry-transmission measurement of the complex refractive indices for a series of organic solvents in the 200–1700 nm spectral range. Infrared Phys Technol 2022;125:104313. https://doi.org/10.1016/j.infrared.2022.104313.

[139] Stchakovsky M, Battie Y, Naciri AE. An original method to determine complex refractive index of liquids by spectroscopic ellipsometry and illustrated applications. Appl Surf Sci 2017;421:802–6. https://doi.org/10.1016/j.apsusc.2016.12.001.

[140] Gu H, Zhu S, Song B, Fang M, Guo Z, Chen X, Zhang C, Jiang H, Liu S. An analytical method to determine the complex refractive index of an ultra-thin film by ellipsometry. Appl Surf Sci 2020;507:145091. https://doi.org/10.1016/j.apsusc.2019.145091.

[141] Youssef J, Zhu S, Crunteanu A, Orlianges J-C, Ho H-P, Bachelot R, Zeng S. Highly Sensitive Plasmonic Biosensors with Precise Phase Singularity Coupling on the Metastructures. Biosensors 2022;12:866. https://doi.org/10.3390/bios12100866.

[142] Zhao X, Wei CM, Yang L, Chou MY. Quantum Confinement and Electronic Properties of Silicon Nanowires. Phys Rev Lett 2004;92:236805. https://doi.org/10.1103/PhysRevLett.92.236805.

License CC BY-NC-ND 4.0

[143] Losurdo M, Bruno G, Kim TH, Choi S, Brown A, Moto A. Nucleation and growth mode of the molecular beam epitaxy of GaN on 4H–SiC exploiting real time spectroscopic ellipsometry. J Cryst Growth 2005;284:156–65. https://doi.org/10.1016/j.jcrysgro.2005.07.016.

[144] Kooij ES, Wormeester H, Brouwer EAM, Van Vroonhoven E, Van Silfhout A, Poelsema B. Optical Characterization of Thin Colloidal Gold Films by Spectroscopic Ellipsometry. Langmuir 2002;18:4401–13. https://doi.org/10.1021/la0256127.

[145] Wormeester H, Henry A-I, Kooij ES, Poelsema B, Pileni M-P. Ellipsometric identification of collective optical properties of silver nanocrystal arrays. J Chem Phys 2006;124:204713. https://doi.org/10.1063/1.2200647.

[146] Flores-Camacho JM, Sun LD, Saucedo-Zeni N, Weidlinger G, Hohage M, Zeppenfeld P. Optical anisotropies of metal clusters supported on a birefringent substrate. Phys Rev B 2008;78:075416. https://doi.org/10.1103/PhysRevB.78.075416.

[147] Ho AH-P, Wu S-Y, Kong S-K, Zeng S, Yong K-T. SPR Biosensors. In: Ho AH-P, Kim D, Somekh MG, editors. Handb. Photonics Biomed. Eng., Dordrecht: Springer Netherlands; 2017, p. 123–45. https://doi.org/10.1007/978-94-007-5052-4_38.

[148] Mandal N, Mayanglambam SD, Moirangthem RS. 3D- printed modular spr platform integrated with ellipsometer for in-situ label-free optical sensing applications. Opt Lasers Eng 2024;181:108422. https://doi.org/10.1016/j.optlaseng.2024.108422.

[149] Rotondi SMC, Canepa P, Bisio F, Cavalleri O, Canepa M. Label-Free Sensing of Coronaviral Sequences via Kretschmann-Configuration Reflectance Spectroscopic Ellipsometry: Sensitivity, Specificity, and Interfacial Effects. Adv Mater Interfaces 2026;13:e00919. https://doi.org/10.1002/admi.202500919.

[150] Caglayan MO, Üstündağ Z, Şahin S. Spectroscopic ellipsometry methods for brevetoxin detection. Talanta 2022;237:122897. https://doi.org/10.1016/j.talanta.2021.122897.

[151] Caglayan MO. Plasmon resonance-enhanced internal reflection ellipsometry for the trace detection of mercuric ion. Int J Environ Sci Technol 2018;15:909–14. https://doi.org/10.1007/s13762-017-1450-8.

[152] Yuan F, Wang Y, Yuan L, Tang T, Ye L, Li Y, Dai X, Cheng H. EGFRvIII-positive glioblastoma contributes to immune escape and malignant progression via the c-Fos-MDK-LRP1 axis. Cell Death Dis 2025;16:453. https://doi.org/10.1038/s41419-025-07771-1.

[153] Department of Neurosurgery, Jordan University Hospital and Medical School, University of Jordan, Amman, Jordan, Tamimi AF, Juweid M, Department of Radiology and Nuclear Medicine, Jordan University Hospital and Medical School, University of Jordan, Amman, Jordan. Epidemiology and Outcome of Glioblastoma. In: Department of Neurosurgery, University Hospitals Leuven, Leuven, Belgium, De Vleeschouwer S, editors. Glioblastoma, Codon Publications; 2017, p. 143–53. https://doi.org/10.15586/codon.glioblastoma.2017.ch8.

[154] Yalamarty SSK, Filipczak N, Li X, Subhan MA, Parveen F, Ataide JA, Rajmalani BA, Torchilin VP. Mechanisms of Resistance and Current Treatment Options for Glioblastoma Multiforme (GBM). Cancers 2023;15:2116. https://doi.org/10.3390/cancers15072116.

[155] Sipos D, Debreczeni-Máté Z, Ritter Z, Freihat O, Simon M, Kovács Á. Complex Diagnostic Challenges in Glioblastoma: The Role of 18F-FDOPA PET Imaging. Pharmaceuticals 2024;17:1215. https://doi.org/10.3390/ph17091215.

[156] Ackerman AB. Biopsy: Why, Where, When, How. J Dermatol Surg Oncol 1975;1:21–3. https://doi.org/10.1111/j.1524-4725.1975.tb00046.x.

License CC BY-NC-ND 4.0

[157] Uecker M, Zhang S, Voit D, Karaus A, Merboldt K, Frahm J. Real-time MRI at a resolution of 20 ms. NMR Biomed 2010;23:986–94. https://doi.org/10.1002/nbm.1585.

[158] Lin E, Alessio A. What are the basic concepts of temporal, contrast, and spatial resolution in cardiac CT? J Cardiovasc Comput Tomogr 2009;3:403–8. https://doi.org/10.1016/j.jcct.2009.07.003.

[159] Van Dijken BRJ, Doff AR, Enting RH, Van Laar PJ, Jeltema H-R, Dierckx RAJO, Van Der Hoorn A. Influence of MRI Follow-Up on Treatment Decisions during Standard Concomitant and Adjuvant Chemotherapy in Patients with Glioblastoma: Is Less More? Cancers 2023;15:4973. https://doi.org/10.3390/cancers15204973.

[160] Ma L, Guo H, Zhao Y, Liu Z, Wang C, Bu J, Sun T, Wei J. Liquid biopsy in cancer: current status, challenges and future prospects. Signal Transduct Target Ther 2024;9:336. https://doi.org/10.1038/s41392-024-02021-w.

[161] Schasfoort RBM, editor. Front Matter. Handb. Surf. Plasmon Reson. 2nd ed., Cambridge: Royal Society of Chemistry; 2017, p. P001–4. https://doi.org/10.1039/9781788010283-FP001.

[162] Doyle L, Wang M. Overview of Extracellular Vesicles, Their Origin, Composition, Purpose, and Methods for Exosome Isolation and Analysis. Cells 2019;8:727. https://doi.org/10.3390/cells8070727.

[163] Nowak M, Górczyńska J, Kołodzińska K, Rubin J, Choromańska A. Extracellular Vesicles as Drug Transporters. Int J Mol Sci 2023;24:10267. https://doi.org/10.3390/ijms241210267.

[164] Indira Chandran V, Gopala S, Venkat EH, Kjolby M, Nejsum P. Extracellular vesicles in glioblastoma: a challenge and an opportunity. Npj Precis Oncol 2024;8:103. https://doi.org/10.1038/s41698-024-00600-2.

[165] Mishra M, Tiwari S, Gomes AV. Protein purification and analysis: next generation Western blotting techniques. Expert Rev Proteomics 2017;14:1037–53. https://doi.org/10.1080/14789450.2017.1388167.

[166] Aydin S, Emre E, Ugur K, Aydin MA, Sahin İ, Cinar V, Akbulut T. An overview of ELISA: a review and update on best laboratory practices for quantifying peptides and proteins in biological fluids. J Int Med Res 2025;53:03000605251315913. https://doi.org/10.1177/03000605251315913.

[167] McKinnon KM. Flow Cytometry: An Overview. Curr Protoc Immunol 2018;120. https://doi.org/10.1002/cpim.40.

[168] Mustafa NH. Comparison of Surface-Plasmon-Resonance Biosensor Measurements and Western Blot Assay for Detection of GPE- Strain of Classical Swine Fever Virus by Using WH211 and WH303 Monoclonal Antibodies. Virol Mycol 2014;03. https://doi.org/10.4172/2161-0517.1000134.

[169] Kim TJ, Cho HS, Park NY, Lee JI. Serodiagnostic Comparison Between Two Methods, ELISA and Surface Plasmon Resonance for the Detection of Antibody Titres of *Mycoplasma hyopneumoniae*. J Vet Med Ser B 2006;53:87–90. https://doi.org/10.1111/j.1439-0450.2006.00917.x.

[170] Wang S, Zhao S, Wei X, Zhang S, Liu J, Dong Y. An Improved Label-Free Indirect Competitive SPR Immunosensor and Its Comparison with Conventional ELISA for Ractopamine Detection in Swine Urine. Sensors 2017;17:604. https://doi.org/10.3390/s17030604.

[171] Clark MJ, Homer N, O'Connor BD, Chen Z, Eskin A, Lee H, Merriman B, Nelson SF. U87MG Decoded: The Genomic Sequence of a Cytogenetically Aberrant Human Cancer Cell Line. PLoS Genet 2010;6:e1000832. https://doi.org/10.1371/journal.pgen.1000832.

License CC BY-NC-ND 4.0

[172] Yuan F, Wang Y, Yuan L, Tang T, Ye L, Li Y, Dai X, Cheng H. EGFRvIII-positive glioblastoma contributes to immune escape and malignant progression via the c-Fos-MDK-LRP1 axis. Cell Death Dis 2025;16:453. https://doi.org/10.1038/s41419-025-07771-1.

[173] Boyer T, Guihard S, Roumier C, Peyrouze P, Gonzales F, Berthon C, Quesnel B, Preudhomme C, Behal H, Duhamel A, Roche-Lestienne C, Cheok M. Tetraspanin CD81 is an adverse prognostic marker in acute myeloid leukemia. Oncotarget 2016;7:62377–85. https://doi.org/10.18632/oncotarget.11481.

[174] Hedhly M, Wang Y, Brunel A, Beffara F, Akil H, Verdier M, Bessette B, Crunteanu A, Ho H-P, Humbert G, Lalloue F, Zeng S. Ultra-sensitive real-time detection of cancer-derived exosomes directly from cell supernatants by a large Goos–Hänchen signal generation on plasmonic sensing interface. Biosens Bioelectron X 2023;15:100391. https://doi.org/10.1016/j.biosx.2023.100391.

[175] Love JC, Estroff LA, Kriebel JK, Nuzzo RG, Whitesides GM. Self-Assembled Monolayers of Thiolates on Metals as a Form of Nanotechnology. Chem Rev 2005;105:1103–70. https://doi.org/10.1021/cr0300789.

[176] Büyükköroğlu G, Şenel B. Engineering Monoclonal Antibodies. Omics Technol. Bio-Eng., Elsevier; 2018, p. 353–89. https://doi.org/10.1016/B978-0-12-804659-3.00016-6.

[177] Coumans RGE, Ariaans GJA, Spijker HJ, Renart Verkerk P, Beusker PH, Kokke BPA, Schouten J, Blomenröhr M, Van Der Lee MMC, Groothuis PG, Ubink R, Dokter WHA, Timmers CM. A Platform for the Generation of Site-Specific Antibody–Drug Conjugates That Allows for Selective Reduction of Engineered Cysteines. Bioconjug Chem 2020;31:2136–46. https://doi.org/10.1021/acs.bioconjchem.0c00337.

[178] Crivianu-Gaita V, Romaschin A, Thompson M. High efficiency reduction capability for the formation of Fab′ antibody fragments from F(ab)2 units. Biochem Biophys Rep 2015;2:23–8. https://doi.org/10.1016/j.bbrep.2015.04.004.

[179] Brückner M, Simon J, Landfester K, Mailänder V. The conjugation strategy affects antibody orientation and targeting properties of nanocarriers. Nanoscale 2021;13:9816–24. https://doi.org/10.1039/D0NR08191D.

[180] Jena SC, Shrivastava S, Saxena S, Kumar N, Maiti SK, Mishra BP, Singh RK. Surface plasmon resonance immunosensor for label-free detection of BIRC5 biomarker in spontaneously occurring canine mammary tumours. Sci Rep 2019;9:13485. https://doi.org/10.1038/s41598-019-49998-x.

[181] Vashist SK, Lam E, Hrapovic S, Male KB, Luong JHT. Immobilization of Antibodies and Enzymes on 3-Aminopropyltriethoxysilane-Functionalized Bioanalytical Platforms for Biosensors and Diagnostics. Chem Rev 2014;114:11083–130. https://doi.org/10.1021/cr5000943.

[182] Yaguchi M, Uchida T, Motobayashi K, Osawa M. Speciation of Adsorbed Phosphate at Gold Electrodes: A Combined Surface-Enhanced Infrared Absorption Spectroscopy and DFT Study. J Phys Chem Lett 2016;7:3097–102. https://doi.org/10.1021/acs.jpclett.6b01342.

[183] Sypabekova M, Hagemann A, Rho D, Kim S. Review: 3-Aminopropyltriethoxysilane (APTES) Deposition Methods on Oxide Surfaces in Solution and Vapor Phases for Biosensing Applications. Biosensors 2022;13:36. https://doi.org/10.3390/bios13010036.

[184] Casula G, Fantauzzi M, Elsener B, Rossi A. XPS and ARXPS for Characterizing Multilayers of Silanes on Gold Surfaces. Coatings 2024;14:327. https://doi.org/10.3390/coatings14030327.

[185] (3-Aminopropyl)triethoxysilane 99 919-30-2 n.d. https://www.sigmaaldrich.com/FR/en/product/aldrich/440140?utm_source=google&utm_

License CC BY-NC-ND 4.0

medium=cpc&utm_id=20847908571&utm_campaign=%7Bcampaignname%7D&utm_content=151884804690&utm_term=aptes+sigma+aldrich&gad_source=1&gad_campaignid=20847908571&gclid=Cj0KCQjwvJHI (accessed December 16, 2025).

[186] Organ SL, Tsao M-S. An overview of the c-MET signaling pathway. Ther Adv Med Oncol 2011;3:S7–19. https://doi.org/10.1177/1758834011422556.

[187] Lal B, Goodwin CR, Sang Y, Foss CA, Cornet K, Muzamil S, Pomper MG, Kim J, Laterra J. EGFRvIII and c-Met pathway inhibitors synergize against PTEN-null/EGFRvIII+ glioblastoma xenografts. Mol Cancer Ther 2009;8:1751–60. https://doi.org/10.1158/1535-7163.MCT-09-0188.

[188] Zhu C, Jiang X, Xiao H, Guan J. Tumor-derived extracellular vesicles inhibit HGF/c-Met and EGF/EGFR pathways to accelerate the radiosensitivity of nasopharyngeal carcinoma cells via microRNA-142-5p delivery. Cell Death Discov 2022;8:17. https://doi.org/10.1038/s41420-021-00794-5.

[189] Sestaioni D, Giurlani W, Ciacci G, Camagni V, Palladino P, Barucci A, Scarano S. Sustainable and effective reconditioning of SPR gold chips functionalized with molecularly imprinted polynorepinephrine. Anal Chim Acta 2024;1321:343037. https://doi.org/10.1016/j.aca.2024.343037.

License CC BY-NC-ND 4.0

Appendices

Appendix 1.....202
Appendix 1.1. HeNe laser specifications 202
Appendix 1.2. PSD specifications.....202
Appendix 1.3. Ondax diode laser specifications 203
Appendix 1.4. Piezoelectric motor specifications 203
Appendix 1.5. Updated holder design.....204
Appendix 1.6. Motorized rotational stage selection guide 205
Appendix 1.7. Specifications of the Brushed DC Servo Motor 206

License CC BY-NC-ND 4.0

Appendix 1.

Appendix 1.1. HeNe laser specifications

Table A1 HeNe Laser specifications.

Specifications	Value
Wavelength (nm)	632.8
Power (mW)	10
Polarization ratio	Linear, 500:1
Linewidth	<< pm
Mode M^2	Single Mode TEM_{00}>95%
Price (k€)	2.5

Appendix 1.2. PSD specifications

Table A2 Specifications of the position sensitive detector (PSD).

Specification	Value
Wavelength range	320 to 1100 nm
Resolution (at 635 nm)	~ 0.75 µm at 100 µW ~ 7.5 µm at 10 µW
Operating power range (at 650 nm)	25 to 100 µW
Laser spot size	Ø0.2 mm to Ø7 mm
Sensor size (active area)	9x9 mm^2
Price	1396 €

License CC BY-NC-ND 4.0

Appendix 1.3. Ondax diode laser specifications

Table A3 Ondax diode laser specifications.

Specification	Value
Supplier	Coherent
Wavelength (nm)	633
Power (mW)	40
Polarization ratio	Linear, 100:1
Beam shape	elliptic Beam Size: 0.6x0.9
Size (mm)	Length: 25.4x76.2
Linewidth	~ pm
Mode M^2	Single Mode TEM_{00}
Price (k€)	3.2

Appendix 1.4. Piezoelectric motor specifications

Table A4 Characteristics of the resonant piezoelectric mount.

Parameter	Value
Travel	360°
Homing repeatability	0.1°
Bidirectional Repeatability	0.05°
Maximum load	50 g
Price	493 €

The movement of rotational mount is assured by 2 piezoelectric motors. When a piezoelectric material (the tip) is excited at its resonance frequency, it undergoes elliptical motion, which pushes the mount into rotation through friction forces. The motor's characteristics, particularly its low price and high accuracy, make it ideal for GH experiments.

License CC BY-NC-ND 4.0

Appendix 1.5. Updated holder design

A newer design has been developed to prevent the prism cracking and ensure uniform oil distribution across the substrate surface. This is achieved by applying an equal tension to all four sides using a torque screwdriver with a preset torque. Additionally, the fluidic channel and tubing were replaced with PEEK components, selected for their biocompatibility. The stability of this design was evaluated. However, the cracking of the substrate occurred when a high torque was applied. On the other side, insufficient torque resulted in measurement drifts. Further investigation is required to determine the optimal tension and fully optimize the design, but due to time constraints, this work was not completed in the scope of this thesis.

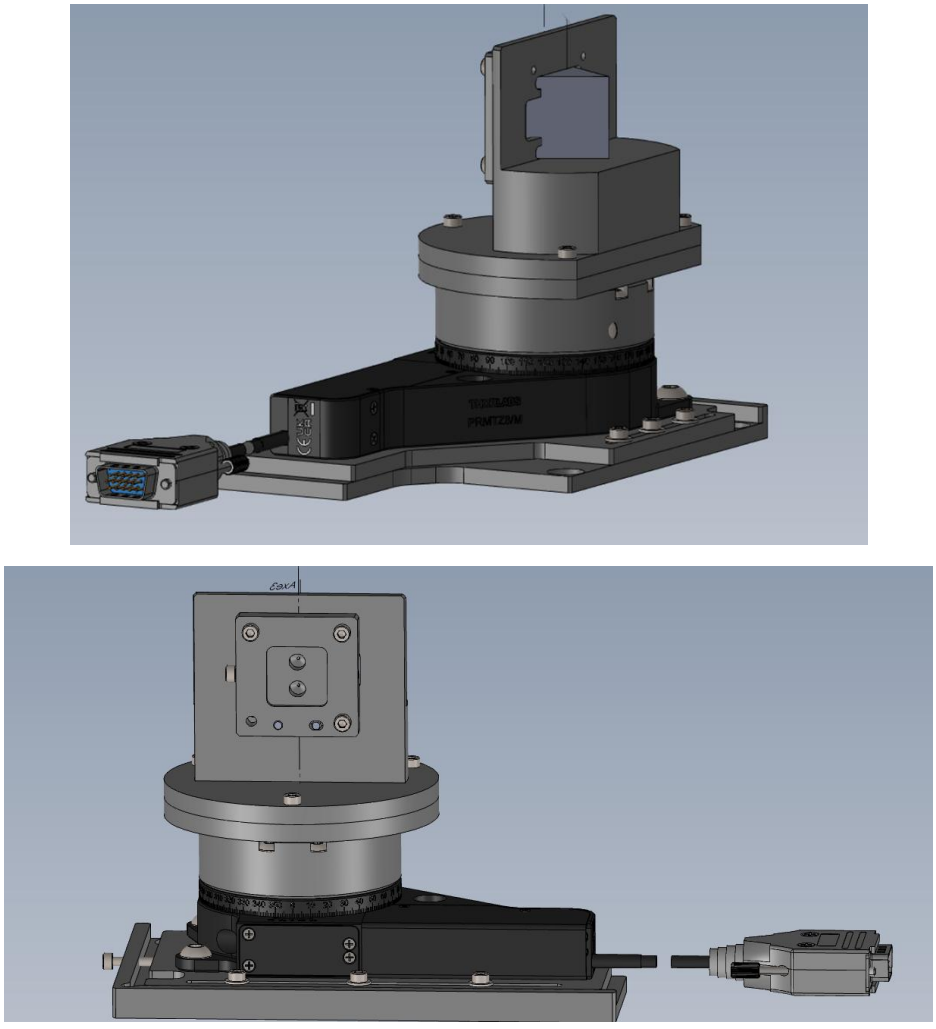


Figure A1 Illustration of the updated final holder design.

License CC BY-NC-ND 4.0

Appendix 1.6. Motorized rotational stage selection guide

Table A5 Rotational stage selection guide.

Supplier	Name	Resolution (°)	Diameter (mm)	Supported load (kg)	Price (k€)
OptoSigma	Small motorized rotation single stage	0.02	25	1	1.353
Thorlabs	Motorized precision rotation stage with dc servo motor	0.0005	66.2	1.5	1.511
	Rotation Stage with Resonant Piezoelectric Motors	0.002	50	0.2	0.276
Newport	Motorized Rotation Stage, PR50CC, Integrated with CONEX-CC Controller	0.02	25.7	1	2.688

Table A5 summarizes the list of motorized stages that were preselected to replace the manual rotational stage in the prototype. The first choice was based on OptoSigma rotational stage due to its smaller size and price. The stage was originally bought but due to technical issues it was replaced by Thorlabs Motorized precision rotation stage with dc servo motor.

License CC BY-NC-ND 4.0

Appendix 1.7. Specifications of the Brushed DC Servo Motor

Table A6 Characteristics of the brushed DC servo motor.

Parameter	Value
Travel	360°
Homing repeatability	0.2°
Bidirectional Repeatability	0.1°
Max Rotation Velocity	25 °/s
Max Acceleration	20 °/s^2
Minimum repeatable Incremental Motion	0.03 °
Maximum vertical load	500 g
Price	1.6 k€

License CC BY-NC-ND 4.0

Développement d'une plate-forme avancée de bio-détection par résonance plasmonique de surface, vers une unité prototype pour le diagnostic du cancer.

Cette thèse porte sur le développement d'un biocapteur à résonance plasmonique de surface (SPR) basé sur la méthode d'interrogation de Goos-Hänchen (GH). Notre objectif principal est de mettre au point une version miniaturisée, stable et plus facile à utiliser de la plateforme existante au sein de XLIM. Parallèlement, de nombreuses puces SPR ont été développées au cours de la thèse afin d'optimiser la sensibilité du prototype. Tous ces développements apportés au prototype ont été appliqués à la détection de vésicules extracellulaires (EV) issues de deux lignées cellulaires de glioblastome. Les résultats démontrent le potentiel de notre approche, qui repose sur le décalage GH et la polarisation incidente rotative, pour la détection sensible d'EVs dans le cadre d'applications biomédicales.

Mots-clés : Résonance plasmonique de surface, plasmons, nanomatériaux

Improvement of advanced surface plasmonic resonance biosensing platform toward a prototype unit for cancer diagnosis.

This thesis focuses on the development of a surface plasmon resonance (SPR) biosensor based on the Goos-Hänchen (GH) interrogation method. Our main objective is to develop a miniaturized, stable, and more user-friendly version of the existing platform at XLIM. In parallel, numerous SPR chips were developed during the thesis to optimize the prototype's sensitivity. All these improvements to the prototype were applied to the detection of extracellular vesicles (EVs) derived from two glioblastoma cell lines. The results demonstrate the potential of our approach, which relies on GH shift and rotating incident polarization, for the sensitive detection of EVs in biomedical applications.

Keywords: Surface plasmon resonance, plasmons, nanomaterials